

**Exploring Scintillometry
in the Stable Atmospheric Surface Layer**

Oscar Hartogensis

Promotor: Prof. dr. A.A.M. Holtslag

Hoogleraar in de Meteorologie en Luchtkwaliteit
Wageningen Universiteit

Co-Promotor: Dr. H.A.R. De Bruin

Universitair hoofddocent bij de Leerstoelgroep
Meteorologie en Luchtkwaliteit, Wageningen Universiteit

Promotiecommissie: Prof. dr. P. Kabat – Wageningen Universiteit

Prof. dr. ir. B.J.J.M. van den Hurk – Universiteit Utrecht

Prof. dr. H.F. Vugts – Vrije Universiteit Amsterdam

Dr. F. Beyrich – Deutscher Wetterdienst, Lindenberg, Duitsland

Dit onderzoek is uitgevoerd binnen de onderzoeksschool “Buys Ballot Onderzoeks-School”.

**Exploring Scintillometry
in the Stable Atmospheric Surface Layer**

**Onderzoek naar Scintillometrie
in de Stabiele Atmosferische Oppervlaktelaag**

O.K. Hartogensis

Proefschrift
ter verkrijging van de graad van doctor
op gezag van de rector magnificus
van Wageningen Universiteit,
Prof. dr. M.J. Kropff,
in het openbaar te verdedigen
op dinsdag 14 Februari 2006
des namiddags te vier uur in de Aula.

ISBN 90-8504-368-9

Voorwoord

Het is een heel goed gevoel dat dit werkstuk er nu eindelijk opzit na jaren van experimenteren, studeren, analyseren, discussiëren en schrijven. Het onderzoek begon feitelijk al in 1999 met het RAPID en CASES-99 experiment in de USA. Toen wist ik nog niet dat ik bezig was data te verzamelen voor mijn eigen proefschrift. Een jaar later haalden Henk de Bruin, de initiator van onze deelname aan deze projecten, en de toen pas aangestelde professor Bert Holtslag, een NWO project binnen op basis van de CASES-99 data-set. Ik was een logische kandidaat en vanaf 2001 begon de promotie officieel. Nu ligt er, ruim 6 jaar na het CASES-99 experiment, dit proefschrift op tafel.

Vanaf hier gaat het voorwoord verder als dankwoord, want het proefschrift is mede tot stand gekomen dankzij de hulp en bijdrage (in allerlei vormen) van anderen.

Allereerst wil ik mijn co-promotor Henk de Bruin bedanken. Henk, je hebt zeer veel betekend voor mijn ontwikkeling als onderzoeker, maar ook voor andere zaken. Dat begon al tijdens mijn studie, toen je mijn interesse voor het vakgebied wekte middels je college micro-meteorologie. Vervolgens gaf je me de mogelijkheid naar Mexico te gaan, waar ik in aanraking kwam met het onderwerp scintillometrie, en - nog belangrijker - waar ik Maria heb ontmoet. Je regelde ook meteen een baantje voor me toen ik uit het vakgebied dreigde te geraken. We hebben samen ook veel meegemaakt op internationale reizen: bijbeldiscussies met Rick in de hot-springs van Idaho, de tour door Damascus van Di'ya (alles was "very old"), de workshop in de oase van Palmyra, en scintillometer plannen maken in de Dode Zee. Je manier van werken is vaak als de stromingen die we proberen te beschrijven: turbulent, dwz vol energie en hectisch. Ik bewonder je energie en dat je door alle hectiek heen altijd de kern van de zaak blijft zien. Bedankt voor je bijdrage aan dit proefschrift, maar ook voor je lessen over het reilen en zeilen in de wetenschappelijke wereld (let op "je eigen winkeltje").

Tevens wil ik mijn promotor Bert Holtslag bedanken. Vooral in de afrondende fase ben je je meer met het proefschrift gaan bemoeien, en gaf je een goede aanvulling op de begeleiding die ik tot dan toe voornamelijk van Henk had ontvangen. Je had oog voor "het proces" en gaf me het vertrouwen dat het allemaal wel goed zou komen, ook toen het met schrijven even wat minder ging. Bedankt.

Verder wil ik iedereen van de vakgroep Meteorologie en Luchtkwaliteit bedanken voor de gezelligheid in de groep die vorm krijgt tijdens de 10-uur koffiepauze. Een aantal mensen wil ik in het bijzonder noemen.

Allereerst de paranimfen Wouter en Bas. We zijn van dezelfde generatie en onze "tijdelijke" aanstellingen houden ons nu al een kleine 10 jaar verbonden aan de groep. In het begin bleven we nog wel eens (te) lang werken na een hapje eten in de mensa. Tegenwoordig wachten

vrouw en kind(eren) thuis op ons en is de frequentie van het mensa-eten en een biertje in de kroeg duidelijk minder. Wouter, we vormen samen een uitstekend team als het om opzetten van veldexperimenten gaat. Dank voor al je hulp bij mijn experimenten en oplossen van LAS-problemen. Bas, als jonge garde binnen de groep is het aan ons om de brug tussen de experimentators en theoretici in de groep (ook fysiek gescheiden op verschillende verdiepingen in het gebouw) te overbruggen.

Gerrie en Kees; je leest het in elk voorwoord van elk proefschrift uit onze groep, want het is nu eenmaal zo; jullie vormen de smering die ervoor zorgt dat de vakgroep goed draait, zonder jullie loopt de machine hopeloos vast. Gerrie, dank voor al je goede en persoonlijke zorg bij de afhandeling administratieve zaken. Kees, dank voor de oplossingen die je altijd had voor computerproblemen op- en buiten het werk, als ook je bijdrage aan de computer infrastructuur rond veldexperimenten (de Libretto's!).

Arjan en Arnold; als niet-begeleiders leverden jullie op de achtergrond behoorlijk wat begeleiding middels discussies, praktische tips, en instant opvulling van kennishiaten. Heren bedankt, niet in de laatste plaats ook voor de ontwikkeling van EC-pack!

In een zelfde rol, maar op geheel eigen wijze, heeft Wim Kohsiek mij ook veel geholpen. Zijn kennis van het onderwerp scintillometrie is ongeëvenaard in Nederland. Ook verschaft hij talrijke, voor ons soms ontoegankelijk, publicaties. Wim bedankt.

Willy en Bert; ik wil jullie beiden bedanken voor de professionele hulp op mechanisch (Willy) en elektronisch (Bert) gebied die jullie hebben geleverd ten behoeve van de veldexperimenten.

Jordi: het was op jouw initiatief dat we mee hebben gedaan met het BBC experiment op Cabauw. Aparte de eso, tienes un espíritu abierto que me cae bien y gracias por ser el mas asiduo cliente de la tortillería de Maria.

Dank ook aan de promotiecommissie bestaande uit Prof. dr. Pavel Kabat, Prof. dr. ir. Bart van den Hurk, Prof. dr. Hans Vugts, en Dr. Frank Beyrich voor het lezen en beoordelen van het proefschrift. Special thanks in this respect goes to Frank Beyrich for carefully revising the manuscript and noting down the many (textual) errors. Frank, thank you very much for this effort that improved the quality of the manuscript considerably.

Chris and Julio; thank you for always having a desk for me available at IMADES every time I visited Maria and Elena in Hermosillo.

Vader en moeder; jullie zijn er altijd voor mij geweest, en zijn er nu ook voor Maria en Elena. Dit werk is ook een product van alles dat ik van jullie heb ontvangen en meegekregen. Dank jullie wel voor alles.

Maria y Elena; pasamos una época de tiempos bastante turbulentos, pero ya desde hace algunos años hemos llegado juntos a una nueva etapa en nuestras vidas. Estoy muy contento de que por fin podemos vivir como una familia. Esto y el amor que recibo de ustedes han sido y es de gran apoyo para terminar este trabajo. Las quiero mucho.

Abstract

The main objective of this thesis is to investigate observation methods of heat and momentum exchange and key variables that characterise turbulence in the atmospheric stable surface layer (SSL), a layer defined as the lower part of the stable boundary layer (SBL) where surface fluxes do not change significantly with height. The SBL is often confined to a shallow layer above the surface and is often intermittent, i.e. quiescent periods with almost laminar flow are interchanged with turbulent bursts. These conditions complicate surface flux measurements considerably, since ideally these then need to take place close to the surface and over short flux averaging intervals. Scintillometers, unlike traditional flux measurement techniques such as eddy covariance (EC), can be operated just above the surface (< 1 m) and over short flux averaging intervals (< 1 minute). These features have led us to explore in more detail the applicability of scintillometers in the SSL.

Two types of scintillometers will be considered, notably the displaced-beam small-aperture scintillometer (DBSAS) and the large-aperture scintillometer (LAS) deployed in three field campaigns we contributed to as part of this thesis: RAPID in Idaho, USA, (1999), CASES-99 in Kansas, USA (1999) and BBC in Cabauw, the Netherlands (2001). In addition, an old dataset is analysed with LAS data gathered during the La Poza experiment in Sonora, Mexico (1996).

The DBSAS and the LAS are optical instruments that consist of a transmitter and a receiver. The receiver records intensity fluctuations of the light beam emitted by the transmitter, which are caused by refraction of the beam upon its passage through the turbulent surface layer. These intensity fluctuations are a measure of the structure parameter of temperature, C_T^2 . The DBSAS obtains also the dissipation rate of turbulent kinetic energy, ε , from the correlation between the two displaced beams. In itself, these quantities are important properties of turbulence. Moreover, when the flow is turbulent they are related to the turbulent fluxes of sensible heat, H , and momentum, τ , usually expressed by the velocity scale u^* , by virtue of Monin-Obukhov similarity theory (MOST).

The DBSAS is the most suitable scintillometer to be used in the SBL, since it gives a measure of the mechanically induced turbulence (i.e. ε), which is the only turbulence generating mechanism in stable conditions. For the LAS - that does not measure ε - the mechanical turbulent transport is usually included using wind speed measurement and an estimate of the roughness length.

Several detailed aspects of the application of scintillometry and EC in obtaining ε , C_T^2 , H and τ are discussed. The most general aspects presented are the following. For CASES-99 and BBC we compared the DBSAS performance against EC in obtaining ε , C_T^2 , H and τ over a wide range of stable conditions and conclude that the DBSAS is superior in obtaining turbulence information over short intervals with remarkably little scatter, but that the derived parameters contain systematic errors. When corrected for the systematic errors (using ad-hoc

solutions) the DBAS appears to provide accurate C_T^2 , ε and resulting H , and τ for short time intervals and close to the ground. In addition, for the BBC we also investigated the LAS and combinations of LAS and DBSAS to jointly solve ε and C_T^2 for both stable and unstable conditions. Furthermore, for CASES-99 we derived new MOST relations for ε and C_T^2 and show how these can be used to evaluate the MOST relations for dimensionless wind speed and temperature gradients. Also, alternative scaling parameters based on ε and C_T^2 are introduced. Last, we investigated an important practical aspect of the scintillometer application, i.e. what effective height to use to calculate H when the beam-height of the instrument varies along the path. This is done based on a data-set from the La Poza experiment in Sonora, Mexico (1996).

Contents

Voorwoord	i
Abstract	iii
Contents.....	v
Chapter 1 Introduction	1
1.1 Backgrounds and objectives	1
1.2 Thesis Structure.....	10
Appendix 1A SBL regime observations with EC system	12
Chapter 2 Description of the Field Experiments and Data Analysis	15
2.1 Introduction	15
2.2 CASES-99 experiment	15
2.2.1 Overview CASES-99 experiment	15
2.2.2 Weather conditions CASES-99 experiment.....	18
2.2.3 Instrumentation CASES-99 experiment.....	19
2.3 RAPID experiment	23
2.3.1 Outline RAPID experiment	23
2.3.2 Weather conditions RAPID experiment.....	26
2.3.3 Instrumentation RAPID experiment.....	28
2.4 BBC experiment	30
2.4.1 Overview BBC experiment	30
2.4.2 Weather conditions BBC experiment.....	31
2.4.3 Instrumentation BBC experiment.....	33
2.5 Data Analysis	34
2.5.1 Structure functions and spectra	35
2.5.1.1 Definitions of moments and structure functions	35
2.5.1.2 Definitions of spectra	37
2.5.1.3 Theoretical atmospheric spectra and structure functions	38
2.5.1.4 Measuring atmospheric spectra	41
2.5.2 C_T^2 and ε from sonic anemometer data	43
2.5.2.1 C_T^2 and ε from sonic anemometer data using structure functions.....	43
2.5.2.2 C_T^2 and ε from sonic anemometer data using spectra	44
2.5.3 C_T^2 and ε from scintillometer data	47
2.5.4 Turbulent fluxes from sonic anemometer data.....	49
2.5.5 Turbulent fluxes from scintillometer data.....	53
Appendix 2A Details on the Eddy Covariance measurements	55

Chapter 3	Displaced-Beam Small Aperture Scintillometer test Part II:	
	CASES-99 stable boundary-layer experiment	59
3.1	Introduction	59
3.2	Theory	60
3.2.1	Determining ε and C_T^2 with a Displaced Beam Small Aperture Scintillometer	60
3.2.2	Determining ε and C_T^2 from eddy-covariance measurements.....	65
3.2.3	Deriving u^* and θ^* from ε and C_T^2 measurements with similarity theory.....	67
3.2.4	Sensitivity of u^* and θ^* to errors in l_0 and C_T^2	67
3.3	Site and data	70
3.4	Results	71
3.4.1	Space and time averaging of turbulence by scintillometers.....	71
3.4.2	DBSAS compared with eddy-covariance data	74
3.4.3	Reanalysed DBSAS data with an adjusted beam displacement.....	79
3.5	Discussion	79
3.6	Conclusions	81
	Acknowledgements	82
	Appendix 3A Path averaging effect of a sonic anemometer in determining C_T^2	83
	Appendix 3B Log-normal averaging of ε and C_n^2	86
	Appendix 3C Dissipation range spectra and ε and C_n^2	89
	Appendix 3D Adjusting the r_{12} versus l_0 relation	91
	Appendix 3E Direct flux estimates from raw DBSAS statistics.....	93
Chapter 4	Monin-Obukhov similarity functions of C_T^2 and ε in the	
	Stable Boundary Layer.....	95
4.1	Introduction	95
4.2	Theory	96
4.2.1	Similarity functions f_ε and f_T for ε and C_T^2	97
4.2.2	Similarity functions ϕ_m and ϕ_h for $\delta u/\delta z$ and $\delta\theta/\delta z$	98
4.3	Experimental	99
4.3.1	Data description.....	99
4.3.2	Determining C_T^2 and ε from raw time series.....	100
4.4	Results and discussion.....	101
4.4.1	Scaling functions for ε	102
4.4.2	Scaling functions for C_T^2	107
4.4.3	Spurious correlations.....	111
4.4.4	Direct flux estimates from ε and C_T^2	112
4.4.5	Fluxes from ε and C_T^2 in intermittent turbulent conditions.....	113
4.5	Conclusions	114
	Acknowledgements	116
	Appendix 4A MOST functions applied for DBSAS in CASES-99.....	116

Chapter 5	Comparison of Field Scale Scintillometers: the BBC experiment at Cabauw	117
5.1	Introduction	117
5.2	Theory	120
5.2.1	Displaced Beam Small Aperture Scintillometer (DBSAS)	120
5.2.2	Large Aperture Scintillometer (LAS)	121
5.2.3	Combined DBSAS and LAS	122
5.2.4	Calculation of turbulent fluxes	123
5.3	Experiment description and Data treatment	126
5.4	Results and Discussion	128
5.4.1	Displaced Beam Small Aperture Scintillometer (DBSAS)	128
5.4.2	Large Aperture Scintillometer (LAS)	133
5.4.3	Combined DBSAS and LAS	136
5.5	Conclusions	139
Appendix 5A	Inner scale sensitivity of the LAS	141
Appendix 5B	Comparing or combining ε and C_T^2 taken at different heights	143
Appendix 5C	Test of Monin-Obukhov scaling functions for ε and C_T^2	146
Chapter 6	Derivation of an effective height for scintillometers: La Poza experiment in Northwest-Mexico	147
6.1	Introduction	147
6.2	Theory	148
6.2.1	Determining the sensible heat flux with a large-aperture scintillometer	148
6.2.2	Derivation of an effective scintillometer height	151
	<i>Slant paths</i>	153
	<i>Topography</i>	154
	<i>Curvature of the earth's surface</i>	155
6.3	Site and instrument description	155
6.4	Results and discussion	157
6.4.1	Calculation of the effective height	157
6.4.2	Comparison of LAS with eddy-covariance results	161
6.5	Conclusions	165
	Acknowledgements	166
Appendix 6A	H sensitivity to Z_{LAS}	166
Appendix 6B	Calculation of Z_{eff_Full} from Equations (6.6) and (6.12)	167
Appendix 6C	Effect of the earth's curvature on the effective height	168
Appendix 6D	Sensible heat flux for Stable Conditions	169
Chapter 7	Summary and Conclusions	171
Appendix I	List of Field Experiments and Related Publications	177
Appendix II	Co-Author Publication – CASES-99	185

Appendix III Co-Author Publication - RAPID	201
References	213
Samenvatting	221
Curriculum Vitae	227

Chapter 1 Introduction

1.1 Backgrounds and objectives

The research presented in this thesis deals with the energy and momentum exchange at the land surface in the stable atmospheric boundary layer (SBL). The atmospheric boundary layer is that part of the atmosphere that is directly influenced by the earth's surface and responds to surface forcings on a timescale of about an hour or less (Stull, 1988). The lowest part of the boundary layer where the surface fluxes do not change more than ~10 % is referred to as the surface layer (e.g. Holtslag and Nieuwstadt, 1986). The atmospheric boundary layer is considered stable when it has a stable stratification, i.e. the potential air temperature is higher than the surface temperature. Over land, SBLs will typically develop at nighttime, in particular during clear sky conditions. Nevertheless, they can also exist during special daytime conditions at low solar angles or when warm air is advected over a cool (evaporating) surface. Our main focus will be on nighttime SBLs, but we will also pay attention to the daytime case. The main transport mechanism of energy and momentum in the atmosphere is *turbulence*. The magnitude of turbulence during nighttime is generally less than that during daytime and is characterised by intermittent bursts of activity. Given the layered structure of the nocturnal boundary layer, the spatial and temporal characteristics of turbulent activity (and resulting vertical mixing) can have a significant effect on local air quality at hourly to diurnal scales. However, while there is a wealth of information concerning turbulent processes operating during daytime conditions, until recently comparatively few studies have focused on the nocturnal case (Salmond and McKendry, 2005).

Turbulence is nowadays considered the last great, unsolved problem of classical physics. Only a very limited amount of laboratory turbulence processes can be resolved from first physical principles. Turbulent processes in the atmosphere can only be described through similarity approaches, which inevitably require experimental work. We state that experiments are a crucial part in broadening our current understanding of the processes that take place in the SBL. For that reason, an important part of the work done in the context of this PhD-thesis project consisted of gathering accurate experimental data under a wide range of stable conditions. We participated in two international field campaigns in 1999, RAPID and CASES-99. CASES-99 took place in October 1999 in Kansas, USA. It was set-up to study all possible aspects of the *nighttime* SBL (more on CASES-99 can be found in Section 2.1). The dominant vegetation type was prairie grass. RAPID took place in August-September 1999 in Idaho, USA. RAPID dealt with the *daytime* SBL that forms when dry desert wind flows over irrigated agricultural fields. In 2001 we participated in the BBC campaign that took place at

Cabauw, the Netherlands over grassland, where we tested some of our CASES-99 semi-empirical results.

Apart from gathering and processing, also fully analysing these extensive data sets proved too much to be carried out in one PhD-project. For that reason we will confine ourselves primarily to the analyses of the CASES-99 and the BBC data. Nevertheless, the three data sets have been made available to other research groups, such as the GEWEX-GABLS research group, the RAPID community and the groups participating in BBC. Two publications based on the RAPID and CASES-99 data-sets in which the candidate co-authored are added to this thesis in the Appendix. Other publications based on these data-sets are: Moene (2003) who used CASES-99 and RAPID data, Van Dijk et al. (2006) who use RAPID data and Steeneveld et al. (2006a and b) who use CASES-99 data. An overview of the twelve field campaigns and resulting publications in which the author participated in are given in Appendix I.

In this thesis we focus on measurements of surface fluxes and other parameters that characterise turbulence in the SBL. The eddy-covariance (EC) method is nowadays considered as the standard tool for estimating surface fluxes, since it directly measures the energy transporting eddies and no similarity theory has to be applied. Although being pretty straightforward conceptually, in practice there are many pitfalls and additional corrections that need to be applied. In addition, in the highly non-stationary and often very shallow SBL the EC method has two distinct disadvantages. First, it requires stationary conditions for at least 10 minutes to gather a statistically stable flux. Secondly, in very stable conditions a significant portion of the turbulent eddies will be smaller than the instruments path and therefore will not be accounted in the measured flux. *This motivated us to explore in more detail the applicability of scintillometers in the SBL.*

The scintillometers used in this thesis are optical instruments that consist of a transmitter and receiver and operate over a path-length of 0.1 to 10 km, depending on the type of scintillometer. They measure intensity fluctuations of the light beam emitted by the transmitter and registered by the receiver, which are a result of the beam's propagation through the turbulent atmosphere.

We used a displaced-beam small-aperture (or laser) scintillometer (DBSAS), which can be operated over distances of 100 – 250 m and the principle physical parameters obtained from this instrument are the turbulent kinetic energy (TKE) dissipation rate, ε , and the structure parameter of temperature, C_T^2 . These follow Monin-Obukhov similarity theory to give the heat flux, H , and the momentum flux, τ . In addition, we investigated the application of the large-aperture scintillometer (LAS) in the SBL, from which only C_T^2 can be obtained, and combinations of DBSAS with the LAS to jointly solve ε and C_T^2 . Scintillometers have the advantage that they combine spatial and time averaging of turbulence statistics rather than time averaging alone as is the case for the EC method, thus allowing flux averaging times of less than 1 minute. In addition, scintillometers are sensible to one dominant eddy size and interpolate the rest of the turbulent scales by using a theoretical form of the spectrum, rather

than integrating over all measured eddy scales, as is the case with the EC method. This means the scintillometer method is not sensitive to path averaging affects and can be used very close to the surface (< 1 m).

We will give some basic backgrounds on the description of turbulence, in which the scintillometer determined parameters ε and C_T^2 , play an important role. In addition the relation of these parameters to turbulent fluxes will be explained.

To start we introduce the turbulent kinetic energy (TKE), which is a measure of the intensity of turbulence. TKE is always given per unit mass of an air parcel and is defined as

$$\bar{e} = TKE / m = 0.5 \left(\overline{u'^2} + \overline{v'^2} + \overline{w'^2} \right), \quad (1.1)$$

where m denotes mass, and $\overline{u'^2}$, $\overline{v'^2}$ and $\overline{w'^2}$ are means of the deviations from the temporal means squared of the three components of the wind speed u , v and w , i.e. their variances. The TKE budget equation is a prognostic equation describing the relative importance of the different processes that generate or destruct turbulence. In homogeneous conditions and using a coordinate system aligned with the mean wind the TKE budget equation reads (e.g. Stull, 1988):

$$\frac{\partial \bar{e}}{\partial t} = \underbrace{\frac{g}{T} \overline{w'T'}}_{\text{I}} - \underbrace{\overline{u'w'}}_{\text{II}} \frac{\partial \bar{u}}{\partial z} + \underbrace{T_{pressure}}_{\text{III}} + \underbrace{T_{transport}}_{\text{IV}} - \underbrace{\varepsilon}_{\text{V}}. \quad (1.2)$$

The different processes contributing to the TKE budget are:

- I TKE tendency
- II Buoyancy - production/destruction of TKE
- III Mechanical shear - production of TKE
- IV Pressure term - redistribution of TKE
- V Transport term - redistribution of TKE
- VI Dissipation - destruction of TKE

The driving force for the buoyancy term is the sensible heat flux ($H = \rho c_p \overline{w'T'}$), the driving force for the mechanical shear is the momentum flux ($\tau = -\rho \overline{u'w'}$). In unstable conditions, the buoyancy term produces TKE, in stable conditions, the heat flux is opposite in sign and the buoyancy term destructs TKE.

Similar to the TKE budget one can also define a prognostic equation for scalar variances. For the temperature variance, $\sigma_T^2 = \overline{T'^2}$, in homogeneous conditions the budget equation reads (e.g. Stull, 1988):

$$\frac{\overline{\partial T'^2}}{\partial t} = \underbrace{-2 \overline{w'T'}}_{\text{II}} \frac{\partial \overline{T}}{dz} + \underbrace{T_{transport}}_{\text{III}} - \underbrace{2\varepsilon_\theta}_{\text{IV}}. \quad (1.3)$$

The different processes contributing to the σ_T^2 budget are:

- I σ_T^2 tendency
- II Heat flux term - production of σ_T^2
- III Transport term - redistribution of σ_T^2
- IV Dissipation - destruction of σ_T^2

Generally, the pressure and transport terms are negligibly small with respect to the production terms and turbulent flows can be considered stationary, so the tendency terms are zero. Then the TKE budget (Equation 1.2) simplifies to

$$\frac{g}{T} \overline{w'T'} - \overline{u'w'} \frac{\partial \overline{u}}{\partial z} = \varepsilon, \quad (1.4)$$

and the σ_T^2 budget (Equation 1.3) simplifies to

$$-\overline{w'T'} \frac{\partial \overline{T}}{\partial z} = \varepsilon_\theta. \quad (1.5)$$

ε and ε_θ relate to each other through the structure parameter of temperature, C_T^2 (e.g. Monin and Yaglom, 1975)

$$C_T^2 = 4\beta_\theta \varepsilon_\theta \varepsilon^{-1/3}, \quad (1.6)$$

where β_θ is the Obukhov-Corrsin constant and is a scaling constant of the 1-dimensional scalar spectrum (Obukhov, 1949 and Corrsin, 1951). We will come back to this relation in the following after having introduced the concept of turbulent spectra.

With Equations (1.4) to (1.6) we have introduced and linked the principle physical parameters determined with scintillimeters, ε and C_T^2 . Now we will extend our simplified turbulence description to turbulent spectra that are defined in terms of ε and C_T^2 , by which also the relation between ε , C_T^2 and the turbulent fluxes becomes clear. The spectrum of a variable describes how the variance of that variable is distributed over wavelength or eddy size. The integration over the spectrum yields the total variance. We will discuss typical spectra of horizontal wind speed u , which is representative of the TKE spectrum, and temperature, T to see at which eddy scales the terms of simplified TKE and σ_T^2 budgets contribute to the total σ_T^2 and \overline{e} . The T and u -spectra are presented in Figure 1-1.

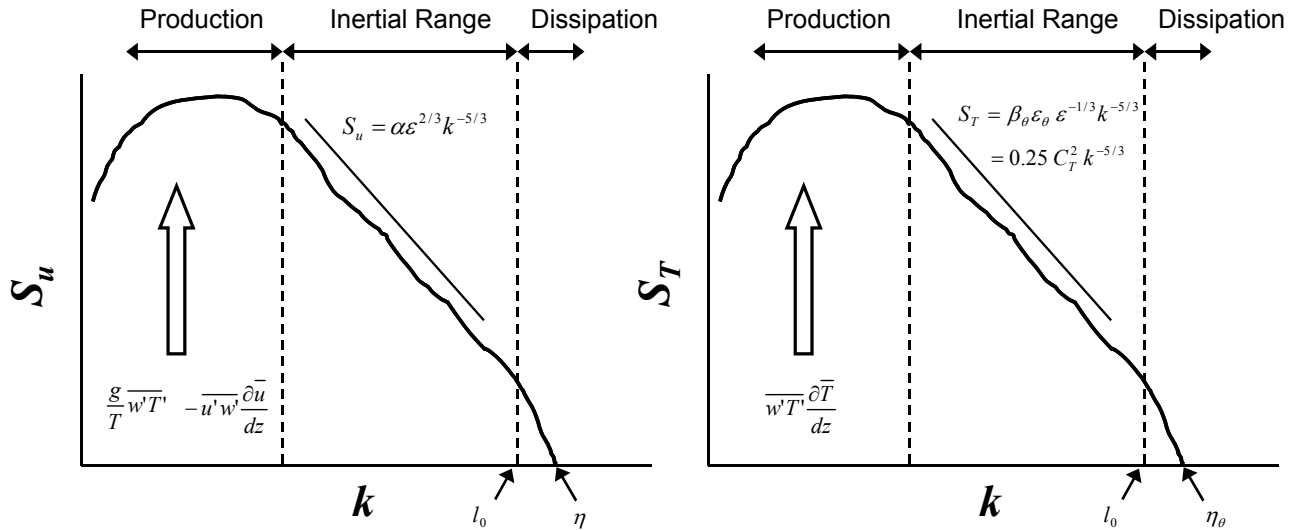


Figure 1-1: Schematic depiction of the spectra of horizontal wind speed, representative of the TKE (left) and temperature variance (right). S_u and S_T are the spectral energy densities of temperature and wind speed and k represents wave-number. Axes are logarithmic.

In the u -spectrum, at low wave-numbers, k , or large eddy scales the TKE is fed by the buoyancy and mechanical shear term, which are largely determined by the heat and momentum flux. This region is referred to as the production region. Note that in stable conditions the heat flux is negative which means that the buoyancy term destructs TKE. On the other end of the spectrum, at the highest wave-numbers corresponding to the smallest eddy scales, eddies are small enough to become susceptible to molecular effects. In this region, the dissipation region, the energy produced at large scales is balanced by dissipation (see Equation 1.4) through viscous processes. The rate at which TKE is dissipated is denoted by ε . In between the production and dissipation regions there is a range in which eddies are chopped up into smaller ones due to vigorous turbulent mixing by which their spectral energy is transferred to smaller scales without adding or losing energy. This region is referred to as the inertial range and the process of passing on energy to smaller scales is often referred to as the energy cascade. Based on dimensional analyses Kolmogorov (1941) derived a description of the velocity spectrum in the inertial range, in which the transferred energy is proportional to ε - thus defining the height of the spectrum - and follows Kolmogorov's well known $-5/3$ power law:

$$S_u = \alpha \varepsilon^{2/3} k^{-5/3}, \quad (1.7)$$

where α is the Kolmogorov constant.

In the dissipation range, gradients in the u -field are eliminated by molecular diffusion. An efficiency measure of this process is the diffusion coefficient of momentum or kinematic viscosity, ν . Eddies still break up into smaller ones but at the same time lose energy due to viscosity. As a result the dissipation range of the spectrum has a steeper fall of than the $-5/3$ -power law of the inertial range. An important length scale in the dissipation range is the

Kolmogorov length scale, η , which is a measure of the eddy scale at which all turbulent motion stops, i.e. the spectrum goes to zero,

$$\eta = (\nu^3 / \varepsilon)^{1/4}. \quad (1.8)$$

The *T-spectrum* exhibits many similarities with the *u-spectrum*, since the *T-field* to a large extent is passively mixed and broken up to smaller scales in the inertial range by the turbulent (TKE driven) motions. The production term of σ_T^2 is always positive and is balanced in the dissipation range of the spectrum by the temperature dissipation rate ε_θ , which is the result of two molecular processes. One is the molecular mixing action of *u*-diffusion (viscosity). The other is the *T-field* smoothing by *T*-diffusion. The ratio of viscosity to thermal diffusion is termed the Prandtl-number (i.e. $\text{Pr} = \nu / \chi$, where χ is the thermal diffusion coefficient). For air the Pr is of the order of 1 ($\text{Pr} \approx 0.72$). Note that Pr is molecular property, not to be confused with the turbulent Prandtl-number, Pr_t . Pr_t is often used in the description of turbulent flows and is defined as the ratio of the turbulent eddy viscosities or exchange coefficients of momentum and heat. The eddy scale representing the smallest temperature fluctuations is the temperature micro-scale, η_θ , which is linked to the Kolmogorov scale through the Prandtl-number:

$$\eta_\theta = (\chi^3 / \varepsilon)^{1/4} = \text{Pr}^{-3/4} \eta. \quad (1.9)$$

The description of the inertial range of the *T-spectrum* depends in part on the *T*-dissipation process that the transferred energy has to feed, i.e. ε_θ , and in part on the mixing action of TKE described in Equation (1.7) as function of ε . The resulting spectrum reads

$$S_T = \beta_\theta \varepsilon_\theta \varepsilon^{-1/3} k^{-5/3} = 0.25 C_T^2 k^{-5/3}. \quad (1.10)$$

It is seen in Equation (1.10) that the height of the inertial *T-spectrum* also scales with C_T^2 , which follows from the relation given in Equation (1.6). The link between C_T^2 and the spectrum is explained in more detail in Chapter 2. The eddy scale that marks the transition between the dissipation and inertial range is the inner scale, l_0 defined as

$$l_0 = 7.4\eta = 7.4\text{Pr}^{3/4} \eta_\theta. \quad (1.11)$$

At the transition between the *T-spectrum* shows a remarkable bump, the so-called Hill bump after Hill (1978) who composed a theoretical model for the dissipation range of the *T-spectrum*. The existence of the Hill bump can be understood as follows. For $\text{Pr} \approx 0.72$ the inertial-dissipation range transition is of a viscous-convective nature, i.e. viscosity already starts to break up TKE when *T*-diffusion still is characterised by convection (the inertial range). Since ν is much smaller than the turbulent *u*-diffusion coefficient the breaking up of turbulent eddies halts, but at the same time the *T*-diffusion is still at its convective intensity

thus leading to a build up of spectral energy at these scales (a bump). At smaller scales, the T -gradients are finally large enough for the molecular diffusivity to compensate the lack of turbulent mixing.

In a nutshell, we have introduced the relevant parameters for the scintillometer method (l_0 , ε , C_T^2) and explained how these are embedded in a general description of turbulence and how they relate to the heat and momentum flux through the TKE and σ_T^2 budgets and u - and T -spectra.

It should be noted that in the stable boundary layer this simplified turbulence description is corrupted from time to time. First of all, the fact that the buoyancy term is a destruction term for TKE under stable conditions makes that TKE production is only due to the mechanical shear. In general the total amount of TKE is much less with respect to unstable conditions, which increases the relative contribution of the pressure and transport term to a level that in some cases these terms do matter (Cuxart et al., 2002). Another complication is that the description of heat and momentum flux that define the buoyancy and shear term is often done with similarity theory that assumes that fluxes originate from the surface directly underneath the measurements in a environment of steady state turbulence. In the SBL, the fluxes are occasionally driven by events that cause non-stationarity and are due to processes that are not generated at the underlying surface. Examples of these events include shear flow instabilities, overturning Kelvin-Helmholtz billows, terrain-generated phenomena, surface heterogeneity and heat and radiative flux divergences.

As a result MOST breaks down which is, amongst others, described by Mahrt et al. (1998), Mahrt (1999) and Cheng et al. (2005). Note that this is most noticeable for flux gradient relationships, which are often used in numerical weather models. Beljaars and Viterbo (1998) discuss the consequences of the breakdown of MOST for the ECMWF model. One of these is that adjusted MOST relations have to be used, since, experimentally obtained MOST relations lead to unrealistic surface cooling and boundary layer heights.

The failure of flux profile relations to represent surface fluxes when turbulence is not stationary but interrupted by non-turbulent (laminar) spells can be understood as follows. During the periods of quasi-laminar flow the gradients are much larger than during the relatively short periods of strong turbulence. As a consequence, in an averaging period in which both events take place, the mean gradients are primarily determined by the laminar periods, whereas the fluxes are largest during the turbulent periods. This feature implies that a direct relation between the mean flux and a mean gradient cannot exist, realising that the similarity relationships, linking gradients and fluxes have a strong non-linear character. In addition, profiles in the SBL often are not determined with fine enough resolution in models nor in measurements to capture the very steep and often locally disturbed gradients. Furthermore, the gradients are based on average measurements that do not contain much direct turbulence information. On the other hand, Mahrt et al. (1998) showed that also higher order turbulence statistics (variances) suffer from the non-stationary events in very stable conditions. We note that (co-)variances are also sensitive to non-stationary conditions

(Vickers and Mahrt, 2003; and Oncley et al., 1996), which is related to the fact that instantaneous values are compared with the mean value of the record considered.

An important part of this thesis concerns direct or indirect measurements of the dissipation term ε and C_T^2 and the way these can be parameterised using the Monin-Obukhov similarity theory. We are aware that C_T^2 and ε scaling might be affected by the non-stationary processes outlined above. However, the strength of scintillometers is that they can determine statistically stable ε and C_T^2 and subsequent fluxes on time-scales (< 1 minute) that are much shorter than the time scales of the non-stationary events. On these very short flux-averaging intervals, the turbulence can thus be considered stationary. In addition, these parameters directly describe the TKE and temperature turbulent spectra, and do not suffer from, as variances do, the length of the averaging record. C_T^2 and ε are based on statistics of temperature and wind speed that compare neighbouring values rather than instantaneous values with respect to the mean of the record. These arguments lead us to state that ε and C_T^2 measured by scintillometers are the preferred statistical parameters to describe surface fluxes through similarity scaling in the SBL.

To illustrate the different states of turbulent transport in the SBL, and to give a taste of the capability of scintillometers in these conditions we present Figure 1-2, which depicts the 6 s averaged sensible heat flux, H , measured with a laser scintillometer for different turbulent conditions during the CASES-99 field campaign. Supplementary to Figure 1-2 is Appendix 1A, where for the same nights 1 s sub-sampled raw eddy covariance data (20 Hz) are plotted, notably the horizontal wind speed vector, vertical wind speed, wind direction, sonic temperature and water vapour density.

To facilitate the discussion of Figure 1-2, we follow the classification of Van De Wiel et al. (2003a-b), who developed a model that predicts the probability of the occurrence of turbulent spells and gives insight into the duration of these spells and the turbulence intensity during these spells, as a function of external 'forcings', such as the large-scale pressure gradient and exchange processes (e.g. radiative cooling) at the surface.

The first class is the case of laminar flow. This occurs in clear sky conditions and a very light background pressure gradient, i.e. almost zero wind speed. The clear sky ensures strong radiative cooling and thus a strong stable stratification at the surface. The omnipresent pressure gradient in this situation is too weak to generate sufficient shear that can break through the strong negative buoyant force of the stable temperature profile. The resulting heat flux is almost zero ($< 10 - 15 \text{ W m}^{-2}$), i.e. for the most part within the error margin with which H can be determined. Still some small-scale organised structures can be seen.

The second class is the case of continuous turbulent flow. This occurs in cloudy conditions with a very strong background pressure gradient, i.e. strong wind speed. The clouds impede the thermal cooling and the strong winds ensure continuous strong wind shear driven mixing of the SBL. In these conditions the heat flux is highest and least organised, i.e. H shows quite a bit of scatter.

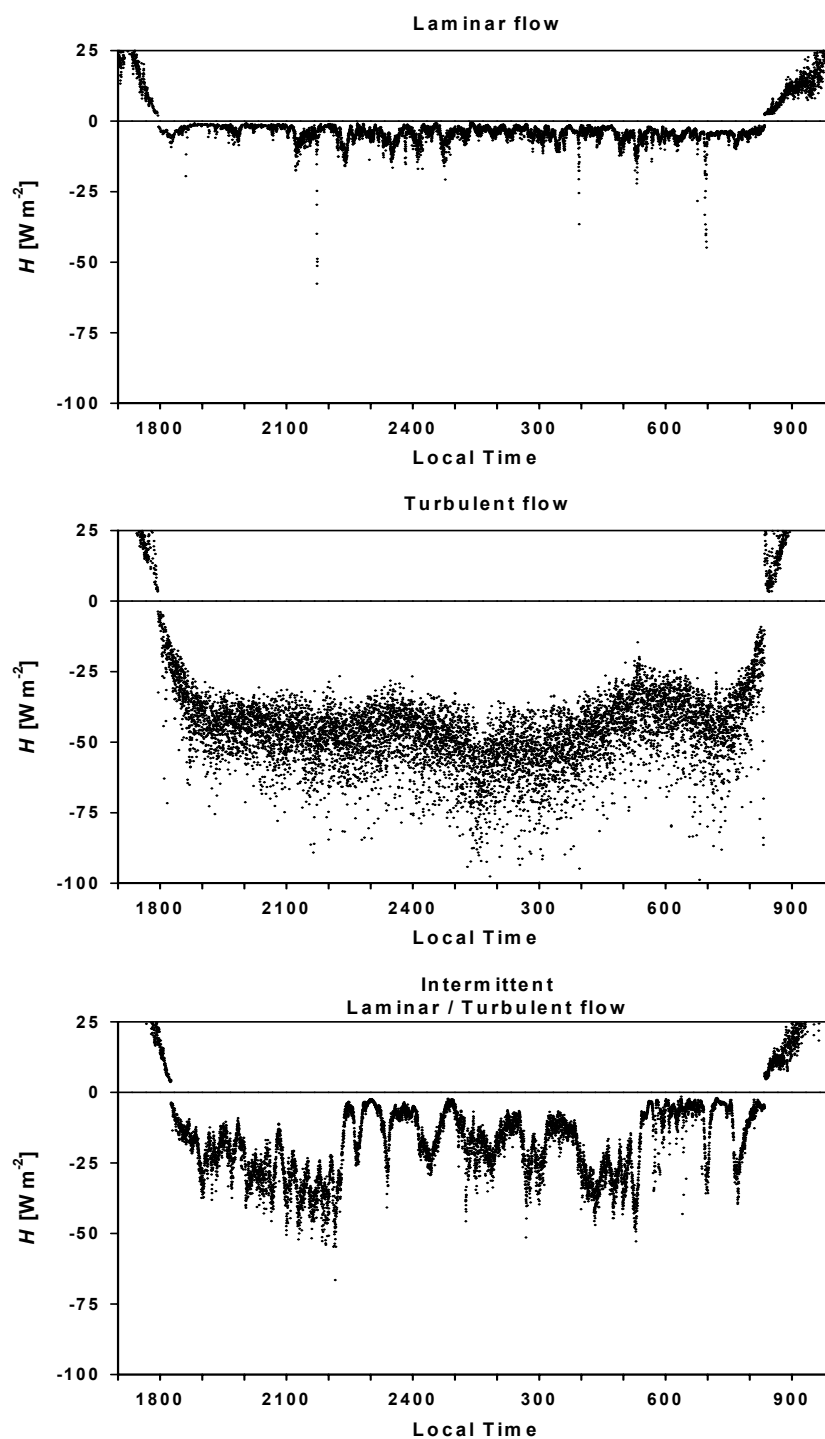


Figure 1-2: Three nocturnal stable boundary layer regimes characterised by the 6 s averaged sensible heat flux, H , observed with a displaced beam laser scintillometer during CASES-99. Depicted are from top to bottom: laminar flow regime in the night of 9-10 October, turbulent flow regime in the night of 6-7 October, and intermittent laminar/turbulent flow regime in the night of 4-5 October.

The third class is the case of intermittent turbulent / laminar flow. In the framework of the model description of Van De Wiel et al. (2003a-b) this is the case of clear sky conditions and a moderate background pressure gradient, i.e. light wind speeds. The pressure gradient is still weak enough to initially allow a strongly stable stratified temperature profile to build up. As

this stratification increases all the turbulent transport that initiates from weak pressure gradient will cease, and the atmosphere decouples from the surface. With no surface friction felt by the atmosphere, the pressure gradient will accelerate the air, until enough wind shear is created to break through the strong thermal build up. Then, suddenly, turbulence will mix the air, and the steep temperature and wind speeds profiles will return to a more neutral build up. From this point onward, with the reduced shear, the radiative cooling takes over and the process starts all over again. Under these conditions, H shows highly organised oscillation patterns with a time scale of 10 – 60 minutes with almost no scatter superimposed. Note, that the process that initiates the break through of the strong initial temperature stratification, which Van De Wiel (2003a-b) use in their model is driven by surface processes. It is a nice conceptual picture of the coming and going of turbulence during very stable conditions, but it is only one mechanism among several that have been recognised. Other mechanisms, that are mainly driven from air layers in or above the SBL include shear flow instabilities in general (e.g. induced by low level jets resulting in overturning Kelvin-Helmholtz billows) and terrain-generated phenomena such as gravity waves.

1.2 Thesis Structure

The bulk of the thesis is based on articles that have been published in international journals (Chapters 3, 4 and 6), or are in preparation for submission (Chapter 5).

Chapter 2 describes the field experiments that have been conducted as part of this thesis, notably CASES-99, RAPID and BBC. In addition, it describes some backgrounds of the sonic anemometer and scintillometer measurements in obtaining ε , C_T^2 and fluxes of heat and momentum.

Chapter 3 concerns the performance of the DBSAS during CASES-99. The DBSAS derived ε , C_T^2 , H and u^* are compared with sonic anemometer derived values. The major conclusions are that the DBSAS can resolve the turbulent fluxes at very short flux averaging intervals, that the comparison between DBSAS and EC for all parameters shows surprisingly little scatter, but that there are systematic differences between DBSAS and EC derived fluxes, differences that are already present in ε and C_T^2 . In this thesis the Appendices 3B to 3E have been added to the original publication.

In **Chapter 4** new MOST scaling relationships for ε and C_T^2 are derived using sonic anemometer data. Applying a simplified TKE budget formulation, these relations are then extended to the flux profile scaling relationships and the Richardson bulk and the flux Richardson-number. This approach allows one to evaluate flux profile relations for a given site using measurements of one eddy covariance system only. Appendix 4A has been added in this thesis applying the found scaling functions to the DBSAS measurements of CASES-99 and comparing these results with those of Chapter 3.

In **Chapter 5** three field-scale scintillometer configurations are compared for the BBC experiment. It elaborates on Chapters 3 and 4. With the combined scintillometer configurations, of DBSAS with LAS, we hoped to find the same low scatter in the flux comparison with EC, but without the systematic errors found in Chapter 3. Also the performance of the LAS during stable conditions is discussed. For completeness also unstable conditions are considered. Chapter 5 also provides an independent test of the new ε and C_T^2 MOST functions presented in Chapter 4.

Chapter 6 deals with an old data-set, the La Poza experiment in Sonora, Mexico, that was not gathered as part of this thesis. It concerns a general issue relevant for the applicability of scintillometry, namely the derivation of a scintillometer effective height for calculating fluxes, when the scintillometer height along its path is not constant. In La Poza we were compelled by the practical situation at the field site to operate the scintillometer with a slanted path. In Chapter 6, however, also varying height along the path due to topography and the earth's curvature is discussed. Initially only unstable fluxes were considered. In this thesis also stable fluxes are discussed calculated with the effective height in Appendix 6C, which was not part of the original publication.

Chapter 7 gives the overall summary and conclusions of this thesis.

In **Appendix I** an overview is given of all the field experiments and accompanying publications the author participated in.

In **Appendix II and III** reprints are given of articles based on the CASES-99 (Van De Wiel et al., 2003) and RAPID (De Bruin et al., 2005) datasets, which were gathered as part of this thesis and in which the candidate co-authored.

Appendix 1A SBL regime observations with EC system

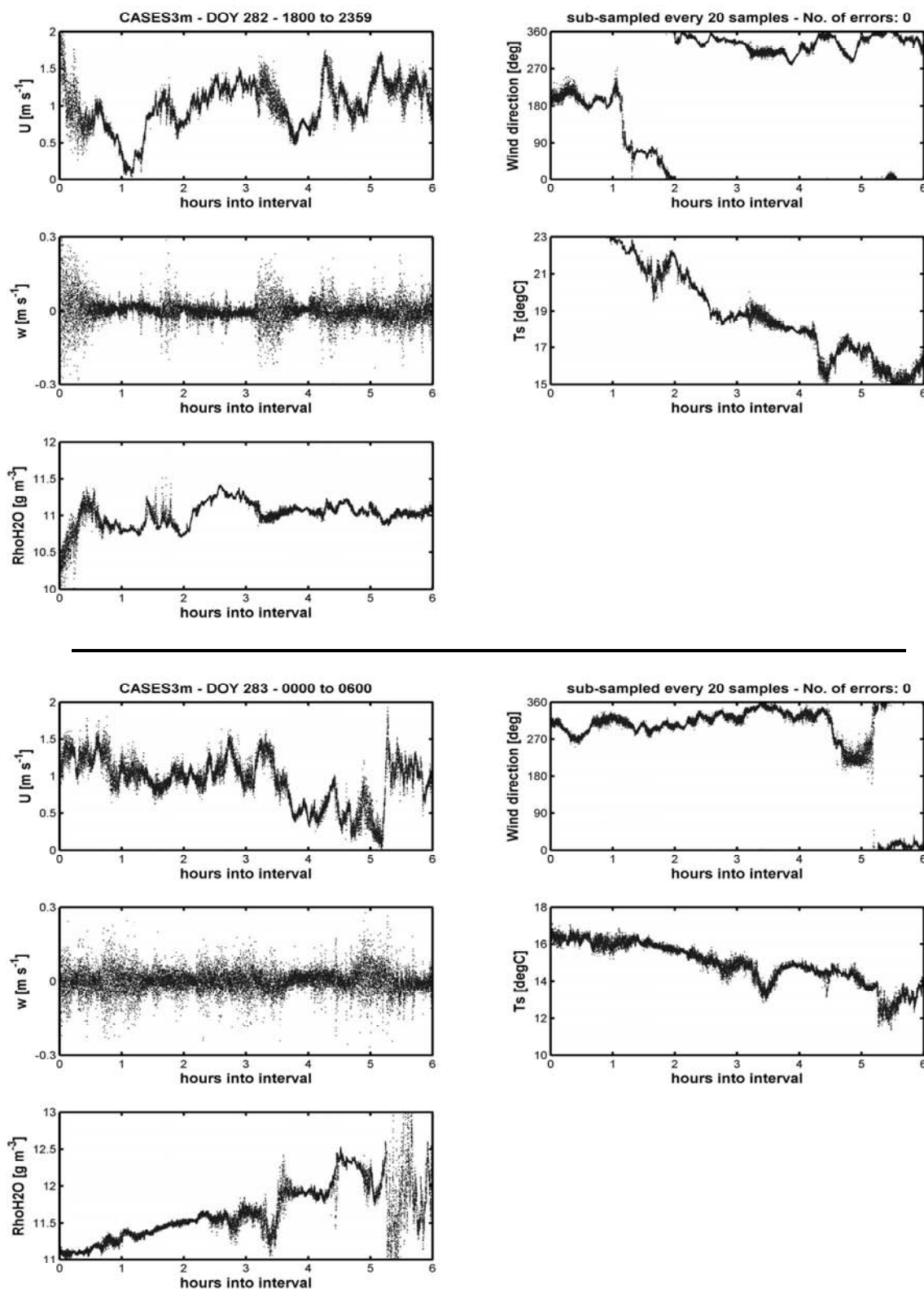


Figure 1-3: Supplementing Figure 1-2(top): Eddy-Covariance (EC) system data for the *laminar flow regime* night of 9-10 October (DOY 282-283) during CASES-99. U = horizontal windspeed vector, w = vertical windspeed, Ts = sonic temperature, RhoH2O = water vapour density. Sub-sample interval is 1 s.

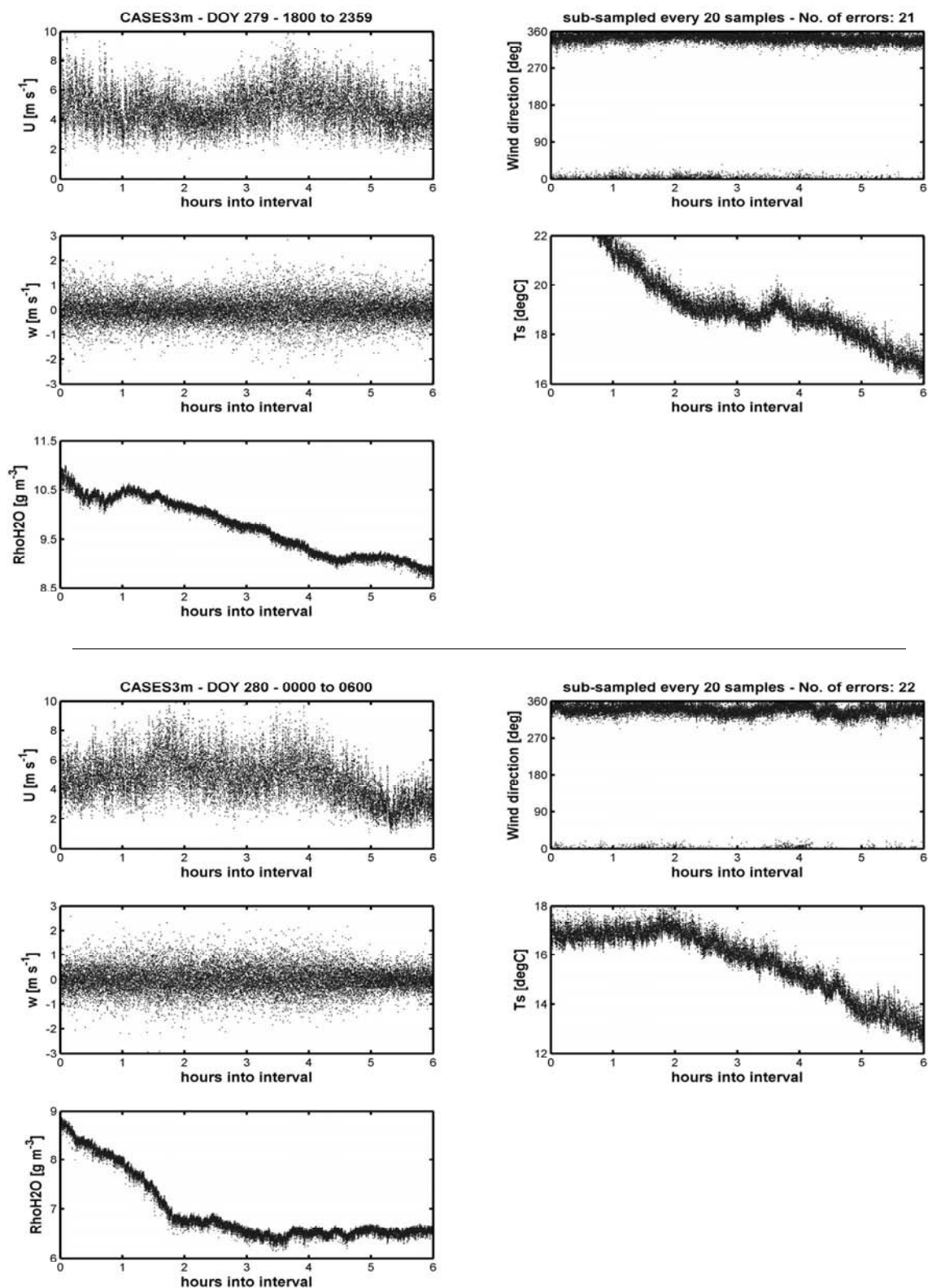


Figure 1-4: Supplementing Figure 1-2 (middle): Eddy-Covariance (EC) system data for the *turbulent flow regime* night of 6-7 October (DOY 279-280) during CASES-99. U = horizontal windspeed vector, w = vertical windspeed, T_s = sonic temperature, RhoH_2O = water vapour density. Sub-sample interval is 1 s.

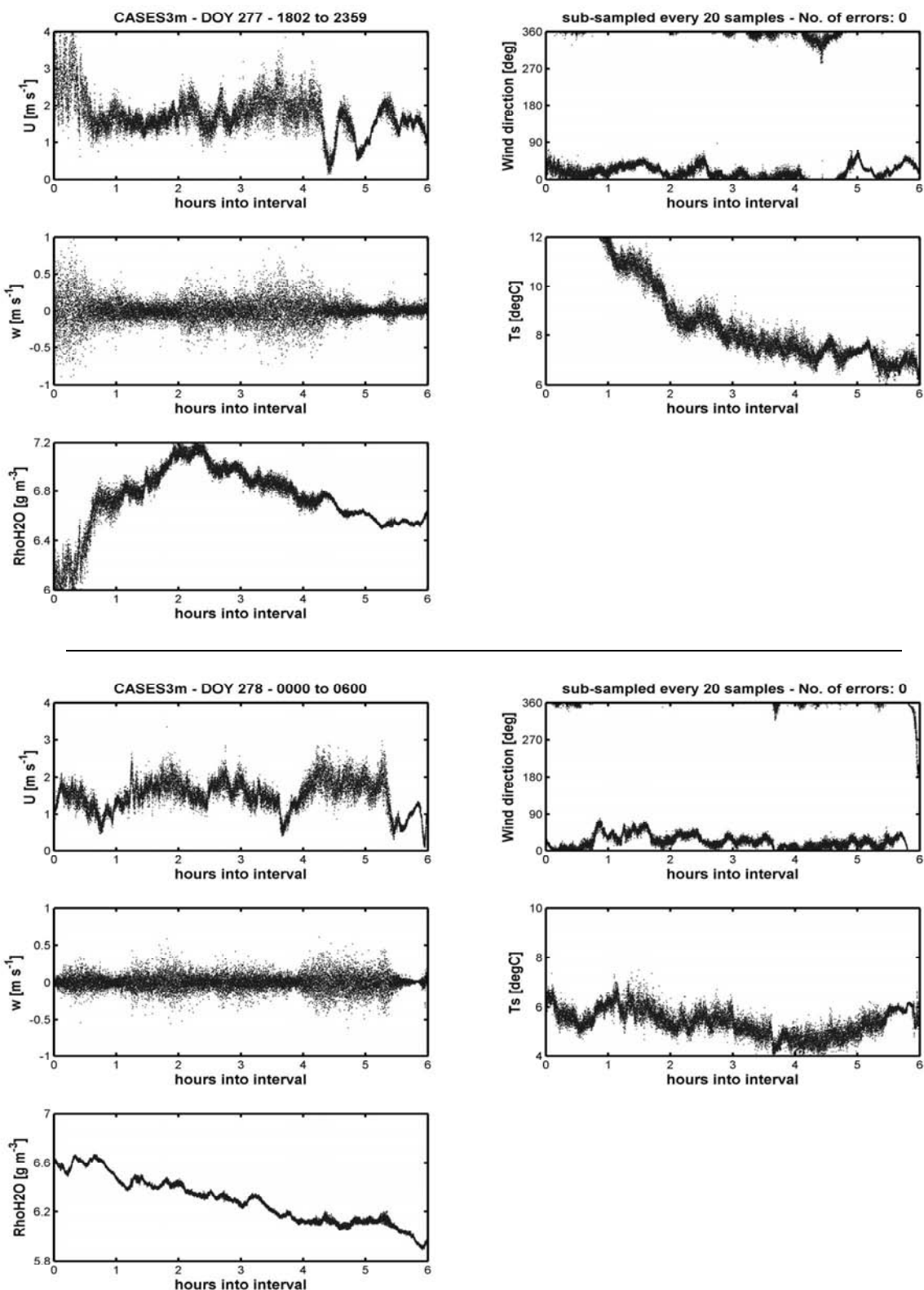


Figure 1-5: Supplementing Figure 1-2 (bottom): Eddy-Covariance (EC) system data for the *intermittent laminar/turbulent flow regime* night of 4-5 October (DOY 277-278) during CASES-99. U = horizontal windspeed vector, w = vertical windspeed, T_s = sonic temperature, $RhoH2O$ = water vapour density. Sub-sample interval is 1 s.

Chapter 2 Description of the Field Experiments and Data Analysis

2.1 Introduction

In this Chapter we will give a description of the field experiments that were carried out in the framework of this thesis, i.e. the CASES-99 (Section 2.2), RAPID (Section 2.3) and BBC experiment (Section 2.4). The emphasis will be primarily on the backgrounds of the experiments and the instrumentation deployed. Further details, especially on data processing, can be found in the following chapters where the datasets are CASES-99 in Chapters 3 and 4 and the BBC data in Chapter 5. It was not possible to include a first author paper based on the RAPID experiment in this thesis. A co-author publication on RAPID is added in Appendix III.

In Chapter 6 an old data-set - also gathered by the author - is studied, dealing with a scintillometer experiment that took place in 1996 in a rangeland site called La Poza in Sonora, Mexico. This experiment will not be dealt with in this chapter. In Appendix I some further background information on La Poza is given.

In Section 2.5 backgrounds on the data analyses are given. This section deals with the techniques to derive C_T^2 , ε and fluxes of heat and momentum from sonic anemometers and scintillometers. Most attention will be paid to the techniques to derive C_T^2 and ε from sonic anemometers as this is dealt with only briefly in the following chapters unlike the description of the scintillometer method.

2.2 CASES-99 experiment

2.2.1 Overview CASES-99 experiment

The CASES-99 stable boundary layer experiment was organised within the framework of the more general goals of the Cooperative Atmosphere-Surface Exchange Study (CASES) concept, which were to provide a long-term facility for scientists to study the meso-scale processes of meteorology, hydrology, climate, chemistry, ecology and their complex linkages, and to serve as a focal point to provide field experience for students of the natural sciences.

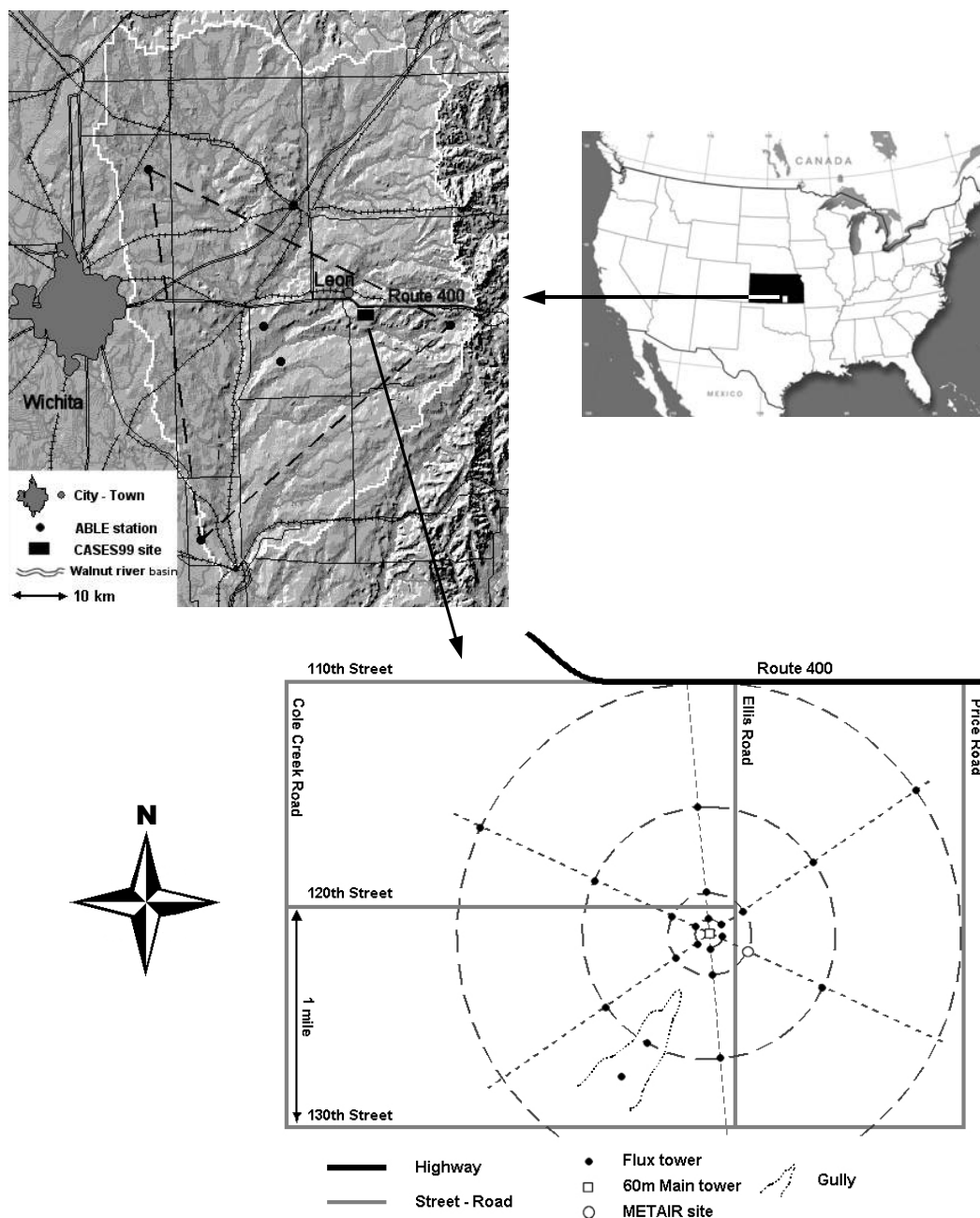


Figure 2-1: Top right: location of the Walnut River Watershed (WRW) within Kansas (marked in black). Top left: outline of the WRW and the positions of the ABL sites and CASES-99 main site therein. Bottom: outline of the CASES-99 main site.

The Walnut River Watershed (WRW) in southeastern Kansas, USA (see Figure 2-1) was chosen by scientists from these many disciplines as an ideal location for the study of these processes. The WRW is a hydrologically confined region of relatively flat terrain, varying ecosystem characteristics and limited quantifiable external sources of chemical constituents. A great benefit of the WRW for atmospheric scientists is that it is nested within ongoing long-term meteorological experiments of the ARM-CART (Atmospheric Radiation Measurement-Clouds and Radiation Testbed) and ABL (Argonne Boundary Layer Experiment) programs. The ARM-CART study area consists of most of the state of Oklahoma (south of Kansas) and

extends into Kansas. ABLE consist of 3 measurement sites lined up in a triangle with ~ 75 km long legs, and one central site in the middle of the triangle. At each ABLE site a wind profiler and a surface flux tower is available (see Figure 2-1).

Until now, two intensive field programs have taken place within the CASES framework: CASES-97 and CASES-99. In this study we use data of CASES-99, which was designed to study investigate the nighttime SBL with an emphasis on turbulence and turbulent “events”. The long-term goal of the program is to gain sufficient knowledge to be able to develop parameterisations of sub-grid scale turbulent mixing processes that characterise the NBL. The detailed scientific goals of CASES-99 are listed in Poulos et al. (1999).

The CASES-99 experiment took place during October 1999. This period was chosen for its climatologically high frequency of clear, calm nights and therefore increased likelihood of SBL development. The CASES-99 main site ($37^{\circ} 39'N$ and $96^{\circ} 44'W$) was located within the ABLE triangle close to the ABLE main site southeast of Leon, Kansas. It comprised a 4.8 km by 3.2 km area of grassland with dust roads running between individual 1.6 km by 1.6 km fields. The surface contained some minor topographical features (slopes of ~ 0.5 degrees), and the surface elevation is approximately 450 m above sea level.

A vast array of instruments was deployed to obtain as much spatial (horizontal and vertical) and temporal information of the nocturnal boundary-layer as possible. At the centre of the main site a 60-m instrumented tower equipped with eddy-covariance flux measurements every 10 m and profile measurements (temperature, humidity and wind speed) every 5 m was deployed by the National Centre for Atmospheric Research (NCAR) Integrated Surface Flux Facility (ISFF). Centred around the 60-m tower a grid of 10-m flux masts was set-up in a tightly spaced array of four concentric triangles sequentially increasing in scale. The radii to the triangle vertices was as follows: 100 m, 300 m, 900 m and 1800 m (see Figure 2-1). ISFF occupied 6 of the 10-m masts in this network. Researchers of other institutes operated the remainder positions. METAIR occupied the position on the 300-m radius south-east of the main tower as indicated in Figure 2-1. The area in and around a gully on the main site was more densely instrumented with the objective to study drainage currents.

Apart from the traditional micro-meteorological instruments installed in towers, also numerous remote sensing techniques were deployed on the main site such as 2 research airplanes, several SODARS, 2 LIDARS, a RADAR, a kite, a blimp, and 3 scintillometers.

The upscaling of spatial information extended from the main site in three additional levels. First, there was a radiosonde network, maintained by NCAR, set-up in a triangle with a 15 km radius around the main site. Second and third level are the already mentioned ABLE network (~ 45 km radius triangle) and the ARM network (~ 100 - 1000 km radius), both of which were not centred around the main site. Most of the non-tower data require hands-on control of the instruments and could therefore not be operated continuously. They were only in operation during so-called intensive operation periods (IOP's), which were chosen during the experiment depending whether the current weather forecasts were favourable for the different phenomena of interest to occur (low level jets, drainage currents in the gully etc.). In total 12

IOP's were chosen. Poulos et al. (2002) provide a complete description of the instruments deployed, the participants and the intensive operation periods and significant events observed. All the CASES-99 data is freely available at <http://www.joss.ucar.edu/cases99>.

In this thesis only data gathered by our group of Wageningen University is used. A description of the instruments used is given in Section 2.2.3.

2.2.2 Weather conditions CASES-99 experiment

Figure 2-2 gives an overview of the local weather conditions at the CASES-99 main site between 1 October (Day of Year, DOY 274) and 31 October (DOY 304) 1999. Temperature and humidity data are averaged from 3 ISFF stations in the direct proximity of the Wageningen University site and are taken at 2 m height. Wind speed and direction are taken at 10 m height.

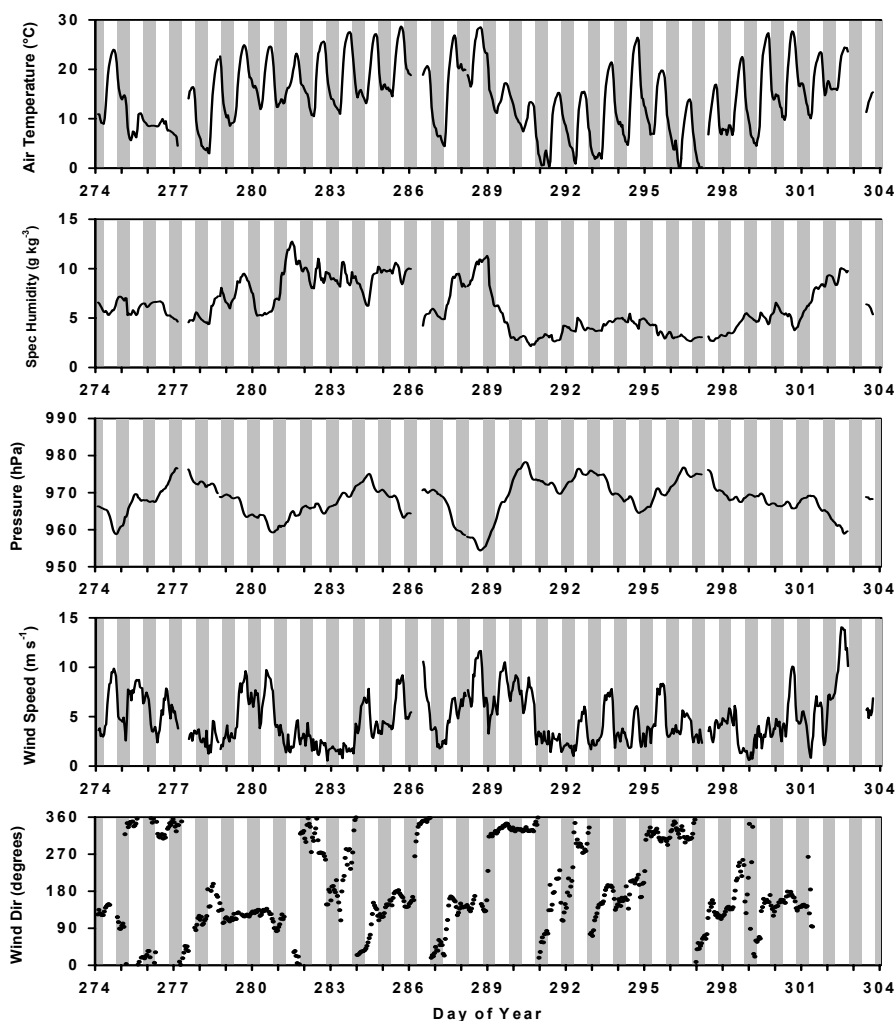


Figure 2-2: Impression of the weather conditions during CASES-99. Day and night time data have alternating white and grey backgrounds.

There were only 3 significant rain events that affected CASES-99, all of which took place either before or after the actual experiment: namely in the morning of 13 September, the night of 27-28 September and the night of 29-30 October.

In general the weather conditions were calm during CASES-99 and favourable to all types of SBLs and SBL events. In fact several nights characterised by “typical” stable turbulent regimes outlined in Figure 1-2 were encountered. Especially very stable cases with almost no turbulent activity were very pronounced during some nights with local stability parameters measured at around 2 m height (i.e. z/L , with L is the Monin-Obukhov length and z the height above the surface) of upto 10.

This study deals with surface fluxes and therefore no larger scale synoptic weather overview is given that influences the dynamics of the SBL at the CASE-99 site. One synoptic event is very noticeable, however, in Figure 2-2, i.e. the passage of a cold front around DOY 290 after which a high-pressure system dominates bringing considerably cooler, dryer and calmer air.

2.2.3 Instrumentation CASES-99 experiment

The instrumentation deployed by Wageningen University during CASES-99 is outlined in Table 2-1. The instruments are divided in 5 instrument groups: the eddy covariance systems, scintillometers, radiation sensors, temperature-humidity probes and soil sensors. More information on the instruments is given in the following descriptions of these groups. The data are available at <http://www.joss.ucar.edu/cases99>, where in the documentation files the instruments and field observations are described in even further detail.

Table 2-1: Instrumentation deployed at the Wageningen University site during CASES-99. Sensors given in *italic* were made available to us by Dr. R. Qualls of the University of Boulder. Different sensor groups are divided by thick lines. Sensor groups are (from top to bottom): eddy covariance systems; scintillometers; radiation sensors; temperature-humidity probes; soil sensors.

Sensor	Manufacturer	Model	Parameters	Sample interval [s]	Stored interval [s]
3D Sonic anemometer (2x)	Campbell Scientific, Logan, USA	CSAT3	u, v, w [m s^{-1}]; T_s [$^{\circ}\text{C}$]	0.05	0.05
Fast response Hygrometer (2x)	Campbell Scientific, Logan, USA	KH20	ρ_{H20} [kg m^{-3}]	0.05	0.05
Fine wire thermocouple (2x)	Campbell Scientific, Logan, USA	FW05	T [$^{\circ}\text{C}$]	0.05	0.05
Large-Aperture Scintillometer	Wageningen University, Netherlands	-	C_n^2 [$\text{m}^{-2/3}$]	1	60
Double-beam Laser scintillometer	Scintec AG, Tübingen, Germany	SLS20	C_n^2 [$\text{m}^{-2/3}$]; ε [m^2s^{-3}]	6	6
Pyranometer	Kipp&Zonen, Delft, the Netherlands	CM14	S_{in}, S_{out} [W m^{-2}]	5	60 / 600*
Pyrgeometer	Kipp&Zonen, Delft, the Netherlands	CG2	L_{in}, L_{out} [W m^{-2}]	5	60 / 600*
<i>Infrared thermometer</i>	Everest Interscience Tucson, USA	4000.4 GL	$T_{surface}$ [$^{\circ}\text{C}$]	5	60 / 600*

<i>Temperature Humidity probe (2x)</i>	REBS, Seattle, USA	THP_1	T [°C]; RH [-]	5	60 / 600*
Heat Flux plate	TNO, Delft, the Netherlands	WS31	G [W m ⁻²]	5	60 / 600*
<i>Heat Flux plate</i>	REBS, Seattle, USA	HFT3	G [W m ⁻²]	5	60 / 600*
Soil thermometers (6x)	Wageningen University, Netherlands	-	T [°C]	5	60 / 600*
<i>Soil thermometer</i>	REBS, Seattle, USA	STP-1	T [°C]	5	60 / 600*
<i>Soil moisture sensor</i>	REBS, Seattle, USA	SMP1R	<i>Mass-ratio</i> [-]	5	60 / 600*

Eddy Covariance Systems:

The Eddy Covariance (EC) systems consisted of a CSAT3 sonic anemometer, a KH20 hygrometer and a fast response thermocouple. It was for the first time that Wageningen University deployed these sensors. To complete the systems we built three “plug-and-play” datalog-units consisting of a Campbell Scientific 23X datalogger pre-wired to connection panel. The instruments cables were fitted with connectors that plug into the datalog-unit. In addition, the systems were equipped with a mini laptop to store the raw data. Only one datalog-unit is needed for two EC systems.

The CSAT3 is a three-dimensional sonic anemometer that consists of three transducer pairs, which are arranged with non-orthogonal axes over a path length of ~10 cm. On each axis of the CSAT3, a transducer pair pulses two ultrasonic signals in opposite directions. From the flight times of the pulses the wind speed and speed of sound can be determined. The wind speeds re-arranged to their orthogonal coordinates are denoted u , v (horizontal wind speed components) and w (vertical wind speed). The speed of sound depends on the density of air, which is a strong function of temperature and a weak function of humidity. From the speed of sound the sonic virtual temperature (temperature including humidity information) can be determined.

The KH20 is a highly sensitive hygrometer designed for measurement of rapid fluctuations in atmospheric water vapour. It consists of a low pressure krypton glow tube that emits radiation in the ultra violet part of the electromagnetic spectrum, where water vapour and also oxygen have strong absorption bands. The emitted radiation is attenuated by water vapour absorption (and some oxygen absorption) and registered by a detector over a path length of ~ 1 - 2 cm. The registered signal is a measure of the humidity absorption, and is inversely proportional to the water vapour concentration. The KH20 does not measure absolute concentrations, since its calibration shifts in time due to weathering of the sensor windows. Prior to the experiment the KH20s were calibrated and their oxygen sensitivity was determined (Van Dijk et al., 2003).

The FW05 is a fine wire (0.0005 inch diameter) chromel-constantan thermocouple with which fast air temperature fluctuations can be measured.

With the measurements obtained from the sensors described here, the surface fluxes of heat, water vapour and momentum can be determined using the eddy covariance method, which is briefly explained in Section 2.5.3. Also we used these data to obtain C_T^2 and ε . The methods used to calculate these are described in Section 2.5.1.

The two EC systems were installed at 2.65 m and 10.20 m height on a ~ 12 m tall tower at position 16 of the CASES-99 observational plan (see Figure 2-1). The instruments were pointed towards the

* 10-minute averaged data (600 s) from all sensors were stored around the clock. In addition, 1-minute averaged data (60 s) were stored from a selection of the available sensors between 17:00 and 9:00 local time (night-time).

Northeast, like to the sonic anemometers on the main CASES-99 tower. The directional off-set ($\pm 5^\circ$) relative to North (0°) of the 2.65 m system was 65° and of the 10.2 m system 50° . The distance between KH20 and middle of the CSAT3 path was ~ 10 cm. The distance between FW05 and middle of the CSAT3 path was ~ 5 cm. The systems were operated at 20 Hz and the raw data were stored at the laptop to be processed afterwards (see Section 2.4.3).

From 30 September until 20 October the datalog system suffered overrun problems in writing the data to the PC. This means that occasionally a line of data missed and effectively the system was not running at 20 Hz. From 20 October onward this problem was solved at the cost of not registering the thermocouple data of the 10.2 m system.

In this thesis we will only use data of the 2.65 m EC system, since we want to compare EC derived parameters with those determined with a double laser scintillometer installed at roughly the same height. In addition, we discovered that the 10.2 m CSAT3 suffered from calibration problems, resulting in a shadow-signal on top of the true signal (see Appendix 2A for an example). This occurred only for a specific range of wind speed and or temperature for which the calibration was corrupted.

Scintillometers:

We deployed two types of scintillometers during CASES-99, a large-aperture scintillometer (LAS) and a double beam laser scintillometer, in this thesis referred to as a displaced-beam small-aperture scintillometer (DBSAS). Scintillometers consist of a transmitter and receiver. The radiation beam emitted by the transmitter exhibits intensity fluctuations due to passage of the beam through the turbulent atmosphere, which are registered by the receiver.

The LAS we operated has a beam-aperture of 15 cm, and the incoherent light source emits at a wavelength of 940 nm (near infrared). The SLS20 DBSAS we operated uses a laser light source at 670 nm (visible) which is split in two parallel beams with orthogonal polarization which are displaced from each other by a distance of 2.7 mm. For both scintillometers the measured intensity fluctuations relate to the structure parameter of the refractive index, C_n^2 . The DBSAS also measures the correlation between the intensity fluctuations of the two beams, from which the inner scale of turbulence, l_0 , can be determined. More on the scintillometer technique and on how surface fluxes can be determined from the principle physical parameters measured by scintillometers can be found in Sections 2.5.2 and 2.5.3.

The LAS was set-up over a path length of 420 m between our EC tower (receiver at 5.17 m) and a tri-pod (transmitter at 3.40 m) in a NNE-SSW direction. In that direction the terrain was not flat. We conducted a small field survey to establish the extent of the sloping terrain along the LAS path. At the transmitter end, the surface elevation was 2 m higher than at the receiver side. Data was logged with a micro-world G2 datalogger built-in in the LAS receiver. The LAS ran continuously throughout the experiment.

The DBSAS was installed on tri-pods, both at 2.46 m height over a path length of 112 m. The receiver was set-up at ~ 40 m South of the EC tower. The path had a NE to SW direction. Figure 2-3 shows a picture with the DBSAS set-up. The terrain had a slight slope of 1 m over the path, but this did not affect the overall height of the DBSAS since this slope was uniform over the direct surroundings of the instrument. The data registration and storage was taken care of by a laptop running the Scintec AG SLSrun software (version 2.03). During 5 nights part of the data was lost due to power failure or misalignment of the instrument.

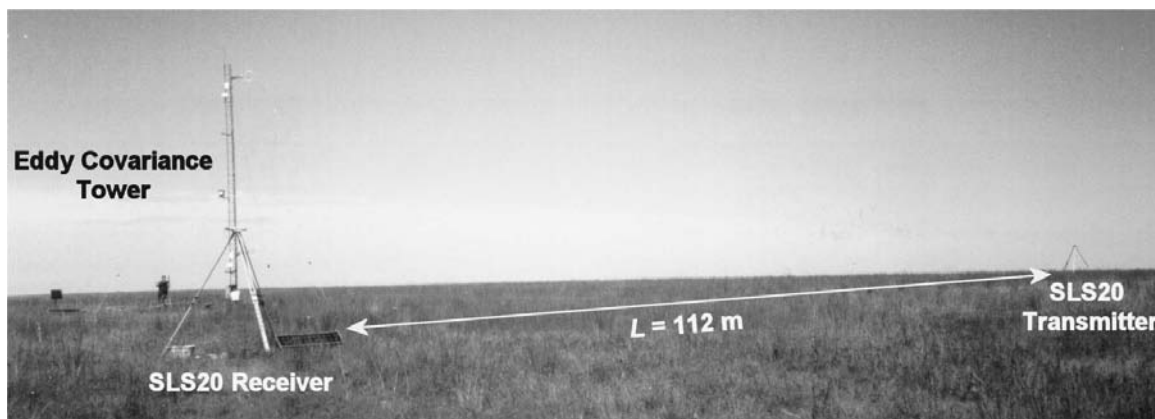


Figure 2-3: Set-up of the SLS20 displaced-beam small-aperture scintillometer with respect to the eddy covariance tower.

Radiation Sensors:

The radiation sensors were set up ~15 m south from the EC tower. All sensors were mounted close together on a tri-pod at approximately 1.5 m height. The area the radiometers “see” was chosen to be as representative as possible for the area, i.e. having the same distribution of grass and open patches. The CM14 albedometer gives incoming and outgoing short-wave radiation, S_{in} and S_{out} . S_{in} and S_{out} were set to 0 W m⁻² at night whenever one of the two was smaller than or equal to 0 W m⁻². The CG2 pyrgeometer gives incoming and outgoing longwave radiation, L_{in} and L_{out} . The housing of the CG2 is heated to avoid dew deposition on the sensor. The temperature of the housing is measured with a Pt100 temperature sensor, with which the internal longwave radiation emissions of the sensor itself can be corrected for. From incoming and outgoing short and longwave radiation the net radiation, R_n , was calculated from the radiation balance:

$$R_n = S_{in} - S_{out} + L_{in} - L_{out} , \quad (2.1)$$

The 4000.4 GL gives the skin temperature from infrared radiation measurements of the surface. We set the surface emission coefficient to 0.98 for the conversion between the two.

A Campbell Scientific 21X datalogger was used with an AM416 multiplexer and SM192 storage modules to store the data. The same system was also used for the temperature- humidity probes and the soil sensors.

Temperature-humidity probes:

Two THP_1 sensors were mounted in the EC tower at 7.65 m and 1.75 m. The sensors are radiation shielded and ventilated and output temperature and relative humidity. From these, the water vapour pressure was calculated on the datalogger for every sampling interval and subsequently averaged to the 1- (night-time) or 10-minute storage interval.

Soil Sensors:

The Pt100 soil thermometer is a 100 Ω platinum resistance thermometer of ~10 cm length and a diameter of ~3 mm. The STP-1 is also a resistance soil thermometer. The WS31 soil heat flux plate has a heat conductivity of 0.25 Wm⁻¹K⁻¹, a diameter of 10 cm and a thickness of 0.5 cm. The HFT3

soil heat flux plate has a heat conductivity of $1.22 \text{ Wm}^{-1}\text{K}^{-1}$, a diameter of 3.86 m and a thickness of 0.39 cm.

The SMP consists of a gypsum plate of about 30x20x3 mm enclosed in a stainless steel screen mesh. The electrical resistance measured over the plate depends on soil moisture potential, here expressed as pressure. REBS provides calibration curves for several soil-types relating this variable to the soil moisture content expressed as a mass ratio. We used the calibration curve for a clay loam soil.

In Table 2-2 the experimental lay out of the soil sensors is given. Note that the 0 cm Pt100 for grass was put right at the surface under the grass, and the 0 cm Pt100 for bare soil was put on the bare soil without any shielding. The soil sensors were not installed until the second half of the experiment (16 October).

Table 2-2: The measured variables T (temperature), G (soil heat flux) and SM (soil moisture) against depth. T and G are measured by two types of sensors. If available, the exact depth and the vegetation type are specified (Gr = Grass, BS = Bare Soil). Accuracy of measured depths is within $\pm 0.3 \text{ cm}$

Depth	T (Pt100)	T (STP-1)	G (WS31)	G (HFT3)	SM (SMP1R)
0 cm	Gr – 0.0 cm	-	-	-	-
	BS – 0.0 cm				
1 cm	Gr – 0.5 cm	-	-	-	-
	BS – 0.8 cm				
3 cm	Gr – 2.8 cm	Gr – 2.6 cm			Gr – 2.7 cm
5 cm	-	-	Gr – 5.4 cm	Gr – 6.3 cm	-
8 cm	Gr – 7.8 cm	-	-	-	-

All systems were powered by deep-cycle batteries and solar panels. The mast and tri-pods were enclosed by an electric fence to keep the grazing cattle out.

2.3 RAPID experiment

2.3.1 Outline RAPID experiment

The Regional Advection in an Irrigated Desert (RAPID) micro meteorological experiment was set-up to investigate a phenomenon often observed in the long lysimeter records gathered over alfalfa at the Kimberley Research Center in Idaho, USA by Wright (1982) (see Figure 2-4). Where evapotranspiration, L_vE , is generally some fraction of net radiation, R_n for climates that have sufficient rainfall to support L_vE , in areas where the air mass is strongly modified by dry, desert conditions, as is the case in Kimberley, the ratio of L_vE to R_n can exceed 2 by late summer. During this period dry air is advected from the large desert areas upwind from Kimberley.

Considering the surface energy balance,

$$R_n - G = L_vE + H, \quad (2.2)$$

where R_n is the net radiation, G is the soil heat flux, $L_v E$ is the latent heat flux or evapotranspiration in energy units and H is the sensible heat flux, we see that, if we for simplicity neglect G , H must be negative when $R_n < L_v E$. For a full cover crop G is relatively small, especially when taken over 24 hours. This means that heat is extracted from the air and transported down to the surface to feed the evapotranspiration. In addition this air is very dry, so it also adds to the vapour density deficit.

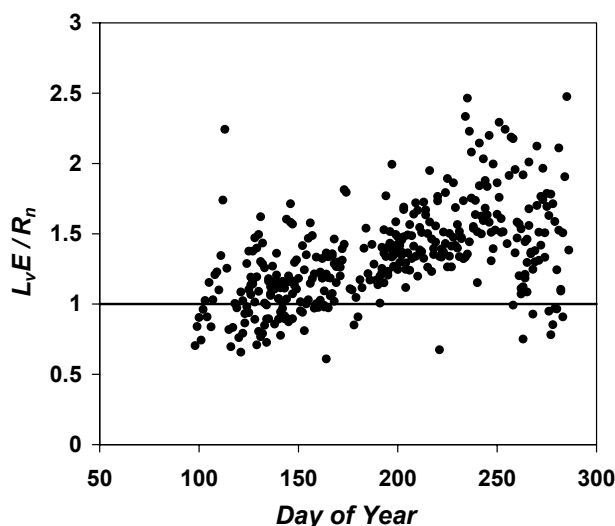


Figure 2-4: Lysimeter measurements taken between 1969 and 1971 at Kimberly, Idaho by Wright (1982) of 24-hour evapotranspiration of full-cover alfalfa divided by the corresponding net radiation, R_n . Evapotranspiration is represented as $L_v E$ and is expressed in energy units.

Here we consider a large irrigated agricultural area in a desert. We define “large” as large enough for the advected desert air mass to be in equilibrium with the underlying surface layer. We refer to this situation as *regional advection*, as opposed to *local advection* where the distance to the advection source area is short and the advected air mass is not in equilibrium with the surface. In the regional advection case at Kimberley, the cool evaporating surface is covered by a blanket of warm and dry desert air creating a special SBL case; the daytime SBL. In the SBL negative buoyancy suppresses turbulent motion. The turbulence, therefore, needed to exchange heat and water vapour between the surface and the lower atmosphere can only be generated in a mechanical way; in this case bringing the warm and dry desert air to the surface and the cool wet air from the surface. This means that $L_v E$ can exceed R_n only if there is enough wind to offset the damping effects of stability. Under calm conditions it is to be expected that daily $L_v E$ cannot exceed R_n (De Bruin et al., 2004).

The situation at Kimberley is not an academic case. Desert areas are widely used for agriculture, as there is always sufficient heat and solar energy available to grow crops, often even a few yields a year. The limiting factor for agriculture in deserts is, of course, the availability of water. This scarce resource has to be managed properly, even more so because the loss of water through evaporation is enhanced due to the advection effect. Methods to

monitor evapotranspiration operationally for water management are generally weather-based equations for predicting daily estimates of L_vE , such as the Penman and Penman-Monteith equations. These do not appear to be well-postured or formulated to “sense” and to account for the enhanced evapotranspiration by regional advection. Some type of empirical or theoretical mechanism is needed to predict the occurrence of and to quantify the impact of this effect in order to correct operational L_vE -estimates.

It was this practical research question together with the more scientific objective to better understand the nature of the extensive turbulent exchange in daily SBL’s that lead to the organisation of the RAPID experiment. RAPID was organised and executed in a short time frame, hence the acronym. Staff members of the University of Idaho, Wageningen University, Campbell Scientific, Inc., Utah State University and USDA-ARS, Kimberly, Idaho, participated in RAPID.

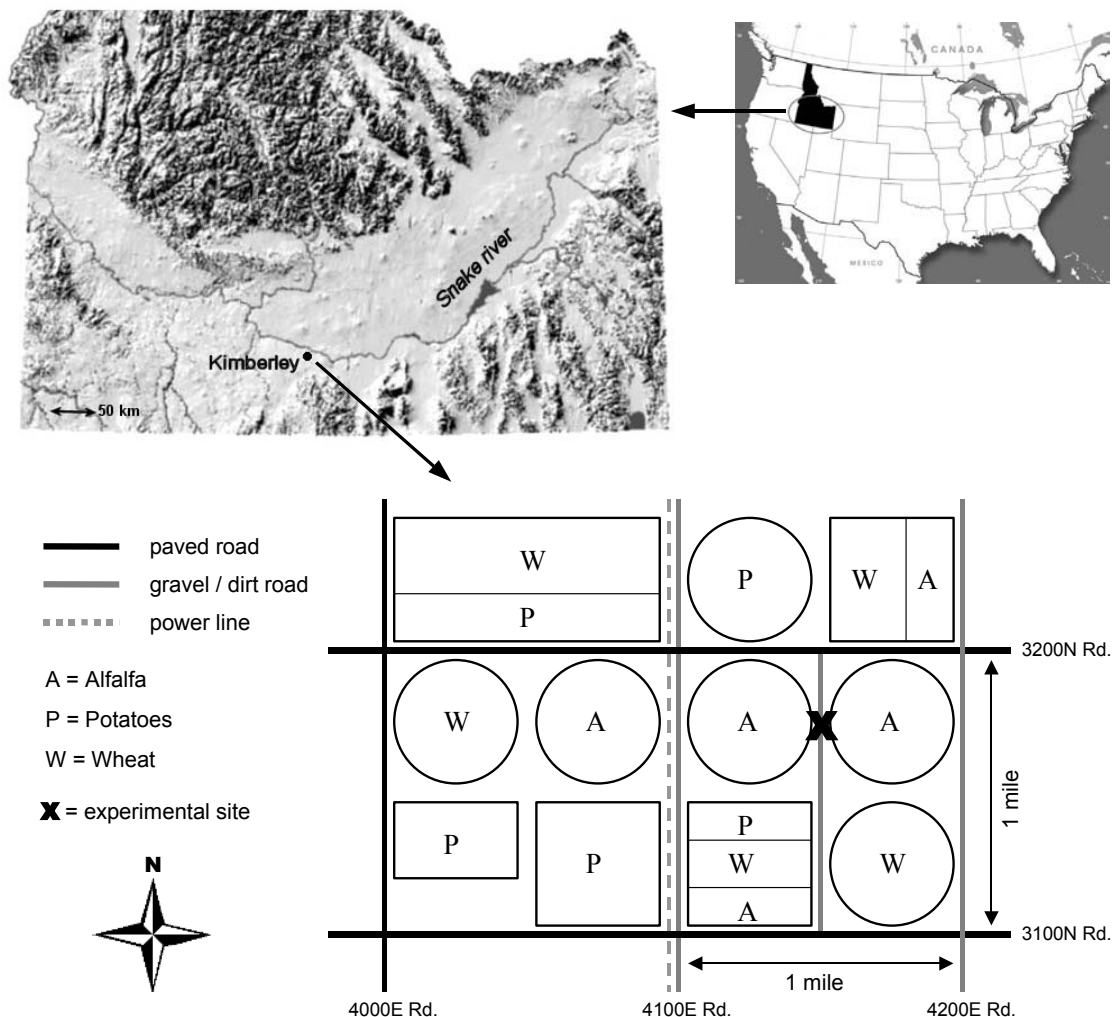


Figure 2-5: Top right: location of the Snake River Plane (SRP) within Idaho (marked in black). Top left: outline of the SRP and the position the experimental site near Kimberly. Bottom: outline of the agricultural fields surrounding the experimental site that is situated between two alfalfa fields. The irrigation types used are sprinkler irrigation (square blocks) and centre pivot irrigation (circles).

The RAPID experiment was carried out prior to the CASES-99 experiment between 25 August and 19 September 1999 (DOY 237 to 262) in an agricultural area near Kimberley in the south of Idaho, USA (see Figure 2-5). Idaho is dominated by mountains and is one of the last regions in the USA to be cultivated. Most agriculture takes place in the south in the Snake River Plain (SRP), a dry plateau that covers one quarter of the state of Idaho. The elevation of the plateau roughly ranges between 1000 and 1500 m.

The main wind direction over northwest USA is westerly. Humid maritime air from the Pacific Ocean is forced over two mountain ranges before it reaches the SRP. First it passes the coastal mountain range (~1000 m), followed by the sea level plain called the Puget Sound and then it passes the Cascades (~2000 m) to reach the SRP. It is the consecutive repetition of adiabatic cooling, and condensation and precipitation of humidity upon ascending a mounting range, followed by adiabatic heating when the air descends that makes the climate in SRP desert like. Typical natural vegetation is sagebrush. The soil exists of a mixture of sand and clay deposited by wind on the lava rock sub-soil. The soil layer is thin at some places the lava sub-soil reaches the surface. The water needed for irrigation comes from the Snake River.

The agricultural area surrounding Kimberley is divided up into 1 mile by 1 mile blocks which are separated by roads. The 1 by 1 mile blocks are generally sub-divided into 4 fields. The RAPID experimental site ($42^{\circ} 27' 21''\text{N}$ and $114^{\circ} 14' 29''\text{W}$) was situated upon a small dust road between 2 alfalfa fields, which were centre-pivot irrigated (see Figure 2-5). The instruments were pointed towards the predominant westerly wind direction. Alfalfa is a very suitable crop for this study. Throughout its growing cycle it remains green with high evaporation rates. In addition, it has a short growing-cut cycle of about 6 weeks. The start of the experiment roughly coincided with the start of a new growing cycle of the two adjacent alfalfa fields. A description of the instruments used is given in Section 2.3.3.

2.3.2 Weather conditions RAPID experiment

As outlined in the previous section, the typical weather pattern for the SRP during August, September is characterised by westerly winds bringing warm and dry air, which is fed to the surface by means of a negative H and enhances L_vE . As the surface layer is stably stratified this process can only persist if there is some minimum wind speed that produces sufficient mechanical turbulent forcing to counteract the negative buoyancy (De Bruin et al., 2004).

Figure 2-6 summarises the weather conditions during the experiment. A strong cold front that dominated the weather conditions during RAPID disrupted the general weather pattern for the SRP.

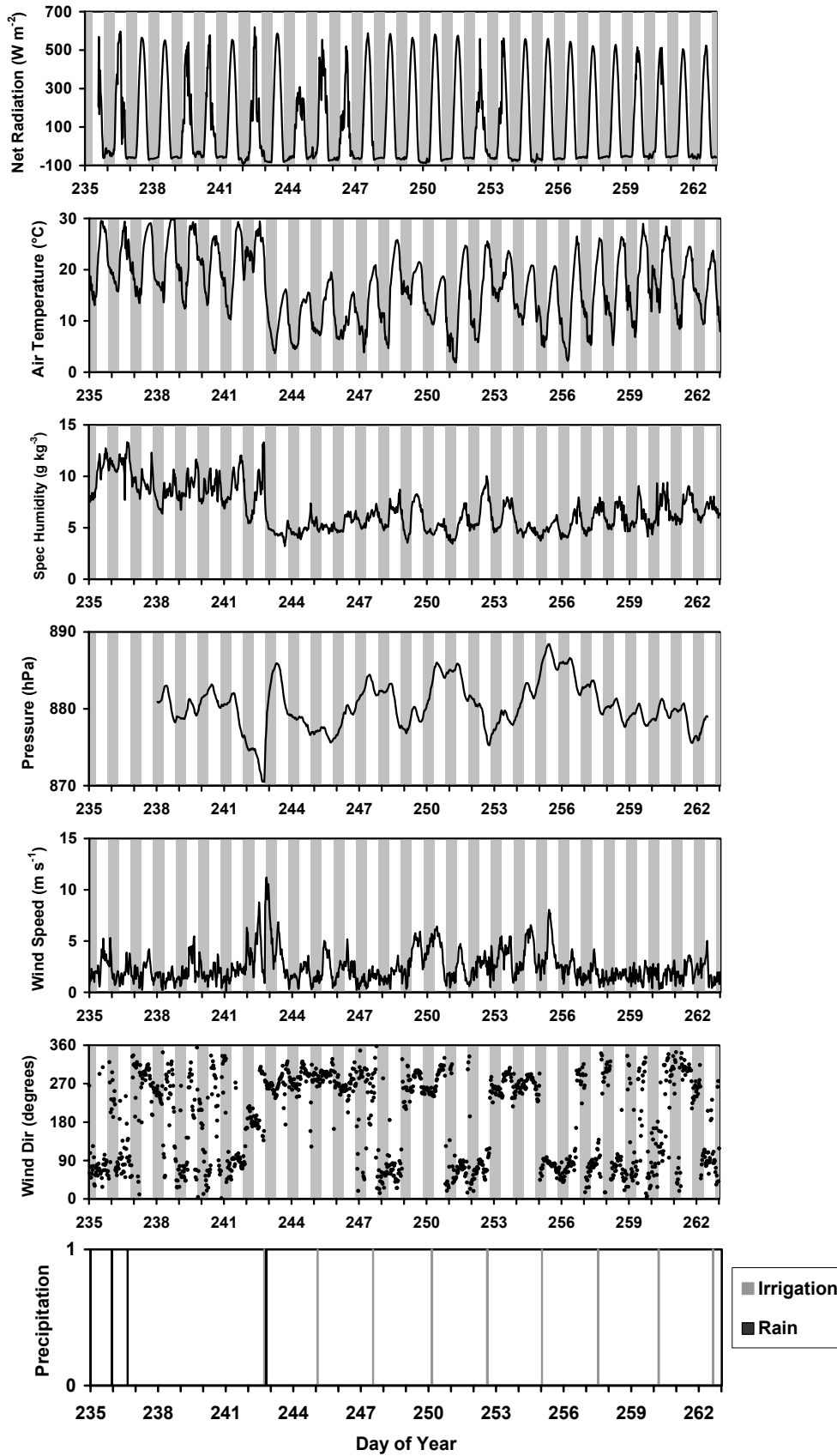


Figure 2-6: Impression of the weather conditions during the RAPID experiment. Day and night time data have alternating white and grey backgrounds. Data are averaged over 1 hour and taken at ~3m height.

The passage of the cold front on DOY 242 can clearly be identified in the data. The temperature and humidity plots show that the air type is completely different after the frontal passage. The advected air is even drier than before, but more importantly it is also much cooler. The maximum temperature dropped from 30 °C on DOY 242 to 15 °C the next day. Apart from the weather conditions and the advection effect, L_vE is largest when the crop is at its maximum growing rate stage and just after irrigation. Figure 2-7 shows the alfalfa crop height development. The bottom plot of Figure 2-6 depicts the registered rain and irrigation in the west field during the experiment. The irrigation did not start until DOY 242.

The following can be concluded from Figure 2-6 and Figure 2-7. At the start of the experiment, the weather conditions were favourable for regional advection. The conditions were warm and relatively dry with occasional winds above 5 m s^{-1} . However, the alfalfa did not receive its first irrigation after the crop was cut. It was in a stage of its growing cycle in which the plant and the water supply, and not so much the weather conditions were the limiting factor for the occurrence of evapotranspiration exceeding the net available energy. After the passage of the front, the air was even drier than before adding to the water vapour deficit but - more importantly - it was considerably cooler. Now, the irrigation started and the crop was in its maximum growing rate stage, but the weather conditions averted enhanced evaporation due to regional advection. Towards the end of the growing season, the temperature started to increase again to their mean climatological values, but the winds were very calm and the evapotranspiration of the crop reduced as it entered the ripening stage. In the middle stage of the experiment there were a few days in which the temperature already started to recover somewhat with moderate wind speeds resulting in a considerable daytime negative H . These ‘golden’ days were DOY 253 and 254 on which we based our advection study (see De Bruin et al., 2004 and Appendix III).

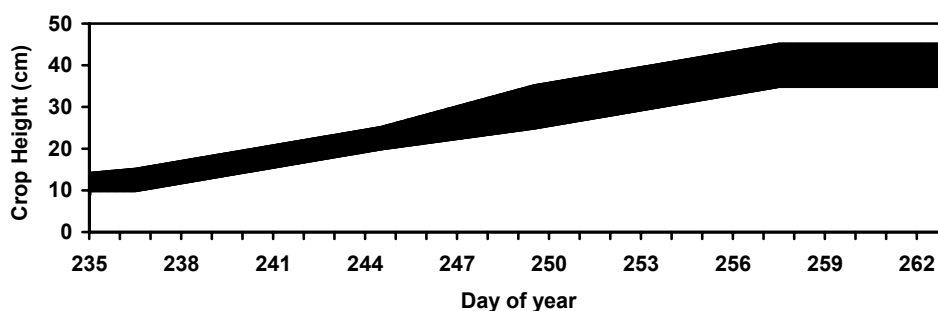


Figure 2-7: Development of the alfalfa crop height during the RAPID experiment. A range is given indicating the crop heights of two fields adjacent to the experimental site.

2.3.3 Instrumentation RAPID experiment

We will discuss the instrumentation used during the RAPID experiment only briefly for three reasons. First, we carried out the RAPID and CASES-99 experiment one after the other between August and October 1999. The instrumentation deployed by Wageningen University,

therefore, is largely the same to what is already described in Section 2.2.3. Second, the dataset was gathered as part of this thesis, but in the end will not be used directly. A co-authored paper that was published is added in Appendix III. Third, the RAPID instrumentation is extensively documented in Kramer (2000).

Most surface flux systems were set-up at 10 to 15 m distance from each other on a north-south aligned dirt road in between two alfalfa fields (see Figure 2-5). Installation of instruments in the fields was hampered by centre-pivot irrigation systems. The centre-pivots had a rotation speed of 2.5 days and their positions were documented on a daily basis (see Kramer, 2000).

Eddy Covariance Systems:

Four eddy covariance systems were set-up. The two EC systems of Wageningen University were installed in a 10 m tall tower at 9.44 m and 3.52 m both pointing towards the west field. North of the 10 m tower, on the same dirt road two additional systems were installed on tri-pods. They were provided by Campbell Scientific Inc. (at 2.90 m, pointing towards the east field) and Utah State University (at 3.06 m, pointing towards the west field). All systems were equipped with a Campbell Scientific 23X datalogger and were operated at 20 Hz. Only for the EC system of Utah State University (USU) we did not have a computer to store the raw data. The fluxes were calculated on the datalogger itself without any further corrections (see Section 2.5.4).

Bowen Ratio Systems:

Two identical Bowen Ratio systems (Campbell Scientific Inc. 1993 model) provided by USU and operated by the University of Idaho were set-up on the dirt road south of the 10 m tower. The systems consist of 2 arms, here pointed towards the south, equipped with chromel-constantan thermocouples for the temperature measurement and air-inlets for the water vapour measurement. From these the air is pumped to a General Eastern chilled mirror system to determine the dew point temperature. The gradients of temperature and humidity were determined between 2.0 m and 3.0 m. In addition, the net radiation was measured in the alfalfa fields with REBS Q7 sensors. Each system was equipped with a soil heat flux system consisting of 2 REBS HFT3 heat flux plates installed at ~ 8 cm depth and a Campbell Scientific TCAV spatial averaging thermocouple probe consisting of 4 temperature sensors installed at ~ 2 cm and 6 cm above each soil heat flux plate to account for the heat storage above the plates. In addition the systems were equipped with a RM-Young wind speed and direction sensors, an Eppley PSP Pyranometer, a Vaisala HMP35C temperature humidity probe, an Everest Interscience 4000 infra-red thermometer, and a Campbell Scientific tipping bucket rain gauge to measure rain and irrigation amounts. The data of both systems were measured by Campbell Scientific 21X dataloggers equipped with an AM416 multiplexer and SM 192 storage modules to store the data. Data was measurement at 2 s intervals and stored at 10 minutes intervals.

Radiation:

The Bowen Ratio systems (see above) were equipped with REBS Q7 net radiometers (R_n) and Eppley PSP pyranometers (S_{in}). In addition, the Kipp and Zonen CM14-CG2 4 way net radiation system (S_{in} , S_{out} , L_{in} , L_{out} and R_n) from Wageningen University was installed some 8 m infield from the dirt road at a height of 1.25 m. On the same mounting structure, also a Swissteco net radiometer was installed from the United States Department of Agriculture (USDA). Kramer (2000) compared

all these sensors in detail and concluded that the Kipp and Zonen system obtained the most reliable measurement of S_m and R_n .

Scintillometers:

A 15 cm aperture LAS from Wageningen University and a Scintec AG SLS20 DBSAS (see Section 2.2.3) were installed parallel to and at 10 m and 13 m from the dirt road. The LAS was installed at 2.85 m height on tri-pods over a path length of 275 m. The DBSAS was installed at 2.50 m height on tri-pods over a path length of 155 m. The scintillometers were positioned in such a way that the centre-pivots passed over them. As a precaution we bagged the sensors when this was to happen (once every 2.5 days). The datalogging was as described in Section 2.2.3.

Soil Humidity:

The volumetric soil water content between 0 cm and 12 cm was measured by two GrowPoint TRT Systems, that register the soil humidity every hour. These measurements were calibrated against gravimetrically determined soil moisture from oven dried soil core samples that were collected every day.

2.4 BBC experiment

2.4.1 Overview BBC experiment

The BALTEX/BRIDGE Cloud (BBC) experiment is a cloud observation campaign that took place in August and September 2001 at the Cabauw research site, the Netherlands in the framework of EU-funded CLIWA-NET project and the German 4D-CLOUDS project.

The cloud liquid water network (CLIWA-NET) is part of the Baltic Sea experiment (BALTEX, see www.gkss.de/baltex). BALTEX is a long-term multinational project under the GEWEX (Global Energy and Water Cycle Experiment) program with the objective to understand and predict the hydrological cycle in the Baltic Sea region. Within BALTEX the BRIDGE program focuses on generating comprehensive data-sets that support the BALTEX research. The main focus of the BBC experiment was on remote sensing of clouds by means of satellites, radars, lidars, sodars supported by aircraft measurements and the standard observations gathered at Cabauw. The main interest of the 4D-CLOUDS program within BBC was the interaction between radiation and clouds.

The Cabauw research site (51° 58'N and 04° 55'E) is located in the west of the Netherlands in a polder 0.7 m below average sea level near the village of Cabauw (see Figure 2-8). The site is maintained and operated by the Royal Dutch Meteorological Institute (KNMI). The surroundings are flat and consist of meadows and ditches, with scattered villages, orchards and lines of trees. The soil consists of a 0.4 to 0.8 m thick bed of river-clay on top of a peat layer and the ground water table is maintained at a fixed depth. The experimental facilities at Cabauw consist of a grassland field where measurements of surface fluxes and soil parameters

are performed. A 213 m tall meteorological tower is used for profile measurements in the lower part of the atmospheric boundary layer.

Wageningen University contributed to the network of surface flux measurements between 21 August (DOY 233) and 26 September (DOY 269) 2001 on the grass covered energy balance site. Taking advantage of the wide infrastructure available during the BBC campaign, we also set-up a scintillometer experiment where we compared different scintillometer configurations to obtain surface fluxes at field scale (~ 100m). The results of this study are presented in Chapter 5. The experimental design is given in Figure 2-8. Furthermore, the CO₂ concentration and fluxes that we measured during the BBC campaign were part of the Wageningen University contribution to the CarboEurope project (www.carboeurope.org), a research project that deals with all aspects of CO₂-monitoring in Europe.

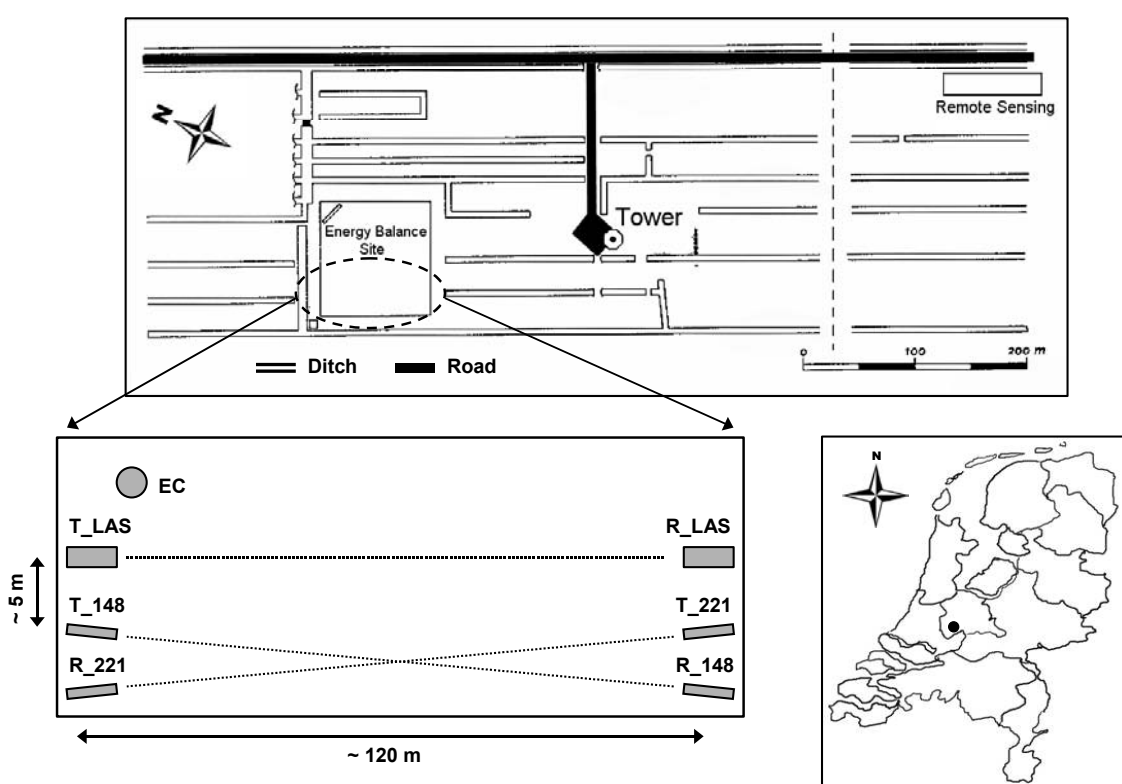


Figure 2-8: Bottom right: location of the Cabauw experimental site in the Netherlands. Top: Outline of the Cabauw experimental site. Bottom left: experimental design of the Wageningen University flux measurements during the BBC experiment (not drawn to scale). T = transmitter, R = receiver and LAS = large-aperture scintillometer. The laser scintillometers are indicated by their serial numbers (221 and 148)

2.4.2 Weather conditions BBC experiment

An overview of the weather conditions during the period in which Wageningen University contributed to the BBC experiment is given in Figure 2-9.

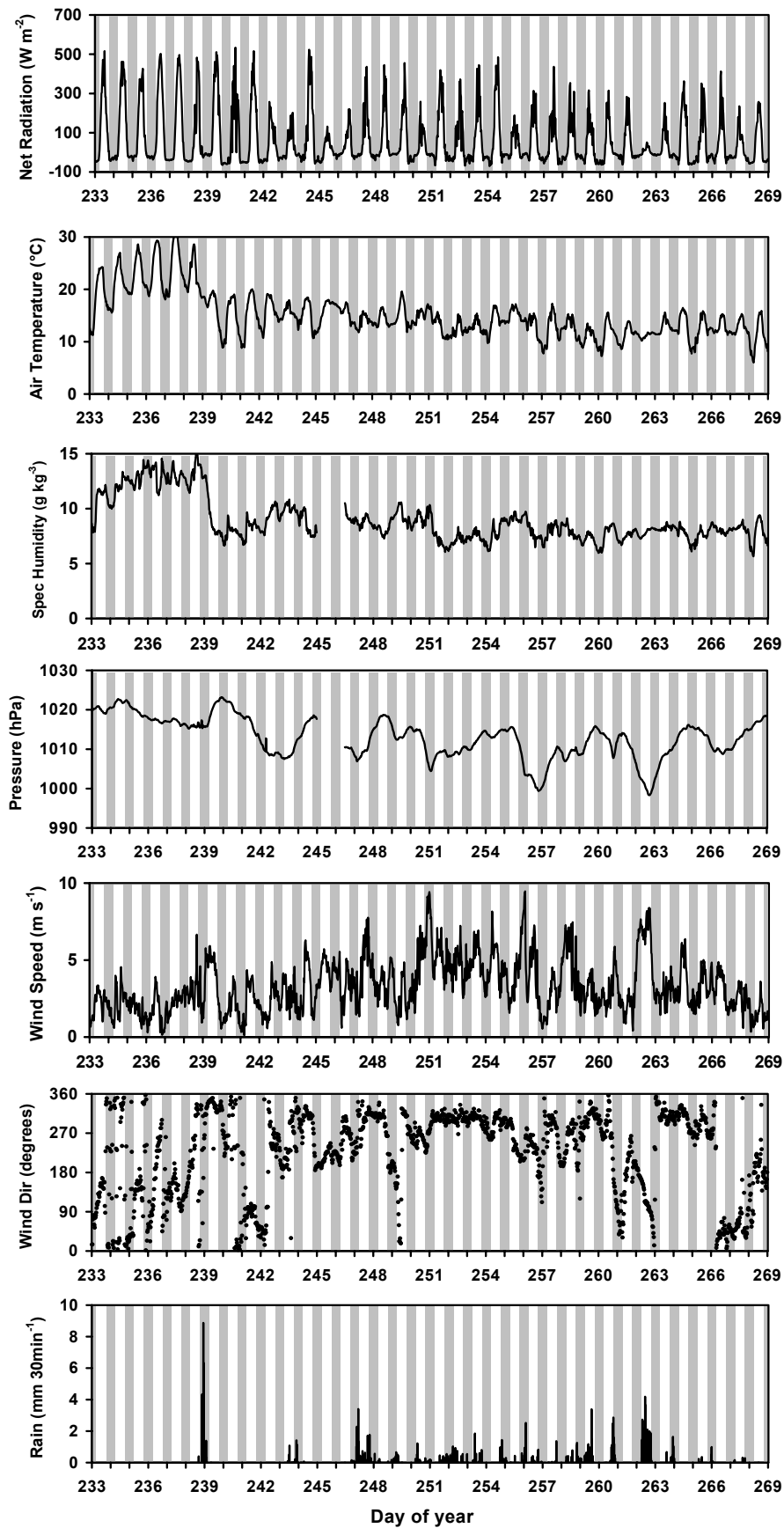


Figure 2-9: Impression of the weather conditions during the BBC experiment. Day and night time data have alternating white and grey backgrounds. Data are averaged over 1 hour.

At the beginning of the experiment, the weather was still summer-like with moderate winds, and temperatures above 20° C. In the beginning of September, clearly a shift in the weather pattern can be seen in Figure 2-9. The temperature dropped by about 10° C, winds tended to be stronger and more consistent from the west and it rained frequently. In the end, September 2001 turned out to be the coldest and wettest in recorded history in the Netherlands. At Cabauw in total 190 mm of rain was collected between DOY 233 and 269. As a consequence, the conditions were near neutral for day- and night time. In addition, the continuous rainfall also corrupted our measurements due to power- or instrument failure, and the high levels of humidity also led to frequent dew formation on the scintillometer windows during night-time.

2.4.3 Instrumentation BBC experiment

The instrumentation deployed by Wageningen University during the BBC experiment is outlined in Table 2-3. As in Table 2-1 they are divided into the instrument groups, here an eddy covariance system and the scintillometers. Some more information on the instruments is given in the following descriptions of these groups.

Table 2-3: Instrumentation deployed at the Wageningen University site during BBC experiment. Different sensor groups are divided by thick lines. Sensor groups are (from top to bottom): eddy covariance system and scintillometers.

Sensor	Manufacturer	Model	Parameters	Sample interval [s]	Stored interval [s]
3D Sonic anemometer	Campbell Scientific, Logan, USA	CSAT3	u, v, w [m s^{-1}]; T_s [$^{\circ}\text{C}$]	0.05	0.05
Fast response H ₂ O-CO ₂ sensor	LiCor, Lincoln, USA	LiCor7500	$\rho_{\text{H}_2\text{O}}$ and ρ_{CO_2} [kg m^{-3}]	0.05	0.05
Pressure sensor	Vaisala, Helsinki, Finland	PTB101B	P [Pa]	1	60
Large-Aperture Scintillometer	Wageningen University, Netherlands	-	C_n^2 [$\text{m}^{-2/3}$]	1	60
Double-beam Laser scintillometers (2x)	Scintec AG, Tübingen, Germany	SLS20	C_n^2 [$\text{m}^{-2/3}$]; ε [m^2s^{-3}]	6	6

Eddy Covariance System:

We set-up an eddy covariance system at the BBC campaign on a tri-pod at 3.32 m height, pointing towards the south-southwest (200° relative to north), consisting of a CSAT3 sonic anemometer and a LiCor7500 open path H₂O-CO₂ sensor. The Licor7500 was installed at 0.27 m directly below the CSAT3. A PTP101B pressure sensor completed the system.

The working principle of the LiCor7500 is comparable to that of the KH20 described in Section 2.2.3. The difference is that the LiCor7500 operates in the infrared region of the electromagnetic spectrum where H₂O and CO₂ have absorption bands. Since the H₂O and CO₂ absorption at these wavelengths is not as strong as in the ultraviolet, the path length of the LiCor7500 is larger (~12.5 cm) than that of the KH20 (~1.5 cm). A major advantage over the KH20 is that the calibration does

not shift in time, and signals are communicated to Campbell Scientific dataloggers with the same digital protocol (SDM) as the CSAT3 ensuring that both signals can be synchronised. The datalogger unit is described in Section 2.2.3.

Scintillometers:

A 10 cm aperture LAS from Wageningen University and two Scintec AG SLS20 DBSASs (more details in Section 2.2.3) were installed parallel to each other to the west of the EC system. The distance between the systems was ~ 5 m. The two DBSASs were set-up with crossing paths and transmitter and receiver installed at opposite sides of the path (see Figure 2-8).

The LAS was set-up at a height of 2.72 m and a path length of 118 m. Data were collected and stored with a Campbell Scientific CR510 datalogger with metal enclosure.

The two SLS20 DBSASs are an old sensor with serial number 148, purchased in 1995, and a new sensor with serial number 221, purchased in 2001. The SLS20 with SN148 we also used in CASES-99 and RAPID. It was installed at 2.52 m height and a path length of 120 m, datalogger and storage was done by means of SLSrun software version 2.03. The SLS20 SN148 was installed at 2.48 m height and a path length of 120 m, datalogger and storage was done by means of SLSrun software version 2.24.

The instruments were powered from mains voltage available at the site. Due to the poor weather conditions, this usually reliable power supply failed on numerous occasions. Upon reestablishment of the power, the systems do not automatically continue their measurements as the DBSAS and EC system datalog system consist of a laptop computer. In addition, the saturated soil made the tri-pods subside somewhat causing misalignment of the scintillometers. We visited the field site only once or twice a week. If problems occurred we did not realise about it until some days later. In all, these circumstances produced a data set with much gaps in it.

2.5 Data Analysis

In this thesis the turbulence parameters ε and C_T^2 play a central role since these are the principle physical parameters that are measured by scintillometers. To compare these measurements, we also derived ε and C_T^2 from eddy-covariance systems. For both techniques to determine ε and C_T^2 a good understanding of structure parameters, spectra and their interdependence is necessary. A description of these concepts is given in Section 2.5.1.

Most attention in this section will be paid to methods to estimate ε and C_T^2 from sonic anemometers. Although the description of these techniques is straightforward, their application in practice is more complicated. Basically there are two techniques. The first technique uses structure parameters, the second technique involves spectra. These are described in section 2.5.2.

The derivation of ε and C_T^2 from the raw scintillometer measurements is extensively described in the Chapters 3 to 5. Therefore, here it will only be described briefly in Section 2.5.3.

Last, Sections 2.5.4 and 2.5.5 describe how turbulent fluxes of heat and momentum are obtained from the eddy covariance and scintillometer technique. The eddy-covariance method for estimating surface fluxes is a standard micro-meteorological method. This technique will be briefly described with a focus on some special issues. The scintillometer method uses ε and C_T^2 to estimate surface fluxes of heat and momentum based on Monin-Obukhov similarity theory.

2.5.1 Structure functions and spectra

2.5.1.1 Definitions of moments and structure functions

Since turbulent flows are not reproducible in detail they can be described in a statistical sense only. Some statistical properties are described in terms of, q' , the deviation of a random variable q . This deviation is defined by the Reynolds decomposition:

$$q \equiv \bar{q} + q', \quad (2.3)$$

where \bar{q} is a mean value and q' is the deviation from that mean. The nature of turbulence is that it concerns random, three-dimensional flows. The turbulent field $q(\mathbf{r})$ then indicates the value of variable q at position \mathbf{r} , ($\mathbf{r} = (x, y, z)$). Note that q can be a scalar or a component of the wind field, in which case q also has a direction represented by u , v or w indicating the components in x , y , and z directions.

The state of the random variable $q(\mathbf{r})$ can be described with the statistical moments $B_{qq\dots q}$. In general, the k^{th} order moments are the mean values of products of k values of the field (Monin and Yaglom, 1971):

$$B_{qq\dots q}(\mathbf{r}_1, \mathbf{r}_2, \dots, \mathbf{r}_k) = \overline{q'(\mathbf{r}_1)q'(\mathbf{r}_2)\dots q'(\mathbf{r}_k)}. \quad (2.4)$$

The statistical description of turbulence can be simplified by adopting two concepts. The first one is that the state of turbulence is homogeneous spatially and stationary in time, i.e. it is insensitive to translation of the co-ordinate system. The second one is that on each point in the turbulent field the turbulent state is equal in all directions or isotropic, i.e. it is insensitive to rotation of coordinate system. Often these assumptions can only be made locally, i.e. only relative motions of the flow are considered in “small” regions and over “small” intervals of time. More elaborate discussion on these concepts can be found in Monin and Yaglom (1971). (Locally) homogenous, stationary and isotropic turbulence implies that the statistical moments defined in Equation (2.4) are independent on lines or planes through $\mathbf{r}_1, \dots, \mathbf{r}_k$. In the

atmosphere the condition of homogeneity and stationarity is not always realistic. A less strict assumption is then to adopt the concept of stationary increments, where the difference $q(\mathbf{r}_1) - q(\mathbf{r}_2)$ is assumed to be stationary. The statistic that follows from this concept is the structure function, $D_{qq\dots q}$ (Tatarskii, 1961):

$$D_{qq\dots q}(\mathbf{r}_1, \mathbf{r}_2, \dots, \mathbf{r}_k) = \overline{(q(\mathbf{r}_1) - q(\mathbf{r}_2))(q(\mathbf{r}_1) - q(\mathbf{r}_2)) \dots (q(\mathbf{r}_1) - q(\mathbf{r}_2))}. \quad (2.5)$$

For simplicity we have so far only considered k^{th} order moments and structure functions for one variable, q , which can be a scalar or a component of the wind vector. Moments and structure functions can, however, also be given as cross terms between scalars and or wind components. For the moment we are only interested in second order moments, $B_{qq}(\mathbf{r}_1, \mathbf{r}_2)$ and structure functions, $D_{qq}(\mathbf{r}_1, \mathbf{r}_2)$ of a single variable, q . The second order moment is also referred to as the covariance function.

For (incremental) *stationary turbulence* B_{qq} and D_{qq} depend only on the separation vector, \mathbf{r} , between \mathbf{r}_1 and \mathbf{r}_2 , $\mathbf{r} = |\mathbf{r}_1 - \mathbf{r}_2|$, and not on the location of \mathbf{r}_1 and \mathbf{r}_2 . B_{qq} is then given for any location \mathbf{r}_1 in the flow by

$$B_{qq}(\mathbf{r}) = \overline{(q(\mathbf{r}_1) - \overline{q(\mathbf{r}_1)}) (q(\mathbf{r}_1 + \mathbf{r}) - \overline{q(\mathbf{r}_1 + \mathbf{r})})}. \quad (2.6)$$

Similarly,

$$D_{qq}(\mathbf{r}) = \overline{(q(\mathbf{r}_1) - q(\mathbf{r}_1 + \mathbf{r}))^2}. \quad (2.7)$$

For (incremental) *stationary and isotropic turbulence* B_{qq} and D_{qq} depend only on the length, r , of the separation vector, \mathbf{r} , between \mathbf{r}_1 and \mathbf{r}_2 , $r = |\mathbf{r}_1 - \mathbf{r}_2|$. B_{qq} is then given for any location \mathbf{r}_1 in the flow by

$$B_{qq}(r) = \overline{(q(\mathbf{r}_1) - \overline{q(\mathbf{r}_1)}) (q(\mathbf{r}_1 + r) - \overline{q(\mathbf{r}_1 + r)})}. \quad (2.8)$$

Similarly,

$$D_{qq}(r) = \overline{(q(\mathbf{r}_1) - q(\mathbf{r}_1 + r))^2}. \quad (2.9)$$

Under the same strict conditions of *isotropy and homogeneity* D_{qq} is also independent of the position in the flow and link between D_{qq} and B_{qq} is then defined by:

$$D_{qq}(r) = 2(B_{qq}(0) - B_{qq}(r)), \quad (2.10)$$

where $B_{qq}(0)$ denotes B_{qq} at any position in the flow (Moene et al. 2004).

2.5.1.2 Definitions of spectra

The 3 dimensional (3D) spectrum of the *homogenous* turbulent field $q(\mathbf{r})$ may be given by the Fourier transform of the covariance function, $B_{qq}(\mathbf{r})$:

$$\Phi_{qq}(\mathbf{k}) = \frac{1}{(2\pi)^3} \iiint B_{qq}(\mathbf{r}) e^{-i\mathbf{k}\cdot\mathbf{r}} d\mathbf{r}. \quad (2.11)$$

$\Phi_{qq}(\mathbf{k})$ represents the spectral density of the turbulent field $q(\mathbf{r})$, and \mathbf{k} represents the wave-number vector. $\Phi_{qq}(\mathbf{k})$ contains complete information on the distribution of turbulent variance of q , σ_q^2 , over wave-number space. The units of $\Phi_{qq}(\mathbf{k})$, therefore, are σ_q^2 per k^3 or $q^2 \text{ m}^{-3}$. In practice Equation (2.11) is very difficult to work with, so we normally work with simplified versions of $\Phi_{qq}(\mathbf{k})$ by adopting the concept of isotropy of a homogeneous turbulent field. Then, $B_{qq}(\mathbf{r})$ becomes independent of direction and depends only on the magnitude r of the vector \mathbf{r} , $r = |\mathbf{r}|$ (see also Equation 2.8). Similarly, $\Phi_{qq}(\mathbf{k})$, will only depend on the length k of vector \mathbf{k} , $k = |\mathbf{k}|$. The distribution of $B_{qq}(\mathbf{r})$ and $\Phi_{qq}(\mathbf{k})$ in r and k space can then be represented by a sphere. This leads to a simplification of the description of the spectra in a number of ways.

First, by introducing spherical coordinates for \mathbf{r} , $d\mathbf{r} = r^2 \sin\theta dr d\phi d\theta$ and $\mathbf{k} \cdot \mathbf{r} = kr \cos\theta$, and integrating over the two angles, Equation (2.11) becomes:

$$\Phi_{qq}(k) = \frac{1}{(2\pi)^3} \int_0^\infty \int_0^{2\pi} \int_0^\pi B_{qq}(r) e^{-ikr \cos\theta} r^2 \sin\theta dr d\phi d\theta = \frac{1}{2\pi} \int_0^\infty \frac{\sin(kr)}{kr} B_{qq}(r) r^2 dr. \quad (2.12)$$

Note that although the directional information in wave-number space has been removed, the dimensions of $\Phi_{qq}(k)$ are still those of $\Phi_{qq}(\mathbf{k})$.

The second simplification is to, similarly to what we have done for \mathbf{r} in Equation (2.12) by introducing spherical coordinates, remove the directional information in $\Phi_{qq}(\mathbf{k})$ by integrating over a spherical shell in wave-number space of radius $k = |\mathbf{k}|$. This operation produces the spectrum $E_{qq}(k)$ which, in analogy with Monin and Yaglom (1971), we call ‘‘the spectrum’’:

$$E_{qq}(k) = \int_{k=|\mathbf{k}|} \Phi_{qq}(\mathbf{k}) d\mathbf{k} = 4\pi k^2 \Phi_{qq}(k). \quad (2.13)$$

Now, $E_{qq}(k)$, represents the power spectral energy of the 3D spectrum projected on one dimension, the radius k . The units of $E_{qq}(k)$ are similar to those of a 1 dimensional (1D) power spectrum, i.e. $\sigma^2(q)$ per k or $q^2 \text{ m}^{-1}$.

The third simplification of $\Phi_{qq}(\mathbf{k})$ is the so-called 1 dimensional spectrum, where the separation vector \mathbf{r} only varies along one line

$$E_{qq}^1(k) = E_{qq}^1(k_1) = \iint \Phi_{qq}(\mathbf{k}) dk_2 dk_3. \quad (2.14)$$

The relation between $E_{qq}(k)$ and $E_{qq}^1(k)$ is given by

$$E_{qq}(k) = -k \frac{dE_{qq}^1(k)}{dk}. \quad (2.15)$$

Evaluation of Equation (2.15) for theoretical expressions of $E_{qq}(k)$ yields a 3/5 factor between $E_{qq}(k)$ and $E_{qq}^1(k)$ (Monin and Yaglom, 1971).

Monin and Yaglom (1971) show that combining Equations (2.10) and (2.12) yields the relation between the second order structure function D_{qq} and the 3D spectrum $\Phi_{qq}(k)$:

$$D_{qq} = 8\pi \int_0^\infty \left(1 - \frac{\sin(kr)}{kr}\right) \Phi_{qq}(k) k^2 dk. \quad (2.16)$$

2.5.1.3 Theoretical atmospheric spectra and structure functions

In this section we will introduce theoretical 1D and 3D spectra and theoretical expressions of the structure function of temperature. For the scintillometer method the theoretical 3D spectra of temperature is needed (Section 2.5.3). For estimation of ε and C_T^2 from measured spectra of sonic anemometer time series, the theoretical 1D spectra of temperature and wind speed are used (Section 2.5.2). These theoretical expressions will be given in terms of key variables that describe turbulence which were introduced in Chapter 1 being the dissipation rate of TKE (ε), the dissipation rate of temperature variance (ε_θ), the structure function of temperature (C_T^2), the inner scale of turbulence (l_θ), the Kolmogorov length scale (η), the temperature micro-scale (η_θ), the kinematic viscosity (ν), and thermal diffusion coefficient (χ). The ratio between the latter two is the Prandtl-number, $\text{Pr} = \nu / \chi$.

In Chapter 1 the 1D inertial range spectra of wind speed and temperature were introduced, which we will repeat here

$$S_u = \alpha \varepsilon^{2/3} k^{-5/3} \quad (2.17)$$

and

$$S_T = \beta_\theta \varepsilon_\theta \varepsilon^{-1/3} k^{-5/3} = 0.25 C_T^2 k^{-5/3}. \quad (2.18)$$

Note that here (and from hereon) we denote E_{uu}^1 with S_u and E_{TT}^1 with S_T . α is the Kolmogorov constant, and β_θ is the Obukhov-Corrsin constant. A review of reported values for the Kolmogorov constants in the literature is given by Höögström (1996). A mid-range value that we adopted is $\alpha = 0.55$. The Obukhov-Corrsin constant is more difficult to determine and less certainty exists about this parameter. Hill (1997) reviews the values reported in the literature and concludes that $\beta_\theta = 0.43$ is the best estimate. Note that also $\beta_\theta = 0.72$ is often used. This is the Obukhov-Corrsin constant for 3D spectra, which relates to the 1D value by a factor 3/5 (see comment below Equation 2.15)

The value 0.25 in Equation (2.18) is not an experimentally determined constant but is derived from theory and has an exact value of $2/(3\Gamma(1/3))$, where $\Gamma(1/3)$ is the gamma-function with argument 1/3 ($\cong 2.6789$).

Next we will introduce theoretical descriptions of the second order structure function of temperature, D_{TT} , in the inertial and dissipation range and from these formally derive the inner scale length. From dimensional arguments it can be shown that D_{TT} for spacing r in the inertial range is given as (Obukhov, 1949):

$$D_{TT} = C_T^2 r^{-2/3}. \quad (2.19)$$

For r at dissipation range scales it can be shown that

$$D_{TT} = \frac{\varepsilon_\theta}{3\chi} r^2. \quad (2.20)$$

The inner scale, l_0 is now defined as the length scale r at the intercept of the D_{TT} inertial range and dissipation range description. Equalizing Equations (2.19) and (2.20) and substituting $\varepsilon_\theta = 2/(3\beta_\theta\Gamma(1/3))C_T^2 \varepsilon^{1/3}$ from Equation (2.18) and the Prandtl-number definition yields

$$l_0 = \left(\frac{9\beta_\theta\Gamma(1/3)}{\text{Pr}} \right)^{3/4} \left(\frac{\nu^3}{\varepsilon} \right)^{1/4} = 7.4\eta. \quad (2.21)$$

The factor of 7.4 follows using $\beta_\theta = 0.43$ and $\text{Pr}=0.72$ adopted from the review of Hill (1997) of this constant. Note that this factor is rather sensitive to the choice of β_θ .

For optical scintillometry the 3D temperature spectrum, Φ_{TT} (from hereon denoted as ϕ_T), is the natural statistic. To evolve the 1D inertial range S_T into the inertial range description of ϕ_T involves two steps outlined in 2.5.1.2 (Equations 2.15 and 2.13). From these it follows that ϕ_T in the inertial range is described by

$$\phi_{T_inertial} = \frac{5}{3} \frac{1}{4\pi} k^{-2} S_T = \left(\frac{5}{18\Gamma(1/3)} \right) C_T^2 k^{-11/3} = 0.033 C_T^2 k^{-11/3}. \quad (2.22)$$

For laser scintillometry also the dissipation range of ϕ_T is relevant. In the dissipation range, the scale of temperature fluctuations is reduced by molecular effects and the spectral decay is stronger than the $k^{-11/3}$ decay in the inertial range. At the transition of inertial to dissipation range, in the so-called viscous-convective range the temperature spectrum exhibits a bump due to different molecular diffusion coefficients for momentum, ν , and heat transfer, χ . (see Chapter 1). The total 3D spectrum is expressed by

$$\phi_T = 0.033 C_T^2 k^{-11/3} f_A(kl_0), \quad (2.23)$$

where f_A describes the decay of the temperature fluctuations in the dissipation range and equals unity in the inertial range. Hill (1978) composed a theoretical model fitted to the dataset of Champagne et al. (1977) that describes f_A as a function of l_0 (see Figure 2-10). In this thesis we will use f_A of Hill (1978) in tabulated form and an alternative expression by Frehlich (1992) who determined f_A from scintillometer measurements (Chapter 3).

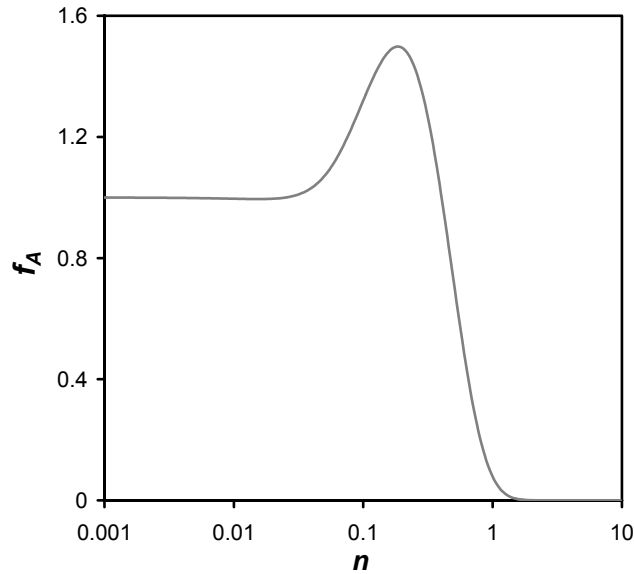


Figure 2-10: Hill model (1978) of f_A , the temperature spectrum in the dissipation range normalised with the inertial range temperature spectrum.

In practice, spectra in terms of wave-numbers are very difficult to measure. Measured spectra are generally based on turbulence time-series (see next section). To convert temporal measurements at a point to spatial patterns in space one adopts Taylors frozen turbulence theory, which assumes that the nature of turbulence does not change as it advects through a sensor. This allows the translation of turbulence measurements taken as a function of time to their corresponding measurements in space using the wind speed adopting

$$l = Ut, \quad (2.24)$$

with l is a space scale, t is time, and U the wind speed.

2.5.1.4 Measuring atmospheric spectra

We will use 1D spectra to estimate C_T^2 and ε from sonic anemometer data times series. There are two main approaches to determine 1D spectra. In the first one, the time series is directly transformed to the frequency domain based on Fourier analysis. The second approach consists of two steps. First, a stochastic model is fitted to the data, which is then transformed to the frequency domain. The stochastic model that we use is a so-called Auto-Regressive Moving-Average or ARMA model.

Fourier Spectra:

The Fourier transform, $F(f)$, of time series $g(t)$ is defined as

$$F(f) = \frac{1}{2\pi} \int_0^{\infty} g(t) e^{-ift} dt, \quad (2.25)$$

where f is the natural frequency [Hz] and t is time [s]. The spectral density $S(f)$ follows from the squared amplitude of $F(f)$, folded back around the Nyquist frequency ($= 0.5 * f_{sampling}$) and divided by the f -stepsize ($f_{sampling} / N$, with N the number of samples). Integration of $S(f)$ yields the variance of $g(t)$. In practice for discrete time series a standard numerical evaluation of Equation (2.25) is used, the Fast Fourier Transform or FFT.

The FFT treats the time series as periodical signal, i.e. begin and end of the time series are considered to be continuous. This is usually not the case and the jump in the signal between end and begin of the signal distorts the spectrum. Another issue with FFT spectra is that generally they exhibit so much scatter in the higher frequency range they need to be smoothed to be of practical use.

We developed a MATLAB routine, `FFT_Spec_OH`, that determines $S(f)$ of a time series based on the MATLAB FFT function, including the following steps:

- The data is detrended to avoid that trend introduces fluctuations around the mean of the signal that are not related to turbulence.
- The time series is filtered by tapering it off to zero at the beginning and end of the data block. This procedure is called data-windowing.
- $S(f)$ is calculated using the MATLAB FFT routine. The frequency domain is expressed as natural frequency, f [Hz].
- Spectral smoothing can be done in two ways or in combination with each other in this order:
 - The time series is sub-divided in a number of blocks that can be specified for which $S(f)$ is determined and subsequently averaged.

- The n^{th} -point in $S(f)$ is smoothed by averaging it with $n \cdot \text{smooth_width}$ neighbouring points around n using a bell-shaped filter defined by $(1-x^2)^2$ for $-1 < x < 1$, where the data points to be averaged are equally distributed over the x -domain and smooth_width is a percentage to be specified. To speed up the smoothing process also smooth_step can be specified which defines how many samples to skip after smoothing the n^{th} point in $S(f)$. After sample n , the next sample to be smoothed is $n + \text{smooth_step} \cdot n \cdot \text{smooth_width}$. Typically smooth_width is set to 0.1-0.15 and smooth_step to 0.5.
- $S(f)$ can be plotted with log-log ($\log[S(f)]$ versus $\log[f]$) or semilog ($f \cdot S(f)$ versus $\log[f]$) representation. The log-log plot serves to detect power-laws in the spectra, the semilog plot is energy conserved, i.e. the area under the curve represents the contribution to the total variance. Plots of consecutive FFT_Spec_OH runs can also be overlaid.

ARMA Spectra:

A model in which the present value of a time series is expressed as a finite linear combination of past values of the same time series plus a random noise factor is called an auto regression (AR) model:

$$X_t = \phi_1 X_{t-1} + \phi_2 X_{t-2} + \dots + \phi_p X_{t-p} + a_t, \quad (2.26)$$

where X_t represents the time series at time t , $\phi_1, \phi_2, \dots, \phi_p$ are parameters to be estimated from the data and a_t is a random noise factors with mean 0 and p represents the order of the AR-model.

A model in which the present value of a time series is expressed as a finite linear combination of present and previous values of a different time series with random noise characteristics is called a moving average (MA) model:

$$X_t = a_t - \theta_1 a_{t-1} - \theta_2 a_{t-2} - \dots - \theta_q a_{t-q}, \quad (2.27)$$

where $a_t, a_{t-1}, \dots, a_{t-q}$ is a set of past random noise factors with mean 0 and a finite common variance σ_a^2 and q represents the order of the MA-model

A model that uses both past values of the time series and a past random noise time series is called an autoregressive-moving average (ARMA) process. An ARMA model of order p, q is given by

$$X_t = \phi_1 X_{t-1} + \dots + \phi_p X_{t-p} + a_t - \theta_1 a_{t-1} - \dots - \theta_q a_{t-q}. \quad (2.28)$$

The spectral density of an ARMA modelled time series follows directly from Equation (2.28) using

$$S(f) = \frac{\sigma_a^2}{2\pi} \left| 1 + \sum_{m=1}^q \theta_m e^{-ifm} \right|^2 \Bigg/ \left| 1 + \sum_{m=1}^p \phi_m e^{-ifm} \right|^2. \quad (2.29)$$

The difficulty of working with ARMA-models lies in determining the model-order and the best method to determine the model coefficients. For this we used the ARMASA toolbox (www.dsc.tudelft.nl/Research/Software/index.html), which is written in MATLAB. ARMASA automatically selects the best model type, model order and method to determine the coefficients that result in the smallest expectation and prediction error of the original time series (Broersen, 2002).

We wrote a MATLAB routine, `ARMASA_Spec_OH`, around the ARMASA toolbox that determines $S(f)$ of a time series and outputs the result in the same manner as `FFT_Spec_OH`. Basic features of this script are:

- The data are not detrended.
- No data-windowing is needed since the signal is not assumed periodic.
- $S(f)$ is calculated using the ARMASA toolbox. The frequency domain is expressed as natural frequency, f [Hz]. Note: ARMASA outputs $S(f)$ scaled with the total variance. A number of parameters can be set in ARMASA, which influence the execution time:
 - The number of points in the spectrum; must be a 2^N number, with N is a natural number.
 - The maximum number of AR- and MA modes.
- Spectral smoothing is not necessary, since the signal is reduced to a model description with a limited number of modes, which are determined based on a robust error evaluation routine (Broersen, 2002).
- $S(f)$ can be plotted in a similar way as with `FFT_Spec_OH`, which allows comparison of FFT and ARMASA based spectra by overlaying the spectral plots.

Advantages of ARMASA over FFT are that no data-windowing has to be applied not arbitrary smoothing of the spectra. Disadvantage of ARMASA over FFT is that it its much slower in computation. Examples of FFT and ARMASA spectra are given in 2.5.2.2.

2.5.2 C_T^2 and ε from sonic anemometer data

2.5.2.1 C_T^2 and ε from sonic anemometer data using structure functions

C_T^2 is related to the second order structure function of temperature, D_{TT} , by

$$D_{TT} = \overline{[T(x) - T(x+r)]^2} = C_T^2 r^{2/3}, \quad (2.30)$$

where $T(x)$ denotes the temperature at position x and $T(x+r)$ denotes the temperature at position separated from x by a distance r (e.g. Monin and Yaglom, 1971).

Using Taylors frozen turbulence approximation (Equation 2.24), C_T^2 can be calculated from a temperature time series of one sensor by replacing r by $U\Delta t$:

$$C_T^2 = \frac{\overline{[T(t) - T(t + \Delta t)]^2}}{(U \Delta t)^{2/3}}, \quad (2.31)$$

with U is the horizontal wind speed and Δt is a time delay.

ε is related to the third order structure function of the longitudinal wind speed component, D_{uuu} by

$$D_{uuu} = \overline{[u(x) - u(x + r)]^3} = -\frac{4}{5} \varepsilon r. \quad (2.32)$$

ε can be calculated from a sonic anemometer time series by replacing r with $U\Delta t$:

$$\varepsilon = -\frac{5}{4} \frac{\overline{[u(t) - u(t + \Delta t)]^3}}{U \Delta t}. \quad (2.33)$$

To determine C_T^2 and ε from structure parameters with T and u measured with a sonic anemometer we wrote the MATLAB scripts Cxy_StructFun_OH and Eps_StructFun_OH that evaluate Equations (2.31) and (2.33). In these scripts r has to be specified and a sample (or time) delay is calculated that matches r best based on the measurements frequency and the U . C_T^2 and ε from structure functions based on sonic anemometer measurements suffer from the path averaging effect of the instrument (see also Section 2.5.4). A correction procedure for this path averaging effect is given in Appendix 3A.

2.5.2.2 C_T^2 and ε from sonic anemometer data using spectra

Using the theoretical expressions of the inertial range spectra of temperature, S_T , and longitudinal wind speed, S_u given in Equations (2.18) and (2.17) one can determine C_T^2 and ε from measured time series spectra adopting Taylors frozen turbulence hypothesis (Equation 2.24), i.e.

$$C_T^2 = 4(2\pi/U)^{2/3} f^{-5/3} S_T(f) \quad (2.34)$$

and

$$\varepsilon = \alpha^{-3/2} (2\pi/U)^{2/3} f^{-5/3} [S_T(f)]^{3/2}. \quad (2.35)$$

Note that in the theoretical spectra the radial wave-number k is used, which relates to f by $k = 2\pi f / U$.

To determine C_T^2 and ε from spectra with T and u measured with a sonic anemometer we wrote the MATLAB scripts Cxy_Spectra_OH and Eps_Spectra_OH that evaluate Equations (2.34) and (2.35). The most difficult part is to identify if and where there is an inertial sub range present in the spectrum, where Equations (2.34) and (2.35) apply. Figure 2-11 to Figure 2-13 illustrate the steps involved on how this is done in the MATLAB scripts for ε using a FFT spectrum (Figure 2-11), for ε using an ARMASA spectrum (Figure 2-12) and for C_T^2 using a FFT spectrum (Figure 2-13). The following recipe is followed, where the references (top left), (top right), etc. refer to the plots in Figure 2-11 to Figure 2-13:

- Spectra of T (for C_T^2) or u (for ε) are calculated based on FFT and/or ARMASA (top left).
- For each point in the spectrum C_T^2 or ε is calculated using Equations (2.34) and (2.35) (top right).
- Automatically determine whether and where there is an inertial sub-range present in the spectrum by performing inertial-range quality checks on the spectrum and the calculated C_T^2 or ε values. These quality checks are performed for an interval around each spectral point. This user defined interval is expressed as a percentage of the total logarithmic f -scale, typically $\sim 15\%$ of the whole spectrum. This means that at high f more samples are included in the analyses than at low f . The script steps point by point (from low to high f) through the spectrum and for each point it evaluates the following quality checks:
 1. Calculate the slope of the spectrum (on a log-log scale) for the block-interval around each point in the spectrum plotted in the top-left. If there is an inertial range the slope must be $-5/3$. A user defined percentage deviation from the $-5/3$ slope defines the margin within which a spectral point passes the $-5/3$ slope check (bottom left).
 2. Calculate the root means square (RMS) for the block-interval around each point in the C_T^2 or ε spectral representation plotted in the top-right. If there is an inertial range C_T^2 or ε should be fairly constant. A user defined maximum RMS defines the margin below which a spectral point passes the C_T^2 -or ε RMS check (bottom right).
 - The inertial range is taken as points in the spectrum that pass both quality checks.
 - From the points that pass the quality checks also some inertial range quality parameters are saved: the percentages of the total spectral that has an inertial range (1 = an inertial range over the entire spectrum; 0 = no inertial range found); a quality parameter of the found $-5/3$ slope (1 = a perfect $-5/3$ slope; 0 = found slope just based the quality check); and a quality parameter of the found RMS of C_T^2 or ε (1 = a RMS of zero, C_T^2 or ε is constant; 0 = found RMS just based the quality check)
 - Note that towards both ends of the spectrum no quality check can be performed for half the defined analysis-block-size. In addition, at low f , there is also a restriction that there is a minimum (user specified) number of samples for the quality estimates.
- Average ε or C_T^2 is calculated for points that lie in the found inertial range.
- Plots such as Figure 2-11 to Figure 2-13 are saved. In the spectrum (top left) and C_T^2 or ε spectral representation (top right), the points that fall in the inertial range and are used for calculating the average C_T^2 or ε are marked.

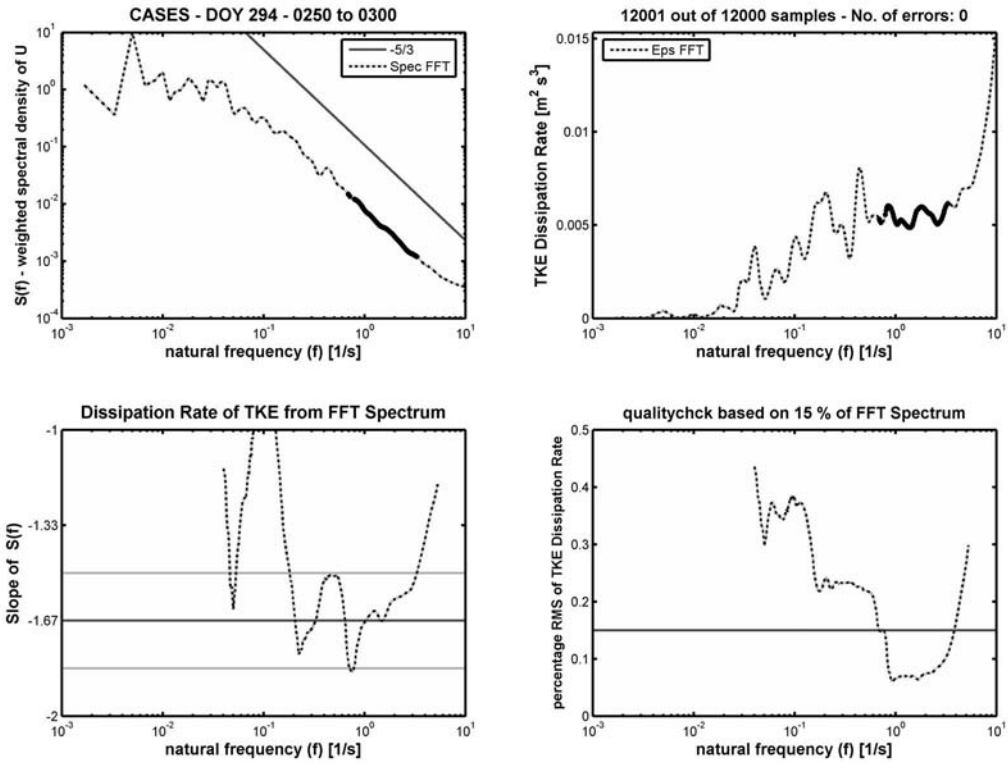


Figure 2-11: Example of the ε calculation from a *FFT-spectrum* with the MATLAB script `Eps_Spectra_OH` described in this section.

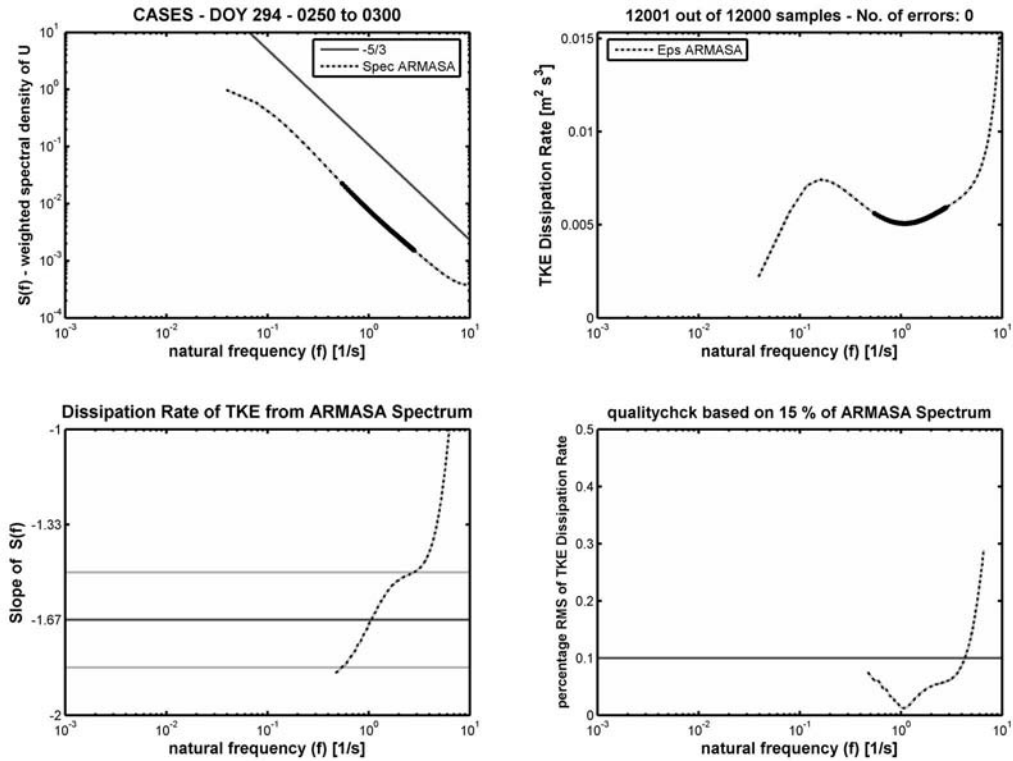


Figure 2-12: Example of the ε calculation from an *ARMASA-spectrum* with the MATLAB script `Eps_Spectra_OH` described in this section. Same interval is used as in Figure 2-11.

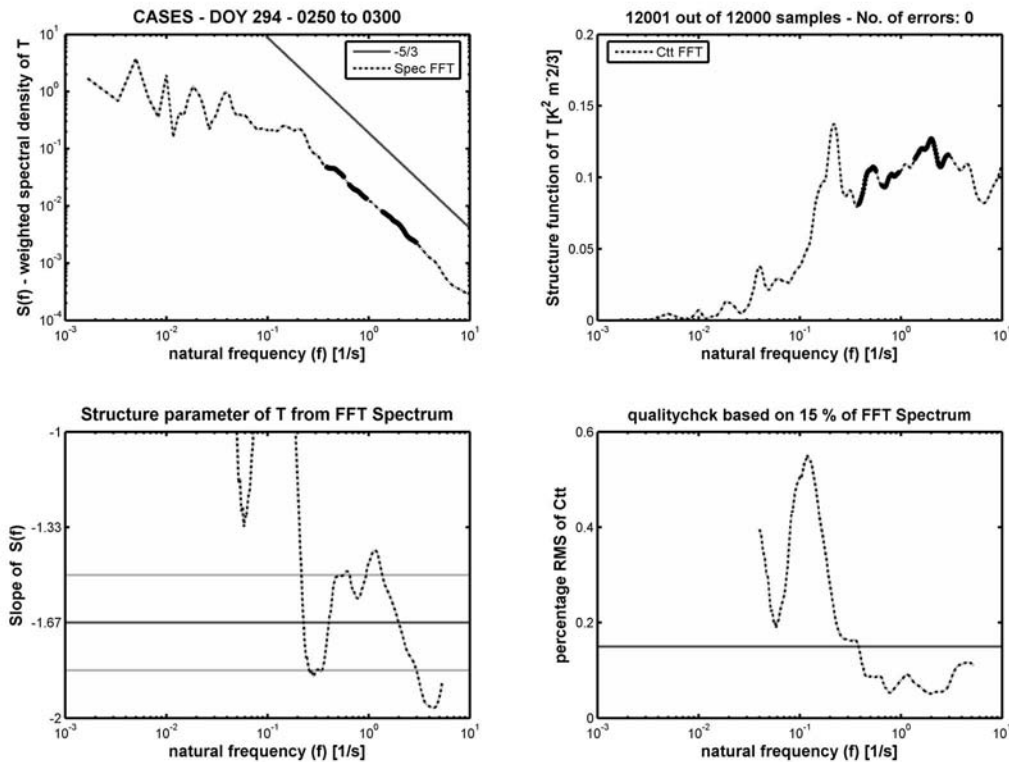


Figure 2-13: Example of the C_T^2 calculation from a *FFT-spectrum* with the MATLAB script `Cxy_Spectra_OH` described in this section. Same interval is used as in Figure 2-11 and Figure 2-12.

2.5.3 C_T^2 and ε from scintillometer data

In this thesis we use two types of scintillometers to characterise turbulence and estimate turbulent fluxes: the large-aperture scintillometer (LAS) and displaced-beam small-aperture scintillometer (DBSAS). A physical description of the instrument is given in Section 2.2.3. In Chapters 3 and 5 we use the DBSAS. In Chapters 5 and 6 we use the LAS. The theory behind the operational principles of the instruments is extensively described in these chapters. Here we will therefore confine ourselves to some main lines.

The DBSAS and the LAS are optical instruments that consist of a transmitter and receiver. The receiver records intensity fluctuations - known as scintillations - of the light beam emitted by the transmitter, which are caused by fluctuations of the refraction index, n upon the beams passage through the turbulent atmosphere. These, in turn, depend on fluctuations of temperature T and humidity q and their correlation.

A property of interest to describe the difference between the LAS and the DBSAS is the first Fresnel zone ($F = \sqrt{\lambda L}$), with λ is the wavelength, and L is the path length. The aperture-diameter, D , of the DBSAS is “small” since $D < F \approx l_0$ applies. The LAS aperture is considered “large” because $l_0 < F \ll D$. The inner scale, l_0 , marks the transition between the inertial and viscous-, energy dissipating range of eddy sizes and is of the order 0.2 cm - 2 cm

near the surface. For the DBSAS F is a measure of the optically most effective eddies (~ 1 cm), which lies in the energy dissipation range of eddy scales. For the LAS D is a measure of the optically most effective eddies (~ 5 cm – 30 cm), which generally lies in the inertial range of eddy scales.

The description of the scintillometer principle measurement, i.e. refractive index fluctuations of the beam, requires a theoretical form of the refractive index spectrum. Since we work with optical scintillometers the T -fluctuations dominate in the measured n -fluctuations. Therefore, we will neglect the humidity effects and use the same expression for the n -spectrum as for the T -spectrum. As seen in Section 2.5.1.3, C_n^2 , the structure parameter of the refractive index, then describes the inertial range part of the n -spectrum and l_0 the dissipation part.

The LAS operates one beam and primarily sees inertial range size eddies. This means that only the inertial range part of the theoretical spectrum is needed to evaluate the raw measurements. This makes that the measured intensity fluctuations, analysed as the variance of the logarithm of the amplitude variations, B_I , relates directly to C_n^2 ,

$$C_n^2 = 4.48 B_I D^{7/3} L^{-3}. \quad (2.36)$$

The DBSAS operates two parallel beams displaced by a distance of 2.7 mm and only sees dissipation range eddies. From the two beams, B_1 and B_2 are analysed, and correlation between the two beams, $r_{12} = B_{12}/B_1$, with B_{12} is the covariance term. The expression that relates r_{12} and B_1 to the spectral characteristics l_0 and C_n^2 is not straightforward, and will not be given here as it is repeated on several occasions in the manuscript. Instead we give its graphical representation in Figure 2-14. First, l_0 is solved from the measured r_{12} using Figure 2-14a. Second, with l_0 known, C_n^2 can be solved using Figure 2-14b. It should be noted that the relations depicted in Figure 2-14 also depend on the displacement distance between the beams, the aperture-size of the detector and the path length.

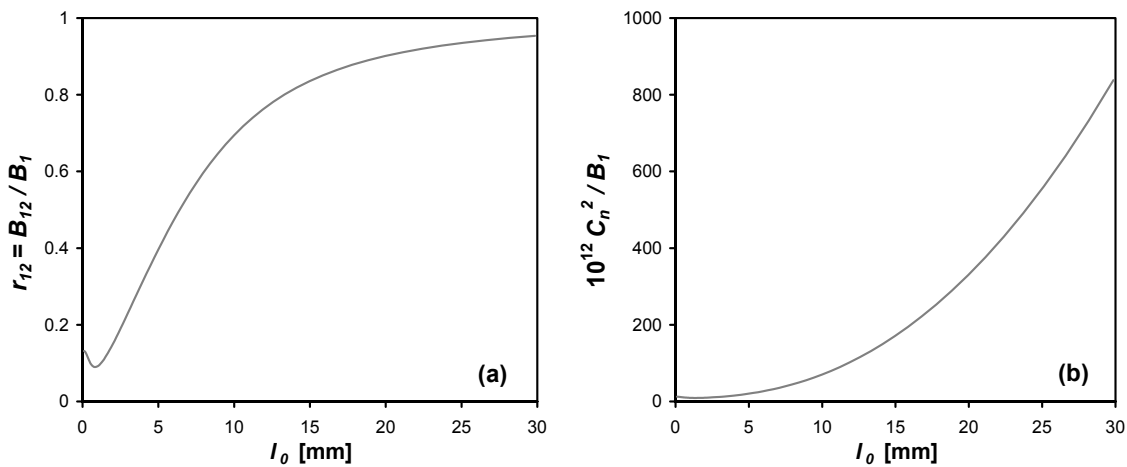


Figure 2-14: Relations between the raw measurements of the DBSAS, r_{12} and B_1 , and the physical parameters that can be derived from them, i.e. l_0 (a) and C_n^2 (b) for $L = 112$ m.

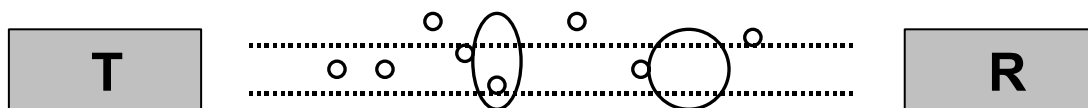


Figure 2-15: Schematic of the two DBSAS beams transmitted between the instruments transmitter (T) and receiver (R) illustrating qualitatively the shape of Figure 2-14a. It is seen that the smaller the smallest (Kolmogorov) eddies are, the less correlation is found between the beams.

Figure 2-15 illustrates the relation depicted in Figure 2-14a, where low r_{12} relates to small l_0 and high r_{12} relates to large l_0 . This can be understood as follows, realising that l_0 is linked to the smallest turbulent scales available in the spectrum, the Kolmogorov scale, by a constant (7.4). If the smallest eddy scale is relatively large in relation to the beam separation distance, it will give a high correlation between the beams. In contrast, if the smallest scale is relatively small less correlation is found.

At high l_0 ($l_0 > 20$ mm) Figure 2-14a levels off, even larger scales do not give much more correlation and small errors in r_{12} lead to large errors in l_0 . At low l_0 ($l_0 < 2$ mm), Figure 2-14a shows a minimum. Below this scale, there are two solutions and l_0 can no longer be resolved.

C_n^2 and l_0 relate directly to C_T^2 and ε . ε can be calculated from l_0 using the definition of l_0 (Equation 2.21). To derive C_T^2 from optical C_n^2 a correction for humidity has to be applied, i.e. in the inertial range there is a difference between the n - and the T -spectrum, which depends on humidity. Moene (2003) reviewed the humidity effect on optical C_n^2 and derived a humidity correction term that depends on the (co-) variances of T and the specific humidity, q , which we will use in Chapters 3 and 5. From this also a more simple relation can be derived that uses the Bowen-ratio ($H/L_v E$) to correct for humidity, which is used in Chapter 6. Note that the effect of humidity is almost negligible on the n -Hill-bump (dissipation range spectrum normalised with the inertial range spectrum) and, therefore, has no effect on l_0 . The basis for the negligible difference in n - and T -Hill-bumps lies in the fact that the molecular diffusivities of temperature and humidity, needed to describe q - and T -Hill-bumps that make up the n -Hill-bump, are not equal. Hill and Clifford (1978) and Van Dijk et al. (2006) reviewed this issue in detail and reached to the conclusion given above.

2.5.4 Turbulent fluxes from sonic anemometer data

Sonic anemometers yield fast response measurements of the three components of the wind speed vector u , v , and w and temperature. If their coordinate system is orthogonal u is defined along the sonic anemometers x -axis, v along the y -axis and w along the z -axis. From these the turbulent fluxes H and τ can be obtained using the eddy-covariance technique which will be explained in this section. To estimate evaporation also a fast response hygrometer is needed.

As remarked in Chapter 1, turbulence cannot be described from first-principle physics. One approach to follow then is to describe turbulence *statistically*. The tool to do this is Reynolds

decomposition, where a signal X is divided in a mean part, \overline{X} , and a deviations from the mean, or turbulent part X' (see Equation 2.3).

We are interested in interactions between the surface and the atmosphere, more in specific in the *vertical transport* of sensible heat, momentum, and mass such as water vapour and CO₂. In principle the mean vertical flux density, that is the 'amount' of turbulent quantity X transported vertically per unit time and area, is given by the general expression:

$$F_x = \overline{w\rho X}, \quad (2.37)$$

where w is the vertical wind speed, ρ is the density of air. Applying Reynolds decomposition to all variables in Equation (2.37), noting that $\overline{w} = 0$ and leaving out negligibly small terms one arrives at

$$F_x \approx \overline{\rho w' X'}. \quad (2.38)$$

Equation (2.38) expresses that the vertical turbulent transport is described by the covariance of the w and the quantity X that is transported. This method is called the eddy-covariance or eddy-correlation (EC) technique. It is important to realise that for the covariance of w and X to be representative of the true turbulent flux, all eddy scales contributing to the flux must be represented. This means that fast response measurements are required or small, fast eddies will not be detected. In addition, the fluctuations should be determined with respect to some minimum time record to include the largest eddies. Finally, measurements should preferably be taken at a high sample rate to quickly converge to statistically stable covariance-estimate. With the EC technique the flux transporting eddies themselves are sampled, and the turbulent fluxes are therefore measured directly. This is why the EC method is often considered the standard method for measuring surface fluxes. In Section 2.5.5, we will introduce an indirect flux measurement method based on similarity theory.

When dealing with mass fluxes, X is the specific density (ρ_x/ρ). For water vapour then

$$L_v E = L_v \overline{\rho w' q'}, \quad (2.39)$$

with E is the mass water vapour flux or evaporation, q is the specific water vapour density, and L_v is the evaporation energy of water, which makes $L_v E$ the energy water vapour flux or latent heat flux.

When dealing with H , the sensible heat X is the enthalpy per unit mass ($\sim c_p T$), so then

$$H = \overline{\rho c_p w' T'}, \quad (2.40)$$

with c_p is the specific heat at constant pressure (De Bruin, 2005).

When dealing with τ , the vertical momentum flux density or stress, X is the horizontal wind speed and

$$\tau = -\rho \left(\overline{w'u'^2} + \overline{w'v'^2} \right)^{0.5}, \quad (2.41)$$

where u is the longitudinal- and v the lateral horizontal wind speed components. Momentum flux is rarely listed explicitly. Instead, the friction velocity, u_* is computed by

$$u_* = \sqrt{\tau / \rho}. \quad (2.42)$$

The exact details and a historic overview of how Equations (2.39) to (2.41) are derived are outlined in Van Dijk et al. (2004).

In concept the eddy-covariance technique is straightforward. In practice additional corrections have to be applied to the raw measurements and the covariance-estimates because of instrumental issues and theoretical considerations. We will qualitatively discuss these corrections in a moment.

With the new EC instrumentation that we started to work with in CASES-99 also a great effort has been made to develop a standardised software package to process raw EC data to fluxes and other higher order moments. The first step was to standardise the data format. We have chosen for the netcdf format, as this was the agreed format to deliver the data to the central CASES-99 database. A program was developed that converts the Campbell Scientific binary format to netcdf (www.met.wau.nl/projects/csi2ncdf by Arnold Moene). The second step involved the EC data processing for which the Joint EddyCovariance Project (JEP) was set-up. JEP is a platform where researchers from Wageningen University and the Royal Netherlands Meteorological Institute (KNMI) were brought together to develop fundamental understanding of the eddy-covariance method and a protocol for practical use. JEP resulted in the EC-pack software package (www.met.wau.nl/projects/jep) and a report with describing the EC method fundamentals and technical details of EC-pack (Van Dijk et al., 2004).

The standardisation of the EC data format in netcdf also facilitated accessing the raw data in easier data-access in other software packages such as IDL and MATLAB. An example is the program `Eplot_OH` we developed in MATLAB to quick-view the raw data for quality checking and visualising the turbulent regimes (see examples Appendix 1A and 2A) and extract (selections of) raw, sub-sampled or averaged data.

The EC-pack corrections that we applied will be described qualitatively here. In Appendix 2A, the impact of some corrections is illustrated, especially for very stable conditions.

Rotation corrections:

Description: Rotate the coordinate system of the sonic anemometer that it is aligned with the mean flow. The rotations are defined as yaw (around z -axis), pitch (around y -axis) and roll (around x -axis). Three rotation methods can be found in the literature:

- *Double Rotation* (DR) method (e.g. Kaimal and Finnigan, 1994): rotation angles are determined for each flux interval such that $\overline{v}=0$ (yaw, axis aligned with the mean horizontal wind), $\overline{w}=0$ (pitch, axes aligned parallel to the surface in the mean wind direction).
- *Triple Rotation* (TR) method (e.g. Kaimal and Finnigan, 1994): in addition to the DR-method also rotates the system such that $\overline{w'v'}=0$ (roll, axes aligned parallel to the surface in the cross-wind direction).
- *Planar Fit* (PF) method (Wilczak et al., 2001): fits the sonics coordinate system to the time-averaged wind field that is assumed to be confined to a plane surface, nominally parallel to the ground. The rotations (pitch and roll) are based on a time interval that is much longer than the flux interval. We use 24 hours. The rotation into the mean horizontal wind (yaw) is done for every flux-interval.

Comments: In low wind speed conditions the mean wind direction for an averaging period is ill defined and the errors in the DR and TR angles can be large. The PF uses long intervals to determine the angles and does not suffer from this problem. We used the TR method in Chapter 3 and the PF method in Chapters 4 and 5. In addition, the DR and TR method force $\overline{w}=0$, whereas sometimes this is not so for short periods due to (daytime) meso-scale effects. The PF method allows w to be non-zero. An aspect that is related to the rotation method used is the in- or exclusion of the crosswind component $\overline{w'v'}$ in the momentum flux (Equation 2.41). The impact of neglecting this term – as is customary for some researchers – in stable conditions is discussed in Appendix 2A.

Impact: Generally large, but very much depends on the set-up (larger in terrain with topography or when the sensors are not level). The difference between the DR/TR and PF approaches is largest for very stable conditions and principally affects low u_* values. This is demonstrated in Appendix 2A for the CASES-99 dataset.

Trend Correction:

Description: Remove a trend that is superimposed on turbulent signal. In EC-pack this done by removing the linear trend per averaging interval from the signals.

Comments: In highly non-stationary conditions, an alternative more suitable trend correction would be dividing the data record of a signal in stationary sub-intervals and determine the turbulent deviations with respect to the means of the sub-intervals.

Impact: Trend and therefore trend correction depends on time of day, the length of the averaging interval and the (non)-stationarity of the signals.

Sonic-temperature Correction:

Description: The temperature measured by sonic anemometers, T_{son} , is derived from the speed of sound measurements, which also weakly depend on humidity. Schotanus et al. (1983) derived corrections for this effect for T_{son} and higher order moments involving T_{son} .

Comments: Schotanus et al. (1983) also derived a correction for the effect that the speed of sound measurement and thus T_{son} , is affected by the side-wind that tilts the sonic wave front and causes a slight delay in the flight times of the sound pulses. This correction is already taken care of by the CSAT3 calibration.

Impact: The correction of T_{son} depends on the absolute humidity, q . The heat flux ($\overline{w'T'_{son}}$) correction depends on $L_v E$.

Frequency response corrections:

Description: Eddies smaller than the sonic anemometers path (~ 10 cm) and smaller than the separation distance between sonic and additional scalar instrument (hygrometer) are not detected. In addition, a sensor can also be too slow to measure the fast eddies on the smallest turbulent scales. As a result, the flux transport on these scales are not taken into account and the total flux will be underestimated. The correction procedure involves filling in the missed flux using theoretical co-spectra, which depend on stability (Moore, 1986).

Comments: The eddy size and therefore also the size of the correction depends on the stability, which in turn depends on two things. First it depends on the ratio of mechanical over buoyancy generated turbulence; eddies generated by buoyancy are larger than mechanically (wind) generated eddies. Second, partly related to the first point, it depends on the height above the surface. Eddies close to surface feel more shear and are therefore smaller. We calculated H using T_{son} and T_c , the thermocouple temperature, and found that H based on T_c was $\sim 25\%$ less in very stable conditions (without applying any frequency response correction). This might be due to the combined effect of sensor separation and maybe the thermocouples slow response. For this reason we only used H based on T_{son} .

Impact: Depends on sensor height, sensor separation and stability. The correction is largest in stable conditions close to the surface. An illustration of the size of the correction on H and u_* measured at 2.65 m during the CASES-99 is given in Appendix 2A.

Specific corrections for the KH20 hygrometer:

Description: In the ultraviolet, where KH20 operates, oxygen also has absorption bands. Superimposed on the humidity density fluctuations, therefore is a small contribution of oxygen density fluctuations. These are caused by temperature fluctuations, which allows correcting for this affect (Van Dijk et al., 2003). Furthermore, the calibration of the KH20 shifts in time due to weathering of the sensors window coating. This can be corrected for by base-lining the sensor with an accurate slow response humidity sensor.

Comments: Note that the infrared hygrometer used in the BBC experiment, the LiCor7500, does not suffer from these effects.

Impact: Oxygen correction on $L_v E$ depends on the Bowen-ratio ($H/L_v E$). It is generally a small correction that has the largest impact when $L_v E$ is small. Base-lining the KH20 q with a slow humidity sensor affects the average signal, not the fluctuations and thus $L_v E$. The corrected fast response q is needed, however, for the sonic-temperature correction.

2.5.5 Turbulent fluxes from scintillometer data

Laser scintillometers yield the turbulence parameters ε and C_T^2 . From these the turbulent fluxes H and τ can be obtained using Monin-Obukhov similarity theory (MOST), which will be explained in this section.

In the previous section we dealt with the problem of the unresolved turbulence description by resorting to *statistics*, leading to the eddy-covariance method, with which the turbulent fluxes can be measured *directly*. Another technique for dealing with turbulence without having to use first-principle physics is *dimensional analysis*, with which turbulent fluxes can be determined *indirectly*.

Dimensional analysis is made up of a number of steps. First, select a list of physical key-parameters relevant to the problem. Next, form dimensionless groups out of these parameters.

Then, determine relationships between the dimensionless groups through an experiment. If the set of parameters involved in the analyses were indeed all relevant and complete, these relations are universal.

For the description of turbulence in the atmospheric surface layer (lowest 10% of the boundary layer) Obukhov (1946) listed the following key parameters: the buoyancy parameter g/T , with g is the gravitational constant, the kinematic heat flux at the surface $\overline{w'T'}$, the surface stress expressed as u_* (Equation 2.42), and the height above the surface, z . From these he derived a universal length scale, L_O , for exchange processes in the surface layer, the Obukhov length

$$L_O = \frac{\overline{T} u_*^2}{\kappa g \theta_*}, \quad (2.43)$$

where κ is the von Kármán constant and θ_* is the temperature scale defined by

$$\theta_* = -\frac{\overline{w'T'}}{u_*}. \quad (2.44)$$

From this Monin and Obukhov (1954) developed their similarity theory stating an atmospheric turbulence property or statistics - when made dimensionless using u_* , θ_* or similar defined scaling variables - is a universal function of the dimensionless Obukhov length, z/L_O . Examples of these atmospheric turbulence property or statistics are gradients, variances and structure parameters. The exact forms of the universal functions are different for each parameter, are not predicted by theory and have to be determined through field experiments. Generally, different functions have to be determined for stable and unstable conditions.

To determine these functions the turbulent fluxes need to be a priori known, which can only be determined with the direct flux measurements technique of eddy covariance. In this sense all MOST applications once have been calibrated against eddy-covariance fluxes.

For the laser scintillometers the dimensionless groups of ε and C_T^2 are defined by:

$$\frac{\kappa z \varepsilon}{u_*^3} = f_\varepsilon(z/L_O) \quad (2.45)$$

and

$$\frac{C_T^2 z^{2/3}}{\theta_*^2} = f_T(z/L_O). \quad (2.46)$$

From these u_* , θ_* and L_O have to be solved by iteration. The heat flux follows from the definition of θ_* (Equation 2.44): $H = -\rho c_p u_* \theta_*$.

Note that for the LAS method only C_T^2 is obtained and no measure of u_* . It is customary to include wind speed measurements at a single height and an estimate of the roughness length, which - following the MOST flux profile relationships - give u_* . Note that for stable conditions mechanically induced turbulence is the only turbulence generating transport mechanism. The DBSAS directly contains this information through ε , whereas the LAS relies on flux profile relationships to include this transport mechanism.

It is important to realise that MOST is valid in stationary flows in the surface layer that are governed by mechanically- and buoyancy-generated turbulence over horizontally homogeneous and flat surface and where turbulent fluxes are constant with height. Higher up in the SBL these conditions are no longer met, i.e. flows are no longer in equilibrium with the surface. Then, turbulence parameters are related to local fluxes rather than with the surface fluxes. This variation on MOST is called local scaling. It is also referred to as z -less scaling, since the height above the surface is no longer a relevant parameter.

Appendix 2A Details on the Eddy Covariance measurements

Some specialist aspects on eddy-covariance method and measurements discussed in this chapter will be illustrated in this Appendix.

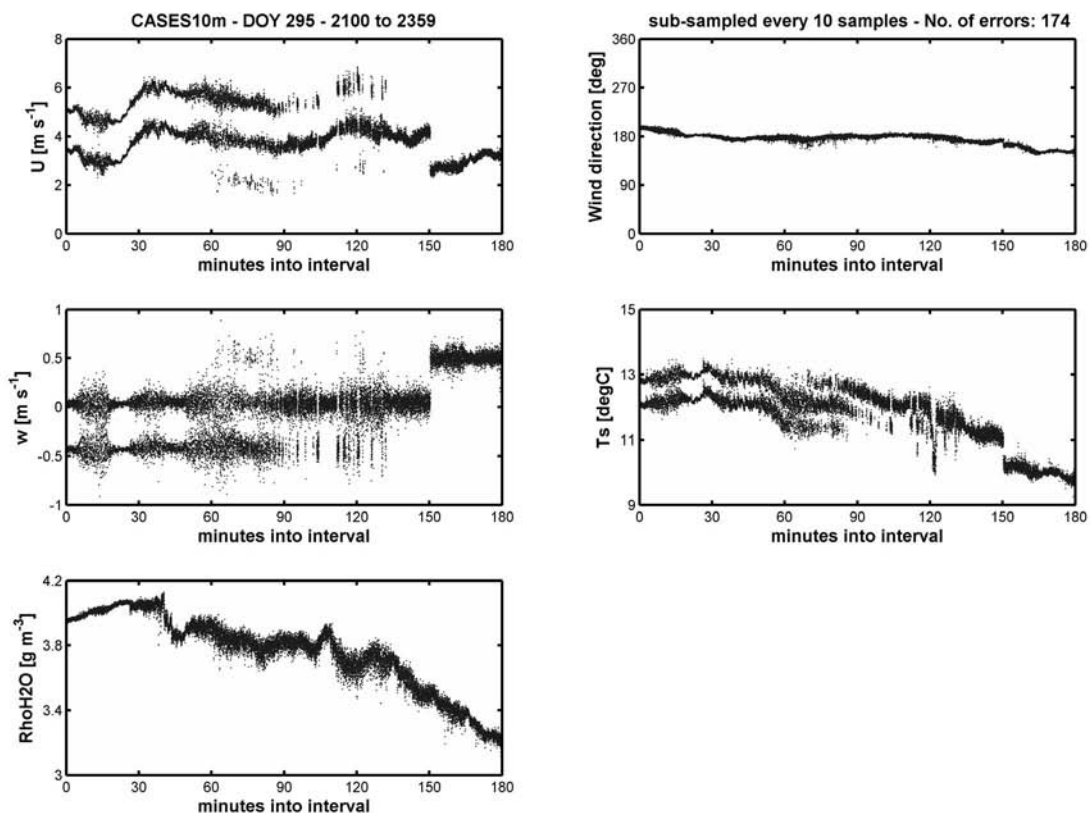


Figure 2-16: Illustration of the calibration errors experienced with the 10.2 m sonic anemometer (CSAT3) during CASES-99. U = horizontal windspeed vector, w = vertical windspeed, T_s = sonic temperature, $RhoH_2O$ = water vapour density. Sample frequency is 20 Hz.

Calibration problems CSAT3:

The CSAT-3 calibration problem is illustrated in Figure 2-16 and occurred occasionally. The CSAT3 is calibrated over temperature. When the CSAT3s calibration starts to shift it usually does so at specific temperatures only. The problem is diagnosed by the sensor itself and an error flag is added to the data. The same CSAT3 was also used during RAPID at 9.44 m.

In- or exclusion cross-wind stress:

In Chapters 4 and 5 we evaluate u^* using the planar fit rotation method and including both longitudinal and lateral components of the vertical stress: $u^*_{*lat+lon} = \left(\overline{u'w'}^2 + \overline{v'w'}^2 \right)^{1/4}$. For some it is customary to use the longitudinal component only: $u^*_{*lon} = \left(-\overline{u'w'} \right)^{1/2}$.

If there is a well-defined flow, i.e. a wind speed of some magnitude that does not change too much in direction during a flux-averaging interval, then $\overline{v'w'}$ is expected to be very small with respect to $\overline{u'w'}$. Figure 2-17a compares $u^*_{*lat+lon}$ with u^*_{*lat} and Figure 2-17b shows the relative contribution of $\overline{v'w'}$ (u^*_{*lat}) to $u^*_{*lat+lon}$ as a function of $u^*_{*lat+lon}$. For the stable night-time conditions during CASES-99 (Chapter 3 and 4). It is seen that the relative contribution of $\overline{v'w'}$ to the total u^* is only important when u^* is small. This might be due to non-stationarity of the flow, causing the horizontal wind direction flaps about it's mean value during the flux averaging interval or non-turbulent contributions to u^* , e.g. due to the gravity wave activity.

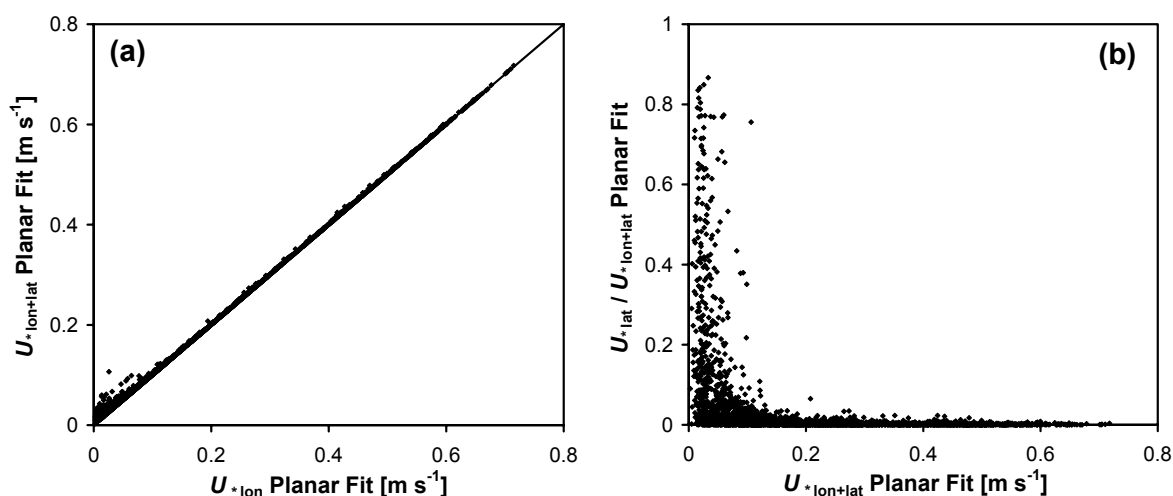


Figure 2-17: Effect of in- or excluding the lateral stress component in u^* for EC system at 2.65 m height during night-time stable conditions in CASES-99.

Planar fit versus Double rotation and Triple rotations:

Figure 2-18a shows that the DR method introduces some scatter with respect to the PF derived u^* , where both u^* -estimates include the lateral stress component. For the TR method $\overline{v'w'}$ is forced to zero, so for this rotation method $u^*_{*lon} = u^*_{*lat+lon}$. Apart from the extra scatter, with the TR method also an underestimation is seen for low u^* (Figure 2-18b).

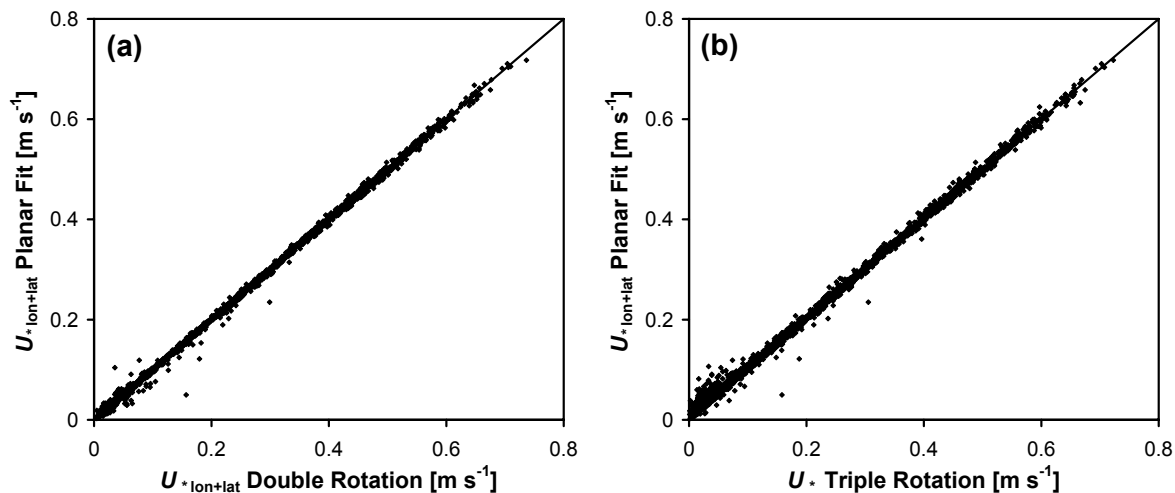


Figure 2-18: Planar fit rotation method compared with Double Rotation method (a) and Triple Rotation method (b) for u_* . Concerns EC system at 2.65 m height during night-time stable conditions in CASES-99.

Effect of frequency response correction:

The frequency response correction always adds flux. The correction is largest for very stable conditions, i.e. small u_* and small H . The correction for H can then be as large as 15%, and 7% for u_* . Towards more neutral conditions, i.e. larger H and u_* the correction remains largest for H , some 5%, whereas the correction for u_* drops to some 2%.

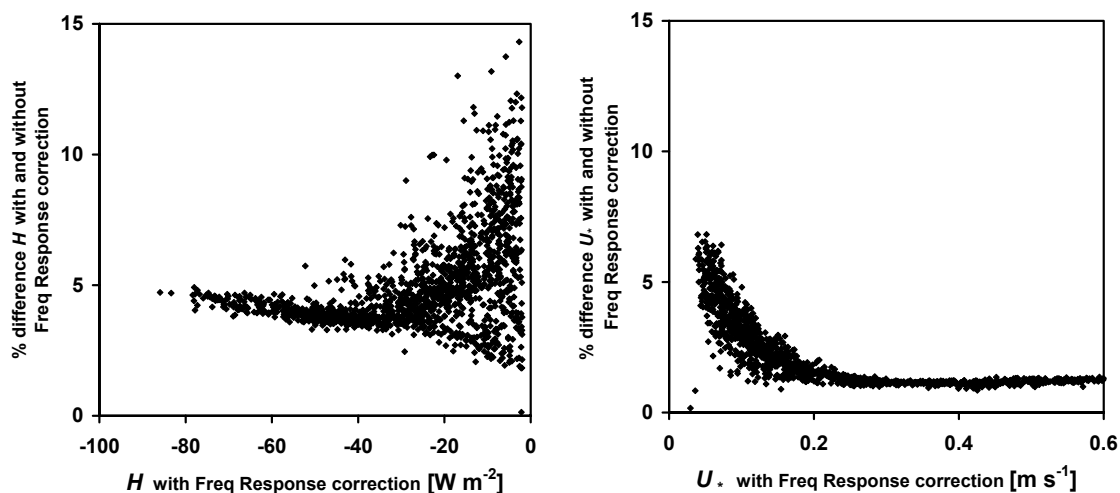


Figure 2-19: Percentage effect on H (left) and u_* (right) of the frequency response correction for EC system at 2.65 m height during night-time stable conditions in CASES-99.

Chapter 3 Displaced-Beam Small Aperture Scintillometer test Part II: CASES-99 stable boundary-layer experiment

3.1 Introduction

Turbulent flows in the very stable stratified atmospheric surface layer are still not well understood. The main problem in studying these flows is that they are often not stationary, not even on short time scales, but intermittent or show irregular behaviour. This intermittent behaviour is poorly understood and not accounted for in atmospheric models (see e.g. Beljaars and Viterbo, 1998). Recently, the international community has shown renewed interest to study transport processes of heat, momentum and mass (water and CO₂) in the stable boundary-layer (SBL); see for instance the Boundary-Layer Meteorology special issue on this subject (Nappo and Johansson, 1999). Also the need to observe the SBL resulted in the international field experiment CASES-99 (Co-operative Atmosphere Surface Exchange Study 1999), which took place in Kansas, USA in October 1999. Poulos et al. (2000) give an overview of this experiment.

During CASES-99 a large number of different instruments and methods of observation have been applied by which now a unique data set is available for a wide range of stable conditions. The Meteorology and Air Quality Group of the Wageningen University (WUMETAIR) participated in CASES-99 with the main goal of studying intermittent turbulence in the SBL. Their experimental contribution focused on the applicability of scintillometry under stable conditions.

A main disadvantage of the generally accepted eddy-covariance method in obtaining surface fluxes is that it requires a significant averaging time, 10 to 60 minutes, to give a statistically stable flux. During this averaging period stationarity of the turbulent flow is a necessary condition. In addition, sonic anemometers average out turbulent motions smaller than their path length of typically 0.1 m. Because stable surface layers can be very shallow, lower observation heights are required where a significant part of the flux is transported by small eddies that are likely to be missed. Furthermore, flow distortion effects also limit the use of eddy-covariance equipment. Consequently, reliable experimental data on turbulence during intermittent stable conditions are scarce. New approaches are therefore required.

-
- This Chapter is based on Hartogensis, O. K., De Bruin, H. A. R., Van De Wiel, B. J. H.: 2002, 'Displaced-Beam Small Aperture Scintillometer Test. Part II: Cases-99 Stable Boundary-Layer Experiment', *Boundary-Layer Meteorology* **105**, 149-176.
 - Part I of the Displaced Beam Small Aperture Scintillometer test is by De Bruin et al. (2002).
 - Appendices 3B – 3E have been added in this thesis.

It has been recognised that small-aperture scintillometers (SAS) are a useful alternative experimental tool in obtaining surface fluxes of heat and momentum. De Bruin et al. (2002) applied a displaced-beam small-aperture scintillometer (DBSAS) during the NOPEX-WINTEX field experiment at Marsta, Sweden (<http://www.hyd.uu.se/nopex>). With these instruments fluxes can be determined over a path of up to 250 m, which means that they are averaged in space as well as time. This allows shorter averaging times, which is a major advantage in the non-stationary conditions encountered in the SBL. Furthermore, averaging out of eddies over the measurement volume, as is the case with a sonic anemometer, does not play a role, which allows for low observation heights. Finally, flow distortion problems do not exist. The drawback of this approach is that empirical Monin-Obukhov similarity theory (MOST) relations have to be used to convert the DBSAS measurements of the inner length scale of turbulence, l_0 , and the structure parameter of the refraction index, C_n^2 , into fluxes of momentum and sensible heat.

De Bruin et al. (2002) found that the DBSAS l_0 measurements seem to be biased for unknown reasons. This leads to an overestimation of the friction velocity u^* for small u^* values and an underestimation in u^* for large u^* values. In the SBL the only turbulent transport mechanism is mechanically generated turbulence, which dominates the heat flux. Therefore, the same pattern of overestimation for low flux values and underestimation for high flux values was found for the heat flux.

It is the objective of this study to explore further the findings of De Bruin et al. (2002) and to examine the performance of the DBSAS under stable to very stable conditions, using DBSAS data gathered during CASES-99.

3.2 Theory

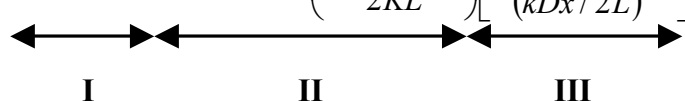
3.2.1 Determining ε and C_T^2 with a Displaced Beam Small Aperture Scintillometer

A scintillometer consists of a transmitter and a receiver. The receiver measures the intensity fluctuations in the radiation emitted by the transmitter caused by refractive scattering of turbulent eddies in the scintillometer path. The path length between transmitter and receiver can range between 50 m to 5000 m. Different types of scintillometers are available. In this study we will use a so-called Small-Aperture Scintillometer (SAS) for which the beam-aperture lies within the dissipation range of turbulence (\sim mm) and is small compared to the Fresnel length scale $F = \sqrt{\lambda L}$, where λ is the optical wavelength and L the path length. For a SAS Tatarskii (1961) was the first to derive an expression relating the variance of the logarithm of the amplitude fluctuations of the measured light intensity, B , to the structure

parameter of the refractive index, C_n^2 , and the inner scale of turbulence, l_0 , under the assumption that the turbulent field the light beam passes through is isotropic and the scintillations are weak, i.e. $B < 0.3$. This last constraint limits the path length over which the SAS can be applied to typically 200 m. To overcome this limitation the Large-Aperture Scintillometer (LAS) was developed, which can be considered as a collection of incoherent point sources; it has a beam-aperture that lies within the inertial range of turbulence and is larger than the Fresnel length scale. For the LAS B is a function of C_n^2 only. The theoretical description was first given by Wang et al. (1978).

In this investigation a commercially available SAS, the SLS20 manufactured by Scintec AG was used (Thiermann, 1992). With this instrument the light beam of one source is split into two parallel, displaced beams with orthogonal polarisations. By determining both the value of B for each beam and the correlation coefficient between the two beams, one can solve for l_0 and C_n^2 . The Scintec SLS20 uses a low power class 3a type laser at a wavelength, λ , of 670 nm, a beam displacement distance, d , of 2.7 mm and a detector diameter, D , of 2.5 mm.

The measured intensity fluctuations of the DBSAS can be analysed as the variance of the logarithm of the amplitude of the two beams, B_1 and B_2 , and the covariance of the logarithm of the amplitude fluctuations between the two beams, B_{12} . Following Hill and Lataitis (1989) B_{12} of the two beams relates to l_0 and C_n^2 as follows

$$B_{12} = 4\pi^2 K^2 \int_0^L \int_0^\infty k \phi_n(k, l_0, C_n^2) J_0(kd) \sin^2\left(\frac{k^2 x(L-x)}{2KL}\right) \left[\frac{4J_1^2(kDx/2L)}{(kDx/2L)^2} \right] dk dx, \quad (3.1)$$


I
II
III

where x is the co-ordinate along path length L , $K = 2\pi/\lambda$ is the optical wave-number, k the turbulent spatial wave-number, d the distance between the two beams, D is the diameter of both detectors, ϕ_n is the three-dimensional spectrum of the refractive index, which is a function of k , l_0 and C_n^2 and J_0 and J_1 are Bessel functions of the first kind. Schematically Equation (3.1) can be described as an integration over both the path length and the entire domain of turbulent length scales of relations describing the turbulent spectrum of the refractive index (part I), wave propagation characteristics (part II) and the averaging of intensity fluctuation over the detector (part III), which unlike the transmitter source cannot assumed to be a point. The relation of part III assumes an uniform intensity distribution over the detector. For $d = 0$, J_0 becomes 1 and the expression for the single detector variances B_1 and B_2 is obtained.

For $\phi_h(k, l_0, C_n^2)$ the following form is assumed:

$$\phi_n = 0.033 C_n^2 k^{-11/3} f_A(kl_0), \quad (3.2)$$

where part A describes the inertial range of the spectrum and part B, i.e. f_A describes the decay of the refractive index fluctuations in the dissipation range and equals unity in the inertial range. With refractive index fluctuation measurements performed in the visible region of the electromagnetic spectrum, the fluctuations are mainly due to temperature fluctuations and the forms of ϕ_h and ϕ_T , the temperature spectrum, can be assumed the same. The form of the inertial range of the spectrum is well known. For f_A Hill and Ochs (1978) developed a physical model, which they fitted to the limited data set of Champagne et al. (1977). For ease of computation Churnside (1991) presented an analytical fit to the Hill model. Frehlich (1992) determined f_A directly from scintillation measurements. All three models are shown in Figure 3-1; f_A shows a small increase in spectral energy (often referred to as the “Hill bump”) at the transition of the inertial range to dissipation range after which the spectrum falls off with a slope steeper than the $k^{-11/3}$ of the inertial range. The applicability of this spectrum under stable conditions has not yet been tested.

For a given DBSAS d , D , and λ are instrumental constants and L is an experimental constant. With measurements of B_{12} and B_I or B_2 the two unknowns of Equation (3.1), l_0 and C_n^2 can be solved. More about the computation strategy to make these calculations can be found in e.g., Thiermann (1992).

Combining Equation (3.1) and Equation (3.2) we now define the spectral weighting functions $W_{12}(k)$ and $W_I(k)$, which show which part of the spectrum f_A is weighted most in determining B_{12} and B_I as a function of L , and the instrumental constants D , d , and λ :

$$W_{12}(k) = 4\pi^2 K^2 0.033 C_n^2 \int_0^L k^{-\frac{8}{3}} J_0(kd) \sin^2 \left[\frac{k^2 x(L-x)}{2KL} \right] \left[\frac{4J_1^2(kDx/2L)}{(kDx/2L)^2} \right] dx. \quad (3.3)$$

$W_I(k)$ follows directly from Equation (3.3) for $d = 0$. Convolution of $W_{12}(k)$ and $W_I(k)$ with f_A results in B_{12} and B_I respectively, from which l_0 is determined. Figure 3-1 shows the weighting functions $W_{12}(n)$ and $W_I(n)$ together with three proposed forms of f_A for a number of path lengths and inner scale lengths. The instrumental constants are those of the Scintec DBSAS. On the x -axis $n = kl_0 / 7.4$ is used rather than k . In this way f_A is stationary whereas $W(n)$ shifts for different l_0 . Furthermore, all $W(n)$ are scaled such that $\int W(n) dn = 1$ to make it possible to compare $W(n)$ for different l_0 and L . Finally, $nW(n)$ is plotted rather than $W(n)$ to ensure that the area under any portion of this semi-log plot is proportional to the total weight.

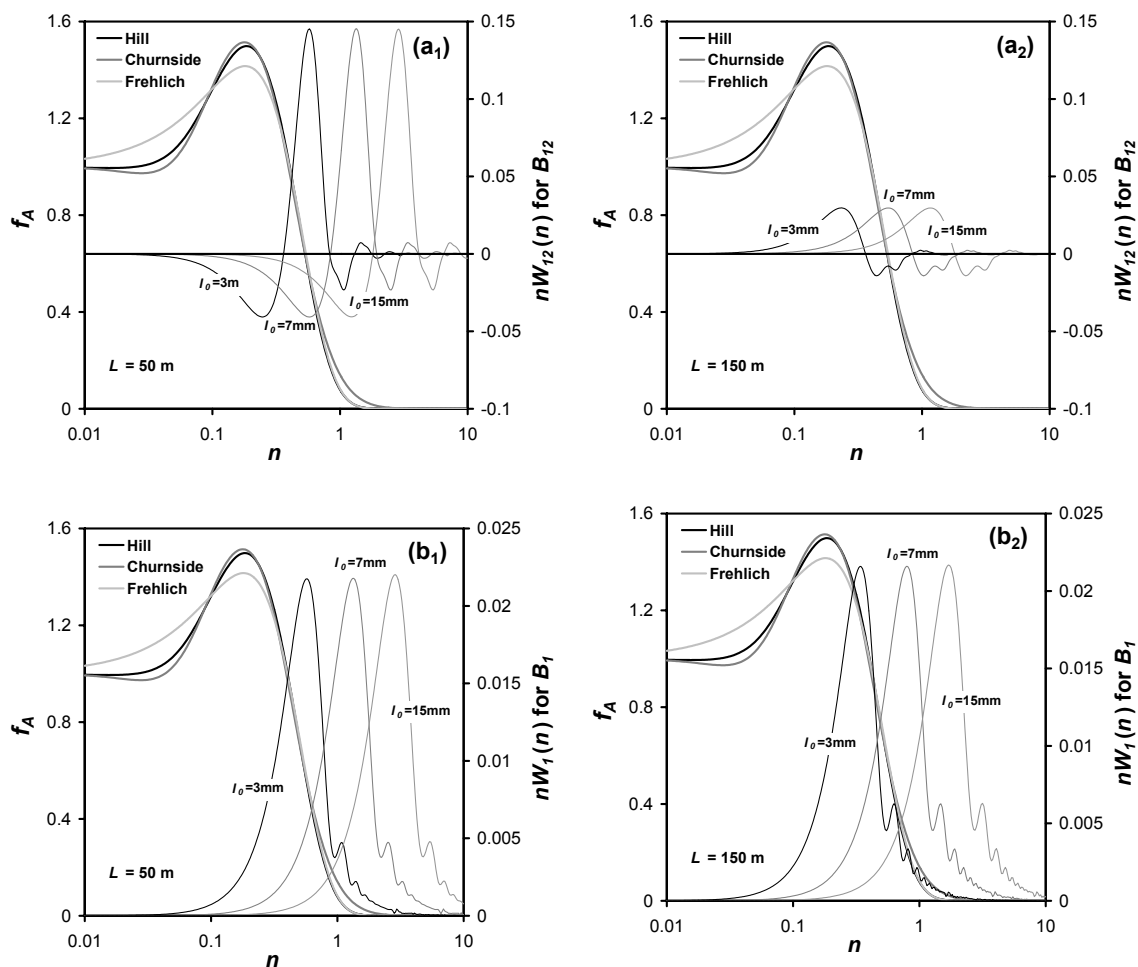


Figure 3-1: Three proposed temperature or refractive index spectra of the dissipation range, f_A (divided by inertial range spectrum) plus their weighting functions W_{12} and W_1 for B_{12} and B_1 respectively (a and b) for 3 values of the inner scale, l_0 and 2 different path lengths, L .

First, Figure 3-1 shows that for small l_0 , $W_{12}(n)$ and $W_1(n)$ comprise the entire f_A spectrum with most weight on the continuous fall-off part of f_A where all models agree. For large l_0 however, most weighting is where f_A is already 0 and only a small part of the spectrum at high wave-numbers contributes to B_{12} and B_1 .

Second, Figure 3-1a shows that for different L , $W_{12}(n)$ is almost stationary, but exhibits large changes in the amplitude. For $L = 50$ m, $W_{12}(n)$ has a large negative peak where f_A is non zero, which is in fact so large that the convolution between $W_{12}(n)$ and f_A , i.e. B_{12} gives a negative number. The large amplitudes in $W_{12}(n)$ for short path lengths will make the determination of B_{12} more sensitive to the actual form of f_A .

Third, Figure 3-1b shows that for different L , $W_1(n)$ has constant amplitude, but shifts to lower wave-numbers for larger L . This means that for large l_0 and short path lengths the total f_A , which contributes to B_{12} and B_1 , is limited even more.

It can be concluded from Figure 3-1 that for large l_0 , especially for short path lengths, the theoretical basis for this type of DBSAS-derived l_0 is quite slim since only a very small part of f_A is weighted, therefore heavily depending on its exact form, as well as that of the weighting function.

When the refractive index structure parameter (C_n^2) and the inner scale (l_0) are known the temperature structure parameter (C_T^2) and the kinetic energy dissipation rate (ε) can be determined.

Inferring C_T^2 from C_n^2 :

Both temperature and humidity fluctuations contribute to C_n^2 :

$$C_n^2 = \frac{A_T^2}{T^2} C_T^2 + 2 \frac{A_T A_q}{Tq} C_{Tq} + \frac{A_q^2}{q^2} C_q^2, \quad (3.4)$$

where C_q^2 and C_{Tq}^2 are the structure parameters of humidity and correlated temperature-humidity fluctuations respectively and A_T and A_q are wavelength dependent ‘‘constants’’. Strictly speaking, fluctuations in total pressure also contribute to C_n^2 but this contribution appears to be relatively small (Hill, 1989) and is neglected here. For scintillometers operating in the visible to near-infrared region, such as the DBSAS, A_q is small compared to A_T , which means that for this type of scintillometer temperature fluctuations, i.e., C_T^2 , contribute more to the total C_n^2 . Under the assumption that temperature and humidity fluctuations are perfectly and positively correlated ($R_{Tq} = +1$), Equation (3.4) has traditionally been evaluated in terms of a direct relationship of C_n^2 to C_T^2 where the humidity contribution to C_n^2 is expressed in terms of a Bowen-ratio term (Wesely, 1976).

In this study we investigate stable boundary-layer fluxes where R_{Tq} is usually negative, and, unlike the daytime convective situation, often far from unity. We will therefore use a more general approximation given by Moene (2003), which expresses C_T^2 in relationship to C_n^2 in terms of the standard deviation of temperature and humidity, σ_T and σ_q and the correlation coefficient between temperature and humidity R_{Tq} :

$$C_T^2 = C_n^2 \left(\frac{T^2}{A_T^2} \right) \left(1 + 2 \frac{A_q}{q} \frac{T}{A_T} R_{Tq} \frac{\sigma_q}{\sigma_T} + \frac{A_q^2}{q^2} \frac{T^2}{A_T^2} \left(\frac{\sigma_q}{\sigma_T} \right)^2 \right)^{-1}. \quad (3.5)$$

For $\lambda = 0.67 \mu\text{m}$, which is the wavelength of the scintillometer used in this study, it can be shown that (Andreas, 1989) $A_T = -0.789 \times 10^{-6} P/T$ and $A_q = -41.75 \times 10^{-6} q$, where P is the air pressure (Pa), T temperature (K) and q the absolute humidity (kg kg^{-1}).

Inferring ε from l_0 :

Amongst others Frehlich (1992) derived the relation between l_0 and ε :

$$\varepsilon = \left[\frac{3\beta\nu}{\text{Pr}} \right]^3 l_0^{-4}, \quad (3.6)$$

where β is the Obukhov-Corrsin constant ($= 3.47$), Pr is the Prandtl-number ($= 0.72$) and ν is the kinematic viscosity of air, which is a weak function of temperature and density, ρ , of air $\nu = [(1.718 + 0.0049(T - 273.15))/\rho]10^{-5}$ with T in [K] and ρ in [kg m^{-3}] after (Thiermann, 1996). The values for β and Pr are taken from Hill (1997) who discussed these constants in detail.

With the Scintec DBSAS values for B_{12} and B_1 are obtained every 6 seconds. The theory presented so far, which links measurements of B_{12} and B_1 to ε and C_T^2 , is valid only for locally stationary and isotropic turbulence. This assumption is valid for short (~ 6 s) time intervals. For longer time intervals the effect of the lognormal distribution of l_0 and C_n^2 has to be taken into account. Moreover, on longer time intervals the influence of intermittency (here meant as instabilities or bursting behaviour within small eddies) is noticeable. Frehlich (1992) gives an estimate of the influence of intermittency on the Obukhov-Corrsin constant, β and its consequent effect on ε . The procedure we followed to calculate 10-minute averaged ε and C_T^2 from 6-sec EC measurements of B_{12} and B_1 and or B_2 is after Frehlich (1992).

For every 6 s, l_0 , C_n^2 , ε and C_T^2 are calculated with the relations given in this Section, using Frehlich's expression for the refractive index spectrum. Next, 10-minute ensemble averages are calculated of l_0 , C_n^2 and C_T^2 using Equation (53) of Frehlich (1992), which accounts for the lognormal distribution of l_0 and C_n^2 . Finally, 10-minute ε is determined using Equation (82) of Frehlich (1992), which accounts both for the lognormal distribution of l_0 and C_n^2 , as well as the effect of intermittency on β .

3.2.2 Determining ε and C_T^2 from eddy-covariance measurements

To test the DBSAS results the derived fluxes of heat and momentum could be compared with those derived from the eddy-covariance method. In this way, however not only the DBSAS performance in obtaining reliable C_T^2 and ε is compared but also the applicability of MOST in a given situation as well as the accuracy of the similarity relationships itself. These are still not well established, especially for C_T^2 scaling in the stable stratification case.

To be able to compare the DBSAS with eddy-covariance in a way that is independent of MOST scaling, C_T^2 and ε need to be determined from point measurements, in this case from eddy-covariance data.

C_T^2 is a scaling parameter of the temperature spectrum in the inertial range of turbulence and is defined as (e.g. Stull, 1995):

$$C_T^2 = \frac{D_T}{r^{2/3}} = \frac{\overline{[T(x) - T(x+r)]^2}}{r^{2/3}}, \quad (3.7)$$

where D_T denotes the structure function, $T(x)$ denotes the temperature at position x and $T(x+r)$ denotes the temperature at position separated from x by a distance r , which should lie within the inertial range of turbulent length scales. Using Taylor's frozen turbulence approximation C_T^2 can be calculated from a time series of one sensor by replacing r by $U\Delta t$ (mean wind speed and time difference between two temperature measurements). We used 20 Hz eddy-covariance data and chose a separation distance, r , of 1 m. Depending on the wind speed a time lag, in this case a multiple of 0.05 s, was chosen such that $U\Delta t$ approximated best a 1-m space separation. Over the total averaging interval of 10-minutes an average $U\Delta t$ was determined with which Equation (3.7) was evaluated to give a 10-minute C_T^2 value. In this case we calculated C_T^2 using a sonic anemometer, which has the advantage that U and T are measured at the same place. The disadvantage, however, is that temperature fluctuations on scales smaller than the sonic path are averaged out. We corrected for sonic path averaging using a correction procedure given by Hill (1991), in which the missed temperature fluctuations are filled in by integration of the temperature spectrum over scales smaller than the sonic path. The correction is in the order of 5 – 10 %. In Appendix 3A we discuss the impact of using just the inertial part of spectrum instead of the entire spectrum of Equation (3.2).

Like C_T^2 , ε is also a scaling parameter of spectra in the inertial range, in this case of the turbulent kinetic energy (TKE). Considering only the longitudinal wind component, u , of the TKE, the inertial range of the spectrum is described by

$$S_u(\kappa) = \alpha \varepsilon^{2/3} \kappa^{-5/3}, \quad (3.8)$$

where S_u is the spectral energy density, α is the Kolmogorov constant ($= 0.55$) and k is the spatial wave-number. To obtain 10-minute values of ε from 20 Hz eddy-covariance data the following procedure was applied: for every individual 10-minute period the axis rotations were performed such that the mean lateral wind components v and w are 0. Next, the rotated u was first detrended and then filtered with a Hanning filter for the first and last 5% of the dataset. A kS_u spectrum was calculated and subsequently averaged by averaging all data within each of the 13.55 spectral bins ($2^{13.55} = 12000$ samples in 10-minutes). The partially filled bin between bin 13 and 14 was ignored. Inertial range behaviour could be found between bins 8 and 12. For each of these bins ε was calculated using Equation (3.8) and all were averaged to obtain one value for ε . As a check whether the $k^{-2/3}$ inertial fall off of the kS_u spectrum was indeed present, a linear regression between bins 9 and 11 was determined. Only ε values were accepted for an inertial range fall-off between $k^{-0.55}$ and $k^{-0.75}$.

3.2.3 Deriving u_* and θ_* from ε and C_T^2 measurements with similarity theory

According to MOST C_T^2 and ε , made dimensionless by respectively scaling them with the temperature scale θ_* and the friction velocity u_* , are universal functions of the stability parameter z/L_{MO} :

$$\frac{C_T^2 z^{2/3}}{\theta_*^2} = f_T(z/L_{MO}) \quad (3.9)$$

and

$$\frac{k_{kar} z \varepsilon}{u_*^3} = f_\varepsilon(z/L_{MO}), \quad (3.10)$$

where z is the measurement height, k_{kar} the von Kármán constant ($= 0.4$) and L_{MO} is the Monin-Obukhov length.

In this study only the stable functions for f_T and f_ε will be considered. Several similarity functions have been proposed in the past, e.g. by Wyngaard (1973), Thiermann and Grassl (1992) and Frenzen and Vogel (1992).

For f_T we will use the revised functions of Wyngaard (1973), which have later been slightly altered to account for $k_{kar} = 0.4$ rather than the $k_{kar} = 0.35$ used by Wyngaard. Andreas (1989) gives

$$f_T(z/L_{MO}) = 4.9 \left[1 + 2.2(z/L_{MO})^{2/3} \right]. \quad (3.11)$$

For f_ε we will use the relations proposed by Frenzen and Vogel (1992)

$$f_\varepsilon(z/L_{MO}) = 0.84 + 5 z/L_{MO}. \quad (3.12)$$

The set of Equations (3.9) – (3.12) can be solved iteratively using $L_{MO} = T u_*^2 / (k_{kar} g \theta_*)$ and in this way one obtains u_* and θ_* . Next the sensible heat flux H and momentum flux τ are calculated from their definitions, i.e., $H = -\rho C_p u_* \theta_*$ and $\tau = \rho u_*^2$.

3.2.4 Sensitivity of u_* and θ_* to errors in l_0 and C_T^2

Hill (1982) and Andreas (1992) presented elaborate error analyses in which the sensitiveness to off-sets in several parameters in Equations (3.1) - (3.12) are discussed. For that reason only

a few remarks will be made about the sensitivity of fluxes to small off-sets in l_0 and C_T^2 in order to facilitate the discussion of the results in Sections 3.4 and 3.5.

The direct relationship between u_* and l_0 is obtained by combining Equations (3.6) and (3.10):

$$u_* = l_0^{-4/3} \nu 7.4^{4/3} \left(\frac{kz}{f_\varepsilon(z/L_{MO})} \right)^{1/3}. \quad (3.13)$$

The power $^{-4/3}$ -dependence shows that in deriving u_* from l_0 measurements great accuracy in l_0 is needed, especially for small l_0 . Note that in stable conditions for small l_0 (say smaller than ~ 7 mm) u_* is large whereas θ_* is nearly constant (Holtslag and De Bruin, 1988). This means that in near-neutral stable conditions, where fluxes in the SBL are greatest, the heat flux is very sensitive to errors in l_0 .

Equation (3.9) shows that in determining θ_* , errors in C_T^2 are smoothed by the square root dependence between C_T^2 and θ_* . C_n^2 is linearly related to C_T^2 (see Equation 3.5), so the same square root dependence holds between θ_* and C_n^2 .

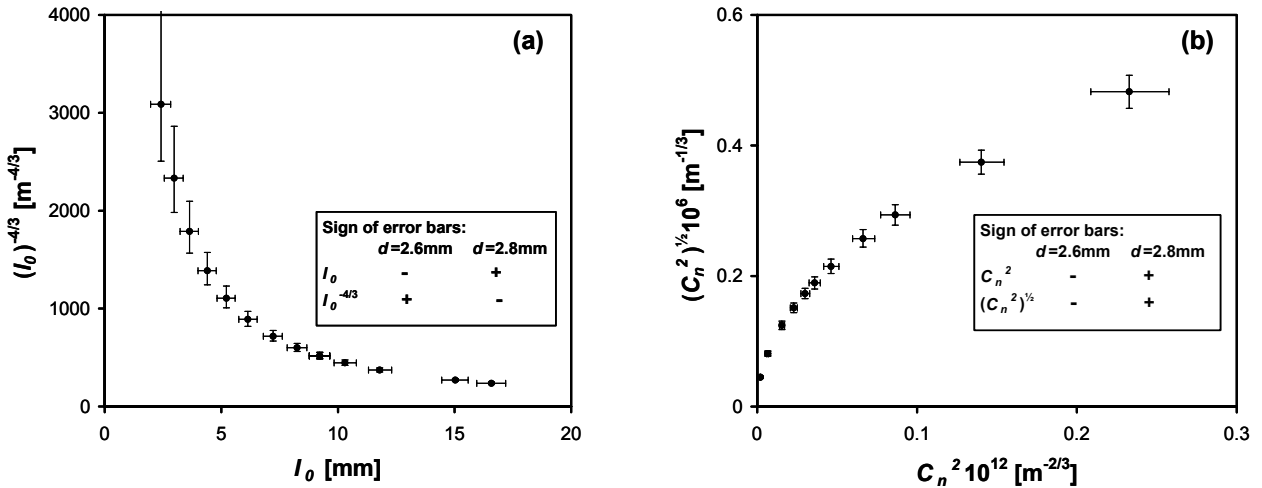


Figure 3-2: Effect of an off-set in the beam displacement distance d of ± 0.1 mm on the inner scale l_0 and the structure parameter of the refraction index C_n^2 , and the subsequent effects on $l_0^{-4/3}$, which is how l_0 relates to the friction velocity u_* (a) and $(C_n^2)^{1/2}$, which is how C_n^2 relates to the temperature scale θ_* (b). Off-sets are shown in terms of error bars, which are specified in the figure.

We found that of all the parameters involved in deriving l_0 and C_n^2 from Equation (3.1) the results are very sensitive to the displacement distance d between the two beams and the choice of the spectrum in the dissipation range f_A . Figure 3-2 shows the effect of a difference in d of ± 0.1 mm around $d = 2.7$ mm, as given by Scintec on $l_0^{-4/3}$ and $(C_n^2)^{1/2}$ (which is how l_0 and C_n^2 relate to u_* and θ_* respectively). The points in Figure 3-2 indicate $l_0^{-4/3}$ or $(C_n^2)^{1/2}$ for $d = 2.7$ mm and $L = 112$ m and are based on actual measurements. The effect of the 0.1 mm off-sets is shown in terms of error bars around these points. Figure 3-2a shows that for small l_0 the

error in l_0 due to a 0.1 mm off-set in d is significantly smaller than for large l_0 . Due to the $^{-4/3}$ power dependence, however, between l_0 and u^* , the error in u^* (or $l_0^{-4/3}$) is in the order of several tens of percent for small l_0 , whereas they are negligibly small for large l_0 . Figure 3-2b shows that the error in C_n^2 due to a ± 0.1 mm off-set in d is largest for large C_n^2 both in C_n^2 and θ^* (or $(C_n^2)^{1/2}$). It should be noted that the error bars represent absolute errors; relative errors would represent better the error in the final flux in terms of percentage.

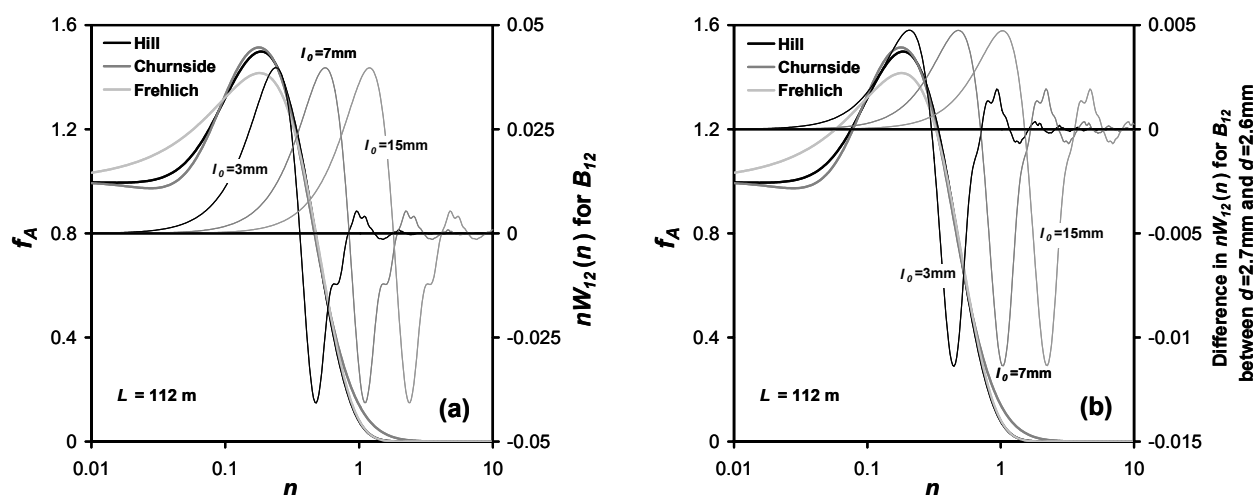


Figure 3-3: Three proposed temperature or refractive index spectra for the dissipation range, f_A (divided by inertial range spectrum) plus their weighting function W_{12} for B_{12} , for 3 values of the inner scale, l_0 and a path length, $L = 112$ m (a), and the difference in W_{12} between a beam displacement $d = 2.7$ mm and $d = 2.6$ mm (b).

Similar to Figure 3-1a, in Figure 3-3a the weighting function $W_{12}(n)$ of the spectrum in the dissipation range, f_A , is given for the path length $L = 112$ m and $d = 2.7$ mm. Furthermore, in Figure 3-3b the difference $W_{diff}(n)$ is given between $W_{12}(n)$ for $d = 2.7$ mm and $W_{12}(n)$ for $d = 2.6$ mm. Note that the secondary y-axis of Figure 3-3a has a different scale than that of Figure 3-1a. Note also that a changed d only affects $W_{12}(n)$ not $W_1(n)$.

With respect to $W_{12}(n)$ for $d = 2.7$ mm, $W_{12}(n)$ for $d = 2.6$ mm is shifted slightly to higher wave-numbers and has a smaller amplitude resulting in $W_{diff}(n)$ depicted in Figure 3-3b. Figure 3-3b shows changes in $W_{12}(n)$, of up to 20% in parts of the spectrum that contribute considerably to the total B_{12} . The greatest impact of an altered d can be expected for small l_0 , where most of the weighted f_A is not equal to 0.

Analyses similar to the ones presented in Figure 3-2 and Figure 3-3 for the other DBSAS instrument parameters D , λ and L show that l_0 and C_n^2 are not sensitive to small off-sets in D and λ , but are quite sensitive to off-sets in L .

3.3 Site and data

The CASES-99 stable boundary-layer experiment took place during October 1999 near the town of Leon (50 km east of Wichita), Kansas, USA. The centre of the site was located at 37° 39'N and 96° 43'W, approximately 450 m above sea level, and it comprised a 4.8 km by 3.2 km area of grassland with dust roads running between individual 1.6 km by 1.6 km fields. The surface was not ideal in that it contained some minor orographical features with, on average, slopes in the order of 0.5 degrees. A vast array of instruments was deployed to obtain as much spatial and temporal information of the nocturnal boundary-layer as possible. More information on the experiment can be found at the official CASES-99 internet site with links to the freely available CASES99 dataset: <http://www.colorado-research.com/cases/CASES-99.html>. Poulos et al. (2000) provide a more complete description of the goals of the experiment, the experimental design, a summary of the intensive operation periods and significant events observed.

The Meteorology and Air Quality Group of Wageningen University (WUMETAIR) occupied one point in the network of flux stations around the main 55 m tower in a part of the CASES-99 terrain that can be considered reasonably flat within the first 100 m around the tower.

An eddy-covariance system was set-up at a height of 2.65 m and operated at 20 Hz; it consisted of a CSAT3 sonic anemometer and a KH20 Krypton hygrometer, both from Campbell Scientific Inc., Logan, USA. Measurements were recorded by a Campbell Scientific CR23X datalogger, while raw data were stored on a laptop and processed afterwards. The following corrections were performed on the eddy-covariance dataset in calculating the 10-minute averaged fluxes:

- axis rotations were performed to force the average lateral wind components, v and w to be zero, as well as $\overline{w'v'}$;
- time series were linearly detrended;
- the sonic temperature was corrected for the influence of humidity on the speed of sound measurement;
- off-sets in the Krypton calibration, due to weathering of the instrument's magnesium fluoride windows, were removed by cross-referencing with a HMP45C temperature humidity probe from Vaisala, Vantaa, Finland;
- the Krypton hygrometer was corrected for its sensitivity to oxygen fluctuations.

We used the SLS20 type DBSAS manufactured by Scintec AG, Tübingen, Germany. It was set-up in the vicinity (~40 m distance) of the eddy-covariance tower at a height of 2.45 m for both transmitter and receiver over a path length of 112 m. Data were recorded and processed online on a laptop to calculate 6-s B_1 , B_2 and r_{12} using the commercial Scintec SLSRUN software (version 2.03). Afterwards the raw B_1 , B_2 and B_{12} measurements from the SLSRUN software were processed with a program we developed in the software package MathCAD to calculate l_0 and C_n^2 as described in Section 3.2.1.

For nearly the whole measurement period between 30 September and 27 October good data were obtained. Generally the conditions were dry, which implied that the humidity influence

on the DBSAS C_n^2 measurements was very small. The eddy-covariance and DBSAS data presented in Section 3.4 have been “cleaned” based on the following criteria:

- only stable conditions ($z/L_{MO} > 0$) between 1900 - 700 local time are included in the analyses;
- H and θ_* in very near-neutral conditions, $0 < z/L_{MO} < 0.01$, are excluded. In that limit θ_* should go to zero and f_T to infinity (see Equations 3.9 and 3.11). However, to keep f_T a continuous function with f_T for $z/L_{MO} < 0$, the used f_T has a neutral limit of 0.84, which leads to unrealistically high DBSAS fluxes for $0 < z/L_{MO} < 0.01$.

3.4 Results

3.4.1 Space and time averaging of turbulence by scintillometers

To illustrate the effect of space and time averaging of turbulence by scintillometers to obtain fluxes versus time averaging only by the eddy-covariance method we present Figure 3-4 to Figure 3-6. Figure 3-4 shows the 6-s averaged sensible heat flux of the DBSAS for the night of 4 to 5 October; this night is a textbook case of intermittent turbulence. Based on these very short period DBSAS fluxes, intermittent turbulent structures at several time scales can clearly be distinguished with very little scatter. With eddy-covariance fluxes, which need a much longer averaging time, some of these short time scale structures will be averaged out. Moreover, even for short eddy-covariance flux intervals of 10-minutes hardly any stationary turbulent period can be found. To avoid large errors in such a case more advanced techniques should be used to estimate the flux-averaging period, such as conditional sampling (Kahlsa, 1980) and ogives (Oncley et al., 1996).

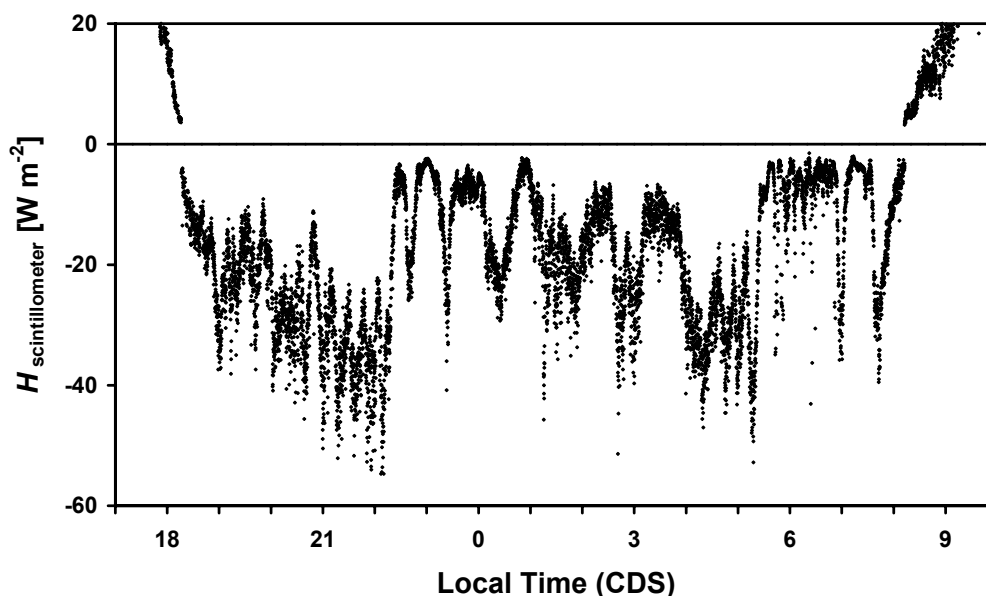


Figure 3-4: 6-s averaged DBSAS sensible heat flux, H , for intermittent turbulence night of 4 to 5 October of CASES-99.

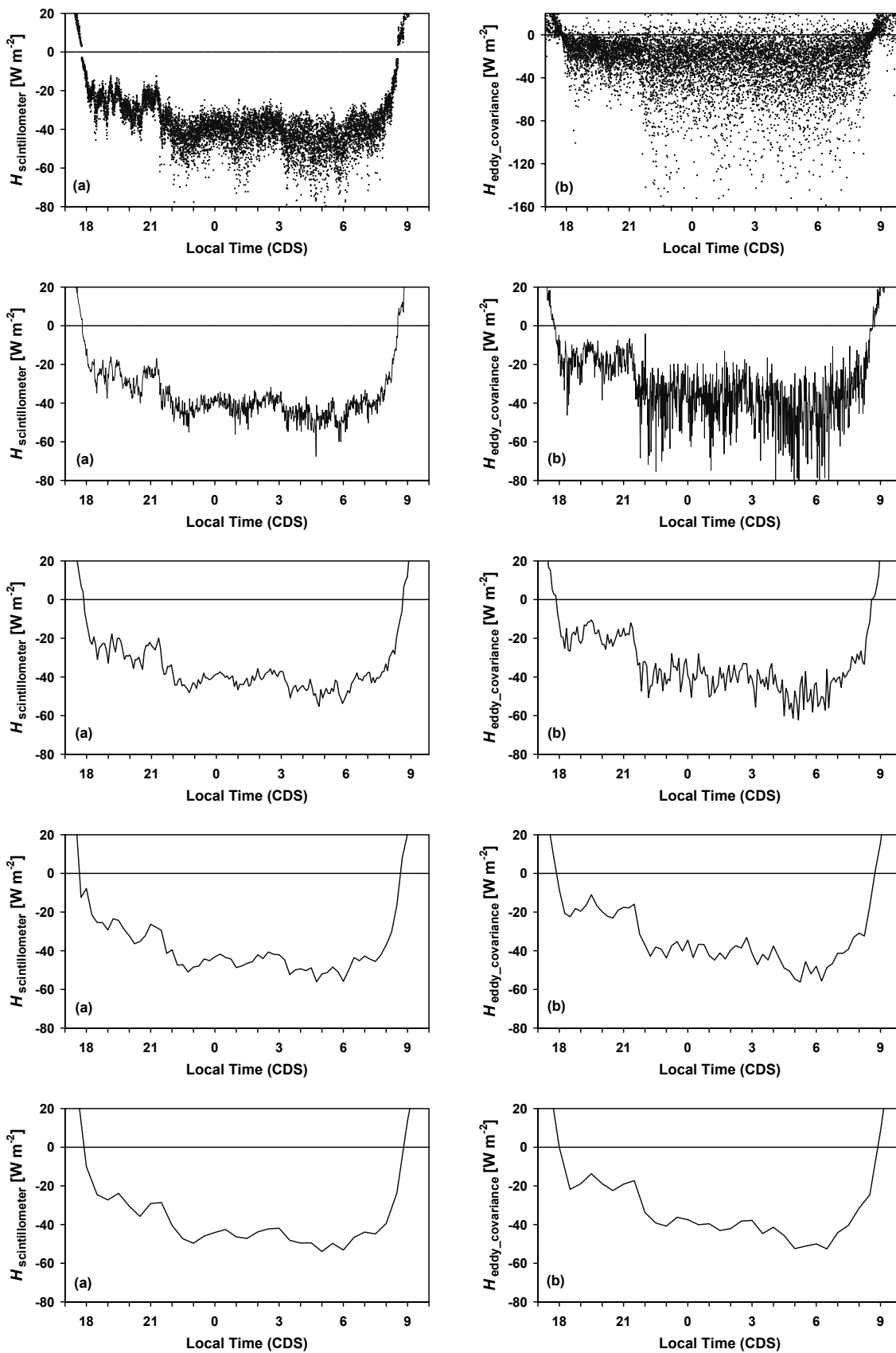


Figure 3-5: Sensible heat flux, H , for the night of 24 to 25 October during CASES-99 of the DBSAS (a) and eddy-covariance system (b) using averaging periods of 6 seconds, 1 minute, 5 minutes, 15 minutes and 30 minutes.

Figure 3-5 shows the heat flux of the DBSAS and eddy-covariance for different flux averaging periods ranging from 6 seconds to 30 minutes for the night of 24 to 25 October. In contrast to Figure 3-4, Figure 3-5 is a night characterised by continuous turbulence after the passage of a warm front at 2130 local time. Note that the y -axis scale is the same for all graphs except for the 6-s eddy-covariance heat flux, which has double the scale of all other graphs.

The signals of the DBSAS and eddy-covariance flux presented in Figure 3-5 fluctuate up and down, in part due to turbulent structures in the signals and in part due to noise because of incomplete statistics of the flux, indicating that the averaging time is still too short. The argument we now follow is that if the statistical error of the sensible heat flux, estimated by the standard deviation, σ_H , of the eddy-covariance and DBSAS flux for a certain averaging interval is the same over the continuous turbulent period, they contain the same turbulent information. Following the same argument, we can say that if σ_H of one instrument remains the same for two consecutive averaging intervals, at the shorter of the two intervals a stable, noise-free flux was already attained.

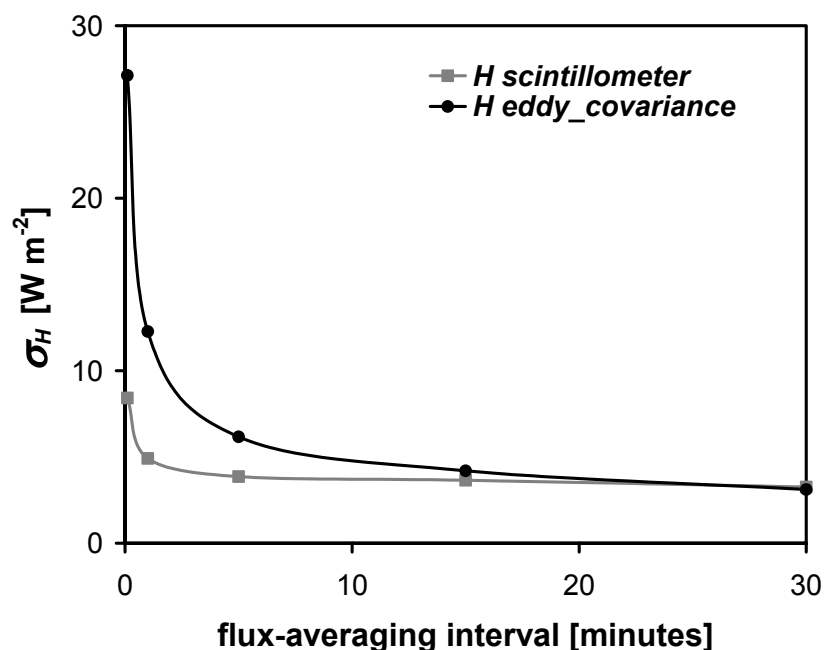


Figure 3-6: Standard deviation of the sensible heat flux, σ_H , as a function of flux-averaging time for the DBSAS and eddy-covariance system between 2230 and 0500 of 24 to 25 October during CASES-99.

Figure 3-6 depicts σ_H for the eddy-covariance method and the DBSAS for the continuous turbulent period of Figure 3-5 between 2230 local time of 24 October and 0500 of 25 October. It quantifies the superiority of the DBSAS statistical error. For this case the DBSAS gives a stable flux for an averaging time between 1 and 5 minutes whereas eddy-covariance needs 10 to 15 minutes to reach the same σ_H . The 6-second DBSAS flux has the same σ_H as the 5-minute eddy-covariance flux.

We note that the DBSAS has a limitation also, set by the path length in averaging large turbulent scales. This is not expected to play a major role in the SBL. The examples shown here are meant as an illustration. To substantiate and generalise the difference between time and space averaging by the DBSAS versus time averaging of the eddy-covariance method for different turbulent flows, a more elaborate study should be performed comparing the number of integral time or length scales of turbulence averaged by each system.

3.4.2 DBSAS compared with eddy-covariance data

In this section the DBSAS and the eddy-covariance data will be compared. The DBSAS data have been processed using the instrument variables as given by the DBSAS manufacturer. First, we will consider ε and C_T^2 in order to be able to compare the eddy-covariance with the DBSAS data independent of Monin-Obukhov scaling. From eddy-covariance data both C_T^2 and ε were calculated following the procedures of Section 3.2.2. In addition, we calculated C_T^2 and ε indirectly using θ^* and u^* from the eddy-covariance fluxes and the MOST relations given in Equations (3.11) and (3.12).

The ε and C_T^2 comparison between DBSAS and eddy-covariance are given in Figure 3-7a and Figure 3-8a respectively. Because both C_T^2 and ε are dependent on height, which was not exactly the same for the DBSAS and the eddy-covariance system they are scaled with z according to their dimensionless groups given in Equations (3.9) and (3.10) respectively.

From Figure 3-7a₁ and Figure 3-7a₂ and it can be seen that the DBSAS ε is too large for small values of ε (large l_0) and too small for high values of ε (small l_0) compared with both ε values derived from eddy-covariance data. The scatter in the comparison DBSAS versus eddy-covariance-derived ε from spectra is surprisingly small, bearing in mind the entirely different techniques used and the different assumptions on which these techniques are based. The comparison with ε derived from eddy-covariance fluxes using MOST introduces somewhat more scatter. The ε values derived from eddy-covariance show good agreement with each other (Figure 3-7a₃), which is an additional indication that the DBSAS ε is incorrect. The strong correlation between DBSAS and eddy-covariance ε shows that the DBSAS does contain information on ε , but for some reason is underestimating it.

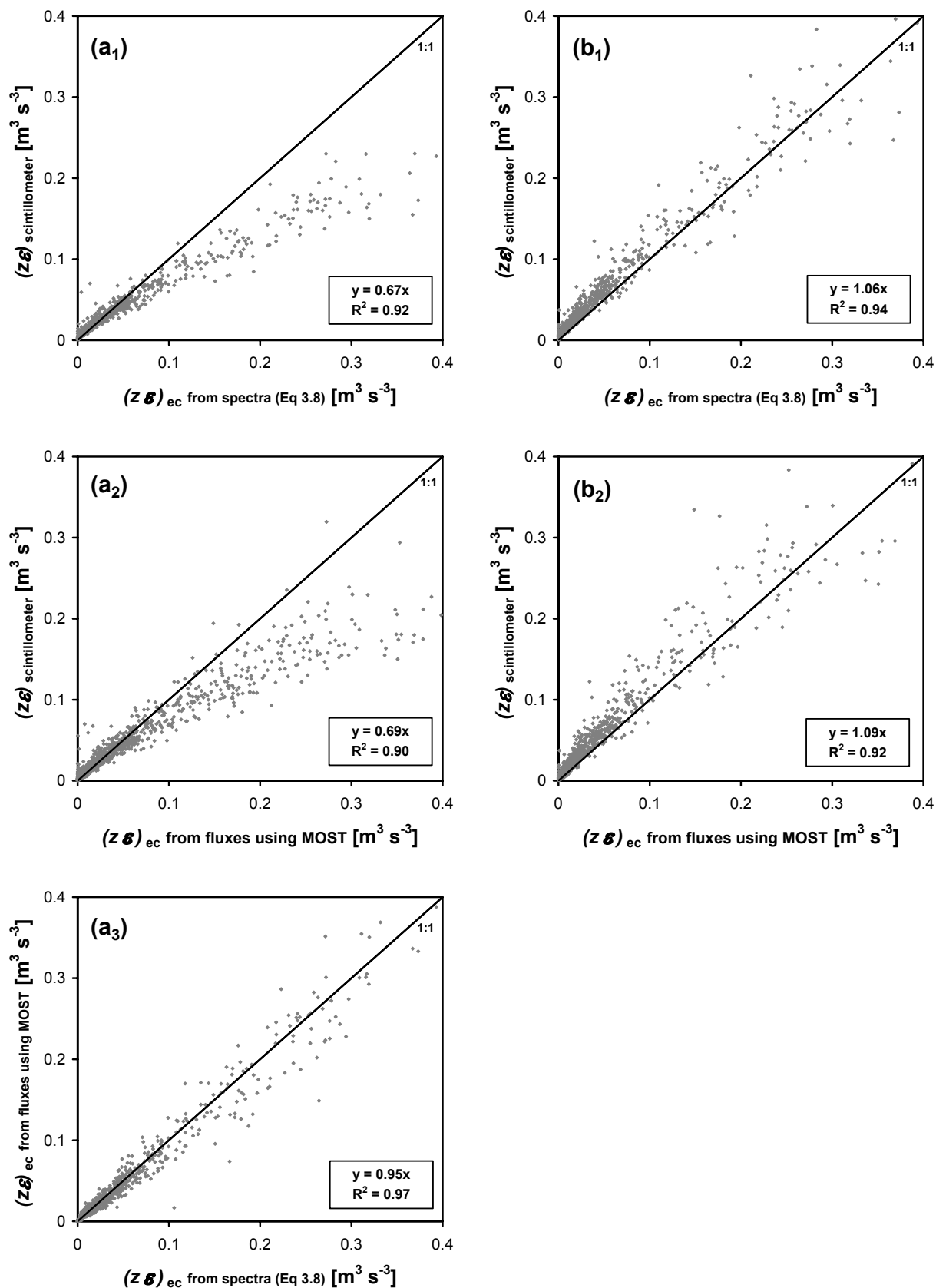


Figure 3-7: Comparison between the TKE dissipation rate, ε determined from DBSAS and eddy-covariance (ec) data. In Figure 3-7a (discussed in Section 3.4.2) the manufacturer specified instrumental constants for the DBSAS was used, i.e. a beam displacement $d = 2.7$ mm. In Figure 3-7b (discussed in Section 3.4.3) an adjusted d ($d = 2.6$ mm) was applied.

In the C_T^2 comparisons depicted in Figure 3-8a much more scatter is seen. None of the three comparisons shows very good agreement. Compared with eddy-covariance C_T^2 derived from fluxes using MOST scaling, the DBSAS C_T^2 is larger (Figure 3-8a₂) and the eddy-covariance C_T^2 calculated from the structure function is smaller (Figure 3-8a₃). As for the ε comparison, the scatter is increased significantly when MOST scaling is used.

In solving C_T^2 from Equation (3.1) once l_0 is known it follows that an underestimated ε , i.e., overestimated l_0 leads to an overestimation of C_n^2 and thus C_T^2 . The underestimation of ε and the overestimation of C_T^2 as determined from the DBSAS are thus correlated. Recall that l_0 is determined independently of C_n^2 .

In Figure 3-9a, u_* , θ_* and the sensible heat flux of DBSAS and eddy-covariance are compared. Similar to the results reported by De Bruin et al. (2002), and consistent with the findings on ε , the DBSAS u_* compared with u_* from eddy-covariance shows a systematic overestimation at small u_* values and an underestimation at large u_* values. Another indication that the DBSAS rather than the eddy-covariance ε is incorrect, is that for neutral situations the DBSAS ε scaled with the eddy-covariance u_* according to Equation (3.10) appears to be significantly less than the neutral limit of 0.84 of Equation (3.12). The eddy-covariance ε does behave according to Equation (3.12) in the near-neutral situation.

The θ_* comparison shows considerably more scatter than u_* . Bearing in mind that scatter in C_T^2 is attenuated in deriving θ_* due to its square root dependence to θ_* , the large scatter must mainly be caused by the use of MOST scaling. The introduction of scatter when MOST was applied for C_T^2 could also be seen in Figure 3-8a. Apart from this the DBSAS θ_* seems to be overestimated, which is in correspondence with the overestimation of C_T^2 .

In line with the findings for θ_* and u_* the DBSAS sensible heat flux, H , overestimates eddy-covariance H for fluxes between 0 and -50 W m^{-2} . For larger absolute values of H , the sensible heat flux is dominated by u_* . The DBSAS underestimation of H for fluxes larger than -50 W m^{-2} corresponds to the underestimation found in u_* for large u_* .

The systematic errors in the DBSAS u_* , which also reflect in H , appear not to be because of break down of MOST in stable conditions, rather they are caused by systematic errors in ε , which is determined independently of MOST. Moreover, De Bruin et al. (2002) found the similar results for u_* for unstable conditions.

We searched for an alternative explanation for the systematic errors found in the DBSAS analyses. In Section 3.2.4 it has been found that the DBSAS ε is extremely sensitive to the beam displacement d . This feature will be explored further in the next section.

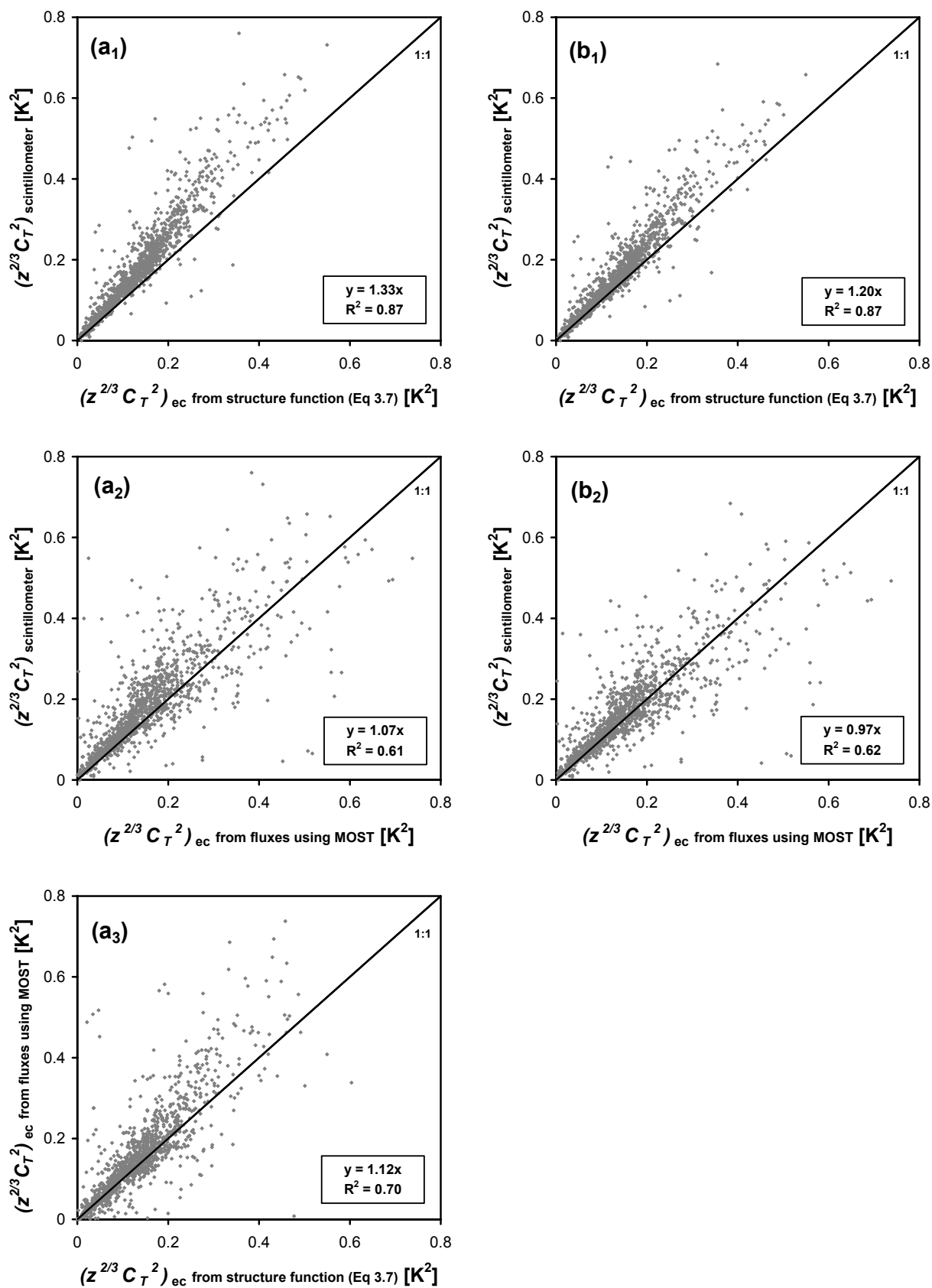


Figure 3-8: Comparison between the structure parameter for temperature, C_T^2 determined from DBSAS and eddy-covariance (ec) data. In Figure 3-8a (discussed in Section 3.4.2) the manufacturer specified instrumental constants for the DBSAS was used, i.e. a beam displacement $d = 2.7$ mm. In Figure 3-8b (discussed in Section 3.4.3) an adjusted d ($d = 2.6$ mm) was applied.

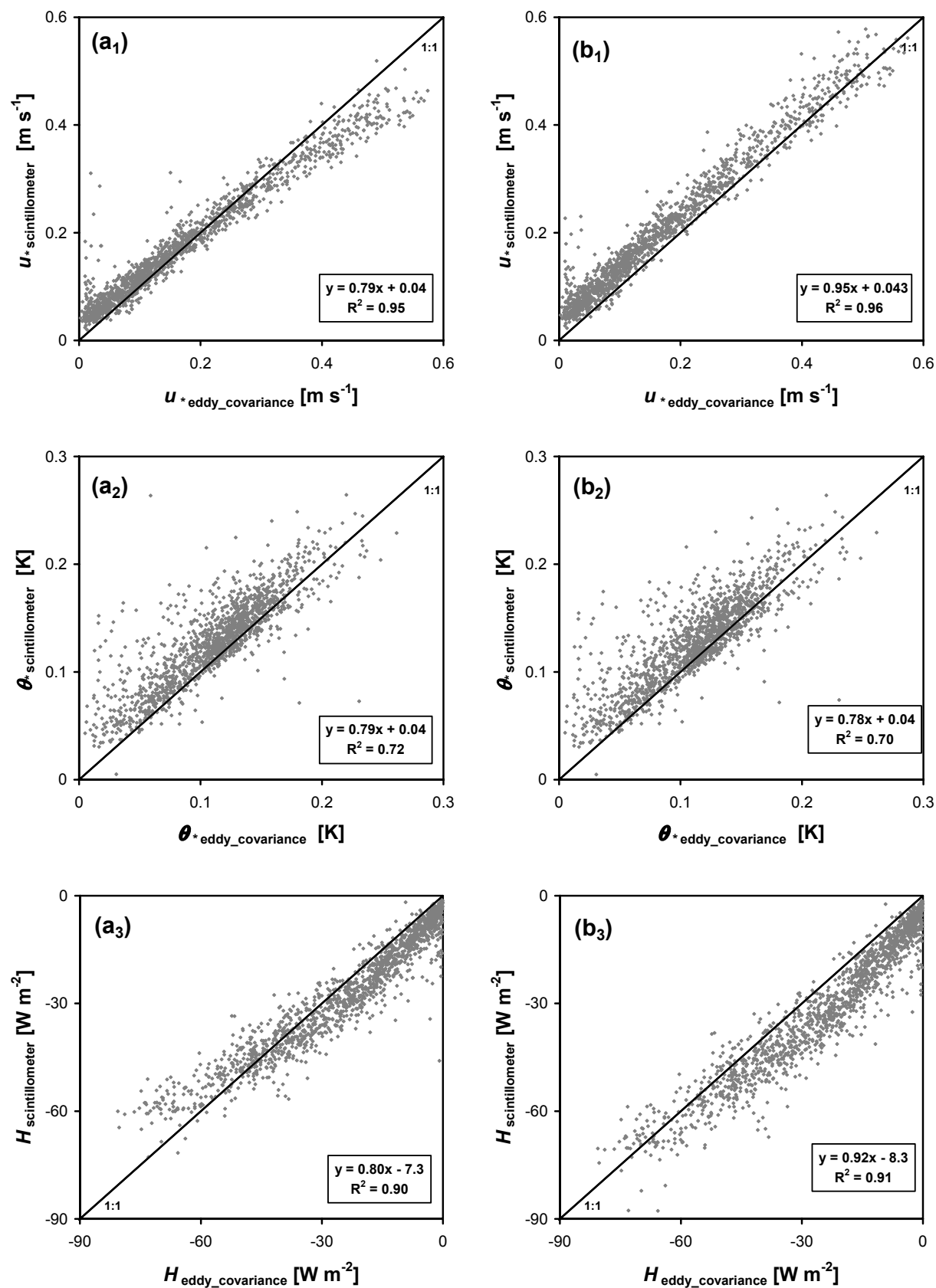


Figure 3-9: Comparison between the DBSAS and eddy-covariance derived friction velocity, u_* , temperature scale, θ_* , and sensible heat flux, H . In Figure 3-9a (discussed in Section 3.4.2) the manufacturer specified instrumental constants for the DBSAS was used, i.e. a beam displacement $d = 2.7$ mm. In Figure 3-9b (discussed in Section 3.4.3) an adjusted d ($d = 2.6$ mm) was applied.

3.4.3 Reanalysed DBSAS data with an adjusted beam displacement

In this section we will try to find a plausible explanation for the errors reported in Section 3.4.2. De Bruin et al. (2002) proposed empirical functions to account for the influence of white noise and inactive turbulence on the DBSAS signal. With these functions they were able to correct for the errors they found, which were similar to the errors reported in Section 3.4.2. In this study we will confine ourselves to trying to attribute these errors to instrumental parameters only.

We found that the systematic errors in l_0 and C_n^2 , resulting in errors in u^* and θ^* , can in part be accounted for by slightly decreasing d . Note that we commented earlier that the DBSAS output is negligibly sensitive to changes in D and λ in comparison with d (see Section 3.2.4). Consequently, we will take these variables as specified by the manufacturer. Furthermore, since we checked carefully the path length L , we will not vary this quantity. After some trial and error calculations the best results are found if we alter d to 2.6 mm instead of the value of 2.7 mm given by the manufacturer.

Figure 3-7b, Figure 3-8b and Figure 3-9b present the same results as Figure 3-7a, Figure 3-8a and Figure 3-9a, except that now $d = 2.6$ mm is used. From these the following can be seen:

- The large underestimation that existed in ε for large ε (Figure 3-7a₁) has disappeared (Figure 3-7b₁). A small overestimation (6%) is now found, which reflects in u^* (Figure 3-9b₁); the u^* comparison has a slope very close to 1, a small intercept and very little scatter;
- the DBSAS C_T^2 overestimation compared with C_T^2 derived from eddy-covariance data reported also in 4.3 still exists, but it is significantly smaller (Figure 3-8b₁);
- DBSAS C_T^2 compared with the eddy-covariance C_T^2 determined from fluxes and MOST shows reasonable agreement, i.e. with much scatter but a slope close to 1 (Figure 3-8b₂);
- compared with Figure 3-9a₂ the results for θ^* are hardly improved (Figure 3-9b₂);
- the DBSAS and eddy-covariance H now show better agreement (Figure 3-8b₃); the slope is closer to 1 with a similar intercept to that found in Figure 3-8a₃.

3.5 Discussion

In this study we showed the advantage of the DBSAS of giving information about fluxes in the SBL over short averaging intervals. This feature has been illustrated in Section 3.4.1, where we presented one night of DBSAS and eddy-covariance data for different integration times. Figure 3-4 to Figure 3-6 showed how intermittent structures seen by the DBSAS remain consistent starting at averaging periods of 6 seconds whereas the eddy-covariance method in this example needs approximately 10 minutes to gather sufficient statistics for a stable flux. With such long averaging intervals it becomes more and more troublesome to resolve some of these short-lived events.

We found that 6-second or 1-minute DBSAS flux time series such as Figure 3-4 and Figure 3-5 are a helpful tool to characterise turbulent features of the flow and to identify particular events.

In this study we found the same problems reported by De Bruin et al. (2002) with the Scintec DBSAS, which were mainly attributed to the u^* determination of the instrument. We showed that these problems are already present in the l_0 determination of the instrument. This is not surprising because in obtaining l_0 from the DBSAS two dissipation range measurements are used and f_A , the spectrum for the dissipation range, is untested for the stable case. Anyhow, the errors in u^* can be considered independent of MOST scaling.

De Bruin et al. (2002) argue that the observed overestimation of u^* for small u^* and underestimation of u^* for large u^* might be due to the influence of white noise and inactive turbulence respectively. They present empirical relationships to correct for these effects. Fitted to the dataset, the corrections give good results.

Here we will try to attribute these errors to instrument variables only. ε and u^* improved considerably by decreasing the beam displacement, d , by 0.1 mm to 2.6 mm. The improvements were mainly for large u^* , i.e. low l_0 and corresponds to that reported in Section 3.2.4. For smaller l_0 the effect of an adjusted d is greatest in the weighting of f_A , the spectrum for the dissipation range. We present the adjustment of d as a working hypothesis, not the final solution. A simple reason for a lower d value is due to off-sets caused by either the beam splitter of the transmitter or the optical configuration in the detector. If this is the case, then d is instrument dependent; consequently, each individual instrument would need to be calibrated for d . The DBSAS manufacturer, Scintec, indicated that a 0.1 mm off-set is within the accuracy of d . Preliminary results of another DBSAS study with the same instrument using a different pathlength showed that another adjusted d should be used to obtain similar improvements in the results as presented here. This indicates that the adjustment of d to 2.6 mm is not a general solution.

Other features might also cause systematic errors. First of all, the findings of de Bruin et al. (2002), which have not been tested for this dataset, might, at least in part, explain the found errors. Furthermore, the application of f_A , the spectrum for the dissipation range, in stable conditions has never been thoroughly examined. We feel that more work has to be done on this issue, i.e. investigation of behaviour of the temperature dissipation spectrum under a variety of stratification classes. By chance, we found that using the approximated f_A as given by Churnside (1990) (see also Figure 3-1 and Figure 3-3) with $d = 2.6$ mm, then the results in ε and u^* give a perfect 1:1 agreement with the eddy-covariance derived variables, also for small ε and u^* , i.e. large l_0 . From Figure 3-3 it can be seen that for large l_0 only the tail of f_A at high wave-numbers is weighted, where the Churnside approximation differs slightly from the other spectra presented. It should be commented that the Churnside approximation at high wave-numbers does not obey the theoretical condition of Equation (21) of Frehlich (1996), and should therefore not be used to solve l_0 . It does however indicate that the exact form of the spectrum is very important. Figure 3-9 of Frehlich (1996) shows that the influence of the lognormal distribution on l_0 and intermittency on β , the Obukhov-Corrsin constant, results in

an “average” spectrum, which at high wave-number shows a similar deviation from the locally stationary spectra of Hill and Frehlich as Churnside’s approximation. We did take the effects of the lognormal distribution on ε and C_n^2 , and intermittency on the parameter β into account, which already improved the results compared with the calculations in which a normal distribution for ε and C_n^2 and no intermittency effects were used.

It might be that the adjusted d indirectly corrects for a stability (z/L_{MO}) dependence of f_A . As can be seen from Figure 3-3, the weighting of f_A is significantly changed due to an adjusted d . This change is very different for different l_0 , which directly relates to u^* and so, indirectly, corresponds to a different stability regime.

After having adjusted d to 2.6 mm, the DBSAS C_T^2 is still larger than the corresponding eddy-covariance values evaluated from the structure function (Equation 3.7). It seems that this is caused by eddy-covariance C_T^2 from the structure function (Equation 3.7) being too small. This follows directly from Figure 3-8a₃, assuming that C_T^2 , derived from the eddy-covariance fluxes and applying MOST, is the ‘truth’. This is confirmed in Figure 3-8b₂, which shows that the DBSAS C_T^2 agrees fairly well with the C_T^2 derived from the eddy-covariance fluxes and applying MOST. Note that we already corrected for the sonic averaging effect on C_T^2 (see Appendix 3A). This issue requires further study.

3.6 Conclusions

In this study we investigated the performance of a displaced-beam small-aperture scintillometer (DBSAS) under stable conditions. This instrument can be used close to the ground and yields information on turbulence for short averaging periods. By analysing fluxes for different averaging times we illustrated the superiority of the DBSAS over the eddy-covariance method in obtaining statistically accurate fluxes over periods of 1 minute or even less. As is well known, this is not feasible with the eddy-covariance technique, even less so for levels below say 2 m, where a significant part of the turbulent flux is averaged out over the sonic path in stable conditions. Both aspects, i.e., short averaging times and the ability to measure fluxes close to the surface, are of importance in the stable boundary-layer (SBL), which is often non-stationary and very shallow.

A significant problem with the DBSAS, however, is that the absolute value of the flux is incorrect when compared with eddy-covariance data over 10-minute or longer time intervals. We corroborated the findings of De Bruin et al. (2002) who reported that the DBSAS overestimates the friction velocity, u^* for small u^* values and underestimates it for large u^* values.

In this study we tried to attribute these systematic errors to instrumental variables only. It was found that the u^* underestimation for high u^* disappears by adapting the working hypothesis that a slightly smaller value should be used for the beam displacement d ($d = 2.6$ instead of 2.7 mm). In preliminary results of a different DBSAS study with the same instrument, the best results were obtained for another d , indicating that the adjustment of d is not a general

solution. In this study we also showed the sensitivity of the DBSAS method to the form of the spectrum in the dissipation range (we used the form proposed by Frehlich, 1992). For large l_0 , i.e., small u^* only a small part of this spectrum is weighted at high wave-numbers. This indicates the theoretical basis for the DBSAS for large l_0 is limited; it depends heavily on the exact form of the spectrum in this region as well as that of the weighting function. Moreover, we showed that the weighting is very sensitive to d . Although the adjusted d of 2.6 mm may not be a general solution, this adjustment is within the accuracy with which the DBSAS manufacturer specifies d , and therefore reflects the margin of error in the weighting function due to errors in d .

We compared also the dissipation rate of turbulent kinetic energy, ε , and the structure parameter of temperature, C_T^2 , derived both from the DBSAS and independently from eddy-covariance data under stable conditions. We found, using the adjusted d of 2.6 mm, a good agreement between the DBSAS ε and ε derived from eddy-covariance spectra (10-minute values). Since a DBSAS can be used close to the surface this is a remarkable result. Other methods to determine ε close to the surface (e.g., with a hot-wire system) are far more elaborate and difficult to operate. The 10-minute values of the DBSAS C_T^2 compared less well with the C_T^2 derived from eddy-covariance data. Our results indicate that this is due to the latter being too low. Note that these results are independent of Monin-Obukhov scaling.

The proposed revision in d leads to improved results for the friction velocity given by the DBSAS (10-minute values). This is of importance for stable conditions, where momentum flux is the dominant mechanism that generates turbulence in the surface layer. The resulting DBSAS sensible heat flux, H , shows a similar good fit with eddy-covariance data as the u^* comparison, i.e., a slope close to 1 with a small off-set. Our results apply to a wide stability range (z/L_{MO} between 0.01 and 10).

Considering the instrumental and theoretical assumptions it can be concluded that the DBSAS made by Scintec has proven to be a good research instrument in studying the SBL. Especially its superiority over the traditional eddy-covariance method in obtaining reliable fluxes close to the ground and over short averaging periods is a major advantage.

Acknowledgements

The authors like to thank Job Kramer who helped us with the fieldwork during the CASES-99 experiment. The help of Steve Oncley and Gordon Maclean of NCAR during CASES-99 in offering technical support and use of the NCAR facilities on site is acknowledged. We also thank Volker Thiermann, Reginald Hill, Wim Kohsiek, and Arnold Moene for their useful comments.

Appendix 3A Path averaging effect of a sonic anemometer in determining C_T^2

The structure function of temperature, D_T , is related to the power spectrum of temperature, ϕ_T , by

$$D_T = 8\pi \int_0^{\infty} \left(1 - \frac{\sin(\kappa r)}{\kappa r}\right) \phi_T(\kappa, l_0) \kappa^2 d\kappa, \quad (3.14)$$

where ϕ_T is given in Equation (3.2). Substituting only the inertial range part of the spectrum ($\phi_T = 0.033 C_T^2 k^{-11/3}$) in Equation (3.14) gives the well-known $r^{2/3}$ -scaling of D_T as follows

$$D_T = C_T^2 r^{2/3}. \quad (3.15)$$

So, by definition Equation (3.15) only holds for measurements made in the inertial range. We determined C_T^2 over a separation distance, r , of ~ 1 m, which is a length scale that lies in the inertial range. However, the sonic anemometer measurements were not made at a point but over a line of ~ 0.1 m length, therefore averaging out temperature fluctuations on scales smaller than 0.1 m. The observed temperature fluctuations will therefore be less and C_T^2 is underestimated.

For wire thermometers Hill (1991) derived the following relation between the measured structure function for temperature, D_{Tm} , and the actual structure function D_T , assuming isotropy of the turbulent flow

$$D_{Tm} = \frac{2}{L^2} \int_0^L (L-x) \left[D_T(\sqrt{r^2 + x^2}) - D_T(x) \right] dx, \quad (3.16)$$

where x is the distance along the wire length L and r is the separation distance between the wires. In this study the distance between the sonic transducers represents the path length L ($= 0.115$ m for the CSAT3) and the time lag between the sonic measurements were, depending on the wind speed, chosen such that r approximated best a 1-m separation distance (see Section 3.2.2).

Using Equations (3.14) to (3.16), and assuming a form for the spectrum, we can fill in the missed temperature fluctuations and correct for C_T^2 . We distinguish between applying the full spectrum of Equation (3.2) (we used the form proposed by Frehlich (1992)) and the simplified assumption of inertial range behaviour down into the dissipation range, i.e., $f_A = 1$ for all k .

Assuming inertial range behaviour for the entire spectrum including the dissipation range, using Equation (3.15) and Equation (3.16) the following corrected C_T^2 can be derived:

$$C_{Tc1}^2 = C_{Tm}^2 r^{2/3} \left[\frac{2}{L^2} \int_0^L (L-x) \left((r^2 + x^2)^{1/3} - x^{2/3} \right) dx \right]^{-1}, \quad (3.17)$$

where subscript 'c' denotes 'corrected' and subscript 'm' denotes 'measured'. The correction is a function of L and r , which for a given experimental set-up is constant.

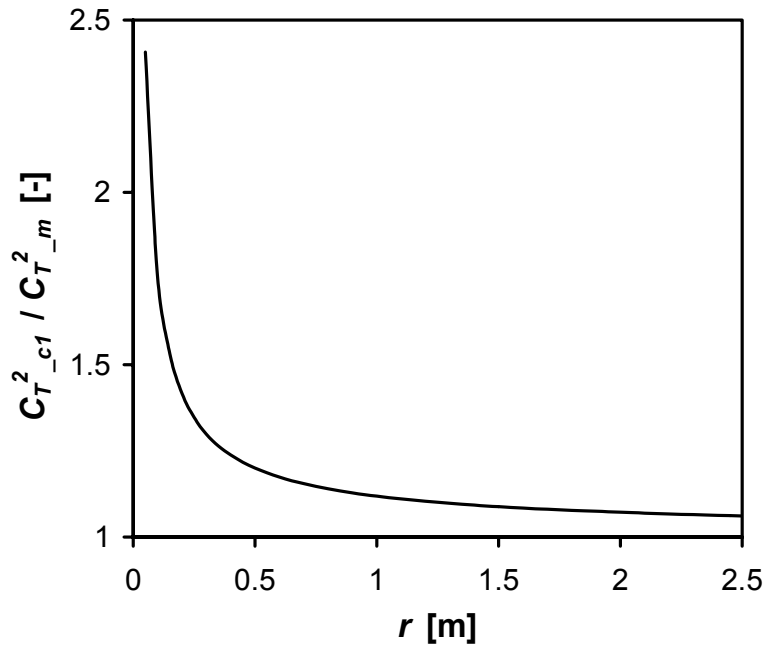


Figure 3-10: The corrected structure parameter of temperature, C_{Tc1}^2 , using inertial range spectrum to correct for sonic path averaging relative to the measured C_{Tm}^2 as a function of the structure function separation distance, r .

For $L = 0.115$ m, the path length of the sonic (a CSAT3 of Campbell Scientific Inc., Logan, USA) used in this study, Figure 3-10 shows the correction factor C_{Tc1}^2 / C_{Tm}^2 as a function of r . Figure 3-10 shows that $r = 1$ m is a minimum separation distance to keep the correction below 10%. Separation distances much larger than $r = 1$ m quickly pose problems as well, since eddy-covariance measurements are generally done close to the surface, and turbulent scales larger than the measurement height will not be detected

Using the spectrum of Equation (3.2), which includes a description of the spectral behaviour in the dissipation range Equation (3.14) to Equation (3.16) yield the following corrected C_T^2 :

$$C_{Tc2}^2 = C_{Tm}^2 r^{2/3} \left[\frac{2}{L^2} \int_0^L (L-x) \left(D'_{Tc2}(\sqrt{r^2+x^2}) - D'_{Tc2}(x) \right) dx \right]^{-1}, \quad (3.18)$$

with $D'_{Tc2}(R) = 8\pi \int_0^\infty \left(1 - \frac{\sin(\kappa R)}{\kappa R} \right) \phi'_T(\kappa, l_0) \kappa^2 d\kappa$, and $\phi'_T = 0.033 k^{-11/3} f_A(kl_0)$.

This procedure is the most accurate. The disadvantage however is that it requires l_0 , and relies on the exact form of f_A , which is still not well established.

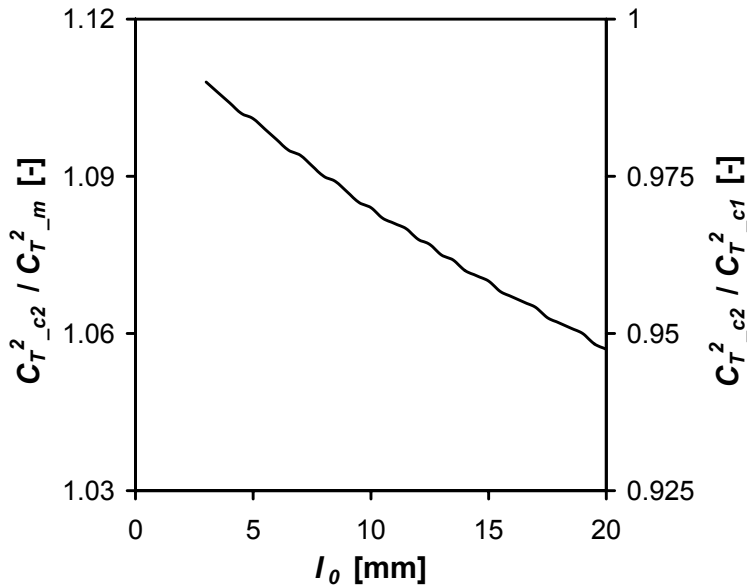


Figure 3-11*: The corrected structure parameter of temperature, C_{Tc2}^2 , using the full spectrum (Equation 3.2) to correct for CSAT3 path averaging relative to the corrected C_{Tc1}^2 using only the inertial range spectrum (primary axis) and the measured C_{Tm}^2 (secondary axis) as a function of the inner scale, l_0 . Here a separation distance of 1 m is used.

Figure 3-11 shows the factors C_{Tc2}^2 / C_{Tm}^2 and C_{Tc2}^2 / C_{Tc1}^2 as a function of l_0 , using the same $L = 0.115$ m as in Figure 3-10. First, it can be seen that C_{Tc2}^2 is smaller than C_{Tc1}^2 . This is because the fall-off of the spectrum in the dissipation range is steeper using f_A than assuming inertial range behaviour down into the dissipation range (see also Section 3.2.2). Secondly, using the inertial range correction, C_{Tc1}^2 , the error made with respect to C_{Tc2}^2 ranges from 6% for large l_0 to less than 2% for small l_0 . Taking into account that for large l_0 the fluxes of heat and momentum are close to zero, the inertial range correction C_{Tc1}^2 is a good alternative for cases where l_0 is not available. In this study we used the full correction C_{Tc2}^2 .

* We later discovered that C_{Tc2}^2 differs only 2% maximum from C_{Tc1}^2 using the original Hill (1978) expression for f_A . Here we used the Frehlich (1992) spectrum.

Appendix 3B Log-normal averaging of ε and C_n^2

Local stationarity is a required condition in calculating ε and C_n^2 from the raw statistics measured by the DBSAS, i.e. the variances, B_1 and B_2 , and the covariance, B_{12} , of the logarithm of the amplitude of the two beams (Frehlich, 1992). Our objective, however, for using the DBSAS is to obtain fluxes in intermittent turbulent (non stationary) conditions. To obtain turbulence measurements that are locally stationary, the averaging time should be taken as short as possible. The DBSAS gives reliable statistical averages for time intervals as short as 6 s. With this notion we followed the approach of Frehlich (1992) to determine ε and C_n^2 estimates at a flux interval time scale (we use 10 minutes) from the raw 6 s statistics. The procedure is as follows. First, one determines ε and C_n^2 at the (local stationary) time scale of the raw statistics, in our case 6 s. Second, one averages these to the flux averaging interval, in our case 10 minutes, taking into account the log-normal distribution of ε and C_n^2 using

$$\langle x \rangle = \bar{x} \exp\left(\frac{\sigma_{\ln(x)}^2}{2}\right), \quad (3.19)$$

where $\langle x \rangle$ denotes the lognormal average and \bar{x} the normal distribution average of parameter x and $\sigma_{\ln(x)}^2$ the variance of $\ln(x)$, where x can be l_0 or C_n^2 . For ε the lognormal average is given by

$$\langle \varepsilon \rangle = \left(\frac{3C_\theta \nu}{\text{Pr}}\right)^3 l_0^{-4} \exp(8\sigma_{\ln(l_0)}^2). \quad (3.20)$$

Last, Frehlich (1992) argues that, at the flux interval time scale, intermittency will affect the spectrum and therefore also the Obukhov-Corrsin constant in Equations (3.6) and (3.20) which relates l_0 to ε . This effect has been parameterised as follows (Frehlich, 1992)

$$\langle \hat{\varepsilon} \rangle = \langle \varepsilon \rangle \exp\left(-\frac{16}{9}\sigma_{\ln(l_0)}^2 - \frac{4}{3}\rho l_0 C_n^2 \sigma_{\ln(l_0)} \sigma_{\ln(C_n^2)}\right), \quad (3.21)$$

where $\langle \hat{\varepsilon} \rangle$ denotes the lognormal average of ε corrected for the intermittency effect on the Obukhov-Corrsin constant.

Contrary to this approach most people use the raw statistics already averaged to the flux interval time scale of and from these determine ε and C_n^2 . According to Hill and Frehlich (1996) this will not violate Equation (3.1) as long as intermittency is stationary in time and homogeneous along the scintillometer path. This is also the procedure followed in the Scintec

AG SLSrun software. In doing so, one ignores the log-normal distribution of ε and C_n^2 and the effect that intermittency may have on the Obukhov-Corrsin constant. Another difference between the two approaches, which is not pointed out by Frehlich (1992), is that because of the highly non-linear relation between the raw statistics and ε and C_n^2 , especially for ε , the flux interval averaged values of ε and C_n^2 based on a *normal* distribution average of 6 s ε and C_n^2 (only step 1 of Frehlich's approach) may already differ significantly from their values determined from flux interval averaged raw statistics.

In this Appendix we will investigate the effect of the different approaches used in the SLSrun software and that of Frehlich (1992) on the flux interval averaged ε and C_T^2 . In comparing the 10-minute values of ε and C_T^2 determined with the different approaches we use the following notation:

- $\{\varepsilon\}$ and $\{C_T^2\}$: based on 10 minute averaged raw statistics
- $\bar{\varepsilon}$ and \bar{C}_T^2 : based on normal average of 6s raw statistics
- $\langle\varepsilon\rangle$ and $\langle C_T^2\rangle$: based on lognormal average of 6s raw statistics
- $\langle\hat{\varepsilon}\rangle$: based on lognormal average of 6s raw statistics including the intermittency effect on Obukhov-Corrsin constant.

Figure 3-12 compares 10-minute average DBSAS ε based 10 minute statistics against $\bar{\varepsilon}$, $\langle\varepsilon\rangle$ and $\langle\hat{\varepsilon}\rangle$. Two main points can be seen in Figure 3-12. First, following the Frehlich approach yields a higher ε compared to using 10 minute averaged statistics. $\langle\varepsilon\rangle$ is on average 15 % larger than $\{\varepsilon\}$, and $\langle\hat{\varepsilon}\rangle$ is 12 % larger. Second, a significant portion (8 %) of the higher ε is not related to the considerations given by Frehlich (1992), i.e. lognormal distribution and intermittency, but simply to the highly non-linear relation between ε and the raw statistics.

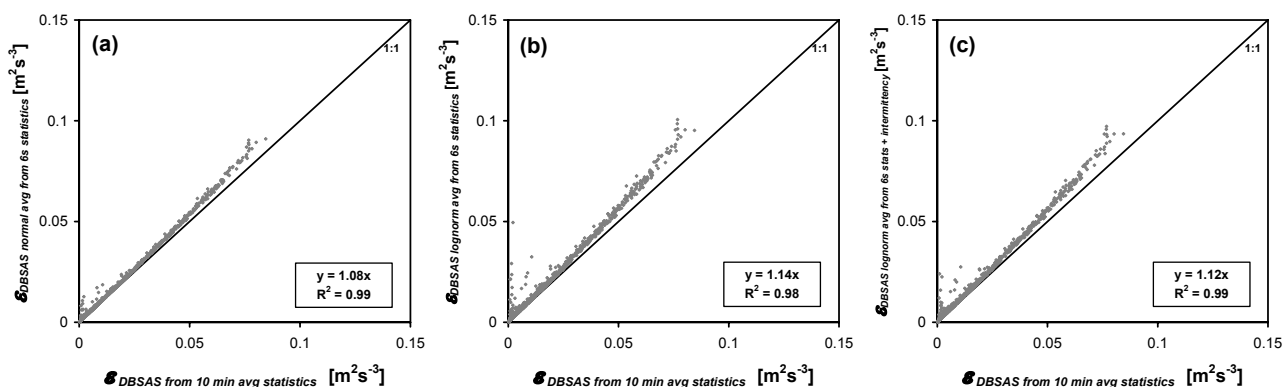


Figure 3-12: For the DBSAS: 10-minute average ε based 10 minute statistics compared against $\bar{\varepsilon}$ (a), $\langle\varepsilon\rangle$ (b) and $\langle\hat{\varepsilon}\rangle$ (c).

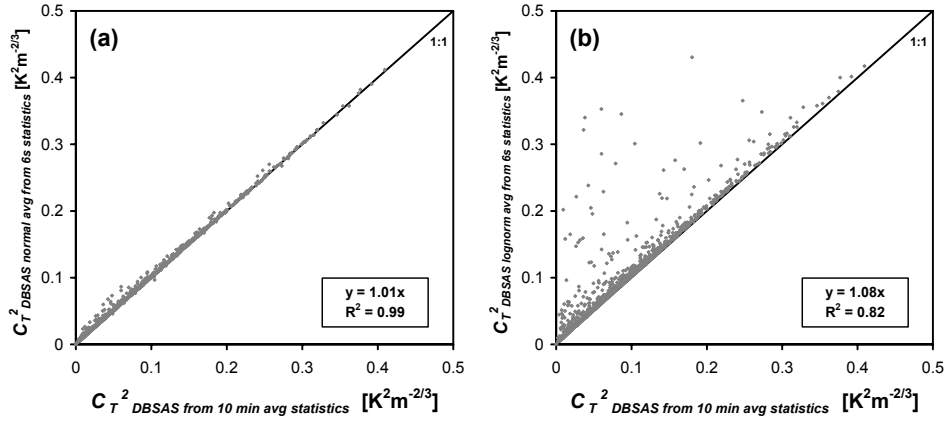


Figure 3-13: For the DBSAS: 10-minute average C_T^2 based 10 minute statistics compared against $\overline{C_T^2}$ (a) and $\langle C_T^2 \rangle$ (b).

Figure 3-13 compares 10-minute average DBSAS C_T^2 based 10 minute statistics against $\overline{C_T^2}$ and $\langle C_T^2 \rangle$. Here the relation between C_n^2 and the raw statistics is linear (see Equation 3.1), and there is no difference between $\{C_T^2\}$ and $\overline{C_T^2}$ (Figure 3-13a). The lognormal averaging introduces more scatter in C_T^2 (Figure 3-13b).

Table 3-1: Linear regressions of DBSAS ε_{DBSAS} and $C_T^2_{DBSAS}$ against Eddy Covariance (EC) data derived ε_{EC} and $C_T^2_{EC}$ for different averaging approaches of ε_{DBSAS} and $C_T^2_{DBSAS}$ (see above for explanation of the symbols). The regressions of Figure 3-7a₁ (for ε) Figure 3-8a₁ (for C_T^2) are bold-faced.

	$z\varepsilon_{DBSAS} = a z\varepsilon_{EC}$		$z\varepsilon_{DBSAS} = a z\varepsilon_{EC} + b$		
	a	r ²	a	b	r ²
$\{\varepsilon_{DBSAS}\}$	0.59	0.92	0.55	0.0069	0.95
$\overline{\varepsilon}_{DBSAS}$	0.64	0.92	0.55	0.0073	0.95
$\langle \varepsilon \rangle_{DBSAS}$	0.68	0.92	0.55	0.0078	0.95
$\langle \widehat{\varepsilon} \rangle_{DBSAS}$	0.67	0.92	0.55	0.0077	0.95

	$z^{2/3} C_T^2_{DBSAS} = a z^{2/3} C_T^2_{EC}$	
	a	r ²
$\{C_T^2_{DBSAS}\}$	1.26	0.90
$\overline{C_T^2}_{DBSAS}$	1.27	0.90
$\langle C_T^2 \rangle_{DBSAS}$	1.33	0.87

Next, we want to see to what extent our choice of averaging method in this article, i.e. $\langle C_T^2 \rangle$ and $\langle \widehat{\varepsilon} \rangle$, affects the systematic errors found in ε and C_T^2 when compared with eddy-covariance measurements derived ε and C_T^2 (see Figure 3-8a and Figure 3-9a). To this end we present Table 3-1 that summarises the linear regressions of DBSAS against eddy covariance (EC) data derived ε for different averaging methods. Table 3-1 shows that without the lognormal averaging, which also includes the non-linear averaging effect between the raw statistics and ε , the systematic errors found for ε would have been even worse, and that applying the adjusted displacement distance of 2.6 mm would not have had the same positive effect on this systematic deviation if $\{\varepsilon\}$ would have been used. In contrast, the C_T^2

comparison is better for the most common $\{C_T^2\}$ than for $\langle C_T^2 \rangle$ what we used. The extra scatter introduced in $\langle C_T^2 \rangle$ due to the lognormal averaging is reflected in the lower correlation coefficient.

Appendix 3C Dissipation range spectra and ε and C_n^2

In this Appendix we will investigate the effect that the choice of theoretical n-spectrum (Equation 3.2), or f_A , has on ε and C_T^2 . We will compare the three spectra plotted in Figure 3-1. The first one is the spectrum of Hill (1978), based on a physical model fitted to measured temperature spectra by Champagne et al. (1977). The second spectrum is by Frehlich (1992), who deduced a fit to n -spectrum measurements performed with a scintillometer technique involving one laser transmitter and an array of receivers with different apertures. The third spectrum expression is that of Churnside (1990), who gave an analytical fit to the Hill model. In this Chapter we have used the Frehlich spectrum, and ε and C_T^2 calculated using the other two f_A expressions are therefore compared with ε and C_T^2 following from the Frehlich spectrum (see Figure 3-14 and Figure 3-15).

Figure 3-14 shows that both the Hill and Churnside spectrum give higher ε values than with the Frehlich spectrum. This is because the Frehlich spectrum puts relatively more spectral energy towards the inertial range (see Figure 3-1), which shifts the relation between the correlation coefficient between the two beams, r_{12} , and l_0 towards higher l_0 . As a result, with the same measurement of r_{12} , a higher l_0 and thus lower ε is obtained.

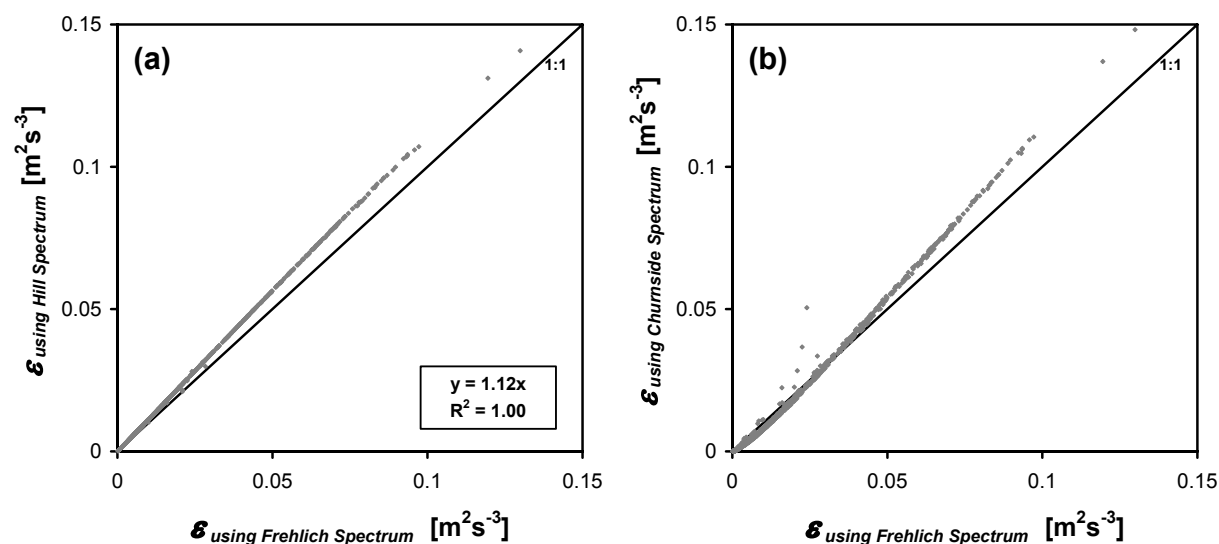


Figure 3-14: For the DBSAS: ε calculated from Equation (3.1) using the Frehlich spectrum compared with ε based on the Hill spectrum (a) and the Churnside fit to the Hill spectrum (b).

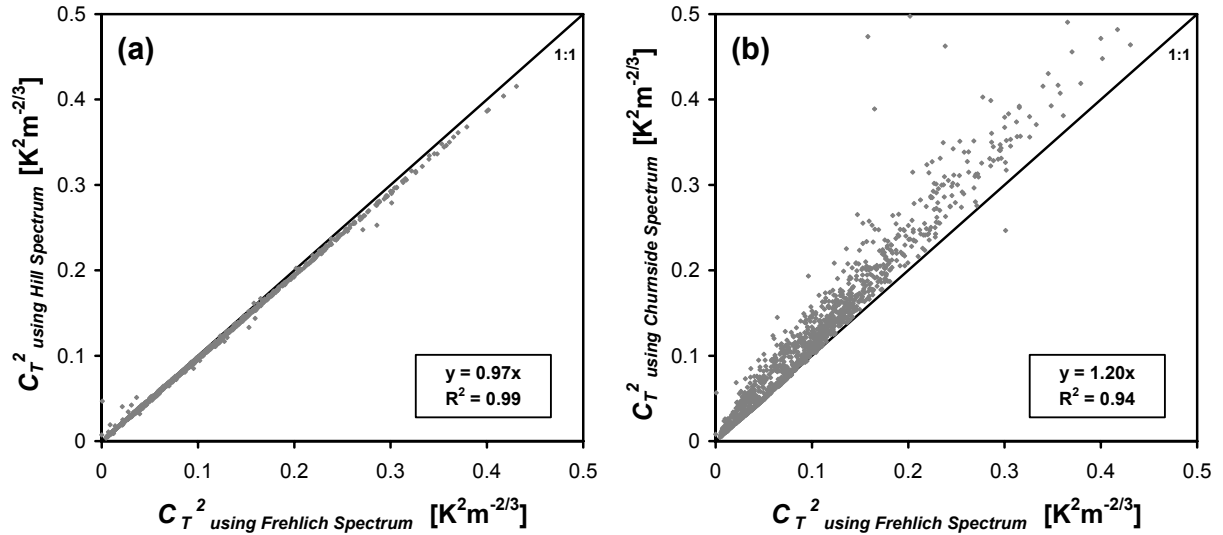


Figure 3-15: For the DBSAS: C_T^2 calculated from Equation (3.1) using the Frehlich spectrum compared with C_T^2 based on the Hill spectrum (a) and the Churnside fit to the Hill spectrum (b).

Figure 3-15 shows that the Hill and Frehlich spectrum yield the same C_T^2 . With the Churnside approximation, however, a significant bias and large scatter is introduced. In Figure 3-14 Churnside also gives a non-linear correspondence with the Frehlich obtained ε . Both features are due to the fact that the Churnside approximation does not meet the n -spectrum condition posed by Frehlich (1992): $\int (kl_0)^{1/3} f_A(kl_0) d(kl_0) \equiv 7.233$. Instead, Churnside yields a factor of 8.1, which is related to the marginally higher energy content of the spectrum at the highest wave-numbers (see Figure 3-1).

The effect of our choice of f_A , on the systematic errors found in ε and C_T^2 when compared with eddy-covariance measurements derived ε and C_T^2 (see Figure 3-8a and Figure 3-9a) are summarised in Table 3-2. It is seen that the Hill spectrum agrees best with the EC derived ε and C_T^2 . The Churnside expression in fact does not qualify since it does not pass the Frehlich condition. When applied, a slightly better result for ε and considerably worse results for C_T^2 are obtained compared to the Frehlich spectrum used here.

Table 3-2: Linear regressions of DBSAS ε_{DBSAS} and $C_{T,DBSAS}^2$ against Eddy Covariance (EC) data derived ε_{EC} and $C_{T,EC}^2$ for different n -spectra used in calculating ε_{DBSAS} and $C_{T,DBSAS}^2$ (see above for explanation of the symbols). The regressions of Figure 3-7a₁ (for ε) Figure 3-8a₁ (for C_T^2) are bold-faced.

	$\varepsilon_{DBSAS} = a \varepsilon_{EC}$			$z^{2/3} C_{T,DBSAS}^2 = a z^{2/3} C_{T,EC}^2$	
	a	r²		a	r²
ε_{DBSAS} Hill	0.75	0.92	$C_{T,DBSAS}^2$ Hill	1.29	0.87
ε_{DBSAS} Churnside	0.71	0.95	$C_{T,DBSAS}^2$ Churnside	1.54	0.80
ε_{DBSAS} Frehlich	0.67	0.92	$C_{T,DBSAS}^2$ Frehlich	1.33	0.87

Appendix 3D Adjusting the r_{12} versus l_0 relation

The strategy to follow to solve l_0 from the raw statistics measured by the DBSAS, i.e. the variances, B_1 and B_2 , and the covariance, B_{12} , of the logarithm of the amplitude of the two beams using Equation (3.1) consists of finding the relation between the correlation coefficient between the two beams, $r_{12} = B_{12} / B_1$, and l_0 . This relation is different for every path length.

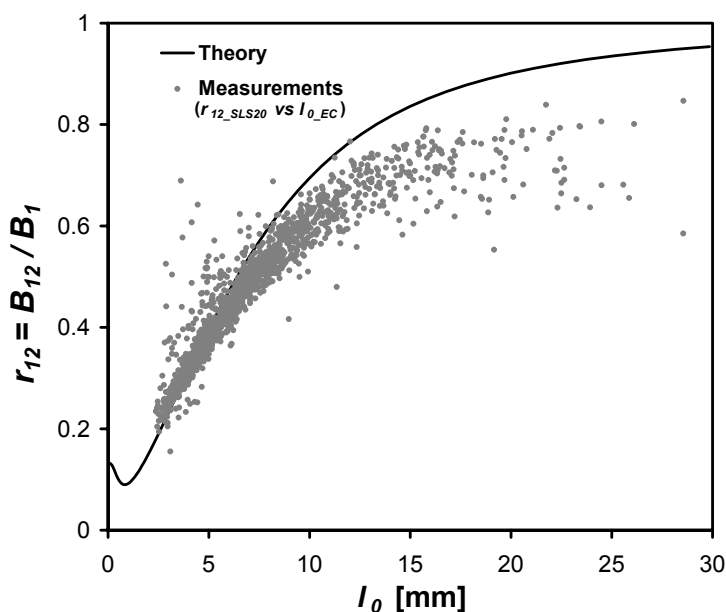


Figure 3-16: Relations between the correlation coefficient of the two DBSAS beams, r_{12} and the inner scale, l_0 for CASES99. The theoretical line is calculated from Equation (3.1). The measurement points depict the relation between the DBSAS measured r_{12} and l_0 determined from Eddy Covariance (EC) measurements.

In Figure 3-16 this theoretical relation is depicted for our DBSAS set-up during CASES-99 (path length of 112 m). Also plotted is the relation between the DBSAS measured r_{12} , and the eddy covariance measurements derive l_0 . Theory and measurements of the r_{12} versus l_0 relation do not agree, which is the basis for the systematic DBSAS errors reported in this study. We will discuss three heuristic approaches that adjust the theoretical r_{12} versus l_0 relation to fit the data. Note that in this Appendix we work with the Hill n -spectrum.

1. Adjusting d from 2.7 mm to 2.6 mm:

In this study, we adopted the working hypothesis of using a displacement distance between the beams, d , of 2.6 mm instead of 2.7 mm, which reduced the systematic errors. In doing so, the r_{12} versus l_0 relation is moved up somewhat (not shown here), which means that for low l_0 values the theoretical line fits better to the data, which improves the DBSAS ε values for high ε . For high values of l_0 , and thus low values of ε , this approach leads to worse results, as can also be seen in Figure 3-7b₁.

2. Adjusting the n -spectrum:

Here we will try to adjust the n -spectrum in the dissipation range (f_A), such that the theoretical r_{12} versus l_0 relation fits the data presented in Figure 3-16. To do this exercise we first need a good analytical expression for the Hill bump. Note that in Appendix 3C we showed that the Churnside approximation is not appropriate. We found an alternative analytical fit that does obey the Frehlich condition discussed in Appendix 3C and Section 5.2.1:

$$f_{A_Hill}(\eta) = \left[1 + 0.7 e^{-[0.924(\ln(\eta) - \ln(0.245))]^2} \right] e^{-2.772\eta^2}, \quad (3.22)$$

with $\eta = kl_0 / 7.4$. We were not able to fit the theoretical r_{12} versus l_0 relation to the data using different base-function coefficients for f_{A_Hill} of Equation (3.22) only. We also had to add an extra term with two extra coefficients:

$$f_{A_Hill_fit}(\eta) = \left[1 + 0.5 e^{-[0.85(\ln(\eta) - \ln(0.7))]^2} \right] e^{-0.05\eta^2} + 0.035 e^{-[1.2(\ln(\eta) - \ln(7.4))]^2}. \quad (3.23)$$

In Figure 3-17, $f_{A_Hill_fit}$ is compared with the f_A functions from Hill (1978) and Frehlich (1992) (Figure 3-17b), and the effect it has on the theoretical r_{12} versus l_0 relation (Figure 3-17a). Note, that $f_{A_Hill_fit}$ unfortunately does not obey the Frehlich condition; the integration yields a value of 6.91 instead of the theoretical 7.233.

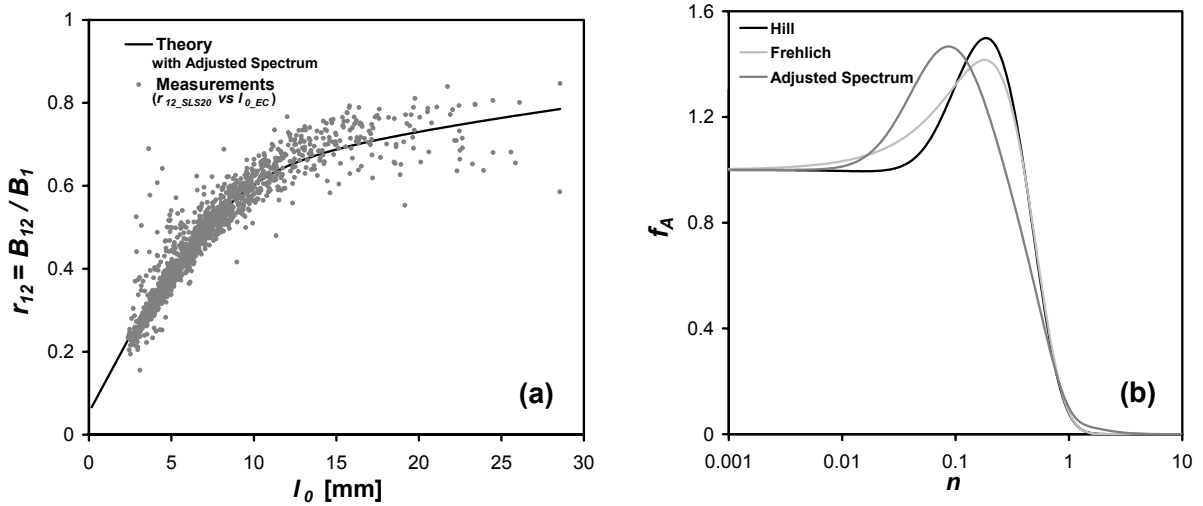


Figure 3-17: (a) is as Figure 3-16 with an adjusted theoretical line fitted to the data by tuning the n -spectrum (Equation 3.23). (b) n -spectra in the dissipation range (f_A); depicted are the f_A from Hill (1978), Frehlich (1992), and the tuned f_A expression discussed in (a).

3. Fitting r_{12} versus l_0 :

The last approach bypasses Equation (3.1) and choice of dissipation spectra all together and directly fits a relation between the DBSAS measured r_{12} and the eddy covariance measurements derived l_0 . A suitable base-function that describes this relation using 4-parameters is:

$$r_{12_fit} = d_1 \tanh\left(\frac{l_0 + d_2}{d_3} \pi\right)^{d_4} . \quad (3.24)$$

For this experiment with a path length of 112 m $d_1 = 0.75$; $d_2 = -0.57$; $d_3 = 29.8$; and $d_4 = 0.8$.

In short (without Figures) we will discuss the effect of approaches 2 and 3 to adjust the r_{12} versus l_0 relation to improve the systematic errors in ε and C_T^2 reported in this study. Approach 1 is discussed already in this Chapter. Both other approaches work directly on the r_{12} versus l_0 relation, and as a logical consequence, the DBSAS and EC ε -estimates agree very well. For C_T^2 there is a large difference between the two approaches however. Approach 2, alters the n-spectrum not only for the l_0 derivation but also for C_n^2 and thus C_T^2 . As a result the overestimation of the DBSAS C_T^2 seen in Figure 3-8 is made worse. Unlike for l_0 , approach 3 still uses Equation (3.1) and the Hill spectrum to determine C_T^2 . With the improved estimate for l_0 to describe the Hill spectrum, also C_T^2 is in better agreement with the EC data derived value.

Appendix 3E Direct flux estimates from raw DBSAS statistics

To infer fluxes from the raw DBSAS statistics, i.e. the variances, B_1 and B_2 , and the covariance, B_{12} , of the logarithm of the amplitude of the two beams requires a number of steps, each with its underlying theory and assumptions.

In Figure 3-18 we bypass all these steps and relate the correlation coefficient between the two beams, $r_{12} = B_{12} / B_1$, and B_1 more or less directly to the eddy covariance (EC) fluxes. Figure 3-18 relates u^* directly to r_{12} . With r_{12} as a measure for u^* , and B_1 as an indirect measure for θ^* we introduce Φ , which has the appearance of the heat flux definition in MOST theory:

$$H \propto \Phi(r_{12}, B_1) = \rho c_p u_{*fit}(r_{12}) \sqrt{B_1} . \quad (3.25)$$

Note that we use $\sqrt{B_1}$ since this reflects the H dependence of B_1 in the near neutral range. In Figure 3-18, H is indirectly related to B_1 through Φ . Figure 3-18 clearly shows that r_{12} and B_1 contain direct information on the turbulent fluxes. We determined fit functions through the plots represented in Figure 3-18. For u^* we found

$$u_{*fit}(r_{12}) = 4.5 e^{-(5.8r_{12}+0.6)} \quad (3.26)$$

and for H we found

$$H_{fit}(r_{12}, B_1) = -\left[3.5 \Phi(r_{12}, B_1) - 0.8 \Phi(r_{12}, B_1)^{1.1}\right]. \quad (3.27)$$

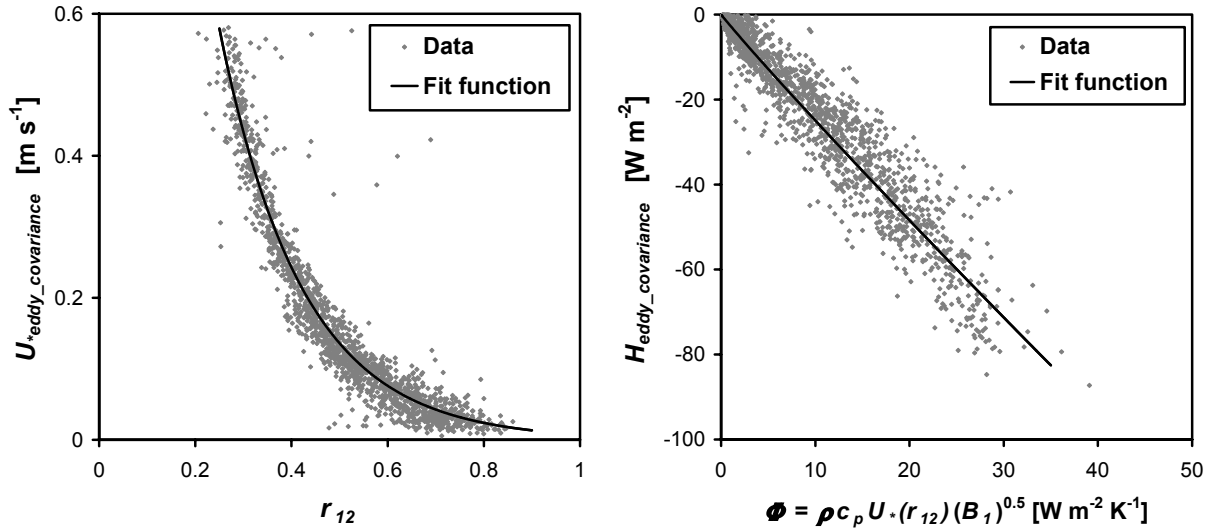


Figure 3-18: Derivation of empirical relations between the DBSAS principle measurements r_{12} and B_1 and the eddy covariance u_* (left) and H (right) for CASES-99. The fitted functions are given in Equation (3.26) for u_* and Equation (3.27) for H .

In Figure 3-19 the direct flux-estimates that result from r_{12} and B_1 using the fit functions of Equations (3.26) and (3.27) are compared with the eddy-covariance fluxes. Note that the scatter in Figure 3-19 is comparable to the complete flux-estimates given in Figure 3-9.

With this very simple approach we obtained u_* and H -estimates without bias and little scatter. Note that the parameters used in the fit functions are not universal but depend on the experimental set-up (instrument height and path length) and possibly the stability conditions.

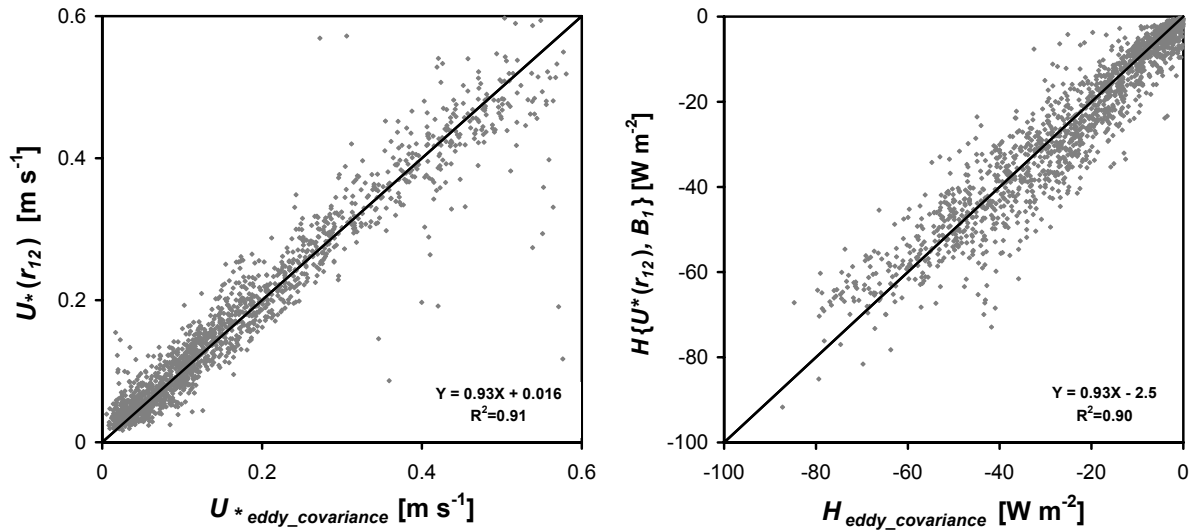


Figure 3-19: Comparison between u_* (left) and H (right) for the DBSAS direct flux-estimates and eddy-covariance for stable conditions during CASES-99.

Chapter 4 Monin-Obukhov similarity functions of C_T^2 and ε in the Stable Boundary Layer

4.1 Introduction

Point source scintillometers have proven to be a good alternative method to obtain fluxes of heat and momentum in the stable boundary layer (SBL) (De Bruin et al., 2002 and Hartogensis et al., 2002). The main advantage over the traditional eddy-covariance method is that turbulent fluxes can be obtained over short averaging intervals (~ 1 minute and less) and close to the surface (less than 1 m), which are necessary conditions for measuring the often non-stationary and shallow SBL. Some key publications on scintillometry are Tatarskii (1961), Andreas (1990), Hill (1997), and De Bruin (2002).

The basic turbulent variables that are measured with scintillometers are the dissipation of turbulence kinetic energy (TKE), ε , and the structure parameter of temperature, C_T^2 . To determine the turbulent fluxes, use is made of the universal relationships between the dimensionless ε , and C_T^2 and the dimensionless height $\zeta = z/L$, where z denotes height and L the Monin-Obukhov length. These functions exist by virtue of the Monin-Obukhov similarity theory (MOST).

In spite of their practical relevance, little ε and C_T^2 data have been presented in the literature for $\zeta > 1$. It is the objective of this study to present experimental ε and C_T^2 data for a stability range $0 < \zeta < \sim 10$, from which we will derive new MOST functions. These data have been gathered in the context of the CASES-99 project (Poulos et al., 2002). We will compare our findings with previously reported MOST functions for ε and C_T^2 ; for instance Wyngaard (1973), Högström (1990), Thiermann and Grassl (1992), Frenzen and Vogel (2001), and Pahlow et al. (2001).

Assuming a production-dissipation balance of the TKE and temperature variance (T-variance) budget, the MOST functions for ε and C_T^2 are related to the MOST functions of the non-dimensional horizontal wind speed and potential temperature gradients, ϕ_m and ϕ_h respectively (Panofsky and Dutton, 1984), and through these also to the flux and gradient Richardson numbers. We will investigate these features and compare the thus derived ϕ_m and ϕ_h groups with the functions reported in the literature, e.g. the well-known ϕ_m and ϕ_h functions proposed by Businger et. al. (1971).

-
- This Chapter is based on Hartogensis, O.K. and De Bruin, H.A.R., 2005: ‘Monin-Obukhov similarity functions of the structure parameter of temperature and TKE dissipation rate in the Stable Boundary Layer’, *Boundary-Layer Meteorol.*, **116**, 253-276.
 - Appendix 4A has been added in this thesis.

4.2 Theory

According to MOST the following relations define the scaling relationships of ε and C_T^2 in the atmospheric surface layer:

$$\frac{\kappa z \varepsilon}{u_*^3} = f_\varepsilon(\zeta) \quad (4.1)$$

and

$$\frac{C_T^2 z^{2/3}}{\theta_*^2} = f_T(\zeta), \quad (4.2)$$

where z is the measurement height, κ the von Kármán constant (here taken as 0.4), θ_* the temperature scale, u_* the friction velocity, $\zeta \equiv z/L$ is a dimensionless height parameter with $L = T u_*^2 / \kappa g \theta_*$ is the Monin-Obukhov length and f_ε and f_T are universal MOST functions. In this study we will confine ourselves to stable conditions, i.e. $L > 0$.

A working hypothesis that is often used in TKE-budget analyses is that, close to the surface, the pressure and flux divergence terms in the TKE equation are negligible (see e.g. Panofsky and Dutton, 1984). Consequently, the TKE locally produced by buoyancy and mechanical turbulence is also locally dissipated. This is often referred to as the “local dissipation assumption”. The simplified TKE budget in non-dimensional form directly relates f_ε to the dimensionless gradient ϕ_m of the mean horizontal wind speed, u :

$$f_\varepsilon = \phi_m - \zeta, \quad (4.3)$$

where ϕ_m , defined as $\phi_m \equiv (\kappa z / u_*) \overline{\partial u / \partial z}$ represents mechanical TKE production, ζ represents buoyancy TKE production or destruction depending on the sign of ζ , and f_ε is the dimensionless dissipation rate.

Similar arguments for the T-variance budget equation lead to (Panofsky and Dutton, 1984):

$$f_T = \frac{3}{\kappa^{2/3}} \frac{\phi_h}{f_\varepsilon^{1/3}}, \quad (4.4)$$

where ϕ_h , the dimensionless gradient of mean potential temperature, θ , is defined as $\phi_h \equiv (\kappa z / \theta_*) \overline{\partial \theta / \partial z}$.

4.2.1 Similarity functions f_ε and f_T for ε and C_T^2

Hill (1997) gives an overview of several f_ε and f_T expressions for stable conditions that can be found in the literature.

In this study we will consider for f_ε :

$$f_\varepsilon(\zeta) = [1 + 2.3\zeta^{0.6}]^{3/2}, \quad (4.5a)$$

proposed by Wyngaard and Coté (1971) and adapted by Andreas (1989) to account for $\kappa = 0.4$ instead of 0.35,

$$f_\varepsilon(\zeta) = [1 + 4\zeta + 16\zeta^2]^{1/2}, \quad (4.5b)$$

proposed by Thiermann and Grassl (1992),

$$f_\varepsilon(\zeta) = 0.85 + 4.26\zeta + 2.58\zeta^2, \quad (4.5c)$$

proposed by Frenzen and Vogel (2001) and,

$$f_\varepsilon(\zeta) = c_{\varepsilon 1} + c_{\varepsilon 2}\zeta, \quad (4.5d)$$

proposed by Wyngaard (1973). Several authors used Equation (4.5d) with different values for the constants $c_{\varepsilon 1}$ and $c_{\varepsilon 2}$; Wyngaard (1973) gave $c_{\varepsilon 1} = 1$ and $c_{\varepsilon 2} = 5$, Högström (1990) found $c_{\varepsilon 1} = 1.24$ and $c_{\varepsilon 2} = 4.7$, and, recently, Pahlow et al. (2001) obtained $c_{\varepsilon 1} = 0.61$ and $c_{\varepsilon 2} = 5$. The original form of Equation (4.5c) given by Frenzen and Vogel (2001) reads $f_\varepsilon = (0.85 + 0.6\zeta)(\phi_m - \zeta)$ with $\phi_m = 1 + 5.3\zeta$. In Equation (4.5c), we inserted their ϕ_m function in the f_ε expression. Frenzen and Vogel (2001) also gave a hyperbolic function of f_ε for the stable and unstable range. They argued this function to be the best form since it is continuous for both the stable and unstable cases and represents more closely the transition regions between the two regimes. Here we are interested in stable conditions and, therefore, will only consider their stable f_ε function.

Note that Hill (1997) wrongly cited Frenzen and Vogel (1992) in his literature overview of f_ε and f_T expressions. He gave $f_\varepsilon = 0.84 + 5\zeta$ for stable conditions after Frenzen and Vogel (1992), who indeed suggested $f_\varepsilon = 0.84$ for neutral conditions, but this result was obtained using only unstable data and no stable data were presented.

For $f_\varepsilon(0) \neq 1$, there is no balance between dissipation and production rates of TKE at neutral conditions. This follows directly from Equation (4.3), where it can be seen that $f_\varepsilon(0) = \phi_m(0)$,

and $\phi_m(0)$ is 1 by the definition of the von Kármán constant. Frenzen and Vogel (1992 and 2001) and Pahlow et al. (2001) found $f_\varepsilon(0) < 1$, whereas Högström (1990) found $f_\varepsilon(0) > 1$.

For f_T we will consider:

$$f_T(\zeta) = c_{T1} [1 + c_{T2} \zeta^{2/3}], \quad (4.6a)$$

after Wyngaard et al. (1971) with $c_{T1} = 4.9$ and $c_{T2} = 2.4$. We will use $c_{T2} = 2.2$ after Andreas (1989) to account for $\kappa = 0.4$ instead of $\kappa = 0.35$ used by Wyngaard. Thiermann and Grassl (1992) found

$$f_T(\zeta) = 6.34 [1 + 7\zeta + 20\zeta^2]^{1/3}. \quad (4.6b)$$

4.2.2 Similarity functions ϕ_m and ϕ_h for $\delta u/\delta z$ and $\delta\theta/\delta z$

We will also investigate ϕ_m and ϕ_h expressions derived from f_ε and f_T , using Equations (4.3) and (4.4). As with f_ε and f_T , there is no unanimity in the literature on the formulations of ϕ_m and ϕ_h . In this study we will consider the Businger-Dyer relations (Businger et. al, 1971; Dyer, 1974; Fleagle and Businger, 1980):

$$\phi_m(\zeta) = \phi_h(\zeta) = 1 + 5\zeta. \quad (4.7a)$$

Recently, Andreas (2002) recommended the formulation of Holtslag and De Bruin (1988):

$$\phi_m(\zeta) = \phi_h(\zeta) = 1 + \zeta \left[a_1 + b_1 \exp(-d\zeta) - b_1 d \left(\zeta - \frac{c}{d} \right) \exp(-d\zeta) \right], \quad (4.7b)$$

with $a_1 = 0.7$ and $b_1 = 0.75$, $c = 5$ and $d = 0.35$. Beljaars and Holtslag (1991) revised these expressions because Equation (4.7a) leads to flux Richardson numbers > 1 for very stable conditions and arrived at:

$$\phi_m(\zeta) = 1 + \zeta \left[a + b \exp(-d\zeta) - bd \left(\zeta - \frac{c}{d} \right) \exp(-d\zeta) \right] \quad (4.7c1)$$

and

$$\phi_h(\zeta) = 1 + \zeta \left[a \left(1 + \frac{2}{3} a \zeta \right)^{1/2} + b \exp(-d\zeta) - bd \left(\zeta - \frac{c}{d} \right) \exp(-d\zeta) \right], \quad (4.7c2)$$

with $a=1$, $b=2/3$, $c=5$ and $d=0.35$

4.3 Experimental

4.3.1 Data description

We will use data gathered during CASES-99. The CASES-99 stable boundary layer experiment took place during October 1999 at a grassland site in Kansas, USA (Poulos et al., 2002). We operated a CSAT3 sonic anemometer from Campbell Scientific Inc., Logan, USA at 2.65 m. Raw 20 Hz data were stored on a laptop and processed afterwards with the latest version of the *EC-pack* flux-software package, developed by Wageningen University. The source code and documentation of the software can be found at <http://www.met.wau.nl/projects/jep/index.html>.

First, 5-minute fluxes were calculated, which were subsequently averaged to 10-minute values. The following corrections were performed in calculating the 5-minute averaged fluxes:

- axis rotations were performed with the so-called planar fit routine after Wilczak et al. (2001). This routine fits the sonics coordinate system to the time-averaged wind field that is assumed to be confined to a plane surface, nominally parallel to the ground. The planar fit rotations are based on a time interval that is much longer than the flux interval, in our case 24 hours. We only used planar fit rotations around the x - and y -axes. The rotation into the mean horizontal wind, around the z -axis, is done for every flux interval;
- sonic temperature was corrected for the influence of humidity on the speed of sound measurement (Schotanus et al., 1983);
- fluxes were corrected for poor frequency response, i.e. flux loss due to sensor separation and sonic path averaging (Moore, 1986). For H this correction ranges between 15% for very stable conditions and less than 5% towards neutral conditions. For u^* the correction ranges between 7% for the very stable case and some 2% towards neutral conditions.

Vickers and Mahrt (2003) show that for stable conditions, more in particular for the CASES-99 dataset, the cospectral gap time scale of turbulence is surprisingly short, often only a few minutes. In this study we did not use flux-averaging periods that are adjusted to the turbulence encountered. Instead, we chose to take a fixed flux averaging period of 5 minutes and assume

that, on average, this time scale is such that we only include the turbulence contribution to the fluxes and exclude, larger scale, non-turbulence influences, such as gravity waves, drainage flows etc. The study of Vickers and Mahrt (2003) show that a 5-minute averaging period gives less scatter than 30-minute averaged fluxes in scaling relationships. Their gap time scale gives less scatter, however, and is regularly even shorter than 5 minutes.

We evaluated u_* including both the longitudinal and lateral components of the stress, i.e.

$$u_* = \left(\overline{u'w'^2} + \overline{v'w'^2} \right)^{1/4}.$$

4.3.2 Determining C_T^2 and ε from raw time series

C_T^2 is a scaling parameter of the temperature spectrum in the inertial range of turbulence and is defined as (e.g. Stull, 1988):

$$C_T^2 = \frac{D_T}{r^{2/3}} = \frac{\overline{[T(x) - T(x+r)]^2}}{r^{2/3}}, \quad (4.8)$$

where D_T denotes the structure function, $T(x)$ is the temperature at position x , $T(x+r)$ the temperature at position $x+r$, where r should lie within the inertial range of turbulent length scales. We calculated 10-minute C_T^2 values from the 20 Hz sonic data using Taylor's frozen turbulence hypothesis to estimate a time lag that approximates best a space separation, r , of 1 m. We corrected for path averaging of the sonic temperature measurements after Hill (1991). Hartogensis et al. (2002) describe in more detail the C_T^2 calculation and correction procedure followed here.

Like C_T^2 , ε is also a scaling parameter of spectra in the inertial range, in this case of TKE. For the longitudinal wind component, u , the inertial range of the spectrum, S_u , is described by

$$S_u(k) = \alpha \varepsilon^{2/3} k^{-5/3}, \quad (4.9)$$

where S_u is the spectral energy density, α is the Kolmogorov constant, and k is the spatial wave-number expressed in cycles per unit length. We adopted $\alpha = 0.55$, which is mid-range of the values found in the literature (e.g. Höglström, 1996).

To obtain 10-minute values of ε from 20Hz sonic anemometer data the following procedure was followed:

First, the wind vector was rotated with the planar fit routine (Wilczak et al., 2001), and aligned to the mean wind direction, similarly as was done for the eddy-covariance fluxes described in Section 4.3.1.

Second, 10-minute spectra of the longitudinal wind velocity, u , were calculated with the ARMASA toolbox, developed at the University of Delft, the Netherlands (Broersen, 2002 and De Waele et al., 2002). ARMASA determines an optimal auto-regression (AR), moving-average (MA) time series model for a given dataset from which $S_u(\kappa)$ can be determined directly. The principle advantages of spectra determined from ARMA models over conventional Fourier transforms are that the signal is not treated as a windowed periodogram where the first data point is treated as a neighbour of the last data point in the record, and no arbitrary smoothing of the spectrum is needed. ARMASA is written for MATLAB and is freely available at www.tn.tudelft.nl/mmr. We performed our analyses with ε determined with ARMASA and traditional Fourier transforms and found less scatter using ARMASA.

Third, we calculated ε using Equation (4.9) for all points of the spectrum.

Fourth, we performed a quality check on the spectrum and the calculated ε values to determine whether an inertial range was present in the spectrum. Moving point by point through the data, we determined the slope of the spectrum and the root mean square (rms) of ε for blocks of 25 % of all the spectral points. An average ε was determined for all blocks for which the spectral slope deviated less than 20 % of the theoretical $-5/3$ slope, and the rms of ε was less than 30 % of its block-average value. When none of the blocks fulfilled these criteria, the ε value was rejected for that 10-minute period.

Only stable conditions ($\zeta > 0$) between 1900 and 0700 local time are considered in this study. The data were selected on the following criteria: $\zeta > 0.0001$, $\overline{w'T'} < -0.0001 \text{ K m s}^{-1}$, and $u_* > 0.01 \text{ m s}^{-1}$. Data with one of these parameters falling below the given threshold values were excluded from the analysis.

4.4 Results and discussion

Before presenting our results, we want to make a general comment on MOST scaling in the SBL. Under stable conditions the MOST assumption that $(g/T)\overline{w'T'}$, u_* and z are the relevant, independent scaling parameters might be questionable, because $(g/T)\overline{w'T'}$ and u_* are often interrelated, as is illustrated in Figure 4-1.

Under stable conditions, the longwave radiation balance determines the 'strength' of the buoyancy parameter, $(g/T)\overline{w'T'}$. Under clear sky conditions the longwave radiation balance is dominated by the cooling rate at the surface, which, in turn, is strongly affected by wind speed. A high interrelationship between $(g/T)\overline{w'T'}$ and u_* exists therefore under clear sky conditions. Under cloudy conditions, the longwave radiation balance is also influenced by incoming radiation from clouds, and $(g/T)\overline{w'T'}$ and u_* will be more independent. Under these conditions, the stability is expected to be close to neutral.

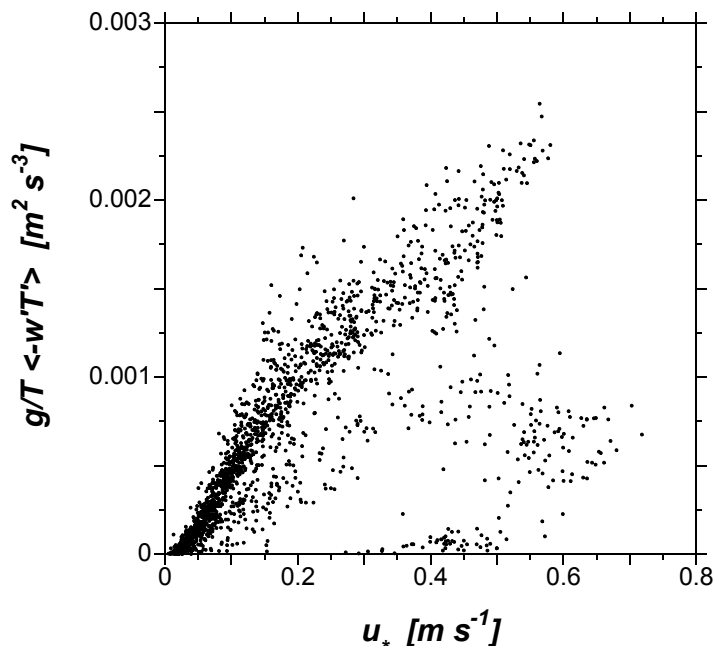


Figure 4-1: Scatter plot of 10-minute eddy-covariance values of the buoyancy parameter, $(g/T)\overline{w'T'}$ against the friction velocity, u_* .

4.4.1 Scaling functions for ε

Figure 4-2 shows our data of the ε dimensionless group, the f_ε scaling functions given by Equations (4.5a) to (4.5d), and two f_ε curves that give a good fit to our data, namely

$$f_\varepsilon = 0.8 + 2.5\zeta, \quad (4.10a)$$

which is the Wyngaard (1973) form (Equation 4.5d) with adjusted parameters $c_{\varepsilon 1}$ and $c_{\varepsilon 2}$, and a 'kink' function

$$f_\varepsilon = \begin{cases} 0.8 + 2\zeta & \text{for } \zeta < 0.1 \\ \sqrt{\zeta/0.1} & \text{otherwise} \end{cases}. \quad (4.10b)$$

Equations (4.10a) and (4.10b) are eye-fitted. In the limit $\zeta \rightarrow \infty$ the formulations of Equations (4.10a) and (4.10b) differ. First, ε becomes independent of z in Equation (4.10a) (Pahlow et al, 2001), whereas in Equation (4.10b) ε remains a function of z . Second, as we will see later, the two formulations lead to different flux Richardson numbers.

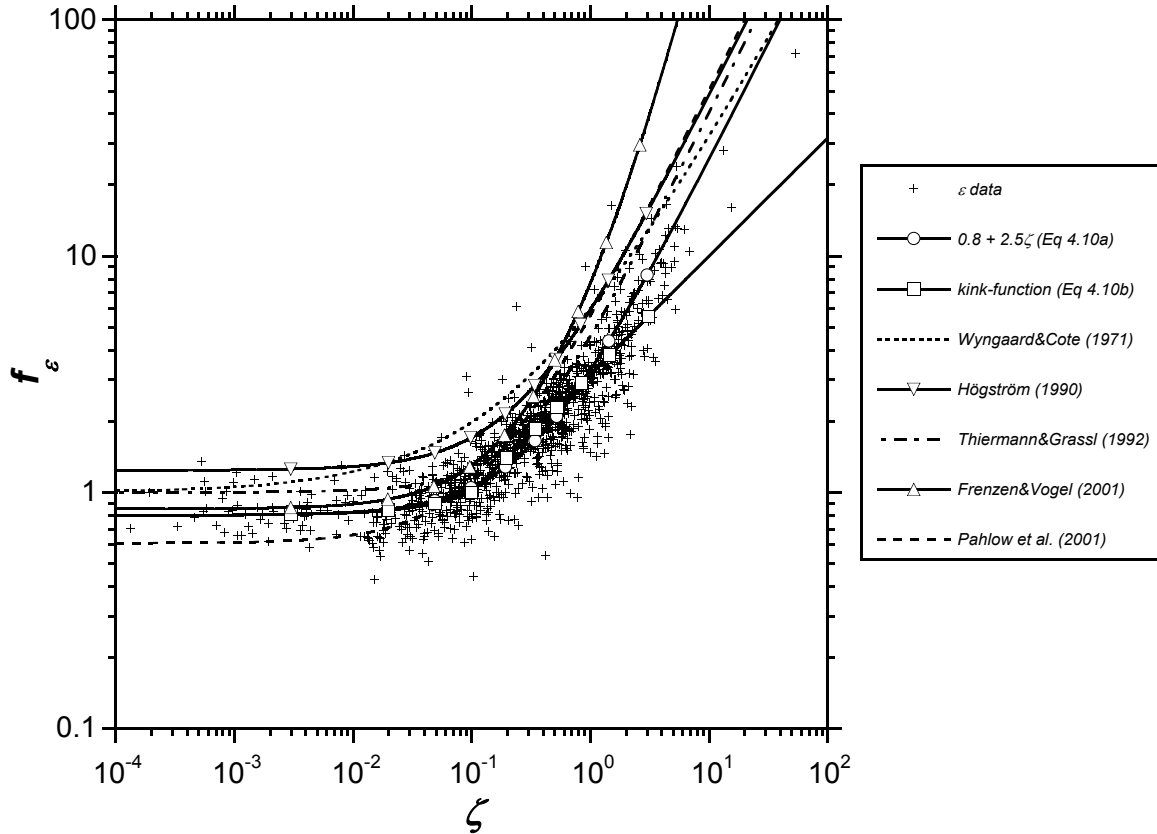


Figure 4-2: Dimensionless scaling group $f_\varepsilon = \kappa z \varepsilon / u_*^3$ of the TKE dissipation rate, ε , against the dimensionless stability parameter, ζ , for 10-minute experimental values and relations found in literature.

For *near-neutral conditions*, we find that f_ε is less than 1, which implies there is an imbalance between TKE production and dissipation as was also reported by Frenzen and Vogel (1992 and 2001), and Pahlow et al. (2001). Our f_ε neutral limit, $f_\varepsilon(0) = \sim 0.8$ corresponds to the findings of Frenzen and Vogel (1992 and 2001). Pahlow et al. (2001) found $f_\varepsilon(0) = 0.61$. Wyngaard et al. (1971) and Thiermann and Grassl (1992) imposed a production-dissipation balance in the TKE budget, their neutral limit of f_ε is therefore 1. Högström (1990) reported $f_\varepsilon(0)$ to be larger than 1, they found $f_\varepsilon(0) = 1.24$. When systematic measuring errors are assumed small, the imbalance between TKE production and dissipation found here implies that the pressure and flux-divergence terms in the TKE budget are not negligible. Högström (1996) suggests that the imbalance is most significant under near-neutral conditions where so-called inactive turbulence is important. Unfortunately, the pressure and flux-divergence terms of the TKE budget are very difficult to measure. Recently, Cuxart et al. (2002) presented data of the full TKE budget for one CASES-99 night, and found that for that night the pressure and flux divergence terms were indeed significant.

For *stable to very stable conditions*, we find that our f_ε values are lower than all other reported scaling functions.

There are several issues that play a role in the found differences between our scaling functions and the ones reported in the literature so far.

First, the Kolmogorov constant, α , which we chose as $\alpha = 0.55$ in obtaining ε from the u spectra. Högström (1996) and Frenzen and Vogel (2001) give extensive discussions on this constant. The different values that have been reported in the literature roughly vary between 0.5 and 0.6. The uncertainty in the Kolmogorov constant gives, relative to the $\alpha = 0.55$ we used, an approximate 10% uncertainty in ε . Note that the approach of Pahlow (2001) in determining ε is parameter free but might be more sensitive to measuring errors since they use third order differences. The much lower $f_\alpha(0) = 0.61$ they found compared to our $f_\alpha(0) = 0.8$, cannot be explained by our choice of α . To obtain $f_\alpha(0) = 0.61$ from our data, we would have to use an α outside the range reported in the literature.

Second, since our aim is to find scaling relations for turbulent transport of momentum and heat, we tried to limit the influence of non-turbulent, non-local and non-stationary processes, such as drainage flows and gravity waves by choosing a short, 5-minute time interval for our flux calculations and we ignored data points for which the u spectrum did not have a clear inertial sub-range (see Section 4.3.2). The study of Vickers and Mahrt (2003) shows that longer averaging periods, e.g. the standard 30-minute period used by many investigators, give larger fluxes, but this is mainly attributed to non-turbulent contributions to the flux.

Third, our f_ε is based on a dataset that has a much larger ζ range than most other functions reported in the literature. This might explain that, apart from the neutral limit behaviour, f_ε from Thiermann and Grassl (1992), Frenzen and Vogel (2001) and Pahlow et al. (2001) are similar to our f_ε for $\zeta < \sim 0.5$, but start to deviate for $\zeta > \sim 0.5$.

We evaluated u_* using the planar fit method to rotate the sonic into the mean wind field and including the lateral stress term $\overline{v'w'}$. Instigated by one of the referees we investigated whether another choice of evaluating u_* would make our results for f_ε more similar to what others have reported in the literature. Alternative rotation techniques we used were the double rotation method (which for each flux interval performs a rotation around the y - and z -axis of the sonic's coordinate system such that the average vertical and lateral wind components, \overline{w} and \overline{v} , are zero) and the triple rotation method (which in addition to the double rotation method also performs a rotation around the x -axis such that the lateral stress, $\overline{v'w'}$, is zero). For the three rotation methods we evaluated u_* including and excluding the lateral stress. Note that for the triple rotation including or excluding the lateral stress makes no difference, since it is forced to zero. From this exercise the following can be concluded. The contribution of the lateral stress to the total u_* is only important when u_* is small ($< 0.1 \text{ m s}^{-1}$) and ζ is large (> 0.8). Then, $\overline{v'w'}$ can contribute up to 80% of the total stress in some cases, whereas for larger u_* ($> 0.1 \text{ m s}^{-1}$) and small ζ (< 0.8), the lateral stress contribution is less than 3%. Comparing u_* including the lateral stress for different rotation methods does not give large differences. The planar fit u_* gives marginally higher values, especially for low u_* , compared with the triple rotation method, and very similar values compared with the double rotation method. The differences found for the various evaluations of u_* have very little effect on the found f_ε functions. The lower u_* values obtained when excluding the lateral stress extend the f_ε data points to higher ζ values, but they follow our f_ε -fit curve. This is due to the fact that both ε

and ζ are scaled with u_*^{-3} , by which 'errors' in u_* appear to cancel when evaluating f_ε as function of ζ . This feature is further discussed in Section 4.4.3.

Next, we want to evaluate the ϕ_m scaling group from ε data using Equations (4.1) and (4.3). Equation (4.3) uses the local dissipation assumption, which, as discussed above, is violated for our dataset. We accounted for the TKE production-dissipation imbalance arbitrarily by dividing f_ε with its value in the neutral limit, i.e. we used

$$\phi_m = f_\varepsilon / f_{\varepsilon_cor} + \zeta, \quad (4.11)$$

with $f_{\varepsilon_cor} = f_\varepsilon(0) = 0.8$. Note, that by scaling f_ε with its neutral value we ignore how the imbalance of TKE production and dissipation, i.e. the transport terms, may vary with stability.

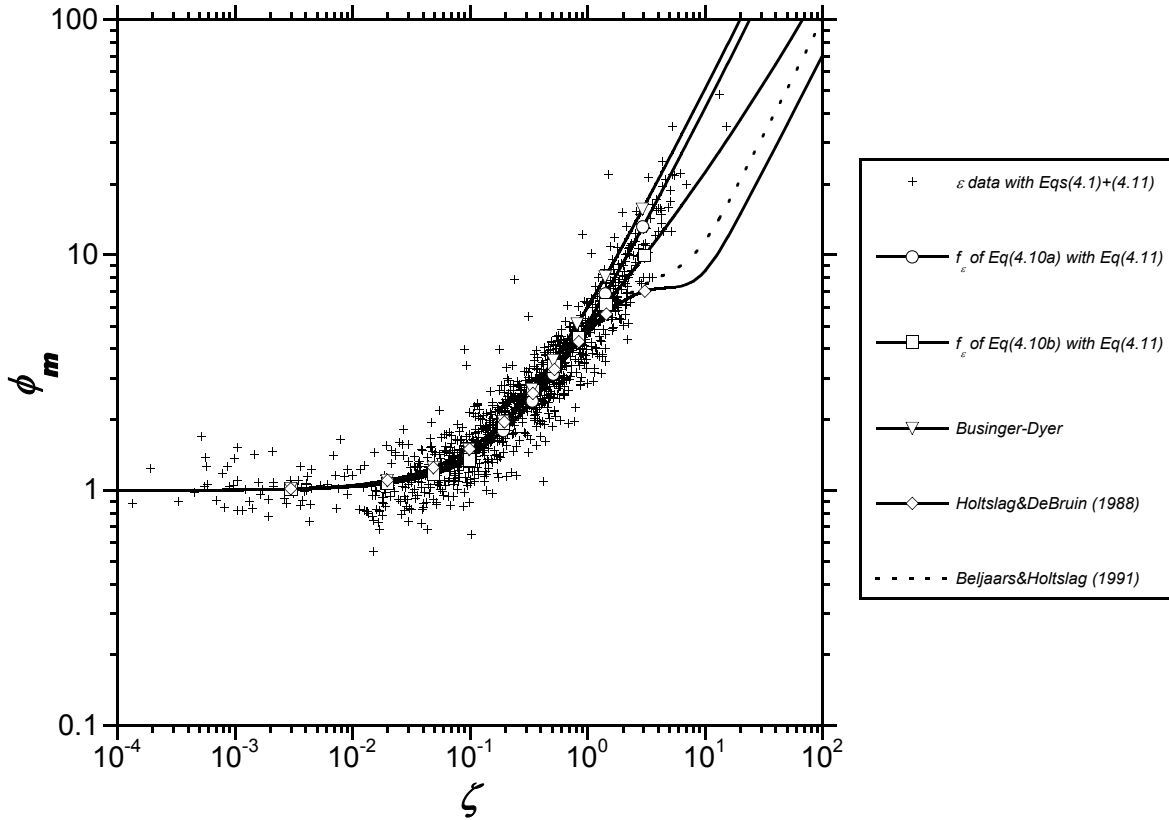


Figure 4-3: Dimensionless scaling group $\phi_m = (\kappa z / u_*) \partial u / \partial z$ of the horizontal wind speed (u) gradient against the dimensionless stability parameter, ζ , for 10-minute experimental values based on $f_\varepsilon = \kappa z \varepsilon / u_*^3$ using Equation (4.11), the f_ε relations of Equation (4.10) using Equation (4.11), and ϕ_m relations found in the literature.

Figure 4-3 shows the comparison between the ϕ_m scaling group derived from ε data using Equations (4.1) and (4.11), the ϕ_m scaling functions derived from our f_ε expression of Equations (4.10a) and (4.10b) with Equation (4.11) and three ϕ_m functions found in the literature.

Now we will consider the ratio of the buoyancy destruction and the shear-production term, which is the definition of the flux Richardson number, R_f . R_f should approach a constant value smaller than 1 for very stable conditions where all turbulent motions are suppressed by buoyancy. Using the same imbalance correction described above for ϕ_m , we calculated R_f from our f_ε data and scaling functions using

$$R_f = \frac{\zeta}{\phi_m} = \frac{\zeta}{f_\varepsilon / f_{\varepsilon_cor} + \zeta}. \quad (4.12)$$

In Figure 4-4, we plotted R_f for the same ε data, and f_ε and ϕ_m scaling functions as in Figure 4-3. For $\zeta < 1$, Figure 4-3 and Figure 4-4 show good agreement between ϕ_m and R_f from our adjusted f_ε functions and derived values from ε data, and the ϕ_m and corresponding R_f functions found in the literature. In the neutral limit, say $\zeta < 0.1$, this agreement is forced by the correction we applied on our f_ε functions and data.

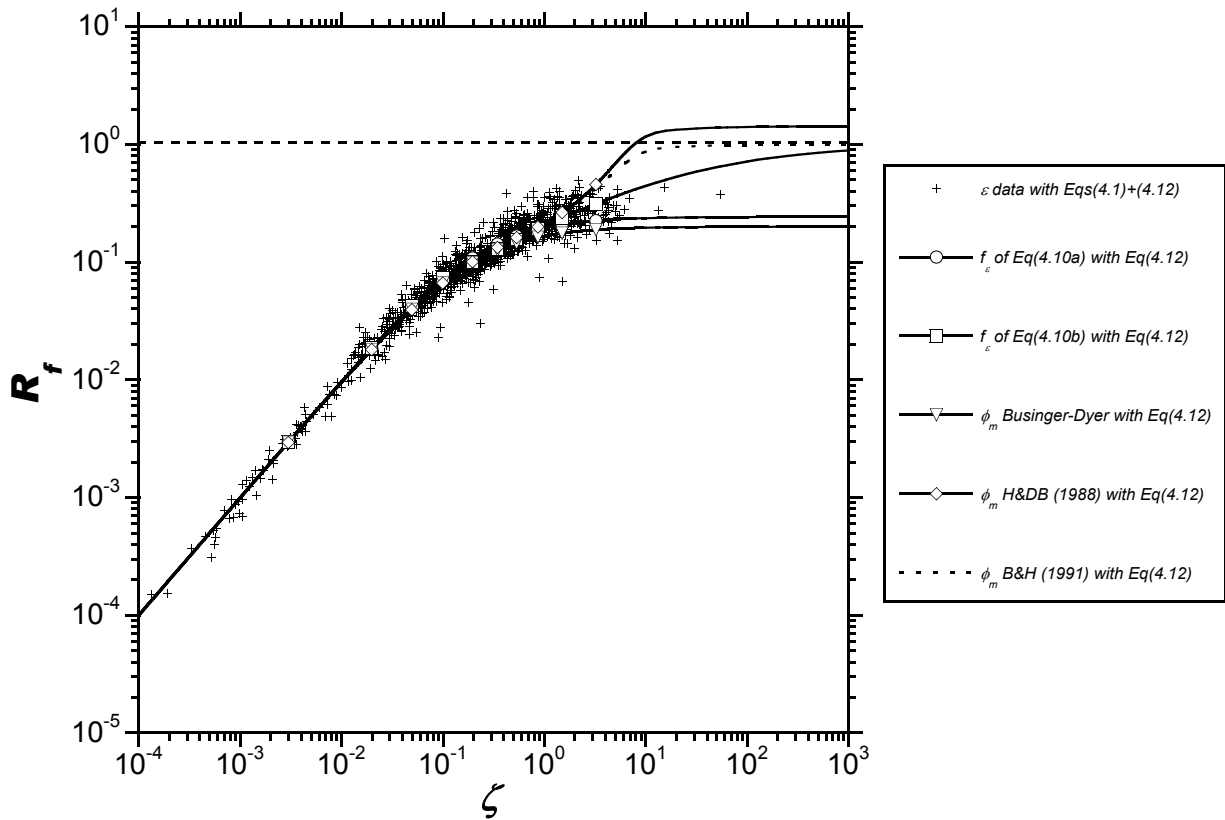


Figure 4-4: Flux Richardson number, R_f , against the dimensionless stability parameter, ζ , for 10-minute experimental values based on $f_\varepsilon = \kappa z \varepsilon / u_*^3$, the f_ε relations of Equation (4.10), and $\phi_m = (\kappa z / u_*) \partial u / \partial z$ relations found in the literature (see Equation 4.12). H&DB (1988) and B&H (1991) are abbreviations of Holtslag&DeBruin (1988) and Beljaars&Holtslag (1991).

For $\zeta > 1$, the different ϕ_m curves and related R_f curves start to deviate. Figure 4-3 shows that from the ϕ_m functions found in the literature the Businger-Dyer relation (Equation 4.7a)

agrees best with the derived values from our ε data. Furthermore, from the ϕ_m groups based on our f_ε functions, f_ε of Equation (4.10a) gives a slightly better fit than f_ε of Equation (4.10b). Figure 4-4, on the other hand, shows that in the stable limit, both the Businger-Dyer relation and the relation based on f_ε of Equation (4.10a) are well below 1. The R_f values from Beljaars and Holtslag (1991) ϕ_m function and our f_ε of Equation (4.10b) do approach the R_f limit of 1 for very stable conditions. The R_f of Holtslag and De Bruin (1988) goes to 1.4 in the very stable limit, which is a physically impossible value. Note that the data extend to $\zeta = \sim 10$, where it does not yet reach the R_f limit of 1.

4.4.2 Scaling functions for C_T^2

Figure 4-5 shows our data of the C_T^2 dimensionless group, the f_T scaling functions given by Equations (4.6a) and (4.6b), and two f_T curves that give a good fit to our data, namely

$$f_T = 4.7[1 + 1.6\zeta^{2/3}], \quad (4.13a)$$

which is the function proposed by Wyngaard et al. (1971) given in Equation (4.6a) with different values for the constants c_{T1} and c_{T2} , and a 'kink' function

$$f_T = \begin{cases} 5.5 & \text{for } \zeta < 0.1 \\ 5.5(\zeta / 0.1)^{2/5} & \text{otherwise} \end{cases}. \quad (4.13b)$$

Equations (4.13a) and (4.13b) are eye-fitted. It is seen that the scatter of the $f_T(\zeta)$ scaling group is much larger than the scatter of the $f_\varepsilon(\zeta)$ scaling group (Figure 4-2). In part this is explained by the difference errors propagate in u^* and H for the f_T - ζ data pair compared to f_ε - ζ . This is further explained in Section 4.4.3. The uncertainty in f_T makes it difficult to discuss the differences between our f_T functions and the ones reported in the literature. As for f_ε , the chosen, short averaging period may affect f_T for $\zeta > \sim 0.1$. We did not investigate the effect of inclusion or exclusion of the lateral stress in u^* on Figure 4-5 as we did for Figure 4-2. If this plays a role it is for high ζ , where we already see a lot of scatter.

The f_T function of Thiermann and Grassl (1992) gives higher values than our observations. This suggests a production-dissipation imbalance of the T-variance budget in our data, since Thiermann and Grassl (1992) imposed a production-dissipation balanced budget.

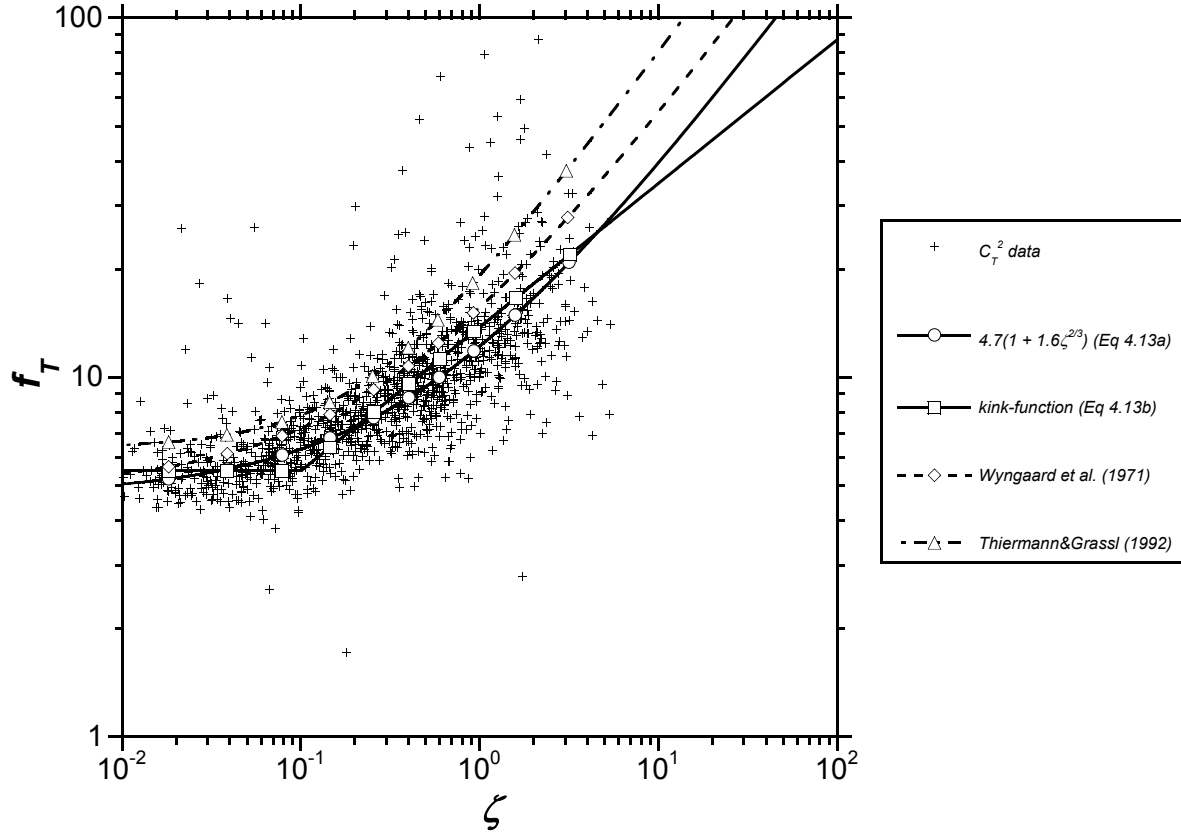


Figure 4-5: Dimensionless scaling group $f_T = C_T^2 z^{2/3} / \theta_*^2$ of the structure parameter of temperature, C_T^2 , against the dimensionless stability parameter, ζ , for 10-minute experimental values and relations found in the literature.

In evaluating the ϕ_h scaling group from C_T^2 and ε data using Equations (4.1), (4.2) and (4.4) we use the local dissipation assumption for the T-variance budget, which, as discussed above, is violated for our dataset. Equivalent to Equation (4.11) we therefore impose budget closure by dividing f_T with a constant value defined by its neutral limit value,

$$\phi_h = \frac{\kappa^{2/3}}{3} \left(f_\varepsilon / f_{\varepsilon_cor} \right)^{1/3} \left(f_T / f_{T_cor} \right), \quad (4.14)$$

with $f_{T_cor} = (\kappa^{2/3} / 3) f_T(0)$ this gives $f_{T_cor} = 0.85$ for f_T of Equation (4.13a) and $f_{T_cor} = 0.99$ for f_T of Equation (4.13b). For the ϕ_h group from data we use $f_{T_cor} = 0.9$.

Analogous to Figure 4-3, Figure 4-6 compares the ϕ_h scaling group derived from C_T^2 and ε data using Equations (4.1), (4.2) and (4.14), the ϕ_h scaling functions derived from our f_T expression of Equations (4.13a) and (4.13b) with Equation (4.14), and three ϕ_h functions found literature.

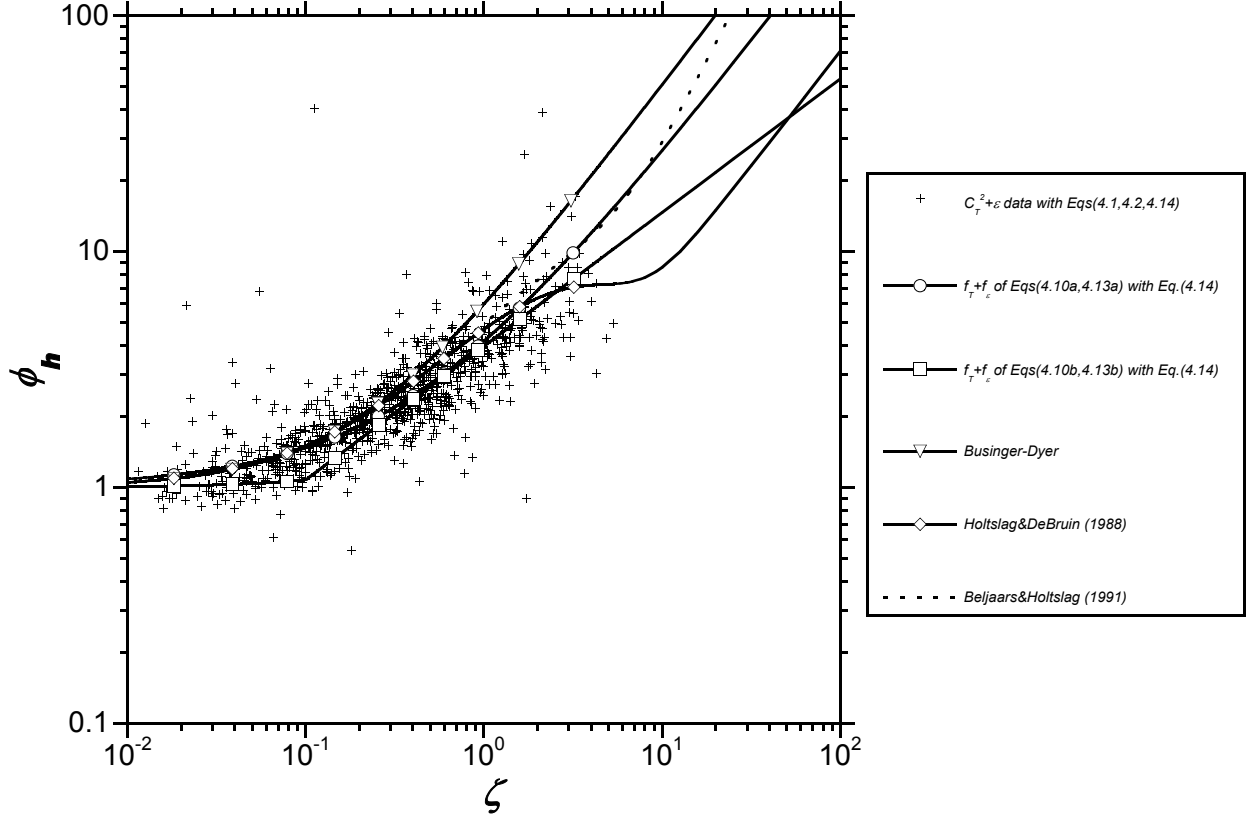


Figure 4-6: Dimensionless scaling group $\phi_h = (\kappa z / \theta_*) \partial \theta / \partial z$ of the potential temperature (θ) gradient against the dimensionless stability parameter, ζ , for 10-minute experimental values based on $f_\varepsilon = \kappa z \varepsilon / u_*^3$ and $f_T = C_T^2 z^{2/3} / \theta_*^2$ using Equation (4.14), the f_ε and f_T relations of Equations (4.10) and (4.13) using Equation (4.14), and ϕ_h relations found in the literature.

Next, using Equations (4.11) and (4.14), the gradient Richardson number can be expressed as

$$Ri = \frac{\phi_h}{\phi_m^2} \zeta = \frac{\kappa^{2/3}}{3} \frac{(f_T / f_{T_cor})(f_\varepsilon / f_{\varepsilon_cor})^{1/3}}{(f_\varepsilon / f_{\varepsilon_cor} + \zeta)^2}. \quad (4.15)$$

In Figure 4-7, we plotted Ri for the same C_T^2 and ε data, and f_ε, f_T and ϕ_m, ϕ_h scaling functions as in Figure 4-3 and Figure 4-6.

For $\zeta < 1$, Figure 4-6 and Figure 4-7 show good agreement between ϕ_h and Ri from our adjusted f_ε and f_T functions and derived values from C_T^2 and ε data, and the ϕ_m, ϕ_h and corresponding Ri functions found in the literature. In the neutral limit, for $\zeta < 0.1$, this agreement is forced by the correction we applied on our f_ε and f_T functions and data.

For $\zeta > 1$, the different ϕ_h curves and related Ri curves start to deviate. Figure 4-6 shows that from the ϕ_h functions found in the literature, the Beljaars-Holtslag relation (Equation 4.7c2) agrees best with the values derived from our C_T^2 and ε data. Furthermore, from the ϕ_h groups based on our f_ε and f_T functions, the $f_\varepsilon - f_T$ of Equations (4.10a) and (4.13a) give a better fit than $f_\varepsilon - f_T$ of Equations (4.10b) and (4.13b).

Recently, Pahlow et al. (2001) determined the dissipation rate of temperature fluctuations, ε_θ , which is related to C_T^2 through $C_T^2 = 2\varepsilon_\theta \varepsilon^{-1/3}$ (Panofsky and Dutton, 1984). They found that $\phi_{\varepsilon\theta}$, which is ε_θ made dimensionless with $\kappa z u_* / (\overline{w'T'})^2$, is about constant for $\zeta > 0.01$. In the case of a balanced temperature fluctuation budget, $\phi_{\varepsilon\theta}$ and ϕ_h are equal. Our ϕ_h data group based on $f_\varepsilon - f_T$ formulations, which were forced to give TKE and temperature fluctuation budget closure in the neutral limit, is not constant for $\zeta > 0.01$.

Figure 4-7 shows that Ri seems to level off for $\zeta \rightarrow \infty$ to a limit just below the value often used for the critical Richardson number, $Ri_c = 0.25$. The Ri values based on Beljaars and Holtslag (1991) and our $f_\varepsilon - f_T$ functions of Equations (4.10b) and (4.13b) do not go to a stable limit value.

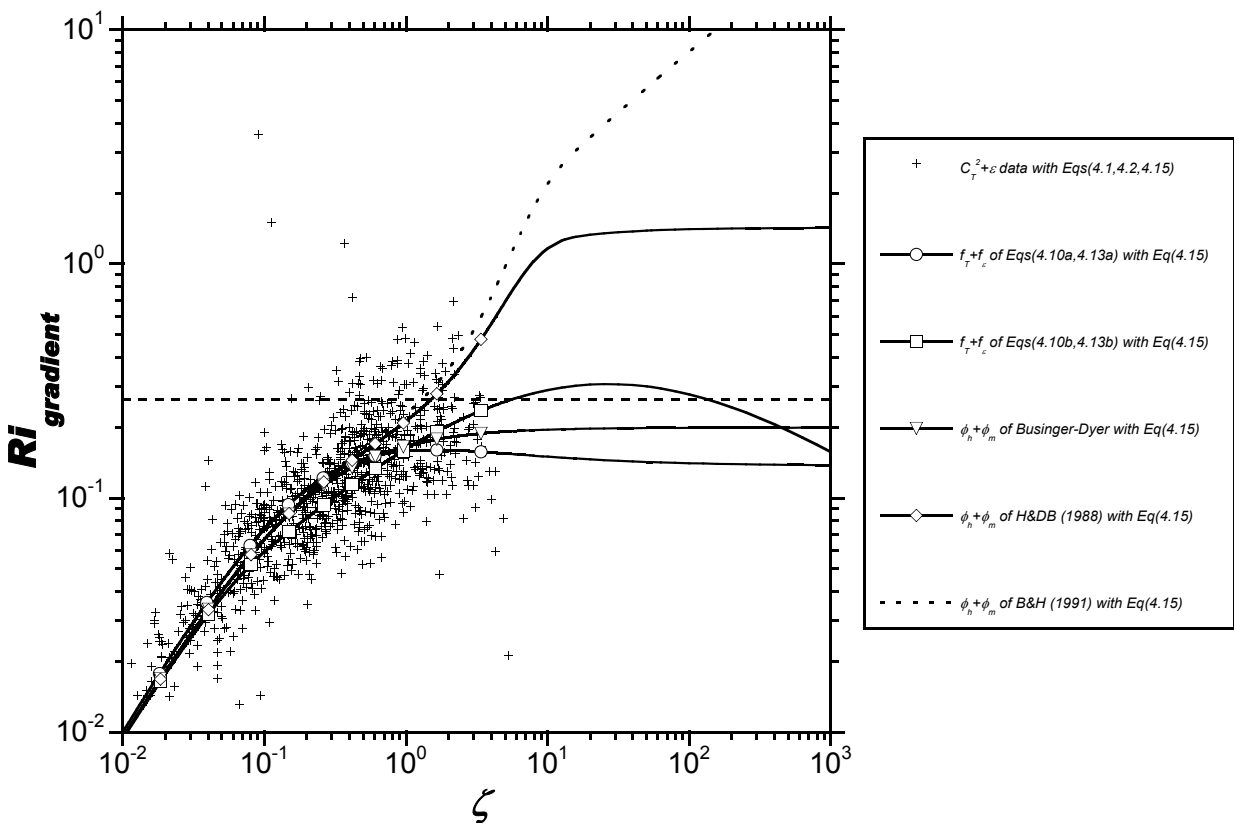


Figure 4-7: Gradient Richardson number, Ri , against the dimensionless stability parameter, ζ , for 10-minute experimental values based on $f_\varepsilon = \kappa z \varepsilon / u_*^3$ and $f_T = C_T^2 z^{2/3} / \theta_*^2$, the f_ε and f_T relations of Equations (4.10) and (4.13), and $\phi_m = (\kappa z / u_*) \partial u / \partial z$ and $\phi_h = (\kappa z / \theta_*) \partial \theta / \partial z$ relations found in the literature (see Equation 4.15). H&DB (1988) = and B&H (1991) are abbreviations of Holtslag&DeBruin (1988) and Beljaars&Holtslag (1991).

Our application of deriving ϕ_m and ϕ_h functions from single level ε and C_T^2 data might be a suitable alternative to ϕ_m and ϕ_h estimation from $\partial \bar{u} / \partial z$ and $\partial \bar{\theta} / \partial z$ for very stable conditions. Firstly, in these conditions gradients are difficult to determine accurately from discrete profile measurements. Secondly, the stable boundary layer can be very shallow by

which the constant flux approximation can be violated. The strong point of our approach is that we use single level data only. Obviously, the weak point is that we have to rely on the assumption that f_ε and f_T both scaled with their neutral value accounts for the non-closure of the TKE and T-variance budgets for the entire stability range. Our simple approach to correct for non-closure of the simplified TKE and T-variance budgets does yield good results; i.e. the derived ϕ_m and ϕ_h functions, and Richardson numbers evaluated in this way behave very similar to the functions found in the literature. Moreover, we were able to investigate ϕ_m and ϕ_h functions, and Richardson numbers for very stable conditions ($\zeta > 10$). In this study we used sonic measurements close to the surface, $z = 2.65$ m, and we already reach $\zeta = \sim 10$. By doing the same analyses for sonics installed at higher levels, we should be able to extend the ζ range substantially.

4.4.3 Spurious correlations

Spurious correlations cannot be avoided when using MOST scaling (e.g. Hicks, 1981; De Bruin et al., 1993), since θ^* and u^* are present on both x - and y -axis of the scaling plots; on the y -axis to make variables dimensionless and on the x -axis because θ^* and u^* define the Monin-Obukhov length. To test the scaling functions independently, without spurious correlation, we compared C_T^2 and ε , calculated indirectly from the eddy-covariance θ^* and u^* using the MOST relations given in Equations (4.10) and (4.13), with C_T^2 and ε determined from the raw data as described in Section 4.3.2. These two methods to obtain C_T^2 and ε are independent. The results depicted in Figure 4-8 show that C_T^2 and ε agree well, and the scatter is comparable to that of the scaling plots of Figure 4-2 and Figure 4-5. This demonstrates that no significant, additional scatter is introduced due to the removal of the spurious correlation, and the effect of spurious correlation can therefore considered to be small.

One of the referees questioned whether the scatter seen in Figure 4-8a contains a hidden correlation with ζ . To demonstrate that this is not the case we plotted the percentage difference between the two independently derived ε values from Figure 4-8a as a function of ζ (not shown here). No systematic behaviour was found, which implies that the scatter seen in Figure 4-8a is indeed random. In addition, we carried out an exercise similar to that presented by Hicks (1981); i.e. we plotted the f_ε scaling group for measured u^* and ζ with random values of ε . If spurious correlation between f_ε and ζ dominates the function found then it is expected that the relation between the two is independent of ε . The measured ε values lie in a range between 10^{-3} and $10^{-1} \text{ m}^2 \text{ s}^{-3}$. A random generator was used to produce the 10-exponent values for ε between -1 and -3 . In a plot similar to Figure 4-2 (not shown here), the f_ε data points with random ε do not follow the fitted f_ε function of Equation (4.10a), which demonstrates that the measured ε values determine the found f_ε function and not the shared u_*^{-3} term on the x - and y -axes.

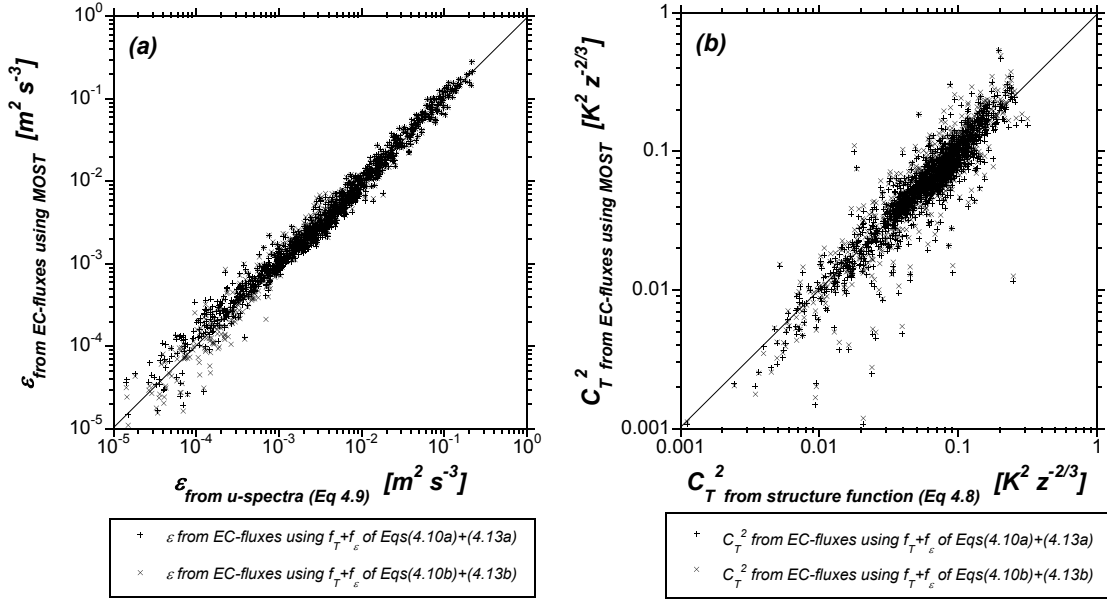


Figure 4-8: Comparison for the TKE dissipation rate, ε (a), and the structure parameter of temperature, C_T^2 (b) between values obtained from eddy-covariance fluxes using MOST and independent methods obtaining ε and C_T^2 from raw time series data.

Although spurious correlation does not seem to determine the shape of the $f_\varepsilon - \zeta$ relation, it does affect the scatter found in the $f_\varepsilon - \zeta$ and $f_T - \zeta$ plots. Andreas and Hicks (2002) show how errors in u^* affect the scatter in ϕ_m and ϕ_h against ζ plots. Johansson et al. (2002) replied to this by stating that also the effect of errors in θ^* should be included. We performed such an analysis for $f_\varepsilon - \zeta$ and $f_T - \zeta$ plots, which shows that errors in u^* lead to a displaced $f_\varepsilon - \zeta$ pair that moves along the fitting curve, while a $f_T - \zeta$ pair moves normal to it. In other words, because of spurious correlation, errors in u^* result in enhanced scatter in f_T , and reduced scatter for f_ε . Errors in H only affect ζ in the $f_\varepsilon - \zeta$ plot, resulting in scatter along ζ axis. For f_T , errors in H result in a $f_T - \zeta$ pair that moves normal to the fitting curve, i.e. more scatter. In reality, the combined effect of errors in u^* and H on f_ε and f_T is more complex. Depending on the sign and size of the H and u^* errors, their individual effect on $f_\varepsilon - \zeta$ and $f_T - \zeta$ described above can either partly cancel out or enhance each other. If the errors in u^* and H are dependent these effects are systematic. In the absence of quantitative error-estimates of u^* and H we conclude, based on the discussion here and the scatter found in Figure 4-2 and Figure 4-5, that the low scatter found for f_ε and high scatter found for f_T is due to spurious correlation.

4.4.4 Direct flux estimates from ε and C_T^2

We recall that our main motivation for this study was to find suitable MOST functions for C_T^2 and ε to obtain fluxes of heat and momentum using scintillometer measurements of C_T^2 and ε .

Calculating these fluxes requires a numerical iteration of the f_ε and f_T functions. To be able to calculate the fluxes directly, without iteration, we introduce the dimensionless length scale, Z , derived from C_T^2 and ε .

$$Z = \frac{g\kappa z}{T} \frac{T_C}{U_\varepsilon^2}, \quad (4.16)$$

in which $T_C = \sqrt{C_T^2 z^{2/3}}$ and $U_\varepsilon = \sqrt[3]{\kappa z \varepsilon}$ are a temperature and a wind speed scale.

Next, we searched for a relationship between Z and ζ and found the best fit for $\zeta = 0.55Z^{1.15}$. By substituting this empirical expression in the f_ε and f_T functions, one can directly calculate θ_* and u_* , and from these the kinematic sensible heat flux, $\overline{w'T'} = u_*\theta_*$.

Figure 4-9 compares u_* and $\overline{w'T'}$ calculated from ε and C_T^2 with this simplified approach against u_* and $\overline{w'T'}$ from ε and C_T^2 calculated by means of iteration. For both approaches the f_ε and f_T functions of Equations (4.10a) and (4.13a) are used. It is seen that the simplified approach can be used with little error.

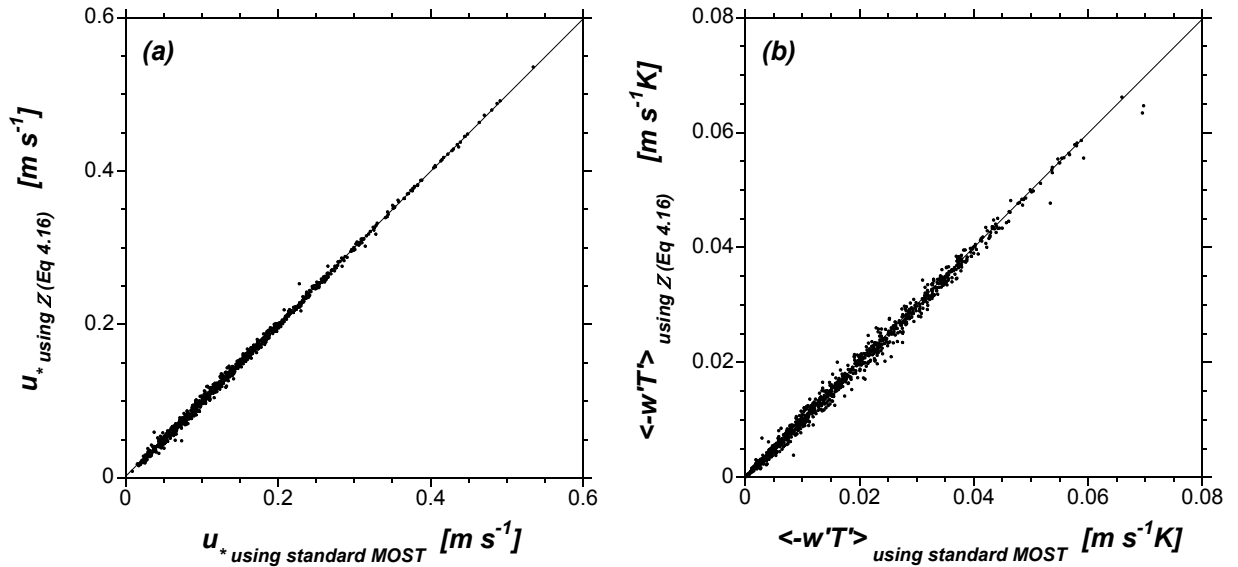


Figure 4-9: Comparison for the friction velocity, u_* (a) and kinematic heat flux, $-\overline{w'T'}$ (b) determined from the TKE dissipation rate, ε , and structure parameter of temperature, C_T^2 , calculated directly with the alternative dimensionless height parameter, Z , of Equation (4.16), against the values calculated by means of numerical iteration of the MOST relationships given by Equations (4.10a) and (4.13a).

4.4.5 Fluxes from ε and C_T^2 in intermittent turbulent conditions

A typical characteristic of turbulence in the SBL is that it is often intermittent, i.e. periods of laminar flow alternate with turbulent bursts. Hartogensis et al. (2002) showed an intermittent

case during CASES-99, where a displaced-beam scintillometer was able to, at least qualitatively, measure the fluxes at a short enough time scale to resolve this phenomenon in great detail. In Figure 4-10 we compare for that same night of 4 to 5 October u_* and $\overline{w'T'}$ calculated from ε and C_T^2 using the f_ε and f_T functions of Equations (4.10a) and (4.13a) with the eddy-covariance u_* and $\overline{w'T'}$.

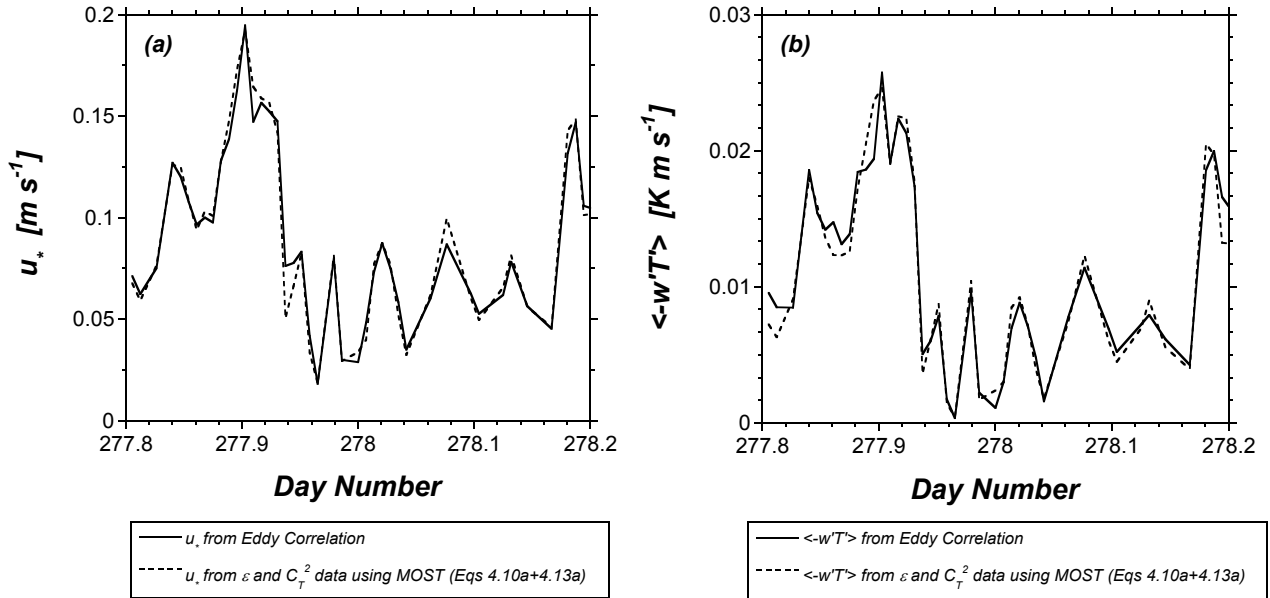


Figure 4-10: The friction velocity, u_* (a) and kinematic heat flux, $-\overline{w'T'}$ (b) determined from the TKE dissipation rate, ε , and structure parameter of temperature, C_T^2 , using MOST and from eddy-covariance as a function of time for the 'intermittent' night of 4 to 5 October.

It is seen that the ε and C_T^2 scaling performs well under these circumstances. De Bruin and Hartogensis (2005) show the same plot for the scaling of the standard deviation of temperature and longitudinal component of the wind speed, σ_T and σ_u , i.e. the variance method, which give less good results than the ε and C_T^2 scaling.

4.5 Conclusions

In this study we analysed the MOST scaling functions f_ε and f_T of the dissipation rate of TKE, ε , and the structure parameter of temperature, C_T^2 , for the stable atmospheric surface layer using data we gathered in the context of CASES-99 (Poulos et al., 2002). These data cover a relatively wide stability range, i.e. ζ up to ~ 10 .

We found that $f_\varepsilon = 0.8 + 2.5\zeta$ and $f_T = 4.7(1 + 1.6\zeta^{2/3})$ gave a good fit with our data. The alternative 'kink' functions, $f_\varepsilon = 0.8 + 2\zeta$ and $f_T = 5.5$ for $\zeta < 0.1$, and $f_\varepsilon = \sqrt{\zeta/0.1}$ and $f_T = 5.5(\zeta/0.1)^{2/5}$ for $\zeta > 0.1$ gave a good fit as well. Our results differ somewhat from those

obtained by others such as Wyngaard and Coté (1971), Wyngaard (1973), Frenzen and Vogel (1992, 2001), Thiermann and Grassl (1992) and Pahlow et al. (2001). This might be related to a different data treatment - we used a short flux-averaging interval to exclude non-turbulent contributions to the flux (Vickers and Mahrt, 2003), and filtered our data based on inertial range behaviour in the longitudinal wind speed, and the fact that our ζ range was much larger than that available elsewhere.

Spurious correlation does not determine the shape of the f_ε function, but does affect the scatter seen in the f_ε - ζ and f_T - ζ plots. The propagation of errors in u_* and H leads to enhanced scatter in the f_T - ζ data pair and reduced scatter in the f_ε - ζ data pair because of spurious correlation.

In determining ε from the raw time series, we found that the ARMASA toolbox developed at the University of Delft (Boersen, 2002) is very suitable to obtain spectra from atmospheric turbulence time series. This approach has several advantages over the traditional Fourier transform method.

Since $f_\varepsilon(0)$ is found to be about 0.8 there is no balance between the production and dissipation terms in the TKE budget equation. Also, our results suggest a production-dissipation imbalance in the temperature-variance budget equation. Others have reported this as well.

Accounting for these imbalances using simple correction factors, we derived alternative expressions for the 'standard' MOST functions for dimensionless wind speed and temperature gradients, ϕ_m and ϕ_h from f_ε and f_T through the simplified budget equations for TKE and T-variance. These compare well with the formulations proposed by Beljaars and Holtslag (1991). Note that our data cover a much wider stability range than most datasets using measured $\overline{\partial u / \partial z}$ and $\overline{\partial \theta / \partial z}$ to determine ϕ_m and ϕ_h . For instance, the Kansas dataset from which Businger et al. (1971) determined their ϕ_m and ϕ_h functions refer to $\zeta < 0.5$. Our results show that using ε and C_T^2 obtained from a single level sonic anemometer to derive ϕ_m and ϕ_h for very stable conditions is a good alternative, since, in that stability region, the measurement errors of gradients, especially $\overline{\partial u / \partial z}$, are large.

Our dataset did not allow us to study the very stable limit value of the flux-Richardson number, R_f , and the gradient Richardson number, Ri ; i.e. no limit values were reached for $\zeta = \sim 10$. R_f derived from f_ε through the TKE budget equation approaches 0.3 for our continuous f_ε function (similar to ϕ_m of Businger-Dyer), whereas our "kink" f_ε function approaches the expected limit of 1 (similar to ϕ_m of Beljaars-Holtslag, 1991). Ri derived from f_ε and f_T through the budget equations for TKE and T-variance approaches a limit just below the value often used for the critical Richardson number, i.e. $Ri_c = 0.25$, for our continuous f_ε and f_T functions, whereas it does not exhibit a limit behaviour for our "kink" f_ε and f_T functions. This issue needs further research, i.e. the analyses need to be repeated for a wider ζ range.

For intermittent conditions, we found f_ε and f_T functions to perform very well in the estimation of u_* and $\overline{w'T'}$ from ε and C_T^2 measurements.

Acknowledgements

We thank Job Kramer and Bas Van de Wiel who helped with the fieldwork during the CASES-99 experiment. The help of Steve Oncley and Gordon Maclean of NCAR during CASES-99 in offering technical support and use of the NCAR facilities on site is acknowledged. The first author received a NWO grant (nr. 810.33.005).

Appendix 4A MOST functions applied for DBSAS in CASES-99

In this Appendix we will apply the MOST functions of ε and C_T^2 (f_ε and f_T) introduced in this chapter to the displaced-beam small-aperture scintillometer (DBSAS) data taken during CASES-99 and compare the resulting fluxes of momentum (expressed as the friction velocity, u_*) and sensible heat, H with eddy covariance (EC) fluxes in Figure 4-11.

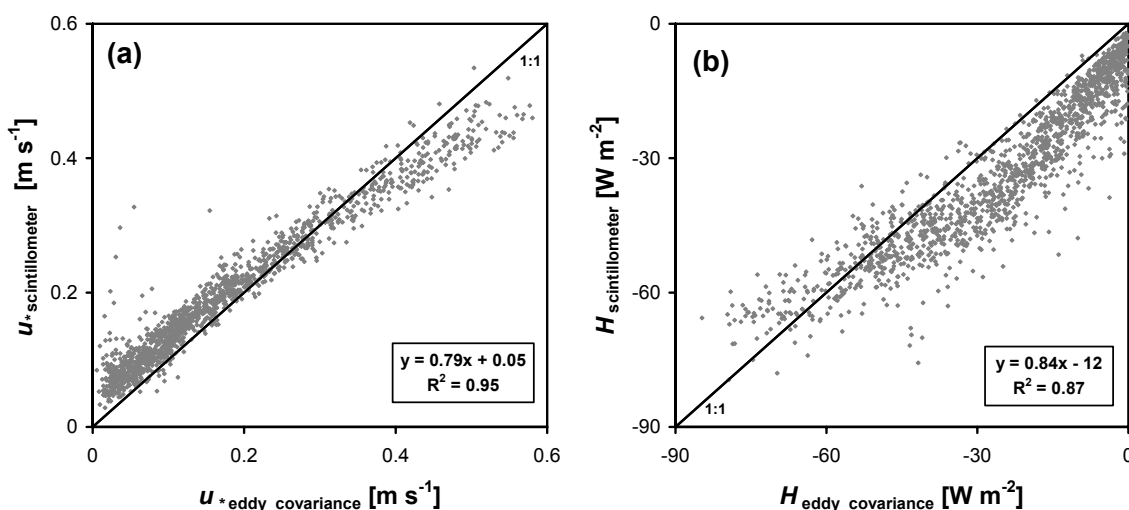


Figure 4-11: Eddy Covariance u_* and H compared u_* and H obtained from DBSAS measurements of CASES-99 (see Chapter 3) using the MOST functions of ε and C_T^2 (Equations 4.10a and 4.13a).

The procedure followed to calculate the DBSAS fluxes depicted in Figure 4-11 is identical to that used to produce Figure 3-9a₁ (for u_*) and Figure 3-9a₃ (for H) with one difference, namely that in Chapter 3 we used MOST functions of Wyngaard (1973) for C_T^2 and Frenzen and Vogel (1992) for ε . Comparing the results of Figure 4-11 with Chapter 3 we see the following. The values of u_* are nearly identical, i.e. both the f_ε relations of Frenzen and Vogel (2003) and Equations (4.10a) produce the comparable u_* . For H , on the other hand, the f_T relation of Wyngaard (1973) gives a slight DBSAS overestimation of H , but a much larger overestimation using Equation (4.13a). One might argue that the Wyngaard relation is thus better. This is a result, however, of the sonic anemometer derived C_T^2 - also used for deriving Equation (4.13a) - being much smaller than the DBSAS C_T^2 (see Figure 3-8a₁).

Chapter 5 Comparison of Field Scale Scintillometers: the BBC experiment at Cabauw

5.1 Introduction

In this paper we compare three scintillometer configurations with the objective to obtain the dissipation rate of turbulent kinetic energy, ε , the structure parameter of temperature, C_T^2 , and the heat and momentum flux, H and τ , on field scale, i.e. a scale of 50 to 500 m. The three types of scintillometers are: the displaced-beam small-aperture scintillometer (DBSAS), the large-aperture scintillometer (LAS) and a combination of the two. The DBSAS and the LAS are optical instruments that consist of a transmitter and receiver. The receiver records intensity fluctuations of the light beam emitted by the transmitter, which are caused by refraction of the beam upon its passage through the turbulent surface layer. These intensity fluctuations are a measure of H , and, for the DBSAS also of τ .

The interest in short path scintillometers is twofold. First, scintillometers have proven to have advantages over the eddy covariance method in stable conditions (e.g. Hartogensis et al., 2002). Second, the transmitter and receiver the instrument consists of can be installed at the borders of the field. Especially for flux measurements in agricultural areas this is of great advantage, because the instrument does not interfere with the farmers activities in the field. In contrast, traditional flux measurements, such as the eddy covariance method, have to be in the middle of the field for fetch considerations. Moreover, data processing, data quality control and correction procedures for these methods require detailed micrometeorological know-how.

Our main motivation to use field scale scintillometers is their application in the very stable boundary layer. Stable boundary layers pose challenges to flux measurement techniques because they are often highly non-stationary, which means that the flux averaging period needs to be short, and they can be very shallow, which means that the flux measurements need to be taken close to the surface. The eddy covariance method needs a minimum averaging time to obtain a reliable flux, and a minimum height, since close to the surface the contribution of the smallest turbulent eddies to the flux is largest and eddies smaller than the sonic-path are not detected by the instrument. For scintillometers in general, turbulence is averaged over space as well as over time, which allows much shorter averaging periods. Where the eddy covariance method relies on statistics of all turbulence transporting eddy scales, scintillometers gather statistics of eddies of only one length scale. For the DBSAS this

• Material of this Chapter is in preparation for submission to international Journals in the form of two papers.

eddy scale is typically 1 cm, an eddy size that cannot be detected by a sonic anemometer, which makes it suitable for flux measurements just above the surface.

A property of interest to describe the difference between the LAS and the DBSAS is the first Fresnel zone ($F = \sqrt{\lambda L}$), with λ is the wavelength, and L is the path length. The aperture diameter, D , of the DBSAS is “small” since $D < F \approx l_0$ applies. The LAS aperture is considered “large” because $l_0 < F \ll D$. The inner scale, l_0 , marks the transition between the inertial and viscous-, energy dissipating range of eddy sizes and is of the order 0.2 cm - 2 cm near the surface. For the DBSAS F is a measure of the optically most effective eddies (~ 1 cm), which lies in the energy dissipation range of eddy scales. For the LAS D is a measure of the optically most effective eddies (~ 5 cm – 30 cm), which generally lies in the inertial range of eddy scales. The description of the scintillometer principle measurement, i.e. refractive index fluctuations of the beam, requires a theoretical form of the refractive index spectrum. C_n^2 , the structure parameter of the refractive index, describes the inertial range part of the spectrum and l_0 the dissipation part.

The DBSAS operates two parallel beams displaced by a distance of 2.7 mm. It sees only dissipation range eddies. The DBSAS method consists of solving C_n^2 and l_0 from intensity fluctuations measurements of one beam and the correlation between the two beams. C_n^2 and l_0 are directly related to C_T^2 and ε , which follow Monin-Obukhov scaling (MOS) to give the sensible heat flux, H , and the momentum flux, τ .

The LAS operates one beam. It sees primarily inertial range size eddies. This means that only the inertial range part of the theoretical spectrum is needed to evaluate the raw measurements. This makes that the intensity fluctuations are related to C_n^2 only. To get to fluxes, one also needs a measure of the mechanically induced turbulence that contributes to the flux. For the LAS method it is customary to include wind speed measurements at a single height and an estimate of the roughness length, which, following the flux profile relationships gives u^* . Note that for stable conditions mechanically induced turbulence is the only turbulence generating transport mechanism. The DBSAS directly contains this information through ε , whereas the LAS relies on flux profile relationships to include this transport mechanism.

The application of scintillometers is bounded to a certain minimum and maximum path length. For field scale application (50 m – 500 m) the DBSAS is limited by a maximum path length of ~ 250 m due to saturation, whereas the LAS is limited by a minimum path length to have a sufficient signal to noise ratio. To found this we will qualitatively outline the relation between the scintillometer signal (measured intensity fluctuations) and the path length, turbulence intensity, measurement height and F (for DBSAS) or D (for LAS). First, the longer the path length and the higher the turbulence intensity, the higher the scintillometer signal. Second, the scintillometer signal also depends on the measurement height as the dominant eddy size encountered in the boundary layer scales with height and F (DBSAS) or D (LAS) define the dominant eddy size seen by the scintillometer. From this it follows that the signal is largest close to the surface, assuming that the measurements take place at a height much

greater than the dominant eddy scale seen by the scintillometer. As $F \ll D$, for a similar set-up the DBSAS gives more signal than the LAS.

When the signal is *too large*, *saturation* occurs, i.e. the instrument no longer senses additional intensity fluctuations. This effect limits the DBSAS application to field scale (Clifford et al., 1974), whereas the LAS can be operated on scales of several hundreds meters up to 10 km (De Bruin et al., 1995; McAneney, 1995; Kohsiek et al., 2002 and Meijninger et al., 2002a). Note, that the LAS also suffers from saturation when operated over very long path lengths. Kohsiek et al. (2005) reviewed various models that correct for LAS saturation.

When the signal is *too low*, the *signal to noise ratio* does not exceed a minimum level, i.e. no reliable measurements are obtained. This effect limits the LAS application at field scale for LAS with small D . Typical aperture sizes for a field scale LAS are ~ 5 cm to 10 cm. It is important to note that at these small apertures the LAS becomes sensitive to dissipation range eddy sizes, i.e. to l_0 as well as C_n^2 (Hill and Ochs, 1978). We will discuss this issue in more detail.

Reginald Hill (personal communication) argued that a weak aspect in the DBSAS method is the fact that C_n^2 , which is an inertial range property, is measured far into the dissipation range. He therefore proposed combining a short-aperture scintillometer (SAS) with a field scale LAS. The LAS solves C_n^2 and the SAS solves l_0 . We applied this idea using the combination of a DBSAS with a LAS installed alongside each other to obtain C_n^2 and l_0 .

This study elaborates on earlier work with the DBSAS based on data gathered during CASES-99 (Hartogensis et al., 2002 and Hartogensis and De Bruin, 2005) and WINTEX (De Bruin et al., 2002). Hartogensis et al. (2002) compared ε , C_T^2 , H and the friction velocity, u_* , between DBSAS and eddy covariance (EC) measurements of the CASES-99 experiment in Kansas, USA. They found systematic differences between the DBSAS and EC fluxes, especially for high and low fluxes, however, with remarkably little scatter. Although with more scatter, De Bruin et al. (2002) found the same results for both stable and unstable conditions during the WINTEX experiment near Uppsala, Sweden. A few LAS studies with the objective to obtain fluxes on field scale have been published so far. De Bruin et al. (1995) over dry-vine grapes, Lagouarde et al. (2002) and McAneney et al. (1995) over two adjacent fields, and Hoedjes et al. (2002) over an irrigated wheat field to indirectly estimate evaporation. The concept of a combined DBSAS-LAS system is not new but, so far, no studies on this scintillometer configuration have been reported in the literature.

The data presented in this paper are gathered during the Baltex Bridge Cloud (BBC) experiment at Cabauw, the Netherlands during the summer of 2001. Installed alongside each other were 2 DBSASs and a 10 cm aperture LAS over a path length of ~ 120 m and an eddy covariance system. We will compare the three scintillometer configurations by comparing them against EC obtained fluxes and C_T^2 and ε . We want to see whether the systematic errors in the DBSAS found in the CASES-99 experiment can be reproduced. Also, we will introduce some new simple, direct flux-estimates from the raw DBSAS measurements. In addition, we will investigate the performance of the field scale LAS and the new combined DBSAS-LAS

system and see whether these give systematic errors as well, since the systematic errors found in the DBSAS interested us in exploring other field scale scintillometer configurations. Last, we will test the new stable Monin-Obukhov similarity (MOS) relationships for ε and C_T^2 based on CASES-99 sonic anemometer data for a stability range up to $z/L_{MO} = 10$ published by Hartogensis and De Bruin (2005). Although our main interest concerns the application of scintillometers in stable conditions, for completeness we will also consider unstable conditions in this study.

5.2 Theory

The raw scintillometer measurements consist of intensity fluctuations, which are analysed as the variance of the logarithm of the amplitude variations, B_1 , and, in addition for the DBSAS, the covariance of the logarithm of the amplitude variations, B_{12} . In Sections 5.2.1 to 5.2.3 we explain how to derive C_n^2 from the raw measurements of the three scintillometer-configurations and l_0 from the configurations involving the DBSAS. In Sections 5.2.4 we discuss how to calculate from these H and u_* .

5.2.1 Displaced Beam Small Aperture Scintillometer (DBSAS)

Following Hill and Lataitis (1989) and Thiermann (1992) the description of the covariance between the logarithm of the amplitude fluctuations of the two DBSAS beams is given by

$$B_{12_DBSAS} = 4\pi^2 K^2 \int_0^L \int_0^\infty k \phi_n J_0(kd) \sin^2\left(\frac{k^2 x(L-x)}{2KL}\right) \left[\frac{2J_1(u)}{u}\right]^2 dk dx, \quad (5.1)$$

where x is the co-ordinate along path length L , $K = 2\pi/\lambda$ is the optical wavenumber, k the turbulent spatial wavenumber, d the distance between the two beams, D is the diameter of both detectors, u is a substitution for $(kDx)/(2L)$, ϕ_n is the three-dimensional spectrum of the refractive index, which is a function of k , l_0 and C_n^2 and J_0 and J_1 are Bessel functions of the first kind. For $d = 0$, J_0 becomes 1 and the expression for the single detector variances B_{1_DBSAS} and B_{2_DBSAS} are obtained.

For ϕ_n the following form is assumed:

$$\phi_n = 0.033 C_n^2 k^{-11/3} f_A(kl_0), \quad (5.2)$$

where the first part ($0.033 C_n^2 k^{-11/3}$) describes the inertial range and f_A describes the decay of the refractive index fluctuations in the dissipation range and equals unity in the inertial range.

The inertial range description of the spectrum is well established and can be found in many textbooks (e.g. Monin and Yaglom, 1971). For f_A we use the model developed by Hill (1978). Applying this model requires solving a differential equation, which is inconvenient in operational use. Churnside (1991) therefore proposed, amongst others, an analytical fit to f_A , which does not give satisfactory results when used with Equation (5.1) (Hartogensis et al, 2002). Recently, Van Dijk et al. (2006) give f_A in table form. They also show that the influence of humidity on f_A is almost never relevant. We found an alternative analytical fit that does work well with Equation (5.1):

$$f_A(\eta) = \left[1 + 0.7 e^{-[0.924(\ln(\eta) - \ln(0.245))]^2} \right] e^{-2.772\eta^2}, \quad (5.3)$$

with $\eta = kl_0 / 7.4$. In Figure 5-10 f_A is plotted. It is seen that f_A shows a small increase in spectral energy (often referred to as the ‘‘Hill bump’’) at the transition of the inertial range to dissipation range after which the spectrum falls off with a slope steeper than the $k^{-1/3}$ of the inertial range. In the remainder of the text we will refer to properties that have been processed including the full spectrum of Equation (5.2) with the subscript ‘‘Hill’’, and to properties that have been processed with only the inertial range part of Equation (5.2) with the subscript ‘‘inertial’’. Frehlich (1992) posed the condition $\int (kl_0)^{1/3} f_A(kl_0) d(kl_0) \equiv 7.233$. Applying this to Equation (5.3) results in a factor 7.176, a small deviation from the theoretical value.

The strategy to solve C_n^2 and l_0 from measured B_{I_DBSAS} from a single beam and B_{I2_DBSAS} between the two beams from Equation (5.1) is as follows. First the correlation coefficient, r_{DBSAS} , is calculated. The expression for r_{DBSAS} , that follows from Equation (5.1), depends only on l_0 , which can thus be solved. Next, with l_0 known, C_n^2 can be calculated from either B_{I_DBSAS} or B_{I2_DBSAS} . For more details see e.g. Thiermann (1992), De Bruin et al. (2002) and Hartogensis et al. (2002).

5.2.2 Large Aperture Scintillometer (LAS)

For the LAS Wang et al (1978) derived the following expression describing variance of the logarithm of the amplitude fluctuations:

$$B_{1_LAS} = 4\pi^2 K^2 \int_0^L \int_0^\infty k \phi_n \sin^2 \left(\frac{k^2 x(L-x)}{2KL} \right) \left[\left(\frac{2J_1(u)}{u} \right) \left(\frac{2J_1(u(L/x-1))}{u(L/x-1)} \right) \right]^2 dk dx. \quad (5.4)$$

Equation (5.4) is similar to Equation (5.1) for a single aperture. The main difference is that for the spectrum only the inertial part applies as long as $D > 20l_0$ (Hill and Ochs, 1978), i.e. for $D > 20l_0$ the most active eddies seen by the instrument lie in the inertial range. For long range

LAS with a large D (> 0.15 cm) this is generally the case. Integration of Equation (5.4) then results in an expression that relates B_{l_LAS} directly to C_n^2 :

$$B_{l_LAS} = 0.223D^{-7/3}L^3C_n^2. \quad (5.5)$$

The LAS used here outputs a voltage that gives C_n^2 based on Equation (5.5), as most other LASs. For a field scale LAS with a small D , however, the condition $D > 20l_0$ is not always met. In that case Equation (5.5) is not longer valid, and Equation (5.4) with the full Hill spectrum should be used instead, which makes the LAS inner scale dependent. In Appendix 5A we introduce a correction routine for C_n^2 obtained with Equation (5.5) in case inner scale dependence of the LAS is an issue. The l_0 needed for this correction is obtained from the u^* in an iterative procedure.

Figure 5-1 depicts this C_n^2 correction factor as function of l_0 for the LAS we use in this study, i.e. with $D = 10$ cm. It can be seen that the correction exceeds 25% for $l_0 = \sim 10$ mm. High values of l_0 (> 10 mm) correspond to low wind speed conditions. Low values of l_0 (< 5 mm) correspond to high wind speed conditions. For stable conditions this means that the C_n^2 correction is largest in low wind speed conditions, when the fluxes are smallest. The effect of this correction on H is discussed in Section 5.4.3.

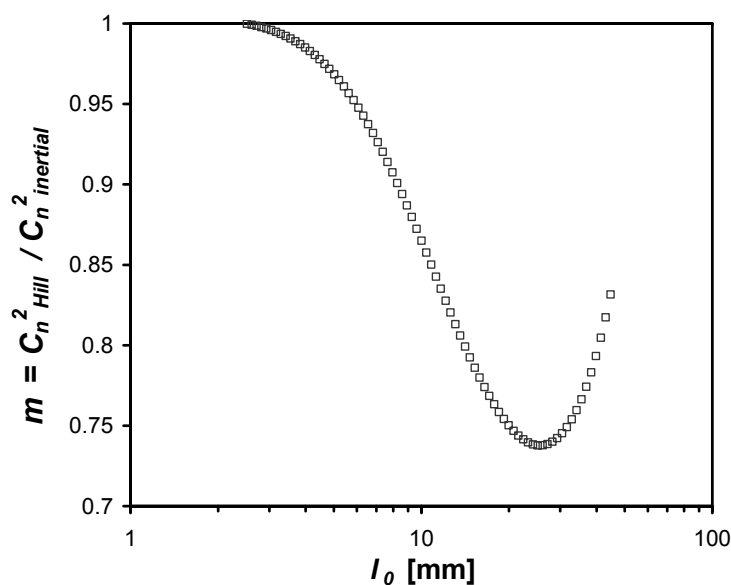


Figure 5-1: Ratio between C_n^2 calculated with the Hill spectrum ($C_n^2_{Hill}$) and C_n^2 calculated with inertial range spectrum ($C_n^2_{inertial}$) as a function of the inner scale, l_0 for a LAS with an aperture of 10 cm.

5.2.3 Combined DBSAS and LAS

C_n^2 is a property describing the inertial range of the n -spectrum. In the DBSAS method, however, one solves C_n^2 far in the dissipation range, where the Hill bump determines the description of the spectrum. Figure 1 of Hartogensis et al. (2002) where the DBSAS spectral

weighting function of the Hill bump is depicted demonstrates this. It is seen that for pathlengths of both 50 m and 150 m and $l_0 > 5$ mm, the bulk of the spectral weighting coincides with the tail of the Hill bump. This leads to the conclusion that the DBSAS is less suitable to determine C_n^2 when compared with the LAS. The LAS applied on field scale, on the other hand, needs a relatively small D (< 10 cm) to have sufficient signal no noise, which makes it inner scale dependant. This is demonstrated in Figure 5-10 of Appendix 5A, where the LAS spectral weighting function of the Hill bump is depicted. It seen that for $D < 10$ cm and $l_0 > 5$ mm at least part of the spectral weighting coincides with the Hill bump.

A DBSAS-LAS configuration combines the better of the two methods to give C_n^2 and l_0 at field scale. C_n^2 is solved from the LAS at near inertial range eddy scales, and l_0 is solved from the DBSAS. As far as the LAS C_n^2 is inner scale dependant, this can be accounted for with the DBSAS l_0 , by either using Equation (5.4) with the full Hill spectrum or the derived correction factor (Equation 5.20) derived in Appendix 5A.

The DBSAS and LAS measurements can be combined in two ways to give C_n^2 and l_0 . The first DBSAS-LAS combination, which we will refer to as *Combi1*, uses only B_{I_DBSAS} of one DBSAS aperture, which effectively makes it a SAS, and B_{I_LAS} to jointly solve C_n^2 and l_0 by iteration. One starts with the LAS inertial-range estimate of C_n^2 from the measured B_{I_LAS} . Next, one solves l_0 from Equation (5.1) from the measured B_{I_DBSAS} , applies the inner scale correction for the LAS C_n^2 , calculates a new l_0 etc., until both C_n^2 and l_0 converge. The second DBSAS-LAS combination, which we will refer to as *Combi2*, solves l_0 from r_{DBSAS} obtained from both DBSAS apertures and subsequently, the inner scale dependency corrected LAS C_n^2 from B_{I_LAS} .

The LAS and DBSAS were installed at slightly different heights (see Section 5.3). This has consequences for the joint calculation of l_0 and C_n^2 , since both variables are height dependent. For *Combi1* for instance, solving l_0 from B_{I_DBSAS} with C_n^2 from the LAS, one has to transfer the C_n^2 value obtained at the height of the LAS to the height of the DBSAS. In Appendix 5B we explain why we do this following the C_T^2 and ε scaling groups for neutral conditions (see next Section) and also discuss the effect of neglecting the effect of stability on the l_0 and C_n^2 height scaling.

5.2.4 Calculation of turbulent fluxes

The DBSAS and DBSAS-LAS combinations give C_n^2 and l_0 , and the LAS only yields C_n^2 . We will briefly outline how to get from these principle physical properties to turbulent fluxes.

The *first step* is to determine the structure parameter of temperature, C_T^2 , from C_n^2 for all three scintillometer configurations, and ε from l_0 for the DBSAS and LAS-DBSAS combinations. For optical wavelengths temperature fluctuations dominate the refractive index fluctuations measured by the scintillometer. The effect of humidity fluctuations is almost negligible in the dissipation range (i.e. on the Hill bump), but can be significant in the inertial

range of eddy scales (i.e. on C_n^2); see Hill and Clifford (1978) and Van Dijk et al. (2006). Moene (2003) reviewed the humidity effect on C_n^2 and derived the following relation between C_T^2 and C_n^2 accounting for humidity:

$$C_T^2 = C_n^2 \left(\frac{T^2}{A_T^2} \right) \left(1 + 2 \frac{A_q}{q} \frac{T}{A_T} R_{Tq} \frac{\sigma_q}{\sigma_T} + \frac{A_q^2}{q^2} \frac{T^2}{A_T^2} \left(\frac{\sigma_q}{\sigma_T} \right)^2 \right)^{-1}, \quad (5.6)$$

with σ_T and σ_q are the standard deviation of temperature and humidity, R_{Tq} is the correlation coefficient between T and q , $A_T = -0.789 \times 10^{-6} P/T$ and $A_q = -41.75 \times 10^{-6} q$, where P is the air pressure (Pa), T temperature (K) and q the absolute humidity (kg kg^{-1}). A_T and A_q formulations are from Andreas (1988).

ε is related to l_0 through:

$$\varepsilon = \nu^3 (7.4/l_0)^4, \quad (5.7)$$

where ν is the kinematic viscosity of air, which is a weak function of T , air temperature, and ρ , air density: $\nu = [(1.718 + 0.0049(T - 273.15))/\rho]10^{-5}$ (after Thiermann, 1996). The factor 7.4 is reviewed by Hill (1997) and reflects the values 0.43 for the Obukhov-Corrsin constant and 0.72 for the Prandtl number.

The **second step** is to evaluate the fluxes of sensible heat and momentum. For this step one relies on the Monin-Obukhov similarity (MOS) theory. In the framework of MOS, the sensible heat flux, H , is defined as $H = -\rho C_p u_* \theta_*$ and the momentum flux, τ , as $\tau = \rho u_*^2$, where θ_* is a temperature scale, u_* the friction velocity and c_p the heat capacity at constant pressure ($1005 \text{ J kg}^{-1} \text{ K}^{-1}$). MOS predicts that physical properties that contain information on turbulence transport in the atmospheric surface layer, such as C_T^2 and ε , are universal functions of the dimensionless length scale $\zeta = z/L_{MO}$, when made dimensionless using the scaling parameters such as u_* and θ_* . L_{MO} is Monin-Obukhov length, which is defined as $L_{MO} = (T u_*^2)/(k_{kar} g \theta_*)$ and z is the measurement height.

For all three scintillometer configurations θ_* follows from the dimensionless C_T^2 group:

$$\frac{C_T^2 z^{2/3}}{\theta_*^2} = f_T(\zeta). \quad (5.8)$$

For the DBSAS and DBSAS-LAS configuration u_* follows from the dimensionless ε group:

$$\frac{k_{kar} z \varepsilon}{u_*^3} = f_\varepsilon(\zeta), \quad (5.9)$$

where k_{kar} is the von Kármán constant ($= 0.4$).

For the LAS one has only C_T^2 and no measure for the mechanically induced turbulence. It is customary to include wind speed measurements at a single height and an estimate of the roughness length, z_0 , which, following the flux profile relationships give u_* :

$$\frac{k_{kar}U}{u_*} = \ln\left(\frac{z}{z_0}\right) - \psi_m\left(\frac{z}{L_{MO}}\right) + \psi_m\left(\frac{z_0}{L_{MO}}\right), \quad (5.10)$$

where ψ_m is the integrated flux profile relation for momentum.

Note that to perform the inner scale dependence correction of the LAS C_n^2 , we take u_* obtained with Equation (5.10) to derive l_0 using Equations (5.9) and (2.21). This correction is fully described in Appendix 5A.

We adopted the following MOS scaling functions:

For f_T we used

$$f_T = \begin{cases} 4.7(1 + 1.6\zeta^{2/3}) & \text{for } \zeta > 0 \\ 4.9(1 - 6.1\zeta)^{-2/3} & \text{for } \zeta < 0 \end{cases}, \quad (5.11)$$

after Hartogensis and De Bruin (2005) for $\zeta > 0$ and Andreas (1989) for $\zeta < 0$. Andreas (1989) adjusted the result of Wyngaard et al. (1971) to reflect a k_{kar} of 0.4 rather than 0.35.

For f_ε we used

$$f_\varepsilon = \begin{cases} 0.8 + 2.5\zeta & \text{for } \zeta > 0 \\ (1 - 15.1\zeta)^{-1/3} - \zeta - 0.16 & \text{for } \zeta < 0 \end{cases}, \quad (5.12)$$

after Hartogensis and De Bruin (2005) for $\zeta > 0$ and Frenzen and Vogel (1992) for $\zeta < 0$.

For ψ_m we used

$$\Psi_m = \begin{cases} 1 - (1 + 6.25\zeta)^{0.8} & \text{for } \zeta > 0 \\ 2 \ln[(1+x)/2] + \ln[(1+x^2)/2] - 2 \arctan(x) + \pi/2 & \text{for } \zeta < 0 \end{cases}, \quad (5.13)$$

with $x = (1 - 16\zeta)^{1/4}$

after Duynkerke (1999) for $\zeta > 0$, who used observations of Nieuwstadt (1984) taken at Cabauw, and Businger et al. (1971) for $\zeta < 0$.

5.3 Experiment description and Data treatment

We will use data gathered during BALTEX Bridge Cloud (BBC) campaign. The BBC campaign was a cloud observation experiment that took place in August and September 2001 at the Cabauw tower, the Netherlands. This campaign is part of the long-term multi-national Baltic Sea Experiment (BALTEX), which in turn is embedded in Global Energy and Water Cycle experiment (GEWEX). On a flat grassland site of approximately 130 by 150 m we operated an eddy-covariance (EC) system consisting of a CSAT3 sonic anemometer from Campbell Scientific Inc., Logan, USA, a LiCor7500 open path CO₂-H₂O sensor from LiCor, Lincoln, USA, and a PTB101B pressure sensor from Vaisala, Helsinki, Finland. Alongside each other (~ 5 m apart), in the direct vicinity of the EC system (< 15 m) we installed two SLS20 DBSAS from Scintec AG, Tübingen, Germany and a 10 cm aperture LAS built at the Meteorology and Air Quality Group of Wageningen University.

The CSAT 3 was installed at a height of at 3.32 m, the LiCor7500 was installed at 0.27m directly below the sonic. Raw 20 Hz data were registered with a Campbell 23X datalogger and stored on a laptop in the field to be processed afterwards with the latest version of the *EC-pack* software package (www.met.wau.nl/projects/jep), developed by Wageningen University. The following corrections were performed in calculating the 10-minute averaged fluxes:

- axis rotations around the x - and y -axes of the sonic coordinate system were performed with the so-called planar fit routine after Wilczak et al. (2001). The planar fit rotation angles were determined per day. The rotation into the mean horizontal wind, around the z -axis, was done for every flux interval;
- sonic temperature was corrected for the influence of humidity and side-wind on the speed of sound measurement (Schotanus et al., 1983);
- fluxes were corrected for poor frequency response (Moore, 1986).

In addition to the turbulent fluxes we also derived ε and C_T^2 from the sonic anemometer measurements using spectral analysis. ε and C_T^2 are scaling parameters of the inertial range parts of the TKE and temperature spectra.

For the longitudinal wind component, u , the inertial range of the spectrum, S_u , is described by

$$S_u(k) = \alpha \varepsilon^{2/3} k^{-5/3}. \quad (5.14)$$

For temperature, T , the inertial range of the spectrum, S_T , is described by

$$S_T(k) = 0.25 C_T^2 k^{-5/3}. \quad (5.15)$$

S_u and S_T are the spectral energy densities, α is the Kolmogorov constant, and k is the spatial wavenumber expressed in cycles per unit length. We adopted $\alpha = 0.55$, which is mid-range of the values found in the literature (e.g. Höglström, 1996).

The 10-minute spectra were determined with the FFT method and subsequently smoothed by averaging each point in the spectrum with 10% of its neighbouring points using a filter defined by $(1-x^2)^2$ for $-1 < x < 1$, where the data points to be averaged are equally distributed over the x -domain. The method we used to automatically detect and quality check the inertial range of the spectra is described in Hartogensis and De Bruin (2005).

The transmitter and receiver of the two DBSASs with serial numbers 148 and 221 were installed right next to each other (separation < 5 m) in a North-South orientation, receiver and transmitter in opposite directions, and the paths of SN148 and SN221 crossing each other. The path length of both DSASs was 121.5 m. The height of the DBSAS with SN148 was 2.52 m. The height of the DBSAS with SN221 was 2.48 m. In Section 5.4.1 we will compare the raw measurements of the two DBSASs. In the comparison of DBSAS with sonic anemometer data, we will only use SN148, since this is the instrument that we used in CASES-99 also, and one of our objectives here is to see whether we can reproduce the CASES-99 results. Further instrument details can be found in Thiermann (1992) and Hartogensis et al. (2002).

We collected 6 s averaged raw measurements of B_{1_DBSAS} , B_{2_DBSAS} and B_{12_DBSAS} with the Scintec commercial software SLSRUN. In processing these to 10-minute average fluxes, we first averaged them to 10-minute values. Note that this is different then the procedure used in Hartogensis et al (2002), where we calculated first 6 s averaged ε and C_T^2 , and log-normally averaged these following the paper by Frehlich (1992). He argued that Equation (5.1) applies for local stationary conditions only, and thus short averaging intervals of only a few seconds should be used, and that in addition, C_T^2 and ε obey a log-normal distribution. In Appendix 3C we show that this approach procedure gives higher ($\sim 15\%$) ε and introduces more scatter in C_T^2 . A great portion (2/3) of the higher ε is not related to the considerations given by Frehlich (1992), but simply because of the highly non-linear relation between the raw measurements and ε . By adopting 10-minute averaged raw measurements, we follow the concept of Hill and Frehlich (1996) who state that as long as intermittency is stationary in time and homogeneous along the path, Equation (5.1) is valid. If these conditions are not met, intermittency will affect the l_0 and C_n^2 -estimates.

The LAS was installed over a path of 118 m and a height of 2.72 m. The aperture diameter is 0.10 m. Further instrument details are described in detail in Meijninger (2003), and also in Meijninger et al. (2002). In solving u^* using the flux profile relations in combination with the LAS C_T^2 we used the wind speed from the sonic anemometer and a z_0 -estimate of 0.02 m.

The step from C_n^2 to C_T^2 from all three scintillometer configurations requires information on humidity and temperature fluctuations, σ_T , σ_q , and R_{Tq} . These were taken from the EC system.

The data we consider is from 21 August to 26 September 2001. The weather during this period was very wet. It rained, on average, 10% of the time amounting to a total rainfall of 190 mm. At night, because of the wet conditions, the scintillometers suffered from dew formation on the aperture windows. Also we lost some days due to power failure. We filtered our data to exclude from the analyses corrupted measurements due to rain and dew formation.

5.4 Results and Discussion

5.4.1 Displaced Beam Small Aperture Scintillometer (DBSAS)

We recall that the raw measurements of the DBSAS are analysed as B_{I_DBSAS} and B_{I2_DBSAS} . From these two we infer the r_{DBSAS} between the two beams, from which l_0 can be solved. Next, with l_0 known, C_n^2 can be determined from Equation (5.1). Additional measurements needed to get to fluxes with the DBSAS method are: some information to account for the humidity effect on C_n^2 (here σ_T , σ_q , and R_{Tq} , see Equation 5.6), and P , T , and q to determine ρ and ν .

Our main objective for the DBSAS were to compare the results with those of the CASES-99 experiment (Hartogensis, 2002), to have an independent check of the MOS functions proposed by Hartogensis and De Bruin (2005), and to introduce some direct flux-estimates from the raw DBSAS measurements.

Figure 5-2 gives an overview of the comparison of ε , C_T^2 , u^* , and H derived from EC (or sonic anemometer) measurements and the DBSAS. Note that ε and C_T^2 are scaled with height according to their dimensionless groups for neutral conditions (see Appendix 5B). Ignoring the stability effect on the ε and C_T^2 height-scaling results in a bias of the ε and C_T^2 comparison between EC and DBSAS. This bias is discussed in Appendix 5B and is introduced as correction terms S_ε and S_{CT2} as follows: $(z\varepsilon)_{DBSAS} = S_\varepsilon (z\varepsilon)_{EC}$ and $(z^{2/3}C_T^2)_{DBSAS} = S_{CT2} (z^{2/3}C_T^2)_{EC} \cdot S_\varepsilon$ and S_{CT2} are 1 for neutral conditions, and smaller or larger than 1 for non neutral conditions, depending on the shape of the stability function f_ε and f_T . To summarise Appendix 5B, in particular its Table 5-1, we can state that ignoring this bias affects Figure 5-2 as follows:

- ε for stable conditions: $S_\varepsilon = \sim 1 - 0.7$ which means $(z\varepsilon)_{EC} > (z\varepsilon)_{DBSAS}$ for small ε affecting small $|H|$ and small u^* .
- ε for unstable conditions: $S_\varepsilon = \sim 1.02 - 0.95$ which means $(z\varepsilon)_{EC} > (z\varepsilon)_{DBSAS}$ for all ε affecting high $|H|$ and all u^* .
- C_T^2 for stable conditions: $S_{CT2} = \sim 1 - 0.7$ which means $(z^{2/3}C_T^2)_{EC} > (z^{2/3}C_T^2)_{DBSAS}$ for large C_T^2 affecting small $|H|$ and small u^* .
- C_T^2 for unstable conditions: $S_{CT2} = \sim 1 - 1.2$ which means $(z^{2/3}C_T^2)_{EC} < (z^{2/3}C_T^2)_{DBSAS}$ for large C_T^2 affecting large $|H|$ and all u^* .

With this in mind we will now discuss Figure 5-2. The overall picture is very similar to what was found by Hartogensis et al. (2002) for stable conditions and De Bruin et al. (2002) for stable and unstable conditions. The DBSAS overestimates u^* for small and underestimates u^* for high u^* . This is not related to our choice of MOS functions, since ε shows the same behaviour.

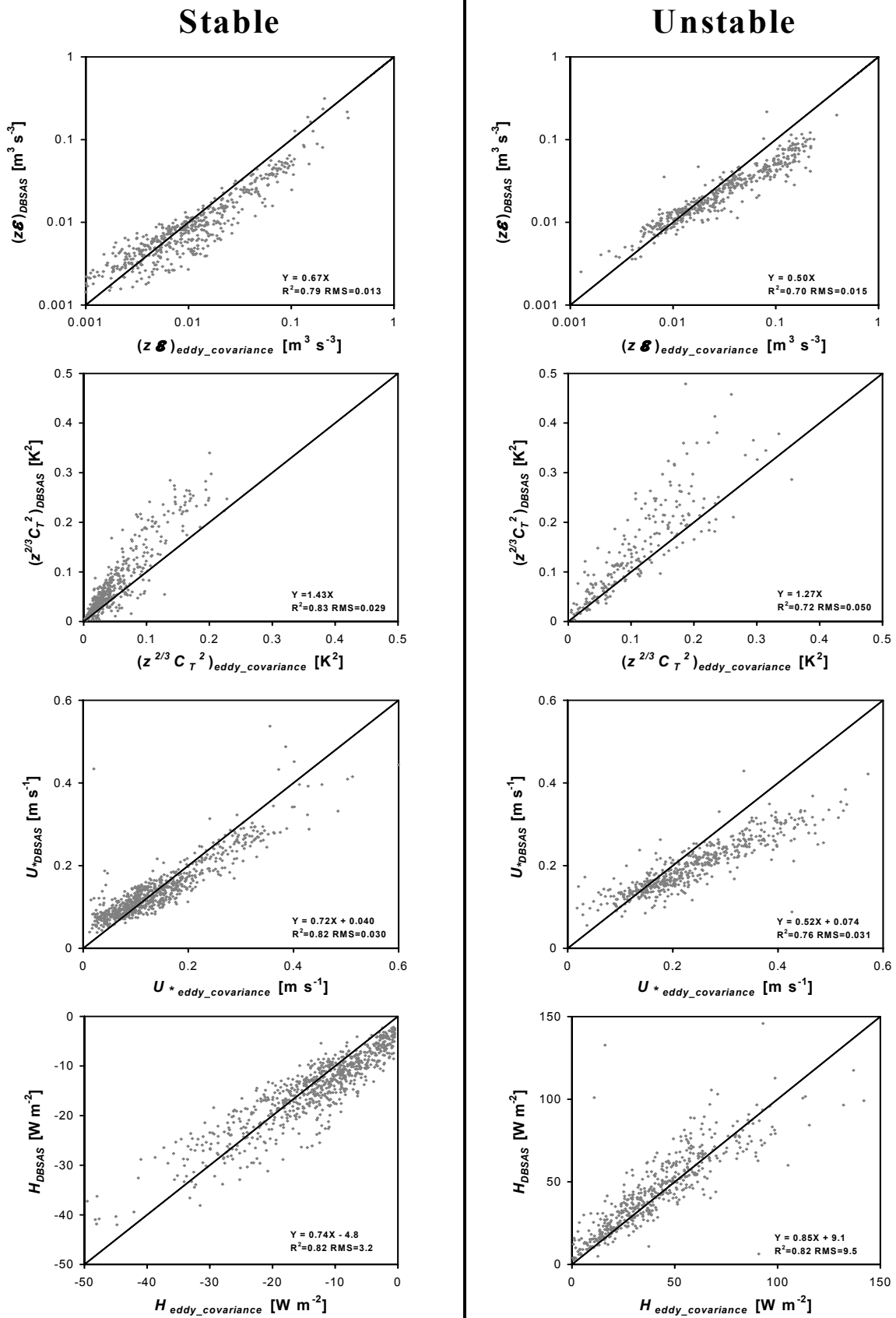


Figure 5-2: Comparison between (from top to bottom) ϵ , C_T^2 , u_* and H determined with a DBSAS and eddy-covariance (sonic anemometer) measurements for stable (on the left) and unstable (on the right) conditions.

For unstable conditions this effect is even more pronounced, i.e. the slope-coefficient of the linear regression is lower (0.67 for stable against 0.50 for unstable conditions for ε , and 0.72 for stable against 0.52 for unstable conditions for u_*) and the intercept is higher (only given for u_* , 0.040 for stable against 0.074 for unstable conditions). Note that by adding the stability effect on the height dependency of ε the DBSAS overestimation for low ε in stable conditions would be even worse, as well as the DBSAS underestimation of ε for high ε in unstable conditions. Nevertheless, the scatter in ε and u_* is surprisingly low.

The DBSAS overestimates C_T^2 for stable conditions, as was also found by Hartogensis et al. (2002) for the CASES-99 dataset. For unstable conditions the DBSAS C_T^2 overestimation is a bit less than for stable conditions, but scatters stronger. The DBSAS C_T^2 gives more scatter than the DBSAS ε . Note that for C_T^2 , adding the stability effect to the C_T^2 height dependency worsens the DBSAS-EC comparison of C_T^2 for stable conditions. For unstable conditions, on the other hand, it improves the comparison.

The resulting H behaves differently for stable and unstable conditions. For stable conditions, where mechanical turbulence dominates, the picture is more similar to ε and u_* , i.e. with an overestimation of the DBSAS H for low H and an underestimation for H for high H . For unstable conditions, where buoyancy turbulence dominates, the picture is more similar to C_T^2 , i.e. with an overestimation of the DBSAS H for all H . De Bruin et al. (1995) comment on this feature and show that the free-convection estimate of H , which is independent of u_* , already can be applied at $\zeta > 0.1$. If u_* is still important for large H , the overestimation of C_T^2 and underestimation of u_* for high u_* may cancel each other partly in the H -estimate.

The systematic errors found in the fluxes cannot solely be attributed to the MOS scaling functions, since they are already present in ε and C_T^2 . The little scatter found in the fluxes indirectly indicates that the MOS scaling functions we used are appropriate. In Appendix 5C, the BBC stable scaling groups of ε and C_T^2 are compared in more detail with the scaling functions f_ε and f_T published by Hartogensis and De Bruin (2005), showing that the f_ε corresponds well to the BBC data-set and the C_T^2 group shows much scatter.

There are three issues that might affect the DBSAS operation and possibly explain the systematic errors found. First, Equation (5.1) is derived for an incoherent source on which the DBSAS operation is based. The SLS20 DBSAS used in this study uses a laser source, which is coherent. Second, the SLS20 makes use of one laser source, which is split into two beams with orthogonal polarization. The different polarisation of the two beams is needed to distinguish one from the other at the receiver. It is known that turbulence can affect the polarisation and thus the SLS20 performance. Third, mast vibrations and random noise will affect the DBSAS measurements (De Bruin et al, 2002 and Thiermann and Rummel, 1998). Random noise increases B_{1_DBSAS} but does not affect B_{12_DBSAS} , thus it lowers r_{DBSAS} . The relative effect is greatest in low wind speed conditions when r_{DBSAS} is large. The effect of random noise will be that u_* is increased for small u_* . Mast vibrations will increase r_{DBSAS} at high wind speeds. The effect of mast vibrations will be that u_* is decreased for large u_* . These issues require further research. Although not shown here, we did investigate the working

hypothesis adopted by Hartogensis et al. (2002) to use a displacement distance, d , between the beams of 2.6 mm instead of 2.7 mm. The difference of 0.1 mm is within the accuracy with which the manufacturer specifies d , and for the CASES-99 data-set this adjustment considerably reduced the systematic errors found. Adopting $d = 2.6$ mm for the BBC data does not improve the results, however, from which we conclude that this working hypothesis is not a general solution to the problem.

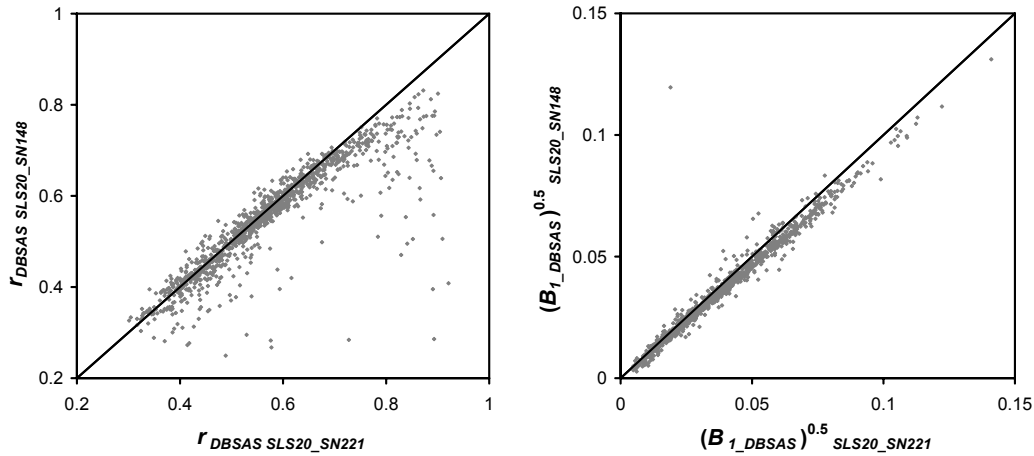


Figure 5-3: Comparisons of the 10-minute averaged DBSAS principle measurements r_{DBSAS} (left) and B_{I_DBSAS} (right) between two SLS20 DBSAS installed over the same path (paths cross each other).

Next, we will compare the two DBSASs that were installed at the same height in a cross-wise manner such that the middle of the path, that is weighed most by the instrument, overlaps. Figure 5-3 compares the principle measurements, r_{DBSAS} and B_{I_DBSAS} of the two instruments and shows that the two instruments agree reasonably with each other. For r_{DBSAS} more scatter is seen, whereas B_{I_DBSAS} shows a systematic deviation, but with less scatter. In terms of fluxes, high fluxes are related to high B_{I_DBSAS} and low r_{DBSAS} , and low fluxes to low B_{I_DBSAS} and high r_{DBSAS} .

To get from r_{DBSAS} and B_{I_DBSAS} to fluxes requires a lot of theory, each with its underlying assumptions. First, applying wave propagation theory, which is the basis of Equation (5.1) implies a great number of theoretical assumptions (Tatarskii, 1961, Hill and Lataitis, 1989). Next, to get from C_n^2 to C_T^2 requires similarity assumptions on temperature and humidity fluctuations (Moene, 2003), and to derive ε from l_0 requires a choice of the constants contained in the factor 7.4 (Hill, 1997). Last, to get to fluxes, one relies on MOS theory and has to choose a set of MOS functions.

In Figure 5-4 we bypass all these steps and relate r_{DBSAS} and B_{I_DBSAS} more or less directly to the EC fluxes. In Figure 5-4 u_* is directly related to r_{DBSAS} . With r_{DBSAS} as a measure for u_* , and B_{I_DBSAS} as an indirect measure for θ_* we introduce Φ , which has the appearance of the heat flux definition in MOS theory:

$$H \propto \Phi(r_{DBSAS}, B_{1_DBSAS}) = \rho c_p u_{*fit}(r_{DBSAS}) \sqrt{B_{1_DBSAS}} \quad (5.16)$$

Note that we use $\sqrt{B_{1_DBSAS}}$ since this reflects the H dependence of B_{1_DBSAS} in the near neutral range. In Figure 5-4 H is indirectly related to B_l through Φ .

Figure 5-4 clearly shows that r_{DBSAS} and B_{1_DBSAS} contain direct information on the turbulent fluxes. Especially for u_* and H in stable conditions the scatter is comparable to the complete flux-estimates given in Figure 5-2. For unstable conditions, apparently, the stability dependence is not captured well enough in the Φ group, and considerably more scatter is seen.

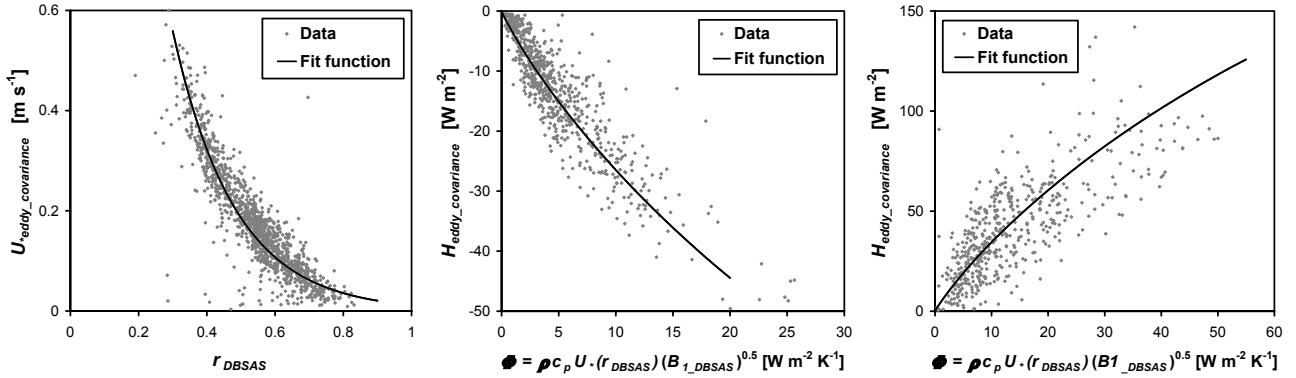


Figure 5-4: Derivation of empirical functions relating the DBSAS principle measurements r_{DBSAS} and B_{1_DBSAS} directly to eddy correlation u_* and H . For u_* (left) one relation is derived for stable and unstable conditions. For H separate relations are derived for stable (middle) and unstable conditions (right).

Next, we determined fit functions through the plots represented in Figure 5-4. For u_* we found

$$u_{*fit}(r_{DBSAS}) = 4.8 e^{-(5.5r_{DBSAS}+0.5)} \quad (5.17)$$

For H we found

$$H_{fit}(r_{DBSAS}, B_{1_DBSAS}) = \pm [c_1 \Phi(r_{DBSAS}, B_{1_DBSAS}) - c_2 \Phi(r_{DBSAS}, B_{1_DBSAS})^{c_3}] \quad (5.18)$$

where \pm defines the sign of the flux, - for stable and + for unstable. $c_1 = 5.5$ for stable conditions and $c_1 = 6.3$ for unstable conditions. $c_2 = 1.8$ and $c_3 = 1.2$ for both stable and unstable conditions.

The direct flux-estimates that result from r_{DBSAS} and B_{1_DBSAS} using the fit functions of Equations (5.17) and (5.18) is given in Figure 5-5. With this very simple approach we obtained a good quality u_* and stable H -estimate without bias and a reasonable, because of more scatter, unstable H -estimate. Note that the parameters used in the fit functions are not

universal but depend on the experimental set-up (instrument height and path length) and possibly the stability conditions.

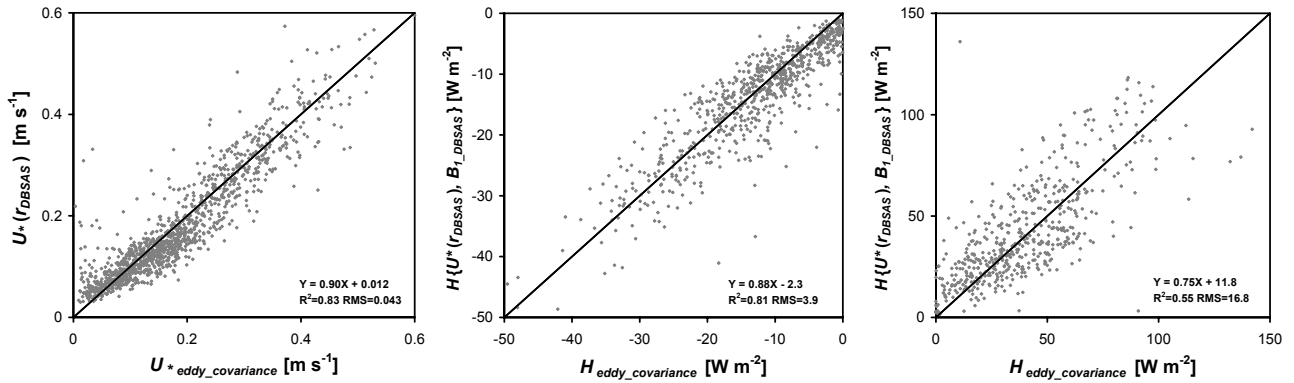


Figure 5-5: Comparison between u_* and H for the DBSAS direct flux-estimates and eddy-covariance during the BBC experiment. For u_* (left) stable and unstable conditions are plotted in one graph. For H separate graphs are given for stable (middle) and unstable conditions (right).

5.4.2 Large Aperture Scintillometer (LAS)

We recall that the raw measurements of the LAS are analysed as B_{l_LAS} . From these C_n^2 can be determined with Equation (5.5) applying an inertial range spectrum of n . Where the DBSAS ε gives information on the mechanically induced turbulence, for the LAS method we use measurements of u and an z_0 -estimate. Further additional measurements needed to get to fluxes are the same as for the DBSAS method. For high values of l_0 (low wind speed conditions) the C_n^2 of our 10 cm aperture LAS becomes sensitive to the Hill bump. To correct for this we applied the correction factor given in Equation (5.20) of Appendix 5A in an iterative scheme with l_0 inferred from u_* obtained from the flux calculations.

Our main objective for the LAS was to compare its results with the DBSAS. Especially for C_T^2 we would expect the LAS to perform better as this parameter is determined more closely to the inertial range scales where it is a scaling parameter. For stable conditions we have to note that the main turbulence generating mechanism is mechanical turbulence, which is taken care of by flux profile relations in the LAS method. The LAS measurements contribute only indirectly to description of this process through the stability functions. Out of curiosity, we also determined ε from the LAS method u_* and compared it with EC measurements derived ε . Again, one has to realise that the LAS itself contains little information on ε (or l_0) itself. It is mainly a product of flux profile relations in combination with MOS relation for ε . It only contains indirect LAS information through the stability function.

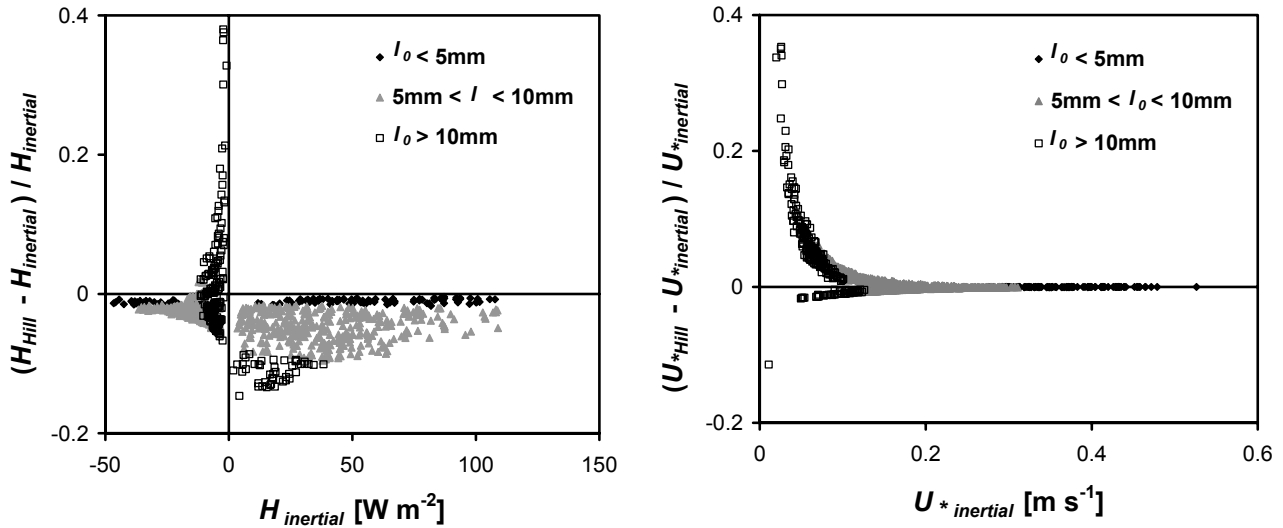


Figure 5-6: For the LAS method: the relative difference between H (left) and u_* (right) calculated from C_n^2 with the Hill spectrum and C_n^2 with the inertial spectrum against u_* and H for the inertial spectrum for three classes of l_0 values. For u_* , corrections above the zero line are related to stable conditions and below the zero line to unstable conditions.

First we show in Figure 5-6 the effect of the C_n^2 inner scale dependence on u_* and H . The size of the correction is given with respect to flux values if no correction would have been applied and is plotted with different symbols for three classes of l_0 . We remind that the maximum effect on C_n^2 was $\sim 25\%$ for $l_0 = \sim 12$ mm (see Figure 5-1). The way this correction works through in the fluxes is not straightforward. The direct effect is that, as $C_n^2_{Hill} < C_n^2_{inertial}$, H will be lower. The indirect effect, or feed back effect, is that the lower H results in a lower ζ , which depending on the shape of the stability functions f_T and f_m alters u_* and θ_* , and thus in its turn H . For unstable conditions the direct effect dominates, which means that the C_n^2 inner scale correction lowers C_n^2 and thus H and u_* . The indirect effect is that both u_* and θ_* decrease, so it enhances the direct effect. For stable conditions, the matter is more complicated. For small l_0 the direct effect dominates. The indirect effect leads to an increase in both θ_* and u_* , so it partly cancels the direct effect. For large l_0 the indirect effect dominates, i.e. it overcompensates the direct effect. This means that the lower $C_n^2_{Hill}$ in the end results in a higher H and u_* through the feed back of stability functions.

Figure 5-7 gives an overview of the comparison of ε , C_T^2 , u_* , and H derived from EC (or sonic anemometer) measurements and the LAS method (see comments above on ε and fluxes during stable conditions).

The LAS basically gives C_T^2 . The LAS C_T^2 gives the same picture for stable conditions as the DBSAS C_T^2 ; it overestimates the EC C_T^2 -estimate, albeit a little less. Again we note that for large C_T^2 this overestimation is worse if we would correct the neutral height scaling for stability. For unstable conditions, the LAS C_T^2 performs a lot better, i.e. it gives a near 1:1 relation with the EC C_T^2 with less scatter than was found for the DBSAS. Surprisingly, the flux profile method in combination with a field scale LAS results in a very good u_* -estimate.

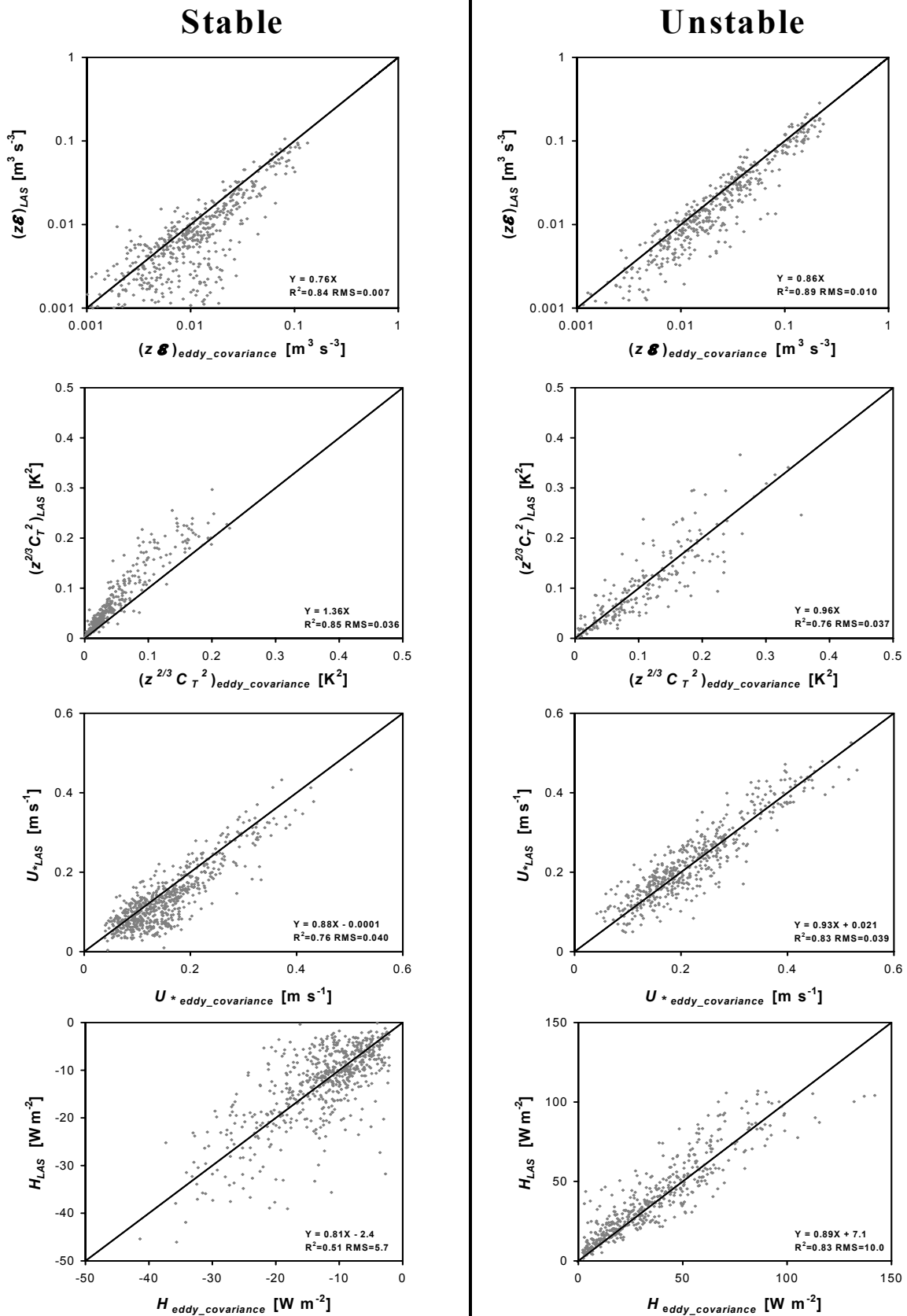


Figure 5-7: Comparison between (from top to bottom) ε , C_T^2 , u_* and H determined with a LAS and eddy-covariance (sonic anemometer) measurements for stable (on the left) and unstable (on the right) conditions.

For both stable and unstable conditions the LAS u^* is closer to the 1:1 line than for the DBSAS u^* . On the other hand, the scatter in the DBSAS u^* is less especially for stable conditions.

We recall that the stable H reflects the quality of the u^* -estimate and the unstable H the quality of C_T^2 . For stable conditions, therefore, H reflects more the scatter found in u^* than the overestimation in C_T^2 and the LAS stable H is inferior to the DBSAS stable H . For unstable conditions, in fact both C_T^2 and u^* -estimates are satisfactory and produce a H that is a little bit better than the DBSAS H , i.e. the slope coefficients are comparable (0.89 for the DBSAS and 0.87 for the LAS), but the intercept is lower for the LAS (7.1 W m⁻² against 9.1 W m⁻² for the DBSAS).

The ε -estimate that follows from the flux profile u^* -estimate performs quite well, which is an indication of the quality of the f_ε scaling functions that we used. Note that applying the stability correction on the neutral height scaling that we used to compare ε between LAS and EC would make the agreement even better, i.e. it raises the LAS ε -estimate for both stable and unstable conditions.

5.4.3 Combined DBSAS and LAS

We recall that we analysed two combined DBSAS-LAS configurations, *Combi1* and *Combi2*. *Combi1* uses B_{I_DBSAS} from one DBSAS aperture and B_{I_LAS} from the LAS. From these C_n^2 and l_0 are jointly solved by iteration. *Combi2* uses r_{DBSAS} from the DBSAS to solve l_0 and B_{I_LAS} from the LAS to solve C_n^2 . The height difference between the LAS and the DBSAS of 8% (2.72 m for the LAS against 2.52 m for the DBSAS) was accounted for using neutral ε and C_T^2 height scaling in combining the l_0 and C_n^2 -estimates from LAS and DBSAS. Note that for $|\zeta| \rightarrow \infty$ systematic deviations from the neutral scaling are introduced in the final combined DBSAS-LAS l_0 and C_n^2 -estimates. Additional measurements needed to get to fluxes are the same as for the DBSAS. Supposedly, these systems combine the best features of both the DBSAS and LAS in obtaining surface fluxes. C_n^2 is determined with the LAS at inertial range eddy scales, unlike the DBSAS that determines C_n^2 far into the dissipation range. l_0 is determined by means of scintillometry (with the DBSAS), unlike the LAS method, where flux profile relations are used. This is an important asset in stable conditions when turbulence is intermittent and the flux profile relations are likely to break down.

Our main objectives for the DBSAS-LAS configurations were to see whether the same quality fluxes could be obtained as with the DBSAS in terms of high correlation and little spread when compared with EC data, but without the systematic error that is found for the DBSAS. We also want to compare *Combi1* and *Combi2*, the main difference between the two being that *Combi1* is much simpler and cheaper to build. A disadvantage of the current set-up is that the LAS and DBSAS are two separate instruments. Ideally, they would have to be integrated into one.

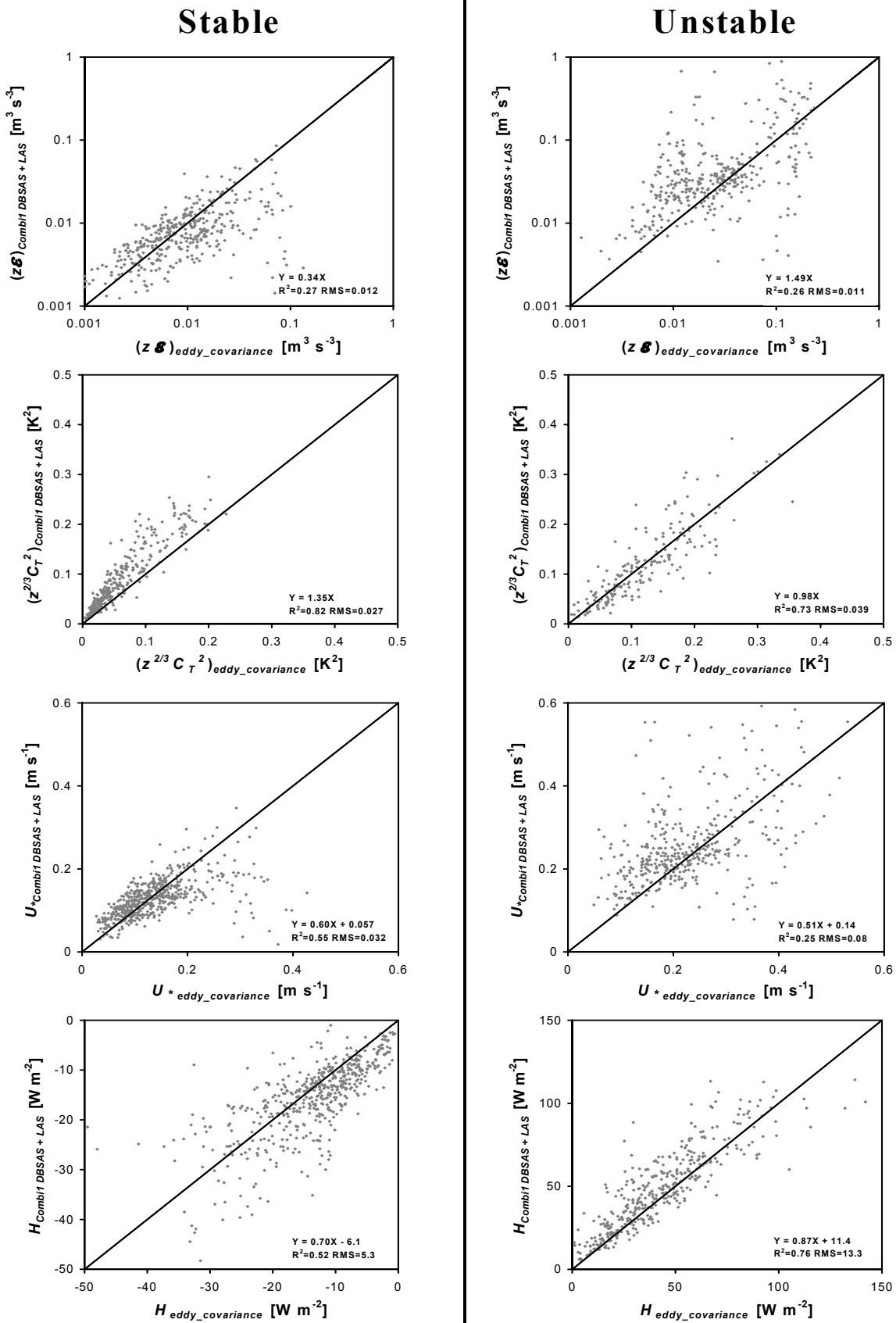


Figure 5-8: Comparison between (from top to bottom) ε , C_T^2 , u_* and H determined with *Combi1*, a combination of a LAS and one beam of a DBSAS and eddy-covariance (sonic anemometer) measurements for stable (on the left) and unstable (on the right) conditions.

Figure 5-8 gives an overview of the comparison of ε , C_T^2 , u_* , and H derived from EC (or sonic anemometer) measurements and *Combi1*. The *Combi1* C_T^2 is basically the LAS C_T^2 . The difference is that the l_0 used for the inner scale dependence comes from flux profile u_* for the LAS and from B_{I_DBSAS} for *Combi1*. The effect of this on the LAS C_n^2 inner scale dependence correction is apparently not very large. Disappointingly, the *Combi1* ε -estimate gives a lot of scatter. For stable conditions there is still some agreement between the *Combi1* and EC ε -estimates, resulting in a more or less systematic agreement for u_* and H , although with a lot of scatter. For unstable conditions, the *Combi1* ε -estimate is so poor that little systematic agreement is found between *Combi1* and EC ε , which is also reflected in their estimates of u_* . Apparently, the method of solving l_0 from Equation (5.1) highly depends on a combination of measured B_{I_DBSAS} and C_n^2 -estimate that are fully consistent with each other. The LAS C_n^2 -estimate is not fully consistent with B_{I_DBSAS} in solving l_0 . This might be related to the fact that we deal with two different instruments each giving information about turbulence intensity at different eddy sizes, placed some 10 m apart with a height difference of approximately 8%. The *Combi1* unstable H -estimate is very reasonable due to the good C_T^2 , which again demonstrates the insensitivity of unstable H to u_* .

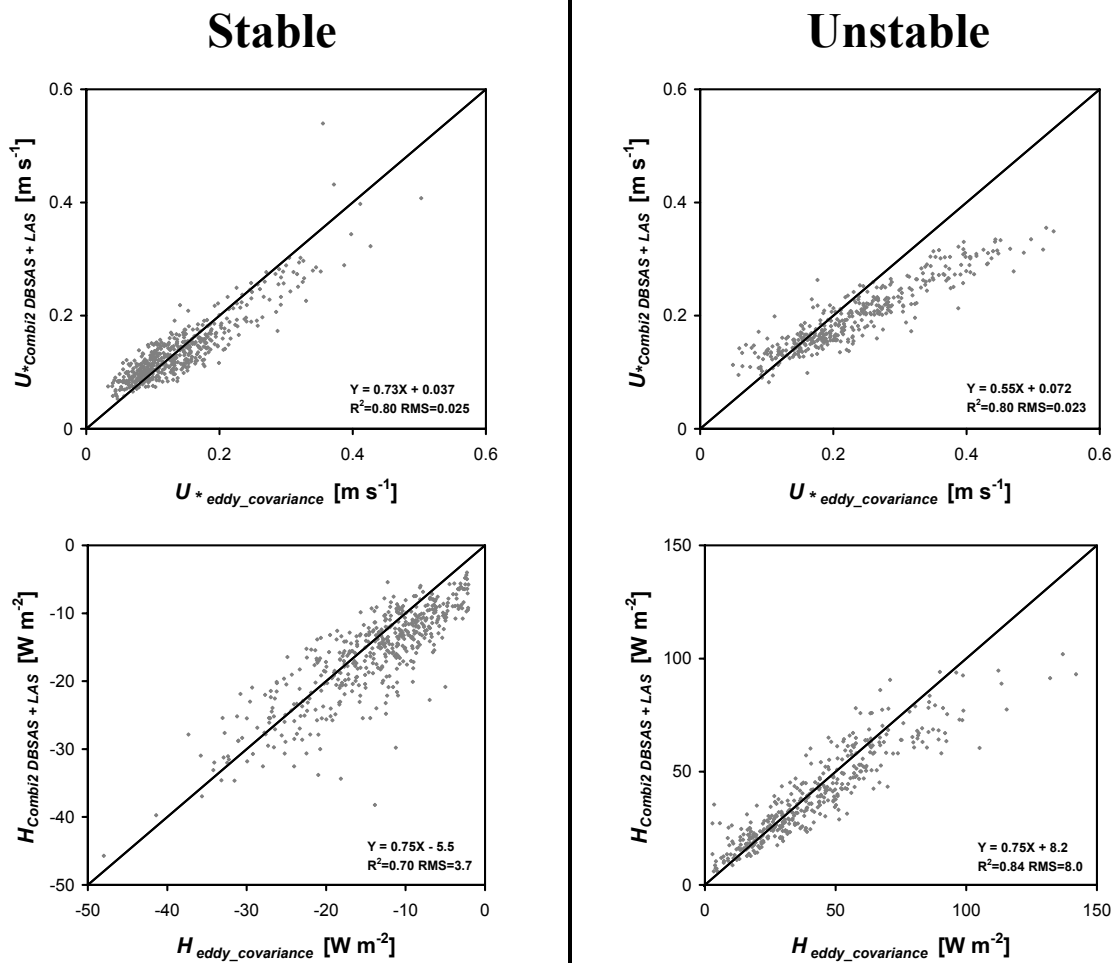


Figure 5-9: Comparison between u_* and H determined with *Combi2*, a combination of a LAS and both beams of the DBSAS and eddy-covariance measurements for stable (left) and unstable (right) conditions.

Figure 5-9 gives an overview of the comparison of u_* , and H derived from EC (or sonic anemometer) measurements and *Combi2*. ε and C_T^2 are not given here because they are basically the same as for the DBSAS (ε) and LAS (C_T^2). For unstable conditions, the agreement between *Combi2* and EC u_* is very similar to what was found for the DBSAS. For stable conditions, however, the range in the *Combi2* u_* is more limited than for the DBSAS u_* , i.e. the *Combi2* u_* groups in a cloud of points between $u_* = 0.1$ and 0.2 m s^{-1} . The same was also seen for *Combi1* and the LAS u_* . With ε being the same between the DBSAS and *Combi2*, it must be the difference between the LAS and DBSAS C_T^2 and its influence on u_* through the stability functions that explains the difference found for u_* . The cluttered u_* results in more spread in the *Combi2* stable H compared with the DBSAS. For unstable conditions, the combination of u_* that shows some systematic deviation but with little scatter and a good estimate of C_T^2 leads to a H -estimate that shows the least scatter of all the scintillometer configurations considered.

5.5 Conclusions

Starting point of this study were the DBSAS experiments at the CASES-99 (Hartogensis et al., 2002) and WINTeX (De Bruin et al., 2002). In both experiments the DBSAS gave systematic deviations in the turbulent fluxes with respect to eddy covariance derived fluxes. We performed an experiment at Cabauw, the Netherlands where we compared three field scale scintillometer configurations: the DBSAS, LAS and combined DBSAS-LAS configurations. The main objective of this study was to see whether the LAS and combined scintillometer configurations show the same systematic deviations in the fluxes as the DBSAS.

Based on the results presented in this paper we conclude the following:

- For the DBSAS we find the same systematic deviations combined with little scatter for ε , C_T^2 and resulting u_* and H as were reported by Hartogensis et al. (2002) for CASES-99 and by De Bruin et al. (2002) for WINTeX, which were the starting points of this study. Generally, the DBSAS ε and u_* are overestimated for small ε and u_* values, and underestimated for large ε and u_* values.
- Direct flux-estimates from the principle DBSAS measurements, r_{DBSAS} and B_{I_DBSAS} give, given the simplicity of the approach, good flux-estimates, especially for u_* and H for stable conditions.
- For the LAS, the C_T^2 -estimate is better than the DBSAS C_T^2 -estimate. u_* in the LAS method is determined with flux profile relations which require a wind speed measurement and an estimate of the roughness length. Surprisingly, the u_* -estimates are quite good, especially for unstable conditions, but for stable conditions much more scatter is seen than for the DBSAS. For unstable conditions this leads to a slightly better estimate of H , when compared with the DBSAS, since for unstable conditions

turbulence is mainly convection (C_T^2) driven. For stable conditions, this leads to a considerably worse H -estimate, when compared with the DBSAS, since for stable conditions turbulence is mainly driven by mechanical turbulence (u^*).

- The DBSAS-LAS configuration in which l_0 and C_n^2 are jointly solved from B_{I_DBSAS} and B_{I_LAS} gives the same results for C_T^2 as for the LAS, but disappointing results for l_0 , especially for unstable conditions. Apparently this set-up is very sensitive to a combination of B_{I_DBSAS} and a C_n^2 -estimate that is fully consistent with each other in solving l_0 . Deviations in C_n^2 due to different sensors, small difference in height and location lead to large errors in the l_0 -estimate. This is also reflected in the flux-estimates. u^* gives a lot of scatter for both stable and unstable conditions. For stable conditions this scatter dominates the H -estimate. For unstable conditions, the H is mainly C_T^2 driven and gives a reasonable agreement with the EC H .
- The DBSAS-LAS configuration in which l_0 and C_n^2 are solved from r_{DBSAS} and B_{I_LAS} give much better results. In this configuration the LAS gives C_T^2 and the DBSAS ε . This set-up combines the better of the two instruments. C_T^2 is determined with the LAS at inertial range eddy scales, and ε is determined from the DBSAS, over the same path as C_T^2 . Unlike the DBSAS, the u^* for stable conditions of the LAS and the two DBSAS-LAS configurations shows a limited range. This has to do with the interaction between C_T^2 and ε in the flux calculations. As a result, H shows more scatter for stable conditions than with the DBSAS. For unstable conditions H of this DBSAS-LAS configuration gives the best results.
- The MOST functions proposed by Hartogensis and De Bruin (2005) for CASES-99. also worked well at Cabauw.
- The working hypothesis of Hartogensis et al. (2002) to adopt a displacement distance between the two DBSAS beams of 2.6 mm instead of 2.7 mm is not a general solution that explains the systematic DBSAS errors in ε and the fluxes.
- We introduced a practical approach to correct for the LAS inner scale dependence, which depends on the instruments aperture and l_0 . The LAS used in this study had an aperture of 10 cm. In low wind speed conditions, when l_0 is large the inner scale correction can be as much as 30% on C_T^2 .
- We introduced a new analytical expression of the model of the temperature spectrum at the dissipation range of Hill (1978), also known as the ‘‘Hill bump’’. The analytical fit obeys the condition set by Frehlich (1992) in his Equation (21) fairly well and facilitates the calculation of l_0 from the principle DBSAS measurements.

We recommend further research on issues that might explain the systematic deviations of the DBSAS fluxes being the coherent light source, the influence of turbulence on the polarisation of the beams and mast vibrations. Furthermore, we recommend integrating a DBSAS-LAS system in one instrument.

Appendix 5A Inner scale sensitivity of the LAS

The C_n^2 measured by a LAS is based on Equation (5.5), i.e. the integrated form of the B_{I_LAS} description given in Equation (5.4) applying the inertial range spectrum for ϕ_n . Hill and Ochs (1978), however, showed that for $D/l_0 < 20$ the LAS becomes sensitive for the Hill bump, which implies that B_{I_LAS} no longer depends on C_n^2 alone, but also on l_0 . In this Appendix we discuss the results of Hill and Ochs (1978) and introduce a practical correction procedure for the inner scale dependence of the LAS.

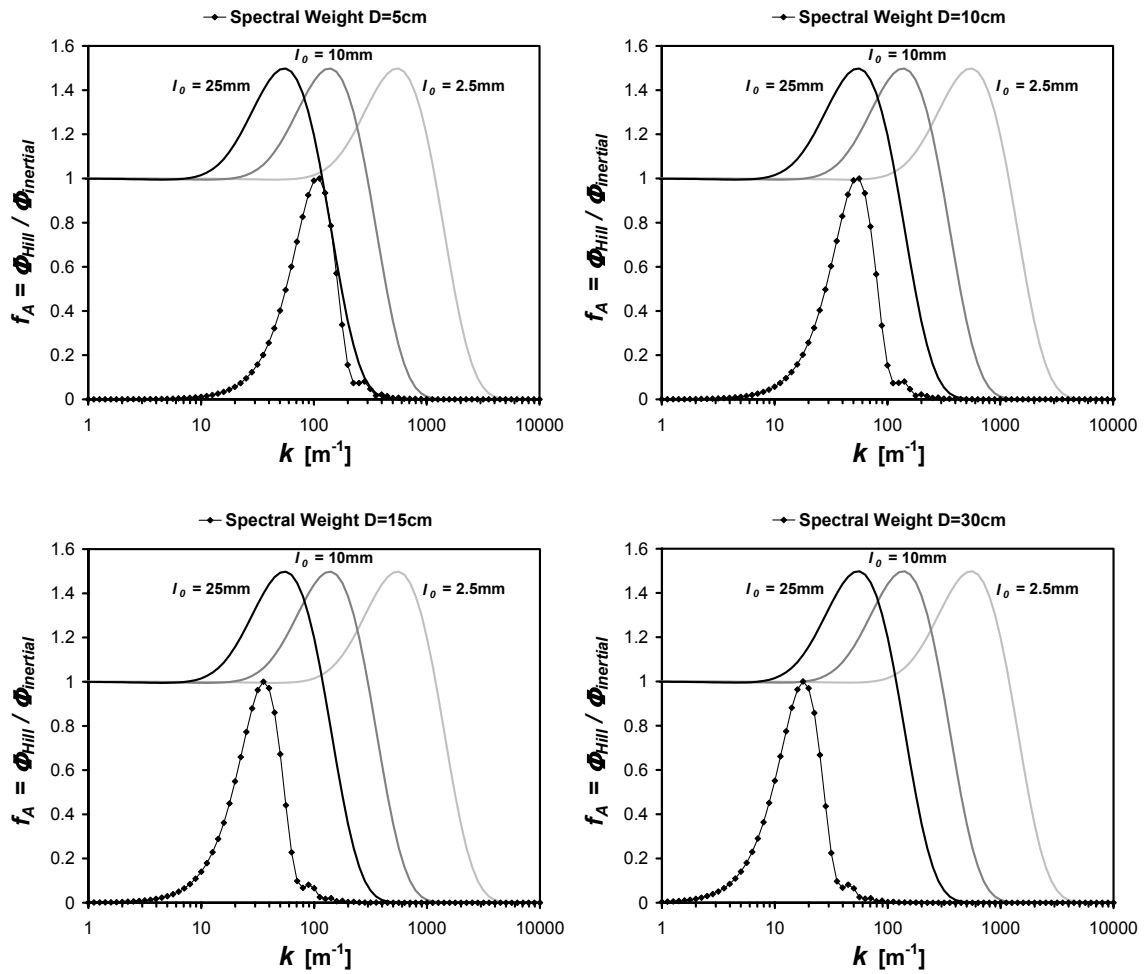


Figure 5-10: Different plots for four aperture diameters ($D = 5$ cm, 10 cm, 15 cm and 30 cm): the LAS spectral weighting function, normalised by its maximum value, and the Hill spectrum normalised by the inertial spectrum (f_A in Equation 5.2) for three values of the inner scale ($l_0 = 2.5$ mm, 10 mm and 25 mm).

To illustrate the effect of the LAS inner scale dependence we present Figure 5-10, where four sub-plots depict the LAS spectral weighting function for different aperture sizes together with the Hill bump (the Hill spectrum normalised by the inertial range spectrum), which is given for three values of l_0 . The LAS spectral weighting function is obtained by removing the spectrum from Equation (5.4) and integrating the x -dependant part of the remainder over the

path length, L (see also Equation 3.3). For $D = 5$ cm we can see the following in Figure 5-10. For $l_0 = 2.5$ mm, the LAS is mainly sensitive to the inertial range eddy sizes, i.e. the bulk of the spectral weighting is in a part of the spectrum where $f_A = 1$. Here C_n^2 is not sensitive to l_0 and applying the inertial range or the Hill spectrum gives the same results. For $l_0 = 10$ mm, the bulk of the spectral weighting is in the middle of the Hill bump, and C_n^2 thus becomes dependant of l_0 . It can be seen from Equation (5.4) that with the added spectral energy of the Hill bump the resulting C_n^2 will be lower than the inertial range C_n^2 . For $l_0 = 25$ mm, the bulk of the spectral weighting is beyond the Hill bump, where spectral fall off exceeds the $k^{-11/3}$ of the inertial range and $f_A < 1$. Here, the Hill spectrum C_n^2 will be higher than the inertial range C_n^2 . With increasing D , the spectral weighting function shifts to lower wave numbers and for a larger range of l_0 the inertial range spectrum can be applied.

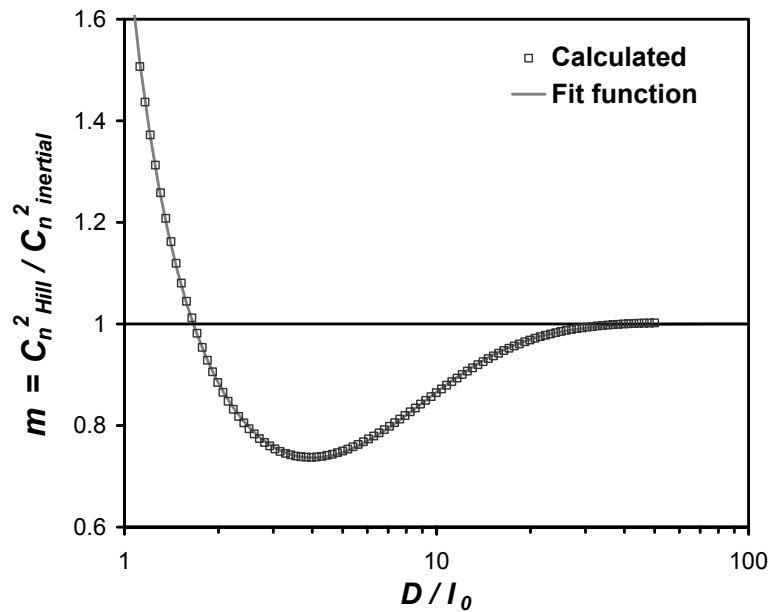


Figure 5-11: Correction factor for the LAS derived C_n^2 using the inertial spectrum for the LAS inner scale dependence (or Hill spectrum dependence) as a function of D/l_0 . The squares represent the calculated values, the drawn line the fit function (Equation 5.20) through the squares.

Figure 5-11 summarises Figure 5-10 for all D and all l_0 . The range in D/l_0 is chosen such that it falls within a physically relevant range, i.e. the minimum value corresponds to $D = 1$ cm with $l_0 = 40$ mm, and the maximum value corresponds to $D = 100$ cm with $l_0 = 1$ mm. Figure 5-11 is the inverse of Figure 1 in Hill and Ochs (1998), who plotted D/l_0 for an even wider range. m in Figure 5-11 is the correction factor for inertial range C_n^2 measured by the LAS:

$$C_{n_cor}^2 = \frac{C_{n_Hill}^2}{C_{n_Inertial}^2} C_{n_Inertial}^2 = m C_{n_Inertial}^2 \quad , \quad (5.19)$$

where $C_n^2_{cor}$ is the corrected LAS C_n^2 . It can be seen that $m = 1$ for $D/l_0 > 20$; $m < 1$ when the LAS spectral weighting function sees the Hill bump; and $m > 1$ for very small D and large l_0 when the spectral weighting function only sees the tail of the Hill bump. The maximum C_n^2 correction for $m < 1$ is 30%.

We found the following fit through the calculated points in Figure 5-11:

$$m(\xi) = \frac{e^{0.72\xi^2}}{1 + 0.433 e^{-[0.89(\ln(\xi) - \ln(3.3))]^2}}, \quad (5.20)$$

with $\xi = D/l_0$. Note that to apply Equation (5.20) $D > 2\sqrt{\lambda L}$ must be met, which is also a necessary condition for Equation (5.4).

Equation (5.20) is applied by adding an iteration loop to the one described in Section 5.4.2 for solving H and u^* from the LAS C_T^2 and the flux profile relations. Initially, H and u^* are iteratively solved with the inertial range C_n^2 . Next, with u^* known, l_0 can be determined from the ε -MOST scaling (Equation 5.12) and the C_n^2 inner scale correction can be applied, with which new fluxes can be determined. This procedure usually converges after 3 to 4 steps. As a bonus also an estimate of l_0 and ε is obtained, albeit indirectly from flux profile relations:

$$l_0 = 7.4 \left(\frac{\nu}{u^*} \right)^{3/4} \left(\frac{k_{kar} z}{f_\varepsilon(z/L_{MO})} \right)^{1/4}. \quad (5.21)$$

Note that for very low values of u^* Equation (5.21) explodes and unrealistically high values for l_0 are obtained. We dealt with this by setting a maximum value to l_0 , and with that also to the C_n^2 inner scale correction, for $l_0 = 30$ mm.

Appendix 5B Comparing or combining ε and C_T^2 taken at different heights

As both the wind speed and temperature variances decrease with height, ε and C_T^2 , which are measures of the height of the energy spectra of wind speed and temperature, also decrease with height. When comparing or combining ε and C_T^2 taken at different levels one has to take into account the height dependence of both parameters. In this study we *compare* ε and C_T^2 determined with a sonic anemometer and three scintillometer configurations. The scintillometers were installed at height between 2.52 m and 2.72 m, and the sonic anemometer was installed at 3.32 m. Furthermore, in this study we *combine* a DBSAS installed at 2.52 m with a LAS at 2.72 m (see Sections 5.2.3 and 5.4.3).

The height dependence of ε and C_T^2 is defined by their scaling groups of Equations (5.9) and (5.8). From these the ratios of ε and C_T^2 taken at heights z_1 and z_2 follow directly:

$$\frac{\varepsilon_1}{\varepsilon_2} = \frac{f_\varepsilon(\zeta_1)\left(\frac{z_2}{z_1}\right)}{f_\varepsilon(\zeta_2)\left(\frac{z_1}{z_2}\right)} = S_\varepsilon\left(\frac{z_2}{z_1}\right) \quad (5.22)$$

and

$$\frac{C_{T1}^2}{C_{T2}^2} = \frac{f_T(\zeta_1)\left(\frac{z_2}{z_1}\right)^{2/3}}{f_T(\zeta_2)\left(\frac{z_1}{z_2}\right)^{2/3}} = S_{CT2}\left(\frac{z_2}{z_1}\right)^{2/3}. \quad (5.23)$$

The subscripts 1 and 2 of the parameters ε , C_T^2 and ζ refer to their measurement heights z_1 and z_2 . We follow the convention that z_1 indicates the lower and z_2 the higher level. It is seen that the height dependences of ε and C_T^2 consist of two terms. The first term, which we introduce as S_ε and S_{CT2} depends on stability. The second term is a constant that depends on the ratio of z_1 and z_2 . S_ε and S_{CT2} are 1 for neutral conditions ($\zeta \rightarrow 0$), which defines the second term as the height dependence for neutral conditions. S_ε and S_{CT2} can be more or less than 1 for non-neutral conditions depending on the shape of the f functions. Note that the neutral height dependence is defined by the ratio of z_1 and z_2 , which means that also a small height difference at low levels can give a considerable correction, whereas S_ε and S_{CT2} depend on the difference between z_1 and z_2 , which at low levels will always be small.

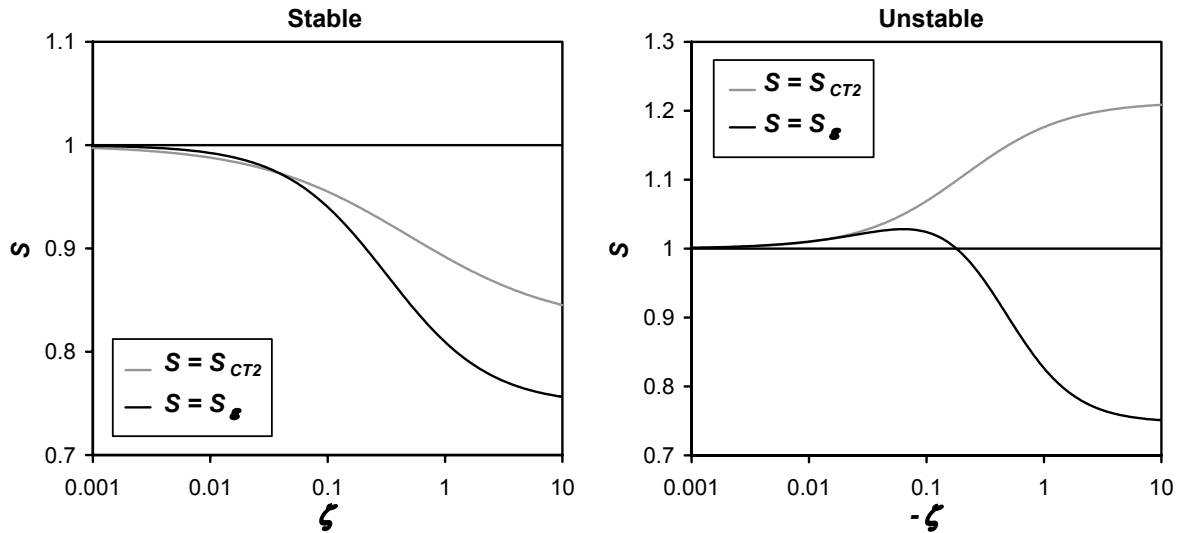


Figure 5-12: Correction factors, S_ε and S_{CT2} (see Equations 5.22 and 5.23), to the neutral height dependence of C_T^2 and ε for stable (left) and unstable (right) conditions as a function of ζ . S_ε and S_{CT2} are based on EC fluxes and C_T^2 -estimates at $z_2 = 3.32$ m and are taken with respect to $z_1 = 2.52$ m.

It is not convenient that, to rescale ε and C_T^2 with height, information on the size of the fluxes is needed. Most probably, the uncertainties in the flux-estimates will add scatter to ε and C_T^2

comparisons rather than removing a bias due to the height dependence. Therefore, in comparing and combining ε and C_T^2 data we will only use the neutral height correction. To have an idea of the influence of stability on the height dependence we give in Figure 5-12 S_ε and S_{CT2} as a function of ζ . S_ε and S_{CT2} are based on EC fluxes and C_T^2 -estimates at $z_2 = 3.32$ m and are scaled with respect to $z_1 = 2.52$ m, the height of the DBSAS.

The neutral height correction predicts that ε_1 and C_{T1}^2 are a factor 1.3 and 1.2 higher than the measured ε_2 and C_{T2}^2 . S_ε and S_{CT2} given in Figure 5-12 are corrections to these factors. It is seen that in stable conditions $S < 1$, which means it lowers the neutral height correction for ε and C_T^2 . In unstable conditions S_ε can be both smaller and larger than 1, and $S_{CT2} > 1$. It is also seen that the impact of S is largest for stable conditions. $S < 1$ expresses an overestimation of ε_2 and C_{T2}^2 with respect to ε_1 and C_{T1}^2 when only the neutral height dependence is taken into account (see Equations 5.22 and 5.23). In contrast, $S > 1$ expresses an underestimation of ε_2 and C_{T2}^2 with respect to ε_1 and C_{T1}^2 .

In this article we only scale ε and C_T^2 taken at different levels with their neutral height dependence in comparing or combining ε and C_T^2 . To facilitate the discussions of Section 5.4 we give Table 5-1, which expresses whether ε , C_T^2 and the fluxes H and u^* are large or small for very stable and very unstable conditions when deviations from the neutral height dependence are largest. For very stable conditions it is seen, for example, that by ignoring the stability effect in the C_T^2 height dependence, we would expect to see in Figure 5-2 that for large C_T^2 ($z^{2/3} C_T^2$)_{EC} overestimates ($z^{2/3} C_T^2$)_{DBSAS}. The contrary is found, which means that DBSAS overestimation of C_T^2 in fact is even worse.

Table 5-1: Qualitative indication of the variables ε , C_T^2 , H , u^* and the correction factors, S_{CT2} and S_ε , to the neutral height dependence of C_T^2 and ε for very stable and very unstable conditions. “Large” is indicated with $>$, “small” with $<$, both large and small values is indicated with $<>$.

	ε	C_T^2	$ H $	u^*	S_{CT2}	S_ε
Stable for $\zeta \rightarrow \infty$	$<$	$>$	$<$	$<$	<1	<1
Unstable for $\zeta \rightarrow \infty$	$<>$	$>$	$>$	$<>$	>1	<1 and $>1^{**}$

** largest effect of the two

Finally, we give based on Equations (2.21) and (5.22) the height dependence of l_0

$$\frac{l_{0_1}}{l_{0_2}} = S_\varepsilon^{-1/4} \left(\frac{z_2}{z_1} \right)^{-1/4}, \quad (5.24)$$

which is relevant for the DBSAS-LAS configurations where l_0 determined at DBSAS height is used at the LAS height to perform the inner-scale dependence correction outlined in Appendix 5A. The $-1/4$ power makes l_0 not very height dependant, which is a convenient feature for the DBSAS-LAS configuration.

Appendix 5C Test of Monin-Obukhov scaling functions for ε and C_T^2

One of the side-objectives of this study was to independently test the new stable Monin-Obukhov similarity (MOS) relationships for ε and C_T^2 based on CASES-99 sonic anemometer data published by Hartogensis and De Bruin (2005), hereafter denoted as HdB. Figure 5-13 compares the ε and C_T^2 MOS scaling based on BBC sonic anemometer data and the f_ε and f_T scaling functions found by HdB based on CASES-99 data. The stability range for the stable BBC data is more limited (max $\zeta = \sim 2$) than for CASES-99 (max $\zeta = \sim 10$). For f_ε , the CASES-99 f_ε function agrees well with the BBC data. An important feature found by HdB is that $f_\varepsilon < 1$ in the neutral limit ($\zeta \rightarrow 0$), which is also seen in the BBC data. For f_T , on the other hand, a lot more scatter is seen in the BBC data than HdB found for the CASES-99 data set. According to these data no relationship exists between the C_T^2 scaling group and ζ .

Indirectly the HdB f_ε and f_T functions were already tested through the stable flux-estimates of the different scintillometer configurations, generally showing more scatter for u^* than for H . In part this is due to less scatter already found in ε than in C_T^2 . As is seen in Figure 5-13, also the poor relation between the C_T^2 and the fluxes for the stable conditions during the BBC campaign adds to the scatter.

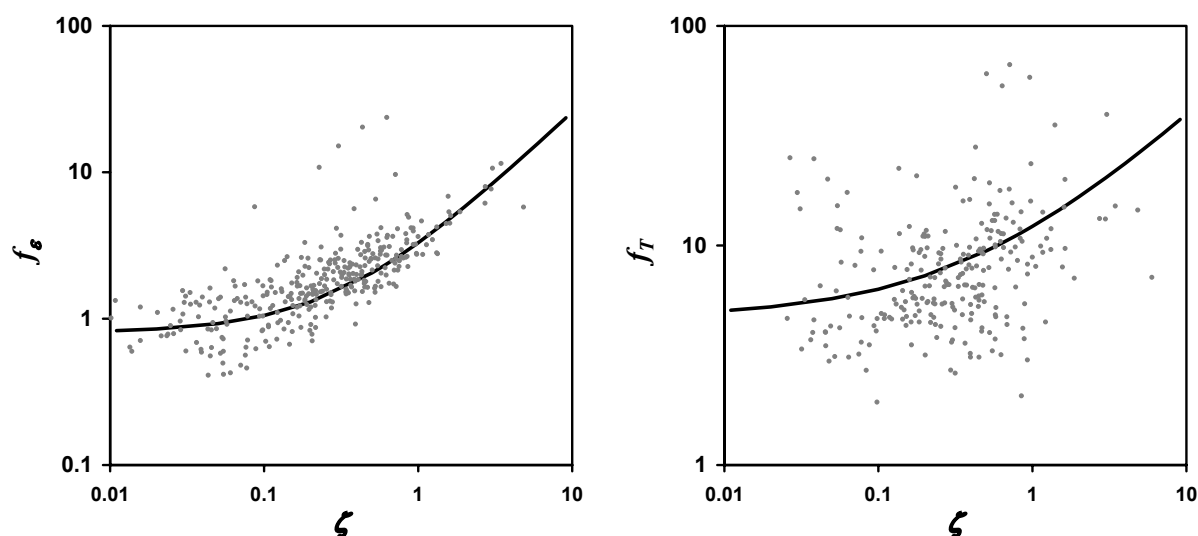


Figure 5-13: MOS scaling groups for ε and C_T^2 based on sonic anemometer measurements taken during the BBC campaign (data points) and the f_ε and f_T scaling functions of HdB based on the CASES-99 dataset (solid lines) for ε (left) and C_T^2 (right).

Chapter 6 Derivation of an effective height for scintillometers: La Poza experiment in Northwest-Mexico

6.1 Introduction

A scintillometer receiver measures intensity fluctuations in the radiation emitted by the transmitter. These fluctuations are caused by refractive scattering of turbulent eddies along the propagation path. From these measurements, depending on the transmitter source used, the structure parameters of temperature, C_T^2 , or humidity, C_q^2 , can be determined. From these, together with an estimate of the roughness length and wind speed measurements at a single level, the sensible heat flux, H , and latent heat flux, $L_v E$, can be calculated using Monin-Obukhov similarity theory (MOST).

Much of the theoretical work on the scintillometer method was done in the 1970s; see, e.g., Andreas (1990) and the overview article by Hill (1997). During the last decade more emphasis has been put on the application of the method to determine area-averaged fluxes of heat and water vapour at a scale of 1 to 10 km on a routine basis; see, for instance, the special issue on scintillometry in *Boundary-Layer Meteorology* (De Bruin, 2002).

The ability to directly determine surface fluxes at these large scales is especially attractive to modellers. They need area-averaged fluxes as input for, or verification of their model at scales similar to, or greater than a model grid cell. Hydrological studies, that require fluxes at catchment scale, and remote sensing techniques, that need fluxes at the scale of a satellite pixel, are fields that benefit from the scintillometer method.

Different types of scintillometers have been developed. The large-aperture scintillometer (LAS) that is used in this study is an optical instrument with which C_T^2 and consequently H can be determined. Over the last decade, a great number of applied LAS studies have been presented, proving the LAS applicability to routinely obtain estimates of H at low cost. De Bruin et al. (1995) and McAneney et al. (1995) tested the LAS over a homogeneous surface. Meijninger et al. (2002a) showed the LAS can also be used to obtain H over heterogeneous surfaces. Poggio et al. (2000) used a LAS with two detectors to measure crosswind speed over complex terrain. Beyrich et al. (2002) described a long-term study in which a LAS is used to determine fluxes on an operational basis. Watts et al. (2000) used a LAS for “ground-truth” verification for fluxes derived from AVHRR satellite images. Kohsiek et al. (2002) deployed an extra large aperture scintillometer (XLAS) to obtain fluxes over a path length of almost 10

-
- This Chapter is based on Hartogensis, O.K., Watts, C.J., Rodriguez, J.-C., De Bruin, H.A.R.: 2003, ‘Derivation of the effective height for scintillometers: La Poza experiment in Northwest Mexico’, *Journal of Hydrometeorol.* **4**, 915-928
 - Appendix 6D has been added in this thesis.

km. Of interest to hydrometeorological applications in particular are the LAS studies over wet/irrigated areas by Green and Hayashi (1996), Meijninger and De Bruin (2000) and Hoedjes et al. (2002), and the publications on radio-wave scintillometry. With the radio-wave scintillometer, C_q^2 , and consequently $L_v E$ can be determined (Green et al. 2001 and Meijninger et al, 2002b).

Scintillometer measurements are increasingly performed over heterogeneous and non-flat terrain. In catchment studies, for example, measurements are required in a certain region of interest, where one often encounters non-ideal circumstances. In addition, for scintillometer set-ups over large distances, the instrument is often installed on hills, or high structures, such as buildings, which might not be available at both ends of the path or are of different height, resulting in a slanted scintillometer beam.

In all these situations, the scintillometer beam height varies along the path. This means that the scintillometer measurements represent not only a horizontal, but also a vertical average of C_T^2 . The average height of transmitter and receiver, in that case, does not represent the height of the vertically averaged C_T^2 , because C_T^2 does not vary linearly with height, and the scintillometer signal is weighted towards the middle of the path. This is an important issue since H derived from the LAS C_T^2 measurements is particularly sensitive to the height of the instrument, as will be discussed in Appendix 6A and Section 6.4.1.

In this study we will explain what effective height to use when analysing scintillometer data to derive H . Several aspects will be covered: slanted path over flat terrain, structured terrain, varying path height due to the curvature of the earth's, and footprint effects in case of irregular variations upstream of the path.

To test the derived effective height formulations, we present LAS data taken during a field experiment in September and October of 1996 at a rangeland site called La Poza in the Sonoran desert in northwest Mexico. We experimented with a LAS set-up in which the heights of the transmitter and receiver above the surface were significantly different (factor of 5). To test the performance of the LAS under a “normal” situation, i.e. for a horizontal path, we also deployed a LAS set-up over a path that was more or less parallel to the surface. The LAS-derived sensible heat flux was compared with eddy-covariance data for both experiments. We will refer to the slant-path experiment as “experiment I” and to the horizontal-path experiment as “experiment II”.

6.2 Theory

6.2.1 Determining the sensible heat flux with a large-aperture scintillometer

The theoretical description of the LAS was first given by Wang et al. (1978). They derived the following expression relating the variance of the logarithm of the intensity fluctuations of the measured light intensity, $\sigma_{\ln(I)}^2$, to the structure parameter of the refractive index, C_n^2 :

$$\sigma_{\ln(I)}^2 = \int_0^1 C_n^2(u)W(u)du. \quad (6.1)$$

$W(u)$ can be seen as a weighting function describing the contribution from $C_n^2(u)$ at each point along the path to the total LAS signal, $\sigma_{\ln(I)}^2$. It is given as

$$W(u) = 16\pi^2 K^2 L \int_0^\infty k \phi_n(k) \sin^2 \left[\frac{k^2 Lu(1-u)}{2K} \right] \left[\frac{2J_1(x_1)2J_1(x_2)}{x_1 x_2} \right]^2 dk, \quad (6.2)$$

where $u = x/L$ is the dimensionless coordinate along a propagation path of length L , $K = 2\pi/\lambda$ is the optical wave-number, k the turbulent spatial wave-number, $\phi_n(k)$ is the three-dimensional spectrum of the refractive index in the inertial range ($\phi_n(k) = 0.033k^{-11/3}$), and $J_1(x_1)$ and $J_1(x_2)$ are Bessel functions of the first kind with $x_1 = kDu/2$ and $x_2 = kD(1-u)/2$, where D is the aperture diameter.

$W(u)$ has a bell-shaped form resulting in a maximum weight towards the middle of the path and zero weight near the transmitter and receiver.

Substituting Equation (6.2) into Equation (6.1) and integrating numerically, Wang et al. (1978) obtained

$$\overline{C_n^2} = 1.12 \sigma_{\ln(I)}^2 D^{7/3} L^{-3}, \quad (6.3)$$

where the over-bar represents a spatial average.

In a turbulent medium like the atmosphere, both temperature and humidity fluctuations affect refractive index fluctuations. Thus, C_n^2 can be expressed as a function of its related variables C_T^2 and C_q^2 , the structure parameters of temperature and humidity, respectively. For the visible and infrared regions of the electromagnetic spectrum - in which our LAS operates - temperature fluctuations, i.e. C_T^2 , dominate the C_n^2 signal. Under the assumption that the correlation coefficient between temperature and humidity, R_{Tq} , is positive and close to 1, Wesely (1976) derived a direct relationship between C_n^2 and C_T^2 where the humidity contribution to C_n^2 is expressed in terms of the Bowen ratio, Bo :

$$C_T^2 = C_n^2 \left(\frac{T^2}{-0.78 \cdot 10^{-6} P} \right)^2 \left(1 + \frac{0.03}{Bo} \right)^{-2}, \quad (6.4)$$

where T is temperature (K) and P is air pressure (Pa). In this study we will consider only unstable daytime conditions, where the condition $R_{Tq} = +1$ is approximately met.

Furthermore, it can be seen that whenever $Bo > \sim 0.6$, the humidity correction is less than 10%. For larger Bowen ratios, this term can be safely neglected.

According to MOST, C_T^2 made dimensionless with the temperature scale θ_* is a universal function of the stability parameter Z_{LAS} / L_{MO} :

$$\frac{C_T^2 Z_{LAS}^{2/3}}{\theta_*^2} = f_T \left(\frac{Z_{LAS}}{L_{MO}} \right), \quad (6.5)$$

where Z_{LAS} is the LAS height, and L_{MO} the Monin-Obukhov length. For unstable conditions, Wyngaard et al. (1971) proposed

$$f_T \left(\frac{Z_{LAS}}{L_{MO}} \right) = c_1 \left(1 - c_2 \frac{Z_{LAS}}{L_{MO}} \right)^{-2/3}, \quad (6.6)$$

with $c_1 = 4.9$ and $c_2 = 7$. We used an adjusted value for c_2 ($c_2 = 6.1$) after Andreas (1989) to reflect a von-Kármán constant, κ_{kar} , of 0.4 rather than 0.35 used by Wyngaard et al. (1971). To calculate the sensible heat flux, H , defined as $H = -\rho C_p u_* \theta_*$, an additional expression is needed to solve for u_* , the friction velocity. Usually a standard Businger-Dyer flux-profile relation is used (see e.g Panofsky and Dutton, 1984):

$$u_* = \frac{\kappa_{kar} U}{\ln \left(\frac{Z_{cup}}{z_0} \right) - \psi_m \left(\frac{Z_{cup}}{L_{MO}} \right) + \psi_m \left(\frac{z_0}{L_{MO}} \right)}, \quad (6.7)$$

where z_0 is the roughness length, U the wind speed at height Z_{cup} , and ψ_m is the integrated stability function for momentum, which for unstable conditions is defined as $\psi_m (Z_{cup} / L_{mon}) = 2 \ln[(1+x)/2] + \ln[(1+x^2)/2] - 2 \arctan(x) + \pi/2$, with $x = (1 - 16Z_{cup} / L_{MO})^{1/4}$

Next, the set of Equations (6.5) to (6.7) can be solved iteratively using $L_{MO} = T u_*^2 / (\kappa_{kar} g \theta_*)$ to give θ_* and u_* from which H follows from its definition. g is the gravitational acceleration.

It can be shown that H becomes independent of L_{MO} for very unstable (or so-called local free convection) conditions (e.g., Andreas, 1991),

$$H = \rho c_p b Z_{LAS} \left(\frac{g}{T} \right)^{1/2} (C_T^2)^{3/4}, \quad (6.8)$$

where $b = 0.47$ for $\kappa_{kar} = 0.4$ and the empirical constants of Equation (6.6), $c_1 = 4.9$ and $c_2 = 6.1$.

Whenever measurements are taken over tall and dense roughness obstacles, such as houses or trees, a displacement distance, d , should be applied such that Z_{LAS} and Z_{cup} in Equations (6.5) and (6.7) are replaced by $(Z_{LAS} - d)$ and $(Z_{cup} - d)$ (e.g Panofsky and Dutton, 1984).

6.2.2 Derivation of an effective scintillometer height

In Appendix 6A, the sensitivity of H to the LAS height, Z_{LAS} , is investigated. There we show that for free convection conditions a relative error in Z_{LAS} causes an equal relative error in H (see also Equation 6.8); whereas for neutral conditions, the relative error in H due to Z_{LAS} is half the relative error in Z_{LAS} . The fact that H is so sensitive to Z_{LAS} indicates the importance of determining Z_{LAS} as accurately as possible. This, in turn, shows the relevance of introducing an effective LAS height for situations where the height of the LAS beam is not constant over the path.

From Equation (6.4) it can be seen that C_n^2 and C_T^2 relate linearly to each other. Thus, combining Equations (6.1), (6.3), and (6.4) yields the path-averaged structure parameter of temperature, $\overline{C_T^2}$:

$$\overline{C_T^2} = \int_0^1 C_T^2(u)G(u)du, \quad (6.9)$$

where $G(u) = W(u) / \int_0^1 W(u)du$ is the weighting function describing the contribution of $C_T^2(u)$ at each point along the normalised path, u , to the total LAS weighted $\overline{C_T^2}$.

When the scintillometer beam does not have a constant height along the path, the resulting LAS weighted $\overline{C_T^2}$ represents both a horizontal and a vertical average of $C_T^2(u)$. The range in $C_T^2(u)$ due to a varying beam height can be very large, as C_T^2 is a strong function of height (see Equation 6.5). To calculate H , however, a single value of Z_{LAS} is needed that corresponds best to the $\overline{C_T^2}$ measurement. We will call this value of Z_{LAS} the ‘‘effective height’’, Z_{eff} . By definition, the full expression for the effective height, Z_{eff_Full} follows from Equation (6.5):

$$\overline{C_T^2} \equiv \theta_*^2 f_T \left(\frac{Z_{eff_Full}}{L_{MO}} \right) Z_{eff_Full}^{-2/3}. \quad (6.10)$$

Similarly, for $C_T^2(u)$ with $Z(u)$ is the scintillometer beam height along the path applies

$$C_T^2(u) \equiv \theta_*^2 f_T \left(\frac{Z(u)}{L_{MO}} \right) Z(u)^{-2/3}. \quad (6.11)$$

Substituting Equation (6.10) and (6.11) into Equation (6.9) and assuming a constant flux layer, i.e. $d\theta^*/dz$ and dL_{MO}/dz are zero yields

$$Z_{eff_Full}^{-2/3} f_T \left(\frac{Z_{eff_Full}}{L_{MO}} \right) = \int_0^1 Z(u)^{-2/3} f_T \left(\frac{Z(u)}{L_{MO}} \right) G(u) du . \quad (6.12)$$

Z_{eff_Full} is solved iteratively in conjunction with θ^* and u^* from the iterative procedure described in Section 6.2.1. Appendix 6B shows that substituting Equation (6.6) into Equation (6.12) produces a quadratic relation with a simple solution for Z_{eff_Full} . Note that the effective height depends on stability, and a different Z_{eff_Full} is obtained for every C_T^2 averaging period. It is important to note that the underlying fundamental assumption of Equation (6.12), i.e. the presence of a constant flux layer, means that C_T^2 is in equilibrium with the surface. For homogeneous, flat surfaces this is generally true. For heterogeneous and structured surfaces this assumption still holds as long as the measurements are taken at a level above the top of the internal boundary layers of the heterogeneous patches, where the individual patch signatures merge due to turbulent mixing. This height is often referred to as the blending height. Meijninger et al. (2002a) present a detailed study of the use of scintillometers over heterogeneous surfaces in terms of blending height and footprint of the measurements. They conclude that, for scintillometer measurements below the blending height over moderately heterogeneous surfaces, the violation of the assumptions underlying Equation (6.12) is small and reliable fluxes can still be obtained if one accounts for the spatial flux distribution in the source area.

When the variation in height along the path is relatively small, the effective height can be estimated with a single value (as opposed to solving Z_{eff_Full} with Equation (6.12) for every flux averaging-interval) with three levels of approximation.

The first approximation considers Equation (6.12) for either neutral or free convection conditions. In these stability limits Z_{eff_Full} becomes stability independent. For the free convection case, i.e. $Z_{LAS}/L_{MO} \rightarrow -\infty$, f_T as defined in Equation (6.6) develops into

$\lim_{Z_{LAS}/L_{MO} \rightarrow -\infty} f_T \propto Z_{LAS}^{-2/3}$ as $|Z_{LAS}/L_{MO}| \gg 1$, and Equation (6.12) simplifies to

$$Z_{eff_Fc} = \left[\int_0^1 Z(u)^{-4/3} G(u) du \right]^{-3/4} . \quad (6.13)$$

For the neutral case, i.e. $Z_{LAS}/L_{MO} \rightarrow 0$, f_T as defined in Equation (6.6) develops into

$\lim_{Z_{LAS}/L_{MO} \rightarrow 0} f_T \propto const$, and Equation (6.12) simplifies to

$$Z_{eff_Neutral} = \left[\int_0^1 Z(u)^{-2/3} G(u) du \right]^{-3/2} . \quad (6.14)$$

The solutions for Z_{eff_Full} lie between Z_{eff_Fc} and $Z_{eff_Neutral}$. Depending on the conditions, Z_{eff_Full} can be estimated by taking either Z_{eff_Fc} or $Z_{eff_Neutral}$ or the average between the two. The second approximation assumes that both the influences of stability and the $-2/3$ height-dependency of Equation (6.12) are negligible, which results in

$$Z_{eff_WeightAvg} = \int_0^1 Z(u)G(u)du , \quad (6.15)$$

where the subscript “WeightAvg” refers to the fact $Z(u)$ is weighted with weighting function $G(u)$. Meijninger and De Bruin (2000) used this approach.

The third approximation leaves scintillometer weighting function, $G(u)$, out of consideration, in addition to the assumptions made in Equation (6.15), and the arithmetic average of $Z(u)$, Z_{eff_Avg} , remains:

$$Z_{eff_Avg} = \int_0^1 Z(u)du . \quad (6.16)$$

Note that in case hills are used to set-up the scintillometer, the reduced surface elevation near the ends of the path will have a large effect on Z_{eff_Avg} . It is then better to integrate $Z(u)$ between $0.15 < u < 0.85$, which, to a first order, simulates the effect of applying the weighting function $G(u)$.

It is difficult to quantify in a general way the error made when the proposed estimates are used instead of Z_{eff_Full} . This is because the error depends on the variation of the beam height, the part of the path where the variation takes place, and, to a lesser extent, also on stability. These aspects will be different for each set-up. Nonetheless, as a rule of thumb, the approximate estimates of Z_{eff_Full} can be used with little error when the difference in height between the highest and lowest point along the path between $0.15 < u < 0.85$ is less than a factor two. For most LAS set-ups, this criterion will be met.

In general, we can distinguish three conditions that cause $Z(u)$ to vary:

1. Slant paths; the heights of transmitter and receiver are not equal,
2. Topography; the surface under the scintillometer beam is not flat,
3. Curvature of the earth’s surface.

Slant paths

To get an idea of how much Z_{eff_Full} differs from the arithmetically averaged beam height, Z_{eff_Avg} , we consider a set-up in which the scintillometer beam describes a slant path over a flat surface. With slant scintillometer paths, the beam height along the path, $Z(u)$, can be described in terms of Z_{high} and Z_{low} , respectively the higher and lower heights of either transmitter or receiver:

$$\frac{Z(u)}{Z_{low}} = 1 + \left(\frac{Z_{high}}{Z_{low}} - 1 \right) u. \quad (6.17)$$

On substituting Equation (6.17) into Equations (6.13), (6.14) and (6.15), we can calculate Z_{eff_Fc} , $Z_{eff_Neutral}$, and Z_{eff_Avg} relative to Z_{low} as a function of Z_{high} / Z_{low} . These relations are depicted in Figure 6-1a. A trivial result seen in Figure 6-1a is that the slope of Z_{eff_Avg} / Z_{low} is 0.5. More noticeable is that $Z_{eff_Neutral} / Z_{low}$ and Z_{eff_Fc} / Z_{low} show an almost perfect linear relation with Z_{high} / Z_{low} . With the regression lines specified in Figure 6-1a, one can determine Z_{eff_Fc} and $Z_{eff_Neutral}$ for slant paths based on the scintillometer set-up, i.e. Z_{high} and Z_{low} , with negligible error. The regression lines are determined for $Z_{high} / Z_{low} > 3$. Figure 6-1b shows the percentage error of using Z_{eff_Avg} rather than Z_{eff_Fc} or $Z_{eff_Neutral}$ as a function of Z_{high} / Z_{low} .

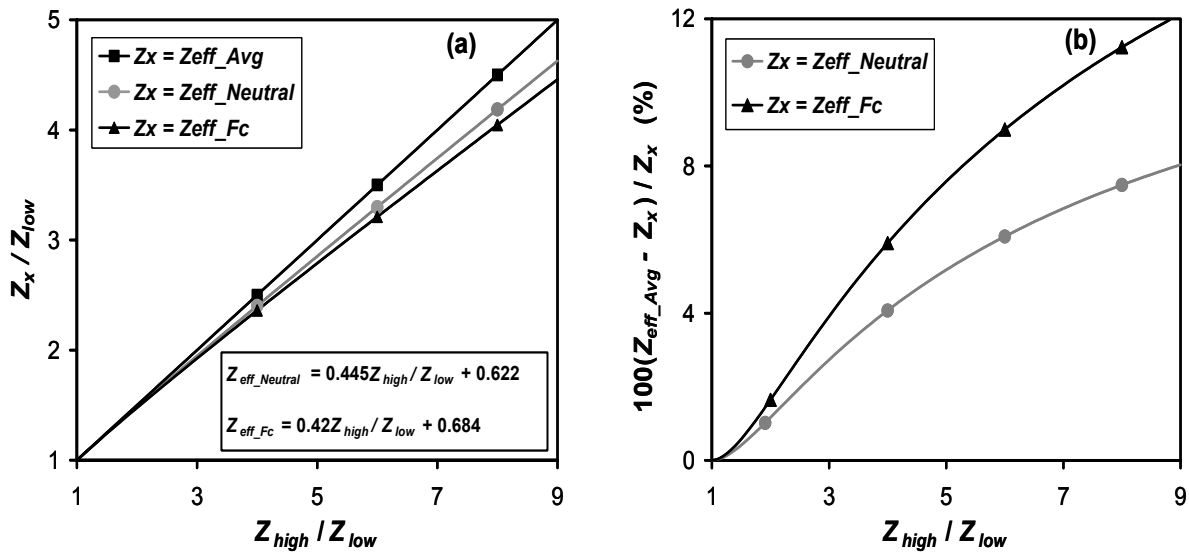


Figure 6-1: Effective heights for neutral conditions, $Z_{eff_Neutral}$, free convection conditions, Z_{eff_Fc} , and the average height, Z_{eff_Avg} , for a slant scintillometer beam path over a flat surface as a function of the ratio of the high and low ends of the path, Z_{high} / Z_{low} (a). Percentage error of using Z_{eff_Avg} rather than $Z_{eff_Neutral}$ or Z_{eff_Fc} as a function of Z_{high} / Z_{low} (b).

Topography

In practice, it is more common to encounter less variation in beam heights along the path than is shown in Figure 6-1. Typically, the height of transmitter and receiver are roughly the same, but topographic features cause the beam height to vary along the path. Height variations near the center of the path are particularly important because the weighting function has its maximum there. In contrast, the influence of the change in height and turbulence properties near both ends of the path, where the weighting function is zero, is negligible. This is a convenient circumstance, since hills or houses are often used to set-up the scintillometer.

Curvature of the earth's surface

The curvature of the earth's surface affects the effective height whenever long scintillometer paths are used (Kohsiek et al., 2002). Correcting for the earth's curvature results in a path-length-dependant reduction of the scintillometer beam height, $\Delta z_{curve}(u)$, along the path ranging from zero at $u = 0$ and $u = 1$, to a maximum at $u = 0.5$. Appendix 6C shows how $\Delta z_{curve}(u)$ is calculated. The correction in $Z_{eff_WeightAvg}$ for the earth's curvature exceeds 0.5 m for path lengths over 5 km.

Topography and the application of slant paths define the scintillometer height along the path relative to the surface. In case the earth's surface curvature correction, $\Delta z_{curve}(u)$, is important and a displacement distance is applicable, $Z(u)$ in Equations (6.11) to (6.16) should be taken as $(Z(u) - \Delta z_{curve}(u) - d)$.

In this paper we will only present data taken in the unstable stratified surface layer. For stable conditions, the effective height is, in principle, defined as in Equation (6.12) with a stable MOST function for f_T . However, the constraint that there must be a constant flux layer, which is generally true for the unstable case, may hold only to a certain degree for the weakly stable case. For stable to very stable conditions this condition will certainly not be met. Another issue is that the surface layer in the stable boundary layer (SBL) is often very shallow (only a few meters deep), and scintillometers installed at great heights will be outside the region where MOST can be applied. On the other hand, in the SBL the sensitivity of H to Z_{LAS} is rather weak (Andreas, 1989). Furthermore, although there are uncertainties in the definition of Z_{eff} and the validity of MOST in the SBL, the absolute error in the flux due to these issues will generally be small, as the fluxes themselves are small. We recommend the use of $Z_{eff_WeightAvg}$ of Equation (6.15) in the SBL.

For other types of scintillometers, a similar derivation of the effective height applies. The difference is that the shape of the weighting function $G(u)$ depends on the type of scintillometer.

6.3 Site and instrument description

We conducted a field experiment in September and October of 1996 at the La Poza rangeland site ($\sim 28.5^\circ$ N, 110° W, ~ 200 m above sea level) 30 km south of Hermosillo, capital of the state of Sonora in northwest Mexico. The La Poza rangeland is used for extensive cattle farming. Nearly all the vegetation is natural and a vegetation survey showed that 25% of the area is covered with trees and bushes and the remaining 75% is short grass or bare soil. Bushes, trees, and cacti are generally not very tall, roughly ranging from 0.5 m to 5 m.

A MK2 Hydra one-dimensional eddy covariance system (Institute of Hydrology, Wallingford, UK) was installed at 13.6 m on top of an 11-m-tall measurement tower. The Hydra consists of a fast-response cup anemometer (Vector Instruments, Rhyl, UK), a one-dimensional sonic

anemometer, an infrared hygrometer, a thermocouple (all built at the Institute of Hydrology), and a REBS Q6 net radiometer (Radiation and Energy Balance Systems, Inc., Seattle, USA). It was designed as a simple, modular eddy-covariance system that includes data storage and data processing software (Shuttleworth et al., 1988). The software calculates fluxes for a fixed averaging interval of 60 minutes. We found that the u^* measurements of the Hydra were not reliable, i.e. we were not able to obtain a reliable z_0 -estimate from u^* applying standard MOST scaling laws. This is probably due to differences in response time between the sonic and cup anemometer.

Several net radiation and soil sensors were installed on and around the tower. A REBS Q7 net radiometer was installed over grass and bare soil. The REBS Q6 of the Hydra system mainly “saw” trees and shrubs. Soil heat flux measurements were performed with six REBS HFT3 soil heat flux plates, which were buried at ~ 5 cm depth under different vegetation types, with a thermocouple placed above to account for heat storage in the top 5 cm. All these sensors were measured on one datalogger at 0.2 Hz and 60-minute averages were stored. We averaged the measurements of the different sensors, where the weights were chosen to conform to the results of the vegetation study.

The LAS used in this study was designed and built at the department of Meteorology and Air Quality of Wageningen University, the Netherlands. The electronics are according to Ochs and Wilson (1993). It has an aperture diameter of 0.15 m, and the light source is a light-emitting diode operating at a peak wavelength of 0.94 μm , which is placed at the focal point of a concave mirror. The receiver employs an identical mirror to focus the light on a photo diode detector. Scintillations appear as intensity fluctuations in the received signal. The received signal is band-pass filtered between 0.03 and 400 Hz. 60-minute averages of C_n^2 , sampled at 1 Hz, were recorded. With Bowen ratio, wind and temperature data from the Hydra, these were subsequently processed to give 60-minute averages of H .

The La Poza experiment consisted of two stages. Experiment I took place between 18 September and 17 October 1996. In total, 23 days of good data were collected during this period. The LAS was setup over a 3200-m path with the transmitter on top of a 50 m hill and the receiver on top of the eddy-covariance tower at a height of 12 m. Experiment II took place between 17 and 24 October 1996. The LAS was setup over an 1100-m path with the transmitter and receiver on top of two opposite hills, both at roughly 30 m above the surface.

The La Poza site is reasonably flat along the scintillometer paths and near the tower. Watercourses can be found at 500-m to 1-km intervals, in the vicinity of which the vegetation is relatively dense and high. Between the watercourses, there are more open patches with grass and bare soil. We can assume that this small-scale heterogeneity is blended below the LAS beam height for both set-ups, at least for the part of the path where the LAS weighting function is non-zero. The Hydra was set-up at the transition of a more dense and a more open patch such, that its measurements can be considered representative of the LAS footprints.

Since we were not able to derive a reliable z_0 -estimate from the Hydra, z_0 and d were determined from the vegetation survey. We estimated $z_0 = 0.15$ m and $d = 1.3$ m. A constant value for pressure of 990 hPa was used.

6.4 Results and discussion

6.4.1 Calculation of the effective height

Figure 6-2a illustrates the LAS beam along the path, $Z(u)$, for experiment I. The height of the LAS beam and the elevation of the surface are given relative to the lowest point of the surface along the path. The surface elevation along the path is determined from a topographic map.

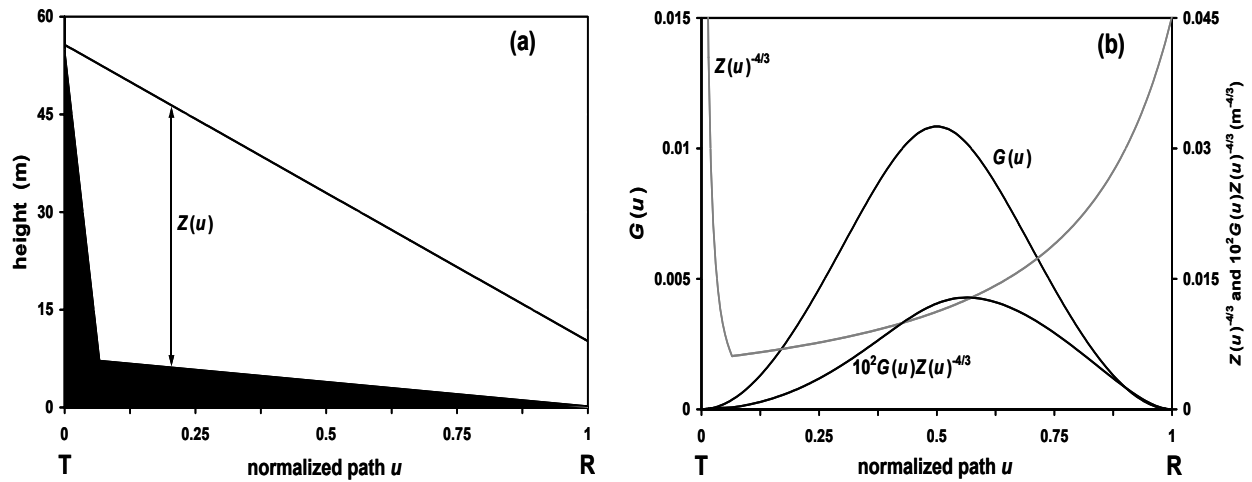


Figure 6-2: Experiment I: Scintillometer beam height, $Z(u)$, along the normalised path, u (a); Scintillometer weighting function, $G(u)$, height scaling of C_T^2 for free convection conditions, $Z(u)^{-4/3}$, and the convolution between the two, $G(u)Z(u)^{-4/3}$, which integrated over the path gives Z_{eff_Fc} (b). T and R stand for transmitter and receiver respectively.

Figure 6-2b shows the different terms involved in calculating Z_{eff_Fc} . It can be seen that the convolution between $G(u)$ and $Z(u)^{-4/3}$ is skewed significantly towards the receiver part of the path, where the LAS beam is lowest. In other words, Z_{eff_Fc} is weighed towards the lower end of the scintillometer beam. It can also be seen that the influence of the hill, which gives considerable weight to $Z(u)^{-4/3}$ near the transmitter end of the path, is negligible in $G(u)Z(u)^{-4/3}$ because $G(u)$ tapers off to zero near both ends of the path.

Table 6-1: For experiments I and II: the effective heights calculated for free convection conditions, Z_{eff_Fc} from Equation (6.13), neutral conditions, $Z_{eff_Neutral}$ from Equation (6.14), and weighted with LAS weighting function, $Z_{eff_WeightAvg}$ from Equation (6.15), and the more conventional height estimates, the average height between $0.15 < u < 0.85$, Z_{eff_Avg} after Equation (6.16), and Z_{LAS} at midpoint, $u = 0.5$.

	Z_{eff_Fc} (m)	$Z_{eff_Neutral}$ (m)	$Z_{eff_WeightAvg}$ (m)	Z_{eff_Avg} (m)	Z_{LAS} at mid-point (m)
Experiment I	27.0	27.6	29.0	29.0	29.0
Experiment II	34.5	34.4	34.6	34.1	35.0

The values of $Z_{eff_Neutral}$, Z_{eff_Fc} and $Z_{eff_WeightAvg}$ are given in Table 6-1, as well as some more conventional estimates of Z_{LAS} in these situations, Z_{eff_Avg} for $0.15 < u < 0.85$ and Z_{LAS} at midpoint, $u = 0.5$. It can be seen that the difference in height between Z_{eff_Fc} and $Z_{eff_Neutral}$ is $\sim 2\%$, and between Z_{eff_Fc} and the conventional estimates is $\sim 7\%$. Figure 6-3 shows how the iteratively determined Z_{eff_Full} relates to $Z_{eff_Neutral}$ and Z_{eff_Fc} as a function of stability.

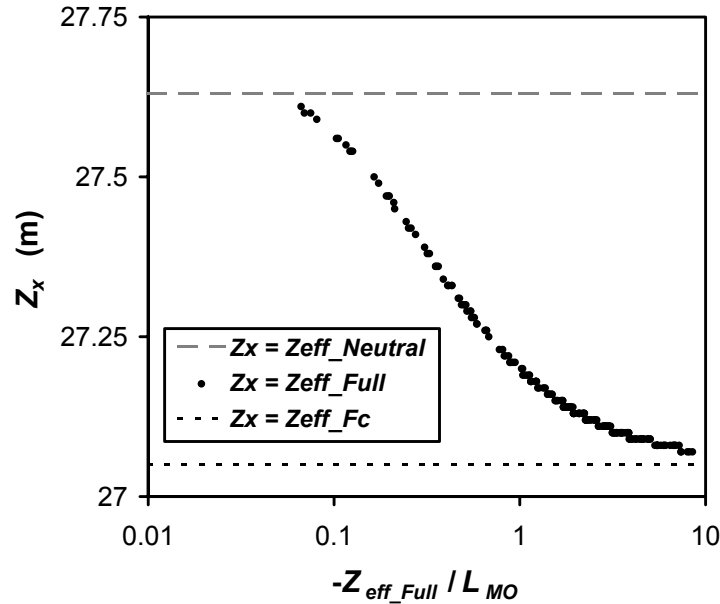


Figure 6-3: Experiment I: Iteratively determined effective height, Z_{eff_Full} from measurements using Equation (6.12) as a function of stability, z/L_{MO} . $Z_{eff_Neutral}$ and Z_{eff_Fc} represent the neutral and free convection solutions of the effective height, respectively.

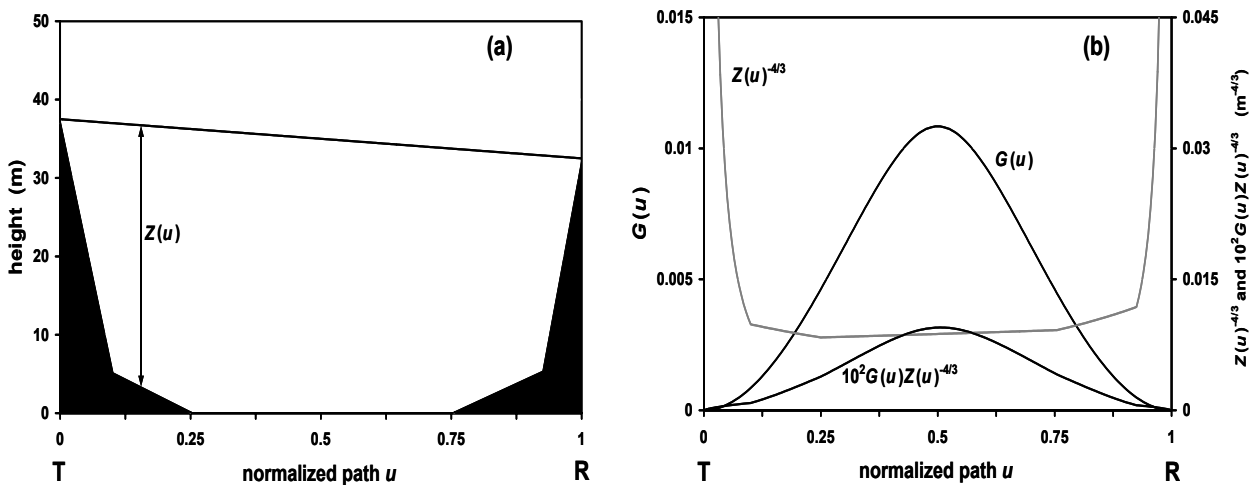


Figure 6-4: Experiment II: Scintillometer beam height, $Z(u)$, along the normalised path, u (a); Scintillometer weighting function, $G(u)$, height scaling of C_T^2 for free convection conditions, $Z(u)^{-4/3}$, and the convolution between the two, $G(u)Z(u)^{-4/3}$, which integrated over the path gives Z_{eff_Fc} (b). T and R stand for transmitter and receiver, respectively.

Figure 6-4 depicts in a similar way as Figure 6-2 how Z_{eff_Fc} is determined for experiment II. Figure 6-4b shows that $G(u)Z(u)^{-4/3}$ is hardly skewed to the lower end of the path because $Z(u)^{-4/3}$ is almost constant over the part of the path which is weighted most by $G(u)$ (for $0.15 < u < 0.85$). From this it follows that the values of $Z_{eff_Neutral}$, Z_{eff_Fc} , and $Z_{eff_WeightAvg}$ presented in Table 6-1 are nearly the same.

The influence of the earth's curvature has been taken into account in the effective height calculations although it was negligibly small: 0.1 m for experiment I and 0.02 m for experiment II.

In Figure 6-2a and Figure 6-4a the surface elevation is given in a rather schematic way; i.e. not every feature of the surface along the LAS beam is specified. This is done because for each stage of the path, the specified $Z(u)$ should be representative for the entire area "seen" by the LAS at that point.

In cases where the LAS footprint exhibits large differences in elevation in all directions, a different approach should be used. Meijninger et al. (2002a) presented a 3D LAS footprint function which results from the convolution of the LAS weighting function, $G(u)$, and a footprint model describing how far downwind the LAS "sees" as a function of path length, wind speed, wind direction, and stability. The effective height is then evaluated by weighting a 3D field of the LAS height above the surface with the 3D footprint function.

Likewise, for each of the roughness parameters, z_0 and d one value has to be found that is representative for the LAS footprint. If large differences in the surface roughness are present over the footprint, one could weigh the roughness variables quadratically, after e.g. Chehbouni et al. (1999).

Figure 6-1 gave us a sense of how much the effective height differs between applying Z_{eff_Avg} , Z_{eff_Fc} and $Z_{eff_Neutral}$ as a function of beam height variation along the path. Appendix 6A, then, illustrates the impact of these differences on H . To judge the full impact of the derived effective height, however, a sensitivity analysis would be needed that includes all input variables that go into the calculation of H . Andreas (1989) present an extensive sensitivity study for a two-wavelength scintillometer method. It is beyond the scope of this paper to present such an analysis for the one wavelength LAS method. Instead, as an example, we will work out, for experiment I only, the relative contribution, dH_{x_i} , to the total relative error in H , dH , due to errors, δx_i , in the input variables, x_i , that go into the calculation of H . dH is estimated as:

$$dH = 100 \left(\sqrt{\sum_{i=1}^N [0.5(H(x_i + \delta x_i) - H(x_i - \delta x_i))]^2} / H \right), \text{ where } N \text{ is the number of input variables.}$$

Then, dH_{x_i} is: $dH_{x_i} = 100 \left(\sqrt{[0.5(H(x_i + \delta x_i) - H(x_i - \delta x_i))]^2} / [dH]^2 \right)$.

The errors in the input variables were taken as follows: Z_{cup} (0.5 m), z_0 (0.05 m), T (1 K), Bo (50 %), L (50 m), and P (20 hPa). We determined the error in Z_{LAS} by estimating the uncertainty in the surface elevation at each position along the path, which is mainly defined

by its variation within the LAS footprint at that point. Weighted with Equation (6.15), the total estimated error in Z_{LAS} results in 1.8 m, which includes an error-estimate for d (0.2 m). This is $\sim 7\%$ of Z_{eff_Full} . Coincidentally, for experiment I, the difference between the more conventional height-estimates and Z_{eff_Full} is of the same order. The impact on H of the error in the estimation of Z_{LAS} and that of the use of simple Z_{LAS} -estimates instead of Z_{eff_Full} will therefore be comparable.

Table 6-2: Statistical summary of the percentage contribution, dH_{x_i} , to the total relative error in H , dH , due to errors, δx_i , in the input variables, x_i , that go into the calculation of H . The variables, x_i considered are: scintillometer height, Z_{LAS} , anemometer height, Z_{cup} , roughness length, z_0 , temperature, T , path length, L , Bowen ratio, Bo , and Pressure, P .

	Mean (%)	Range (%)		
		St. Dev.	Min.	Max.
$dH_{Z_{LAS}}$	67	16	12	82
$dH_{Z_{cup}}$	0.03	0.07	0.00	0.34
dH_{z_0}	4	7	0	30
dH_U	6	11	0	48
dH_T	0.27	0.04	0.12	0.31
dH_L	14	2	6	16
dH_{Bo}	8	7	0	60
dH_P	0.70	0.27	0.05	1.18

In Table 6-2 a statistical summary is presented of dH_{x_i} , where Z_{eff_Full} from Equation (6.12) has been used to calculate H . The total error in H , dH , is in the order of 10%. Clearly, the error in Z_{LAS} dominates dH . This also illustrates the impact of using simple estimates of Z_{LAS} instead of Z_{eff_Full} . The second important contributor to dH is L . The strong power-3 dependence of C_n^2 to L is responsible for this (see Equation 6.3). Especially for short path lengths, where large relative errors in L are more likely to occur, it is very important to determine L as accurately as possible. The contributions to dH of errors in Z_{cup} , T and P are negligible. Those of errors in z_0 and U are on the average small, but the high maximum values and standard deviations of the errors show they are important in some situations (neutral conditions). The contribution of Bo to dH is generally small as well, although it was assigned a 50 % error. Only for very small Bo , dH_{Bo} is important. This due to the steep shape of the Bowen-term in Equation (6.4) for $Bo < 0.6$.

Note that the impacts of possible violations of the theoretical assumptions behind Equations (6.1), (6.4), (6.5), and (6.12), have not been examined. Also, the impact of using another similarity function for f_T than Equation (6.6) has not been included. Hill (1997) in his overview article summarises the different functions found in the literature. It can be seen, that for the neutral limit most functions agree quite well, whereas as for the free convection limit differences can be found of up to 20 % in H .

6.4.2 Comparison of LAS with eddy-covariance results

For experiment I, Figure 6-5 compares the 60-minute averaged sensible heat fluxes from the LAS, H_{LAS} , and Hydra eddy-covariance system, H_{EC} . Only unstable conditions were analysed, i.e. data taken between 8:00 AM and 6:00 PM local time. Figure 6-5a shows the comparison for H_{LAS} based on Z_{eff_Full} determined with Equation (6.12). Figure 6-5b shows the comparison between H_{LAS} and H_{EC} for H_{LAS} based on $Z_{eff_WeightAvg}$ determined with Equation (6.15). In Table 6-3, the linear regression results for Figure 6-5 are summarised.

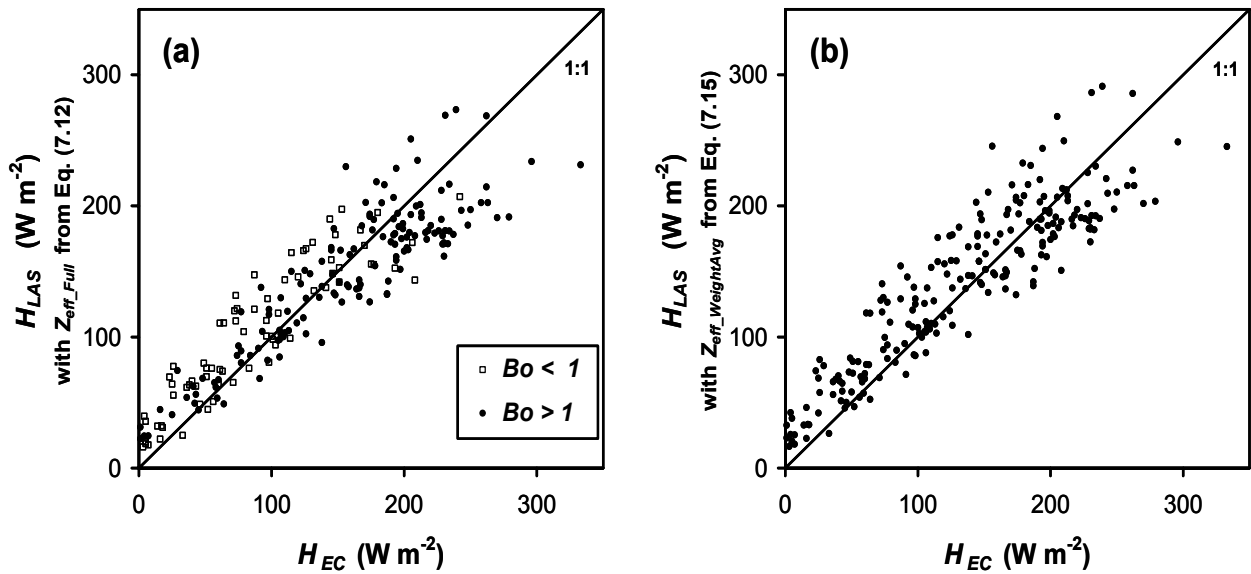


Figure 6-5: Comparison for experiment I between 60-minute-averaged scintillometer and eddy-covariance sensible heat fluxes, H_{LAS} and H_{EC} , respectively. H_{LAS} calculated with Z_{eff_Full} from Equation (6.12) is depicted in (a). Different markers are used for Bowen ratio values, Bo , larger and smaller than 1. H_{LAS} calculated with $Z_{eff_WeightAvg}$ from Equation (6.15) is depicted in (b).

It can be seen from Figure 6-5 that H_{LAS} and H_{EC} compare reasonably, although a considerable scatter is observed. Using Z_{eff_Full} yields a marginally better fit than when the approximated $Z_{eff_WeightAvg}$ is applied, i.e. the RMS of the fit is marginally better. On the other hand, the slope is closer to 1 for $Z_{eff_WeightAvg}$. The differences between Figure 6-5a and Figure 6-5b are most apparent for large H , when the free convection limit is approached. This is because, under these conditions, the difference between the fixed $Z_{eff_WeightAvg}$ and Z_{eff_Full} is largest (see Table 6-1 and Figure 6-3), and H_{LAS} is most sensitive to Z_{LAS} (see Appendix 6A).

Figure 6-5a will be used in the discussion of the results of H_{LAS} versus H_{EC} because it is based on a more accurately determined effective height. Two regions can be distinguished in Figure 6-5a: one region in which the H_{LAS} overestimates H_{EC} (ranging roughly from 0 to 200 W m⁻²), and another in which H_{LAS} underestimates H_{EC} (ranging from 150 W m⁻² and higher). To discuss possible reasons behind these discrepancies between H_{LAS} and H_{EC} , we present Figure 6-6 and Figure 6-7.

Table 6-3: Overview of linear regressions between the sensible heat fluxes of the scintillometer, H_{LAS} , and eddy-covariance, H_{EC} . Regression parameters are specified for the zero-intercept-model, $H_{LAS} = aH_{EC}$ and the non-zero-intercept-model, $H_{LAS} = aH_{EC} + b$. The numbers in parentheses are uncertainties based on a 95% confidence interval.

	# points	$H_{LAS} = aH_{EC}$			$H_{LAS} = aH_{EC} + b$			
		a (-)	r^2 (-)	rms ($W m^{-2}$)	a (-)	b ($W m^{-2}$)	r^2 (-)	rms ($W m^{-2}$)
Experiment I $Z_{eff-Full}$ (Eq. 6.12)	220	0.93 (0.013)	0.74	29.7	0.72 (0.022)	36.0 (3.4)	0.83	24.3
Experiment I $Z_{eff-WeightAvg}$ (Eq. 6.15)	220	0.98 (0.014)	0.74	31.7	0.77 (0.024)	37.7 (3.7)	0.82	26.2
Experiment II $Z_{eff-Full}$ (Eq. 6.12)	89	1.0 (0.017)	0.87	25.3	0.88 (0.032)	21.7 (5.2)	0.89	23.2

Figure 6-6 shows H_{LAS} and H_{EC} as a function of the available energy for turbulent fluxes given by the net radiation, R_{net} , minus the soil heat flux, G . Only data-points are shown for which both LAS and Hydra data were available. It can be seen that the Hydra produces more scatter than the LAS. We thus conclude that much of the scatter seen in Figure 6-5 can be attributed to H_{EC} .

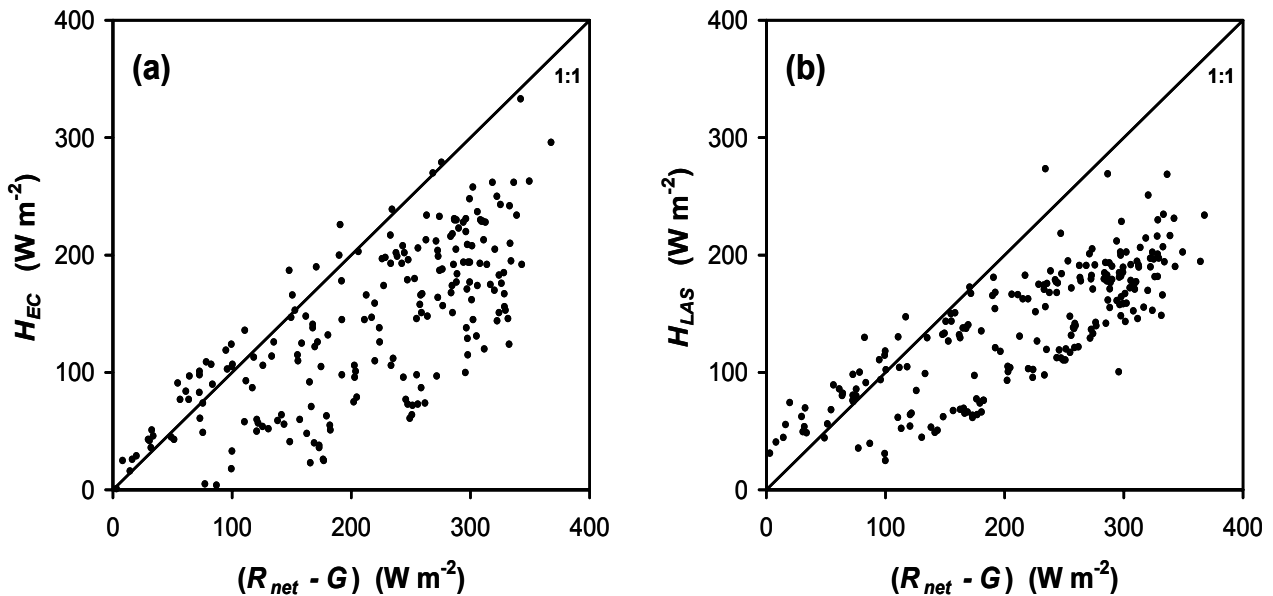


Figure 6-6: Experiment I: Relation between the eddy-covariance heat flux, H_{EC} , and the net available energy for turbulent fluxes given by the difference in net radiation, R_{net} , and soil heat flux, G (a). Same for scintillometer heat flux, H_{LAS} , in (b).

Figure 6-7 depicts the Bowen ratio, B_o , for experiment I and II (Figure 6-7a) and the difference between H_{LAS} and H_{EC} relative to H_{EC} for experiment I (Figure 6-7b) as a function

of time. Only data between 9:00 and 16:00 local time are plotted to exclude fluxes near the morning and evening transitions when fluxes are small and the relative error in H and Bo can be very large. Prior to the experiment, a heavy thunderstorm brought 90 mm of rain, whereas during the experiment it did not rain at all. These conditions are reflected in the development of Bo during the experiment, which show that the experiments took place in drying conditions. The decrease in Bo around DOY 280 is related to a frontal passage. We take $Bo = 1$ as the transition value between wet and dry conditions. Although there is a lot of scatter, a relation can be seen in Figure 6-7 between Bo and the relative error between H_{LAS} and H_{EC} . In the beginning of the experiment, when the conditions were predominantly wet, H_{LAS} tends to overestimate H_{EC} , and, contrary, later in the experiment, when the conditions were predominantly dry, H_{LAS} tends to underestimate H_{EC} .

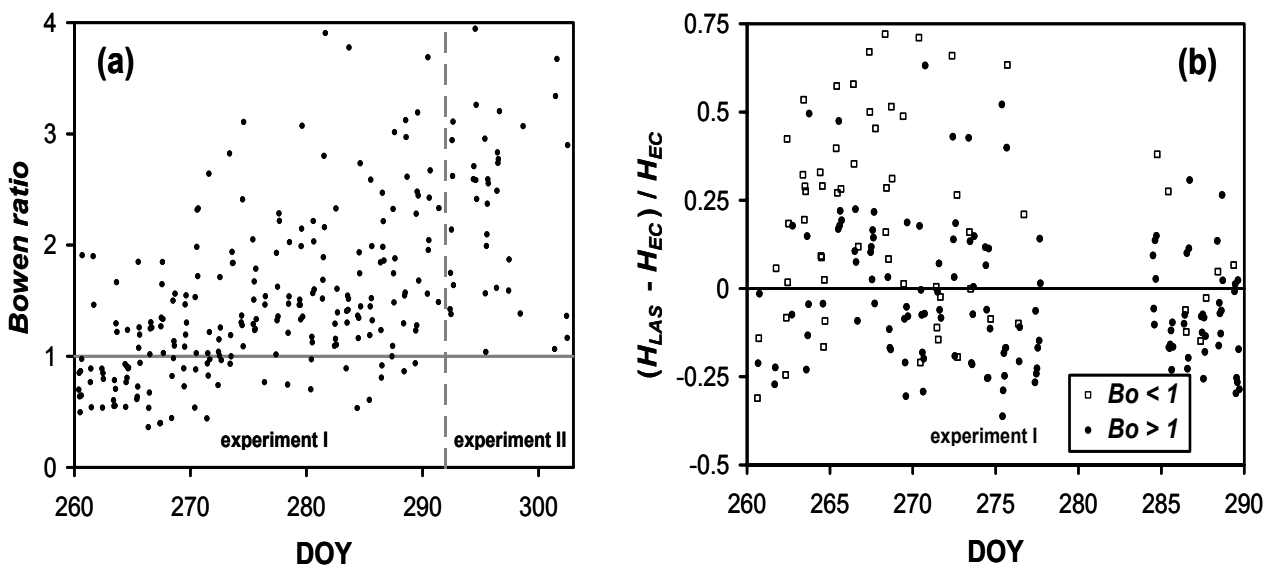


Figure 6-7: Bowen ratio as a function of day of year, DOY, for experiment I and II (a), and relative error between scintillometer heat flux, H_{LAS} , and eddy-covariance heat flux, H_{EC} , as a function of DOY for experiment I (b). In (b), different markers are used for Bowen ratio values, Bo , larger and smaller than 1.

The *overestimation* of H_{LAS} seen in Figure 6-5a corresponds for a large part with wet conditions, i.e. nearly all points for $Bo < 1$ are above the 1:1 line. This is most likely due to absorption fluctuations of water vapor in the LAS signal caused by moisture-transporting eddies. Water vapor has strong absorption lines around $0.94 \mu\text{m}$, the wavelength at which the LAS operates. The LAS will erroneously interpret these absorption fluctuations as additional refractive index fluctuations, which finally results in a higher H_{LAS} . Scintillations due to absorption and refraction are spectrally separated at the low frequency end of the spectrum. Using a similar LAS to that used in this study, Nieveen et al. (1998) found that the transition between the two regions lies between 0.071 and 0.36 Hz. The LAS we used in this study had a high-pass filter of 0.03 Hz and was therefore susceptible to absorption fluctuations. Based on the experiences with the La Poza experiment and the findings of Nieveen et al. (1998), the high pass filter was changed to a cut off frequency of 0.1 Hz in later models.

One of the reviewers also pointed out that for near neutral conditions, i.e. small H , the LAS is under all circumstances sensitive to overestimation of H . Unlike, for instance, eddy-covariance instruments the scintillometer cannot distinguish between ascending and descending warm air parcels (i.e. positive and negative H), and will record intensity fluctuations for both. Around neutral stability, ascending and descending warm air parcels are more likely to occur with the same intensity at the same time, and will thus result in a higher H_{LAS} . See for example Frederickson et al. (2000), who demonstrate that a bulk flux method, which is based on equations like Equations (6.5) and (6.6), underestimates C_n^2 near neutral stability.

The *underestimation* of H_{LAS} seen in Figure 6-5a for high values of H , corresponds for the most part with dry conditions, i.e. for $H > 150 \text{ W m}^{-2}$, nearly all points below the 1:1 line are with $Bo > 1$. The cause of this is unclear. A hypothesis is that the LAS saturates, which means that measured intensity fluctuations above a certain level are no longer proportional to C_n^2 . For the LAS, Ochs and Hill (1982) derived $C_n^2 < 0.185D^{5/3}\lambda^{1/3}L^{-8/3}$ as a saturation-free condition. Note that C_n^2 itself is a strong function of height (see Equation 6.5). Since D and λ are instrument constants, z and L determine whether saturation occurs. In general, the longer the path, the higher the LAS needs to be installed to avoid saturation. For all points of Figure 6-5a, the measured C_n^2 is within an order of magnitude of the saturation limit defined by Ochs and Hill (1982). For $H > 150 \text{ W m}^{-2}$, this limit is approached to within 50 to 80%. Saturation, therefore, possibly did occur for $H > 150 \text{ W m}^{-2}$ in the absence of the assumed effect of absorption fluctuations, i.e. $Bo > 1$.

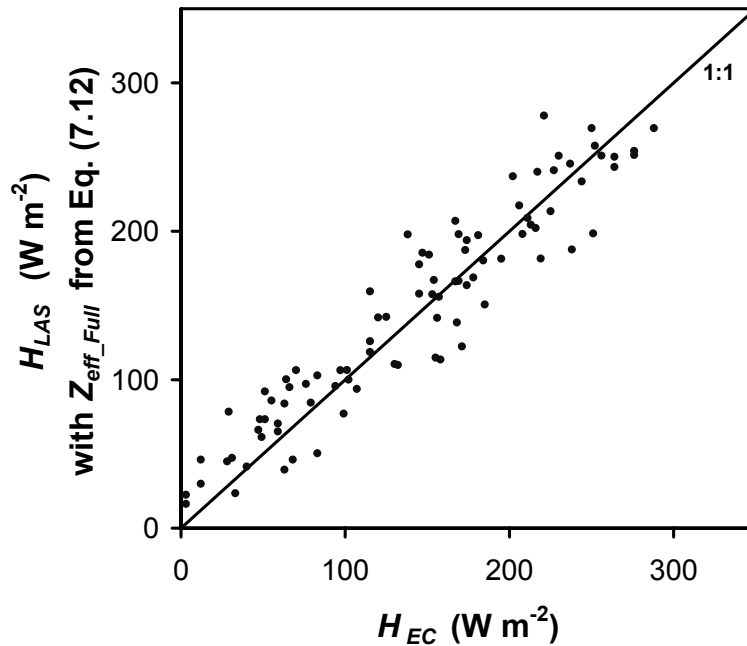


Figure 6-8: Comparison for experiment II between 60-minute averaged scintillometer and eddy-covariance sensible heat fluxes, H_{LAS} and H_{EC} respectively.

Figure 6-8 shows the comparison between the LAS and Hydra-derived sensible heat fluxes for experiment II. The agreement between the two instruments and methods is better than in experiment I as can be seen from both Figure 6-8 and Table 6-3. The hypotheses which have been discussed above to explain the scatter that was observed in experiment I are less of an issue in experiment II. To begin with, for unknown reasons less scatter was found for H_{EC} versus $(R_{net} - G)$ than in experiment I. Furthermore, absorption fluctuations were not expected to interfere with the LAS refractive index measurements during experiment II, since the conditions were very dry. Neither was saturation of the LAS signal likely to be an issue with a shorter LAS path length, comparable LAS height and similar atmospheric conditions to those at the end of experiment I. The measured C_n^2 was 2 to 3 orders of magnitude below the saturation limit defined by Ochs and Hill (1982).

6.5 Conclusions

For many applications, the error in the scintillometer heat flux calculation, H , is for most part determined by the uncertainties in the estimated instrument height. These uncertainties arise in part from the error in estimating the height of the scintillometer along the path, and in part from the method by which one path integrated height value is obtained. In this paper, we focused on the latter issue. We derived an effective height for scintillometers as a function of stability, and discussed different sources of varying scintillometer beam height along the path. In addition, approximate formulations of the effective height have been proposed that are independent of stability.

In general it can be concluded that to reduce the influence of a varying beam height on H , it is best to set up the transmitter and receiver as high as possible. First of all, if the instrument is above the so-called blending height, validity of similarity scaling is ensured, which is at the basis of the derived effective height and the flux calculations. Also, as is described in Section 6.4.1, the effect of small-scale topography along the path is blended. Secondly, slant paths are less likely to be an issue. The effective height for slant paths scales with ratio of the higher to the lower height of either transmitter or receiver. At high levels, an absolute difference in height between transmitter and receiver will affect this ratio to a lesser extent than at low levels. Finally, as one approaches the free convection limit at high levels, the stability dependence of the effective height vanishes and a single value can be used.

In most cases, however, the variation in height of the scintillometer beam along the path will not be very pronounced, and an approximate effective height formulation can be applied with little error. The influence of the earth's curvature exceeds 0.5 m for path lengths over 5 km.

We experimentally tested the effective height formulation in terms of its effect on the heat flux. For the slant path experiment, we showed that using the stability dependent effective height, a marginally better fit was found between LAS and eddy-covariance heat fluxes than

with an approximated effective height, i.e. the scatter was reduced. The horizontal path experiment yielded a better agreement between scintillometer and eddy-covariance fluxes. It is difficult to compare the results between these two experiments, as there were indications that for the slant path experiment the LAS heat fluxes were biased due to humidity absorption effects and possibly saturation of the scintillometer signal.

Acknowledgements

We thank Bert Heusinkveld for his assistance in installing the LAS, and Mike Stroud and John Stewart for their efforts in getting a Hydra system operational in La Poza. This study was financed by the European Union (CEC project C11*CT91-0900).

Appendix 6A H sensitivity to Z_{LAS}

We will briefly discuss the sensitivity of the sensible heat flux, H , to the LAS height, Z_{LAS} , for unstable conditions to stress the importance of determining Z_{LAS} as accurately as possible and, thus, showing the relevance of the effective height proposed in this study.

When we combine the definitions of H ($H = -\rho c_p u_* \theta_*$) and L_{MO} ($L_{MO} = T u_*^2 / \kappa_{kar} g \theta_*$) with Equations (6.5) and (6.6), H can be written as

$$H = B Z_{LAS} \left(\frac{1 - c_2 Z_{LAS} / L_{MO}}{-Z_{LAS} / L_{MO}} \right)^{1/2}. \quad (6.18)$$

with $B = \rho c_p (4.9)^{-3/4} (C_T^2)^{3/4} (\kappa_{kar} g / T)^{1/2}$. The variables in B and the constant c_2 are specified in Section 6.2.1. The free convection expression of H given in Equation (6.8) follows directly from Equation (6.18) for $Z_{LAS} / L_{MO} \rightarrow \infty$.

From Equation (6.18), we obtain the partial derivative of H with respect to Z_{LAS} :

$$\frac{\delta H / H}{\delta Z_{LAS} / Z_{LAS}} = \frac{1}{2} \left(\frac{1 - 2c_2 Z_{LAS} / L_{MO}}{1 - c_2 Z_{LAS} / L_{MO}} \right). \quad (6.19)$$

Equation (6.19) expresses the relative error in H due to a relative error in Z_{LAS} as a function of stability. Andreas (1989) derived a similar equation; see his Equation (B22) and Figure 6-3. Equation (6.19) is plotted in Figure 6-9, which shows that, for free convection conditions, a relative error in Z_{LAS} causes an equal relative error in H . For neutral conditions, on the other hand, the relative error in H due to Z_{LAS} is half the relative error in Z_{LAS} . This can also be seen directly from Equation (6.19).

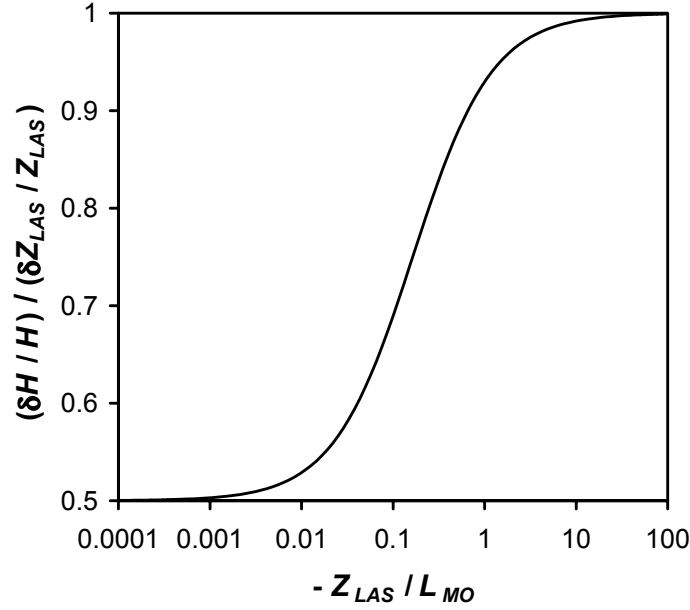


Figure 6-9: The relative error in the sensible heat flux, H , due to a relative error in the scintillometer height, Z_{LAS} , as a function of stability, Z_{LAS}/L_{MO} .

Appendix 6B Calculation of Z_{eff_Full} from Equations (6.6) and (6.12)

In this Appendix, we derive an expression for Z_{eff_Full} from Equations (6.6) and (6.12). On substituting Equation (6.6) into Equation (6.12), one obtains, after rearranging the variables, the following quadratic equation for Z_{eff_Full} :

$$-\frac{c_2}{L_{MO}} Z_{eff_Full}^2 + Z_{eff_Full} - \left[\int_0^1 \left[Z(u) \left(1 - c_2 \frac{Z(u)}{L_{MO}} \right) \right]^{-2/3} G(u) du \right]^{-3/2} = 0. \quad (6.20)$$

Equation (6.20) has only one solution for Z_{eff_Full} that is physically relevant:

$$Z_{eff_Full} = \left\{ -1 + \sqrt{1 - \frac{4c_2}{L_{MO}} \left[\int_0^1 \left[Z(u) \left(1 - c_2 \frac{Z(u)}{L_{MO}} \right) \right]^{-2/3} G(u) du \right]^{-3/2}} \right\} \left[\frac{-2c_2}{L_{MO}} \right]^{-1}. \quad (6.21)$$

From the set of Equations (6.5) to (6.7) and Equation (6.21), Z_{eff_Full} , θ_* and u_* can now be iteratively solved using $L_{MO} = T u_*^2 / k_{kar} g \theta_*$. H then follows from its definition, $H = -\rho C_p u_* \theta_*$.

Appendix 6C Effect of the earth's curvature on the effective height

Figure 6-10 sketches how the earth's curvature affects (reduces) the height of the scintillometer along the propagation path. Z_{LAS} , u , and $\Delta z_{curve}(u)$ are as defined in Section 6.2.1.

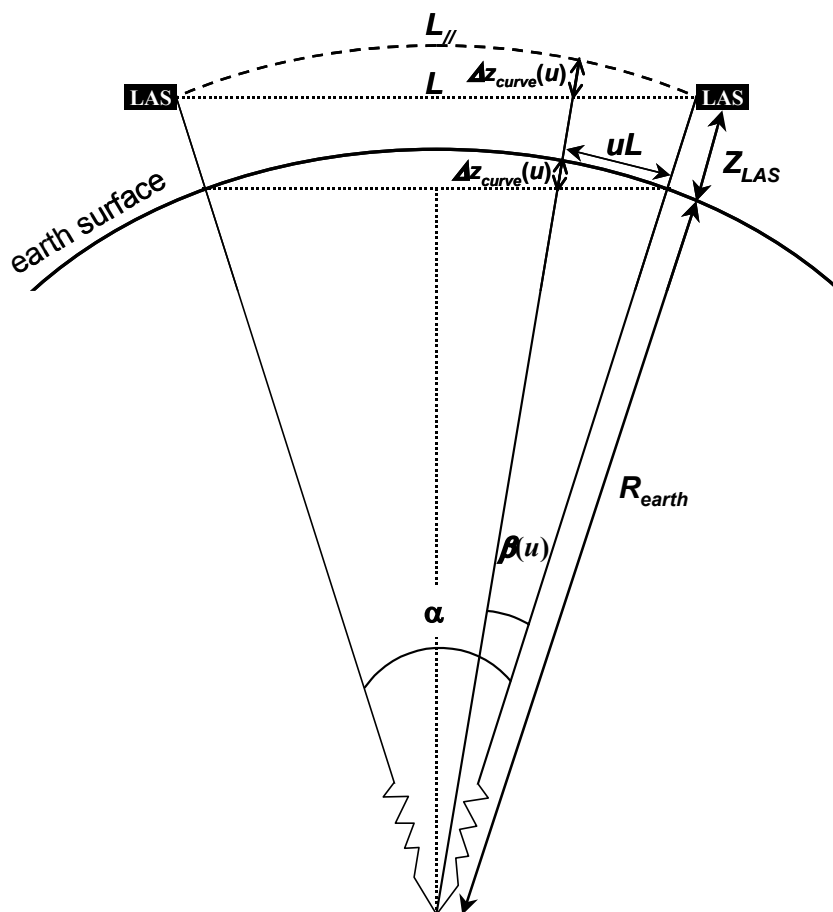


Figure 6-10: Effect of the earth's curvature on the effective scintillometer height. Symbols are explained in the text. The figure is not drawn to scale.

Normally, one assumes the scintillometer path length parallel to the earth's surface ($L_{//}$). In reality, however, the true path length, L , is straight, whereas the surface is slightly curved, which causes the scintillometer height to vary along the path. The difference in height between L and $L_{//}$ along the path is represented by $\Delta z_{curve}(u)$, which should be evaluated as indicated in Section 6.2.2 in obtaining an effective scintillometer height. Since $Z_{LAS} \ll R_{earth}$, the earth's radius ($R_{earth} = 6387$ km), $\Delta z_{curve}(u)$ can be evaluated independently of Z_{LAS} :

$$\Delta z_{curve}(u) = R_{earth} \left(1 - \frac{\cos(0.5\alpha)}{\cos(0.5\alpha - \beta(u))} \right), \quad (6.22)$$

with $\alpha = L / R_{earth}$, and $\beta(u) = uL / R_{earth}$. Since the correction will always be small with respect to the overall scintillometer height, its effect along the path can be weighted according to Equation (6.15) with negligible error. Figure 6-11 shows the total path weighted correction (reduction) for the earth's curvature as a function of path length. It can be seen that this correction exceeds 0.5 m for path lengths over 5 km. Note that the influence of the earth's curvature on the path length, L is negligible.

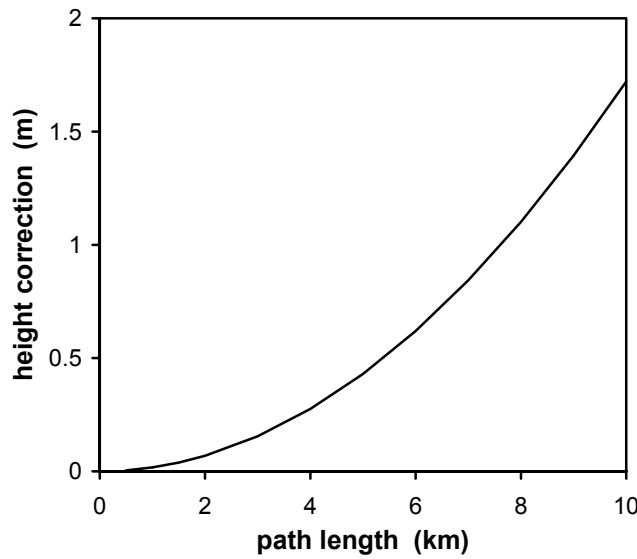


Figure 6-11: The total path weighted correction (reduction), $\Delta z_{curve}(u)$ for the earth's curvature as a function of path length.

Appendix 6D Sensible heat flux for Stable Conditions

This study was published as a separate article that deals only with unstable, daytime conditions. In this Appendix we will consider the stable, night time conditions as this is the main focus of this thesis.

At the end of Section 6.2.2 there is short discussion on the scintillometer effective height in stable conditions, where it was recommend to use $Z_{eff_WeightAvg}$ of Equation (6.15) in stable conditions, given the uncertainties of the validity of MOST high in the SBL. In estimating the fluxes we used the following MOST functions for f_T and ψ_m (see Equations 6.5 and 6.7):

$$f_T = 4.7 \left(1 + 1.6\zeta^{2/3} \right), \quad (6.23)$$

after Hartogensis and De Bruin (2005) and

$$\Psi_m = 1 - (1 + 6.25\zeta)^{0.8}, \quad (6.24)$$

after Duynkerke (1999).

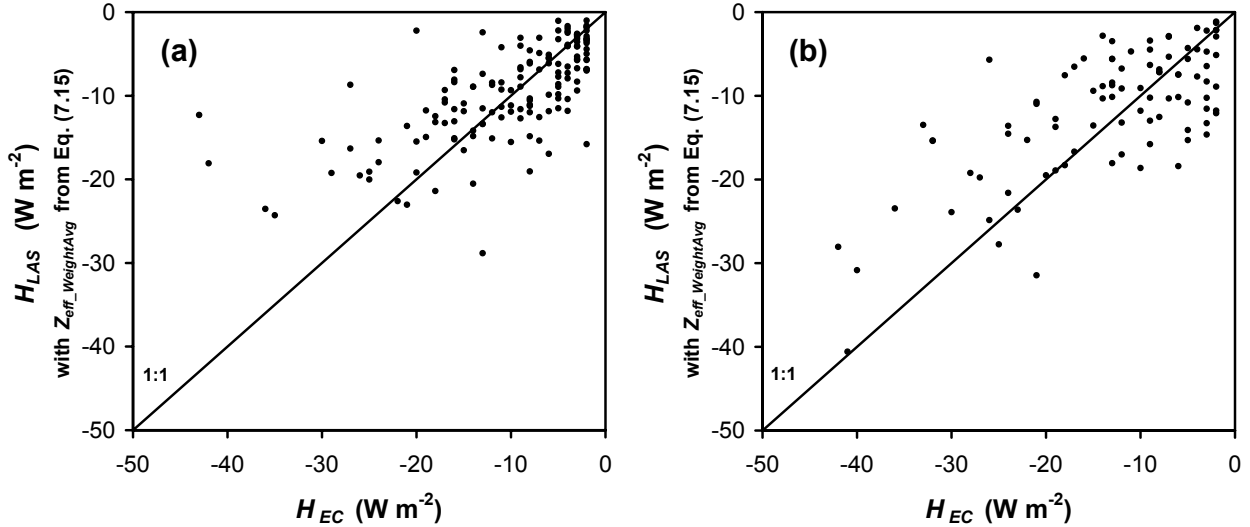


Figure 6-12: Comparison of the LAS and eddy covariance (EC) sensible heat flux, H , for stable conditions of La Poza experiment I (a) and La Poza experiment II (b).

Figure 6-12 compares the LAS and eddy covariance (EC) H for stable conditions of La Poza experiment I and II using $Z_{eff_WeightAvg}$ of Equation (6.15) as effective height-estimate. We recall that we used 60 minute averaging intervals, as this was the only EC flux interval period we had available (see Section 6.3). This period, ideally, is too long to be used in stable conditions given the non-stationary nature of SBLs. In addition, for both experiments the LAS was set-up at ~ 30 m. This is much higher than the EC system, which was installed at 12 m, and mostly also higher than the stable surface layer. Given the non-constant flux layer in the SBL, this may affect the comparison between the LAS and EC fluxes. In spite of all of this, the scatter seen in Figure 6-12 is comparable to what we found for the BBC LAS experiment (Figure 5-7) for which the set-up was more accommodated to stable conditions: i.e. the experiment was conducted over a shorter distance, closer to the surface, at a comparable height as the EC system and using a shorter flux-averaging interval. The conclusion we can draw from this is that the adopted effective height formulation in stable conditions gives flux-estimates with the accuracy that can be expected.

Chapter 7 Summary and Conclusions

The main objective of this thesis is to investigate observation methods of heat and momentum exchange and key variables that characterise turbulence in the atmospheric stable surface layer (SSL), a layer defined as the lower part of the stable boundary layer (SBL) where surface fluxes do not change significantly with height. The SBL is often confined to a shallow layer above the surface and of an intermittent nature, i.e. quiescent periods with almost laminar flow are interchanged with turbulent bursts. These conditions complicate flux measurements in the SBL considerably, since ideally they need to take place close to the surface and over short intervals to avoid averaging non-stationary conditions. A standard method to measure fluxes, the eddy-covariance (EC) method is straightforward conceptually, but in practice there are many pitfalls and additional corrections that need to be applied. In addition, in the highly non-stationary and often very shallow SBL the EC method has two distinct disadvantages. Firstly, it requires stationary conditions for at least 10 minutes to gather a statistically stable flux. Secondly, in very stable conditions a significant portion of the turbulent eddies will be smaller than the instruments path and therefore will not be accounted in the measured flux. These features have led us to explore in more detail the applicability of scintillometers in the SSL. This is the objective of this thesis.

The scintillometers used in this thesis are optical instruments that consist of a transmitter and receiver. Two types of scintillometers will be considered, notably the displaced-beam small-aperture scintillometer (DBSAS) and the large-aperture scintillometer (LAS). The DBSAS uses a laser split into two beams displaced by 2.7 mm and can be operated over distances of 100 – 250 m. The LAS uses one beam of, in this case, 10 cm diameter and can be operated over distances of ~100 - 2000 m. Both scintillometers measure intensity fluctuations of the light beam emitted by the transmitter and registered by the receiver, which are caused by refraction of the beam upon its passage through the turbulent surface layer. These intensity fluctuations are a measure of the structure parameter of temperature, C_T^2 . The DBSAS obtains also the dissipation rate of turbulent kinetic energy, ε , from the correlation, r_{12} , between fluctuations of the two displaced beams. In itself, these quantities are important properties of turbulence. Moreover, when the flow is turbulent they are related to the sensible heat and momentum flux, H and τ by virtue of Monin-Obukhov similarity theory (MOST). For the LAS, only C_T^2 can be obtained. It is customary to include a single level wind speed measurement and an estimate of the roughness length to the LAS method, to solve H and u^* . We also investigated combinations of the DBSAS with the LAS to jointly solve ε and C_T^2 . The DBSAS is the most suitable scintillometer to be used in the SBL, since it gives a measure of the mechanically induced turbulence (i.e. ε), which is the only turbulence generating mechanism in stable conditions.

In all scintillometry applications assumptions have to be made about the mathematical form of the turbulent n -spectrum (n is the refractive index), which for optical scintillometers can be assumed equal to the temperature spectrum. The DBSAS primarily sees the smallest eddy sizes of the turbulent spectrum falling in the dissipation-range. A model description of this part of the spectrum is given by Hill (1978), which is based on only a few observations. It shows that at the transition of the inertial to the dissipation-range the spectrum exhibits a small bump, the so-called Hill-bump. A length scale that marks this transition is the inner scale, l_0 , which is used to describe the dissipation-range spectrum. The DBSAS method solves l_0 from which ε can be derived directly. The LAS mainly sees inertial-range sized eddies and only needs the well-established description of the inertial-range temperature spectrum to solve C_T^2 .

Scintillometers have the advantage that they combine spatial and time averaging of turbulence statistics, rather than time averaging alone as is the case for the EC method, thus allowing flux averaging times of less than 1 minute. In addition, scintillometers are sensible to one dominant eddy size and interpolate the rest of the turbulent scales by using a theoretical form of the spectrum, rather than integrating over all measured eddy scales, as is the case with the EC method. This means the scintillometer method is not sensitive to path averaging affects and can be used very close to the surface (< 1 m).

We contributed to two field-experiments that form the basis of this thesis, notably the CASES-99 experiment (Kansas, USA, 1999, used in Chapters 3 and 4) dealing with night-time SBL and the BBC experiment (Cabauw, the Netherlands, 2001, used in Chapter 5) in which we compared different field-scale scintillometer configurations. A third experiment, RAPID (Idaho, USA, 1999), dealing with daytime SBLs was not analysed as part of this thesis. It resulted in a co-author publication, which for illustration is added to the Appendix and will not be discussed here. We also analysed an old scintillometer data-set from the La Poza experiment (Sonora, Mexico, 1996, used in Chapter 6), where we investigated the effect of a varying scintillometer beam height along the path. The conclusions of these studies are summarised per Chapter.

Chapter 3: Application of the DBSAS in stable conditions during CASES-99 experiment

The performance of the DBSAS in the SBL operated over a path length of 112 m was investigated using data gathered during the CASES-99. It was illustrated that the DBSAS is superior to the EC method in determining H and u_* close to the surface and over short (< 1 minute) averaging intervals.

To have independent measure of ε and C_T^2 , we developed an automated script that estimates these values from EC-data, i.e. sonic anemometer measurements. These methods are based on the definition of structure functions and theoretical inertial-range spectra.

Systematic errors were found, in the DBSAS ε and C_T^2 when compared with EC-data derived values, which also resulted in systematic errors in H and u_* . On the other hand, the scatter

found in the DBSAS ε , C_T^2 and fluxes was surprisingly low. The systematic errors in H primarily reflect the errors in u^* , which the DBSAS overestimates for low u^* and underestimates for high u^* . We were able to correct for this by adjusting the beam displacement distance, d , from 2.7 mm to 2.6 mm in the calculations, which is within the level of accuracy with which the manufacturer specifies this d . The latter adjustment is presented as a working hypothesis, not a general solution.

We also showed the sensitivity of the DBSAS method to the form of the spectrum in the dissipation-range (we used the form proposed by Frehlich, 1992). For large l_0 , i.e., small u^* only a small part of this spectrum is weighted at high wave-numbers. This indicates the theoretical basis for the DBSAS for large l_0 is limited; it depends heavily on the exact form of the spectrum in this region as well as that of the spectral weighting function.

In an appendix added in this thesis to the original publication, in addition to the d -adjustment, three more heuristic approaches to deal with the systematic deviations are discussed. Firstly, we adjusted the dissipation-range spectrum such that the theoretical r_{12} versus l_0 relation converged with the DBSAS measured r_{12} versus EC-data derived l_0 . This approach fixes the deviations in ε , but worsens them for C_T^2 and H . Secondly, we directly fitted a mathematical expression between the DBSAS measured r_{12} and EC-data derived l_0 . This approach works satisfactory for both ε and C_T^2 . Third, we bypassed all the steps involved in inferring fluxes from the DBSAS raw measurements and related these two directly to each other. This approach gives surprisingly good results. The ad-hoc relations we derived can be applied to a particular set-up only and stability range for which the relations were established.

Chapter 4: Derivation of MOST scaling functions for ε and C_T^2 in the SSL.

To derive surface fluxes from scintillometers the MOST functions f_ε and f_T of dimensionless ε and C_T^2 have to be known. According to MOST, these then are universal functions of the dimensionless height, $\zeta = z/L$, where z is height and L the Monin-Obukhov length. In stable conditions, f_ε and f_T were still not well-established. Using the CASES-99 data-set which has an exceptionally wide stability range for stable conditions (ζ of up to ~ 10 , for $z = 2.5$ m) these relations were derived based on ε and C_T^2 and flux-estimates from EC-data taken at 2.65 m. The best fits were given by $f_\varepsilon = 0.8 + 2.5\zeta$ and $f_T = 4.7[1 + 1.6(\zeta)^{2/3}]$, which differ somewhat from previously published functions.

The neutral limit $f_\varepsilon = 0.8$ implies that in the simplified TKE budget equation there is an imbalance between TKE production and dissipation. Similarly, we found a production-dissipation imbalance for the temperature fluctuation budget equation. Correcting for these imbalances, the 'standard' MOST functions for dimensionless wind speed and temperature gradients (ϕ_m and ϕ_h) were determined from f_ε and f_T and compared with the ϕ_m and ϕ_h and flux- and gradient Richardson-number formulations found in the literature. Our results show that using ε and C_T^2 obtained from a single level sonic anemometer to evaluate ϕ_m and ϕ_h for very stable conditions is a good alternative since, in that stability region, the measurement errors of gradients are large.

Chapter 5: Test of field scale scintillometers during the BBC experiment.

We compared three field scale scintillometer configurations during the BBC experiment: the DBSAS, LAS and combined DBSAS-LAS configurations. With field scale we refer to short path lengths of 100-200 m. The main objective of this study was to compare the three scintillometer configurations and to see whether the LAS and combined scintillometer configurations show the same systematic deviations in ε , C_T^2 and the fluxes as the DBSAS for stable conditions during CASES-99 (Chapter 3). In addition, it served as an independent test of the newly derived stable MOST functions based on CASES-99 data (Chapter 4).

We used a 10 cm aperture LAS that is somewhat l_0 dependant, i.e. sensitive to the Hill bump. The concept of a combined LAS-DBSAS is entirely new. Although unstable conditions were analysed as well as stable conditions, here we will only consider stable conditions. The comparison between the different scintillometer configurations was performed with respect to EC-data derived ε , C_T^2 and fluxes. The path length of all scintillometers was ~ 120 m.

For the DBSAS the same systematic deviations were found with little scatter for ε , C_T^2 and resulting u^* and H as were reported in Chapter 3 for CASES-99.

The LAS C_T^2 -estimate is better than the DBSAS C_T^2 -estimate. H and u^* are considerably worse for the LAS than for the DBSAS method however. In stable conditions turbulence is driven by mechanical turbulence (u^*), which in the LAS method is estimated indirectly using wind speed and an estimate of the roughness length.

The DBSAS-LAS configuration in which l_0 and C_T^2 are jointly solved from the single beam information of the LAS and DBSAS gives the same results for C_T^2 as for the LAS, but disappointing results for l_0 , i.e. a lot of scatter. This is also reflected in the flux-estimates; u^* gives a lot of scatter, which in its turn is also reflected in the H -estimate.

The DBSAS-LAS configuration in which l_0 and C_T^2 are solved from both DBSAS beams and the single LAS beam yields better results. In this configuration the LAS gives C_T^2 and the DBSAS ε . This set-up combines the better of the two instruments. C_T^2 is determined with the LAS at inertial-range eddy scales, and ε is determined from the DBSAS, over the same path as C_T^2 . Unlike the DBSAS, however, u^* for stable conditions of the LAS and the two DBSAS-LAS configurations shows a limited range when compared with EC u^* . This has to do with the interaction between C_T^2 and ε in the flux calculations. As a result, H of these configurations shows more scatter in stable conditions than the DBSAS H .

We introduced a practical approach to correct for the LAS inner scale dependence, which depends on the instruments aperture and l_0 . The LAS used in this study had an aperture of 10 cm. In low wind speed conditions, when l_0 is large, this correction can then be as large as 30% on C_T^2 .

We introduced a new analytical expression for Hills model of temperature spectrum at the dissipation-range (Hill, 1978). The analytical fit obeys the condition set by Frehlich (1992) fairly well and facilitates the calculation of l_0 from the raw DBSAS measurements.

Chapter 6: Derivation of a scintillometer effective height

In practice, the LAS beam height often varies along the path due to a variety of reasons. In this study we explain what effective height to use in such situations, when analysing scintillometer-data to derive H . Several aspects are covered: a slanted path over flat terrain, structured terrain, and varying path height due to the curvature of the earth's surface.

To test the derived effective height formulation we present LAS-data taken in September and October 1996 at a rangeland site in Sonora, Mexico. In experiment I, the LAS was set-up over a slant path, ranging roughly between 10 and 45 m above the surface over a 3200 m path. In experiment II, a horizontal LAS path was used at approximately 30 m over a path length of 1100 m. The resulting H was compared with EC-data and shows satisfactory results for both the full effective height formulation, which is a function of stability, as well as for one of the approximate effective height formulations for both stable and unstable conditions.

Considering the instrumental and theoretical assumptions it can be concluded that the DBSAS has proven to be a good research instrument in studying the SBL. Especially its superiority over the traditional EC method in obtaining fluxes close to the surface and over short averaging periods with very little scatter is a major advantage. The systematic deviations in ε , C_T^2 and the resulting fluxes is still an unresolved issue, however. Introducing the LAS and combinations between DBSAS and LAS did not yield better results. The systematic errors were dealt with successfully using ad-hoc solutions that cannot be applied universally. We realise that details of these approaches might be questionable, but feel that a DBSAS is very useful for obtaining valuable information on variables that drive stable turbulent flows.

Issues that still remain to be investigated that we feel may help towards a better understanding of the DBSAS systematic errors and alternative scintillometer methods with potential in the SBL:

- Perform measurements of atmospheric dissipation-range temperature spectra under a variety of stability conditions. We have attempted to do these measurements with fine cold wires, but were not successful. Point measurements of fine scale turbulence are technically extremely demanding on the materials used, noise free electronics of the bridge measurement, datalogging system etc. An alternative method infers the spectrum from scintillometer measurements after Frehlich (1992), who used a single transmitter with an array of receivers. This idea can be extended using photosensitive chips, which, in principle, represent an infinite array of finite-aperture receivers of various sizes in all directions (Hill, personal communication).
- Explore the possibility of a combined laser – large-aperture scintillometer integrated into one sensor. In Chapter 5 we experimented with this idea using separate sensors, which was not successful. Integrating the sensors ensures that exactly the same path is measured and that timing of the measurements and datalogging is the same.
- Explore the possibility of combining a LAS transmitter with a single- or multiple-apertures that is l_0 sensitive (aperture of less than 10 cm) and two or more LAS receivers (e.g. with aperture of 1 and 5 cm) to jointly solve l_0 and C_T^2 .

Appendix I List of Field Experiments and Related Publications

The authors professional record clearly shows his interest in experimental research in micro-meteorology. To put the research presented in this thesis in a wider framework an overview is given of the experiments the author organized or participated in, with a choice of references to publications based on these experiments. The experiments are given in chronological order. The period of the experiments indicated reflects the time of author spent in the field, not necessarily the time frame of the entire program.

1. Experiment: **La Poza**

Period: November 1995 – April 1996 + September 1996 – October 1996

Location: Sonora, Mexico

Topic: The La Poza experiment took place at a rangeland site in Sonora in the North-West of Mexico. The dominant vegetation there consists of grasses, cacti and prickly bushes and shrubs. In the period of November 1995 – April 1996 a 12 m high tower was erected with a Hydra eddy covariance (EC) system (built at IH, Wallingford, England) and additional measurements of radiation, surface temperature, and soil heat flux. This set-up provided ground-truth data for a model that estimates evapotranspiration from the GOES geo-stationary satellite. From April – October 1996 one of the first large aperture scintillometers built at Wageningen University was installed in the same area to test it. As there were not enough high-points in the landscape, the receiver was installed on the eddy covariance tower and the transmitter on top of a hill at 50 m height, resulting in a slanted LAS set-up. In the flux calculations, however, one effective LAS height is needed. The practical problem encountered with the LAS set-up at La Poza resulted in the derivation of general effective height formulations for calculating fluxes when the height of the scintillometer beam along the path is not constant (Hartogensis et al., 2004). This article is included in this thesis in Chapter 6.

Publications:

Hartogensis, O.K., 1997: *Measuring Areally-Averaged Sensible Heat Fluxes with a Large Aperture Scintillometer*. M.S. thesis, Wageningen Agricultural University, Wageningen, the Netherlands, 41 pp

Hartogensis, O.K., Watts, C.J., Rodriguez, J.-C., De Bruin, H.A.R.: 2003, 'Derivation of the effective height for scintillometers: La Poza experiment in Northwest Mexico', *J. Hydrometeorol.* 4, 915-928.

2. Experiment: **SALSA**

Period: May – August 1997

Location: Zapata, Sonora, Mexico + Sierra Vista, Arizona, USA

Topic: SALSA stands for "Semi-Arid Land-Surface-Atmosphere Program" (<http://www.tucson.ars.ag.gov/salsa/salsahome.html>). SALSA studies the human-induced environmental change in semi-arid regions. The research area of interest was

the Upper San Pedro river basin located partly in Sonora, Mexico and partly in Arizona, USA. Land degradation due to overgrazing and extensive extraction of ground water for industrial, domestic and agricultural use in the Upper San Pedro Basin has led to a change from the original prairie grasses to desert shrubs such as Mesquite. To determine the effect of this change on the energy and water balance of the basin, flux measurements over large areas had to be determined. The LAS, with its capability of measuring the average sensible heat flux over a line of ~200m to 5km is well suited for this task. Wageningen University contributed to the SALSA program in cooperation with the CESBIO/IRD group from France and IMADES from Mexico. In both 1997 and 1998 a Large Aperture Scintillometer (LAS) manufactured at Wageningen was deployed at two experimental sites in the Upper San Pedro Basin; the first one near a town called Zapata, Sonora, Mexico and the second one near a town called Lewis Springs, Arizona, USA. The author participated to SALSA in setting up the Zapata experimental site including an Edisol EC system (built by the university of Edinburgh), additional radiation, soil temperature and soil heat flux sensors and a LAS. In the Lewis Springs experiment the author was responsible for the installation of the LAS.

Publications:

- Chehbouni, A., Kerr, Y. H., Watts, C., **Hartogensis, O.**, Goodrich, D., Scott, R., Schieldge, J., Lee, K., Shuttleworth, W. J., Dedieu, G., De Bruin, H.A.R.: 1999, 'Estimation of area-average sensible heat flux using a large-aperture scintillometer during the Semi-Arid Land-Surface-Atmosphere (SALSA) experiment', *Water Resour. Res.*, 35, No. 8, p. 2505
- Watts, C.J., Chehbouni, A., Rodríguez, J.C., Kerr, Y.H., **Hartogensis, O.**, and De Bruin, H.A.R.: 2000, 'Comparison of sensible heat-flux estimates using AVHRR with scintillometer measurements over semi-arid grassland in northwest Mexico', *Agricultural and Forest Meteorology* 105, 81-89
- Chehbouni, A., **Hartogensis, O.**, Kerr, Y.H., Hipps, L., Brunel, J.-P., Watts, C., Rodriguez, J., Boulet, G., Dedieu, G., and De Bruin, H., 'Sensible heat flux measurements using a large aperture scintillometer over heterogeneous surface' Proceedings Special Symposium on Hydrology, Phoenix, Arizona, 11-16 Jan 1998 Boston: American Meteorological Society, 1998

3. Experiment: FLEVO

Period: July - August 1998

Location: Flevopolder, the Netherlands

Topic: The FLEVO experiment (<http://www.met.wau.nl/projects/flevo/flevo.html>) was set-up to study the applicability of the LAS over heterogeneous terrain, and to study the blending height concept for the structure parameter of temperature and the sensible heat flux. In addition a test was carried out with a radio-wave scintillometer, with which in combination with a LAS area averaged latent heat flux can be determined. The selected area in Flevoland, the Netherlands is very flat and consists of rectangular fields of about 500 m × 250 m covered with different crops. Eddy covariance equipment was installed over these crops to provide independent flux measurements. From these fluxes the area-averaged fluxes corresponding the footprint of the LAS measurements was composed and compared with the fluxes derived from the scintillometers. This study is the basis of the PhD thesis of Wouter Meijninger (Meijninger, 2003). The author participated in organizing and carrying the experiment and in the data analysis.

Publications:

- Meijninger, W.M.L., **Hartogensis, O.K.**, Kohsiek, W., Hoedjes, J.C.B., Zuurbier, R.M. and De Bruin, H.A.R.: 2002, 'Determination of area averaged sensible heat fluxes with a large aperture scintillometer over a heterogeneous surface – Flevoland field experiment', *Boundary-Layer Meteorol.* 105, 37-62
- Meijninger, W.M.L., Green, A.E., **Hartogensis, O.K.**, Kohsiek, W., Hoedjes, J.C.B., Zuurbier, R.M. and De Bruin, H.A.R.: 2002, 'Determination of area averaged water vapour fluxes with large aperture and radio wave scintillometers over a heterogeneous surface – Flevoland field experiment', *Boundary-Layer Meteorol.* 105, 63-83

4. Experiment: RAPID

Period: August-September 1999

Location: Kimberley, Idaho, USA

Topic: RAPID stands for "Regional Advection in an Irrigated Desert" and deals with stable boundary layers during daytime. Wageningen University participated in the RAPID field experiment, which was set-up in Kimberley, Idaho, USA to investigate the influence of regional advection on the locally measured evapotranspiration (ET). Advection of dry desert air to an area with irrigated agriculture contributes heat and vapour deficit to the evapotranspiration (ET) process. The author was responsible for organizing and executing the Wageningen contribution to the experiment. Backgrounds of the RAPID experiment are described in detail in Section 2.2. In Appendix III a reprint of the article referenced below is given.

Publications:

- De Bruin, H.A.R., **Hartogensis, O.K.**, Allen, R.G., and Kramer, J.W.J.L., 2005: 'Regional Advection Perturbations in an Irrigated Desert (RAPID) Experiment', *Theor. Appl. Climatol.* 80, 143-152.

5. Experiment: CASES-99

Period: October 1999

Location: Leon, Kansas, USA

Topic: CASES stands for "Cooperative-Surface Exchange Study" and deals with stable boundary layers during night time (<http://www.co-ra.com/cases/CASES-99.html>). The CASES-99 experiment was set-up to study all thinkable aspects of the stable nocturnal boundary layer. The data gathered by Wageningen University during CASES-99 forms the basis of a major part of this thesis (Sections 3 and 4). The author was responsible for organizing and executing the Wageningen contribution to the experiment. Backgrounds of the CASES experiment are described in detail in Section 2.1. In Appendix II, a reprint of the article of Van de Wiel et al. (2003), to which the author contributed, is given.

Publications:

- Hartogensis, O.K.**, De Bruin, H.A.R., Van De Wiel, B.J.H.: 2002, 'Displaced-Beam Small Aperture Scintillometer Test. Part II: Cases-99 Stable Boundary-Layer Experiment', *Boundary-Layer Meteorol.* 105, 149-176
- Van De Wiel, B.J.H., Moene, A.F., **Hartogensis, O.K.**, De Bruin, H.A.R. and Holtslag, A.A.M.: 2003, 'Intermittent turbulence and oscillations in the stable boundary layer over land Part III: a classification for observations during CASES99', *J. Atmos. Sci.* 60, 2509-2522.
- De Bruin, H.A.R., and **Hartogensis, O.K.**, 2005: 'Variance method to determine fluxes of momentum and sensible heat in the stable atmospheric surface layer', *Boundary-Layer Meteorol.*, 116, 385-392 .

Hartogensis, O.K. and De Bruin, H.A.R., 2005: ‘Monin-Obukhov similarity functions of the structure parameter of temperature and TKE dissipation rate in the Stable Boundary Layer’, *Boundary-Layer Meteorol.*, 116, 253-276.

Van De Wiel, B.J.H., **Hartogensis, O.K.**, Ronda, R.J., Moene, A., De Bruin, H.A.R. and Holtslag, A.A.M.; 2002. *Predicting the occurrence of intermittent turbulence in the stable boundary layer*. In: Proceedings European Geophysical Society – Nice, France: 2002

Hartogensis, O.K. and De Bruin, H.A.R.; 2002. *Displaced-Beam Small Aperture Scintillometer test: CASES-99 stable boundary layer experiment*. In: 15th Symposium on Boundary Layers and Turbulence Diffusion, Wageningen, the Netherlands. American Meteorological Society (2002)

Hartogensis, O.K. and H.A.R. De Bruin, 2004: *Monin-Obukhov similarity functions of the structure parameter of temperature and TKE dissipation rate in the Stable Boundary Layer*. In: Proceedings 16th Symposium on Boundary Layers and Turbulence Diffusion: Portland, ME, USA. American Meteorological Society (2004)

6. Experiment: **Yaqui2000**

Period: January 2000 – April 2000

Location: Obregon, Sonora, Mexico

Topic: The aim of Yaqui2000 was to investigate the performance of the LAS under conditions similar to those during RAPID, i.e. stable conditions during daytime due to advection of warm, dry desert air over irrigated agriculture. The project was carried out in collaboration with the local institutes IMADES and ITSON. A scintillometer was set up in a wheat field over a path length of 758 m, with an eddy correlation system installed near the centre of the path. The author was responsible for organizing and installation of the Wageningen contribution to the experiment. The research, carried out by students of Wageningen University (Hoedjes et al, 2002), revealed that the LAS performed well under a mixture of unstable (morning) and stable (afternoon) conditions as long as the net radiation was larger than zero.

Publications:

Hoedjes, J. C. B., R. M. Zuurbier, and C. J. Watts, 2002: Large aperture scintillometer used over a homogeneous irrigated are, partly affected by regional advection. *Bound.-Layer Meteor.*, 105, 99-117.

7. Experiment: **Spain Scintillometer Network**

Period: March 1999 – June 2002

Location: Spain

Topic: The objective of this experimental campaign was to collect ground-truth measurements for remote-sensing estimates of the surface energy balance. To this end a network of three large aperture scintillometers was installed at different locations in Spain in March 1999. These locations are near Lleida (north-east Spain), Tomelloso (central Spain) and Badajoz (south-west Spain). The three LASses were equipped with a pyranometer for the measurement of global radiation, and a GSM modem to monitor the instruments from the Netherlands. The data from the network were used in collaborations of Wageningen University with EARS in the EWBMS project (www.ears.nl/ewbms) and Alterra (www.alterra.wur.nl).

The author was involved in the installation and maintenance of the Wageningen contribution to the experiment.

Publications:

Rosema, A., Verhees, L., Putten, E. van, Gielen, H., Lack, T., Woord, J., Lane, A., Fannon, J., Estrela, T., Dimas, M., DeBruin, H.A.R., Moene, A.F., Meijninger, W.M.L., 2001. European Energy and Water Balance Monitoring System Project - Final report. Delft : EARS, 2001. - p. 147.

Jia, L., Su, Z., Van den Hurk, B., Menenti, M., Moene, A., De Bruin, H., Baselga Yrisarry, J., Ibanez, M., Cuesta, A.: 2003, 'Estimation of sensible heat flux using the Surface Energy Balance System (SEBS) and ATSR measurements', *Physics and Chemistry of the Earth* 28 75–88.

Moene, A.F., De Bruin, H.A.R., 2001. Sensible heat flux data derived from the scintillometers. In: Su, Z., Jacobs, C. (Eds.), BCRS Report, Advanced Earth Observation—Land Surface Climate. Final Report, 01-02, pp. 85–90.

8. Experiment: **EBEX**

Period: July - August 2000

Location: San Joaquin Valley, California, USA

Topic: EBEX stand for Energy Balance EXperiment. It is an international effort in seeking after the causes for failure of the closure of the energy balance at the earth's surface. It turns out that if one adds the sensible, latent and ground heat flux, the result is more than often less than the net radiation. The main focus was on eddy covariance fluxes of sensible and latent heat, since net radiation measurements are fairly accurate and the soil heat flux is small in comparison with the energy balance closure error found. The experiment was conducted over a horizontal, homogeneous terrain of a well-watered cotton crop.

The contribution of Wageningen University to EBEX was a joint effort with KNMI, the Netherlands. The equipment consisted of two eddy correlation packages, a net radiometer and background temperature and humidity measurements. The main objective of these measurements was to observe vertical divergence of the fluxes, if any, and closure of the energy balance. Because our instruments were taken close to the canopy, we had installed special short path (5 cm) sonic anemometers (Kaijo Denki TR90AH) and Krypton hygrometers, the latter at 5 cm downwind from the sonic w transducers. This compact configuration is necessary to resolve the small eddies that carry flux close to the canopy. The disadvantage is that in particular the Kryptons distort the airflow in the sonic path. To account for this disturbance, extensive measurements of the sonics response characteristics were taken in a wind tunnel before the experiment.

The author was involved in organizing the Wageningen part of the joint Wageningen-KNMI contribution to the project, but did not install the equipment.

Publications:

Kohsiek, W., Meijer, E.W., Versteeg, P.J.B., **Hartogensis, O.K.**, De Bruin, H.A.R.: 2001, 'EBEX-2000: the KNMI/WAU contribution' *KNMI Technical Reports* TR 240.

9. Experiment: **HEBEX**

Period: June - July 2001

Location: Wageningen, the Netherlands

Topic: HEBEX stands for "Haarweg Energy Balance Experiment". It was conducted at the Haarweg meteorological station, Wageningen, the Netherlands as a prelude to the international EBEX campaign later that summer. In contrast to the EBEX experiment,

the ground cover of the Haarweg station and the surrounding fields is short grass. Data from five 3-D sonic anemometers (three different types: Campbell Scientific CSAT3, Kaijo Denki TR61A and Kaijo Denki TR90AH) were compared in combination with three different types of hygrometers (Campbell Scientific KH20, Mierij Meteo Lymann- α and a LiCor 7500). All anemometers were mounted at a height of approximately 3.4 meter. The various masts were roughly five meters apart and installed along one line.

Until so far, from this only a comparison-study on the different methods to perform the sonic axis rotations has been presented (Moene et al., 2002).

The author was co-responsible for organizing and executing the experiment.

Publications:

Moene, A.F.M., **Hartogensis, O.K.**, Heusinkveld, B.G., Meijninger, W.M.L., and Van Dijk, A.; 2002. *Significance of axis rotation for eddy-covariance measurements*. In: Proceedings 15th Symposium on Boundary Layers and Turbulence Diffusion: 15th Symposium on Boundary Layers and Turbulence Diffusion, Wageningen, the Netherlands. American Meteorological Society

10. Experiment: BBC

Period: August - September 2001

Location: Cabauw, the Netherlands

Topic: The BBC (BALTEX Bridge Cloud) experiment was a cloud observation campaign that took place in August and September 2001 BBC at Cabauw, the Netherlands. The contribution of Wageningen University comprised the deliverance of surface fluxes measured with scintillometers and eddy covariance to the project database. With the different types of scintillometers we performed a comparison study of field –scale scintillometers, which is presented in Section 5. The CO₂ concentration and fluxes have also been used as a contribution to the CarboEurope project (www.carboeurope.org), a research project that deals with all aspects of CO₂-monitoring in Europe. Backgrounds of the BBC experiment are described in more detail in Section 2.3.

The author was responsible for organizing and executing the Wageningen contribution to the experiment.

Publications:

Vilà-Guerau de Arellano, J., **Hartogensis, O.**, Vermeulen, A.T., Holtslag, A.A.M.: 2002. *Application of surface layer similarity theory to carbon dioxide, moisture and temperature*. In: Proceedings 2nd CarboEurope meeting – Budapest, Hungary

11. Experiment: MATADOR2002

Period: May - June 2002

Location: Eloy, Arizona, USA

Topic: The main objective of the Martian ATmosphere And Dust in the Optical and Radio (MATADOR) 2002 field campaign was to quantify the intensity and variability of the contribution of dust devils and other convective plumes in the atmospheric boundary layer. Dust devils are frequently observed over terrestrial deserts and are ubiquitous features of the Martian landscape. They belong to family of organized structures in convective atmospheric turbulent boundary layers. So far, little experimental data on

these phenomena have been collected. Wageningen University participated in MATADOR together with the institutes IMADES and ITSON from Mexico and the Lunar and Planetary Laboratory, Tucson, Arizona. The experimental set-up consisted of three measurement towers placed in an equilateral triangle with sides of 10 m length. Towers were equipped with 4 eddy-covariance systems operated at 20 Hz. Infra-red thermometers and radiation sensors were mounted on one of the 3m towers. Just outside the triangle of towers, several soil sensors were buried. The author was responsible for organizing and executing the Wageningen contribution to the experiment. Preliminary results of this study have been presented at the EGS conference and an overview paper (Renno et al., 2003).

Publications:

- De Bruin, H.A.R., **Hartogensis, O.K.**, Renno, N.O., Burose, D., Smith, P.H., and Watts, C., 2003: *Dust devils and other organized structures in the convective boundary layer*. In: Geophysical Research Abstracts, Vol. 5, 08567 - Nice, France: 2003
- Renno, N.O., Abreu, V.J., Koch, J., Smith, P.H., **Hartogensis, O.K.**, De Bruin, H.A.R., Burose, D., Delory, G.T., Farrell, W.M., Watts, C.J., Garatuza, J., Parker, M., Carswell, A., 2004: 'MATADOR 2002: A Pilot Field Experiment on Convective Plumes and Dust Devils', *J. Geophys. Res. – Planets*, 109, No. E7, E07001 10 p.

12. Experiment: IRRIMED

<i>Period:</i>	September - October 2002	<i>Location:</i>	Marrakech, Morocco
<i>Period:</i>	December 2003 – February 2004	<i>Location:</i>	Jordan Valley, Jordan
<i>Period:</i>	February 2004	<i>Location:</i>	Palmyra, Syria
<i>Period:</i>	May 2005 -	<i>Location:</i>	Toulouse, France

Topic: The IRRIMED project is an Euro-Mediterranean Research project on improved management tools for water-limited irrigation combining ground and satellite information through models (www.irrimed.org). The general scientific objective is the assessment of temporal and spatial variability of water consumption of irrigated agriculture under limited water resources condition. Measurements with sophisticated equipments will allow to combine ground and satellite data into models, to ultimately produce simple and robust methods to assess evapotranspiration (ETR) over large areas. The task of Wageningen University in this project is the transfer of micrometeorological know-how. To this end a micro-meteorological course was given at Palmyra, Syria and several groups were assisted in setting up micro-meteorological field experiments. The first experiment took place in an olive yard, being the royal gardens of Agdal in Marrakech, Morocco. The Wageningen contribution consisted of two eddy-covariance systems and two LASses. The preliminary results of this study are presented in the M.S. theses of Van den Bersselaar (2003) and Van de Kroonenberg (2003). Williams et al. (2003) used the data as well. The author also set-up an eddy covariance system in the Jordan Valley and gave a course on the method. The system has been used to estimate K_c -factors for several crops in the Jordan valley, based on which Jitan (2003) defended his PhD thesis. Currently Wageningen University installed an extra large aperture scintillometer in an irrigated agricultural area south-west of Toulouse.

The author was responsible for organizing and executing the Wageningen contribution to the experiments.

Publications:

- Van den Bersselaar, D., 2003: *Surface flux estimates over an olive yard: Eddy covariance and Scintillometer method*. M.S. thesis, Wageningen University, Wageningen, the Netherlands, 47 pp
- Van den Kroonenberg, A., 2003: *Surface flux estimates over an olive yard: SEBAL method applied to NOAA-KLM and Landsat-7*. M.S. thesis, Wageningen University, Wageningen, the Netherlands, 61 pp
- Williams, D.G., Cable, W., Hultine, K., Hoedjes, J.C.B., Yezpe, E., Simonneaux, V., Er-Raki, S., Boulet, G., De Bruin, H.A.R., Chehbouni, A., **Hartogensis, O.K.** and Timouk, F., 2004: 'Components of evapotranspiration determined by eddy covariance, sap flow and stable isotope techniques', *Agricultural and Forest Meteorology* 125, 241-258.
- Jitan, M.A., *Evapotranspiration of Major Crops in the Jordan Valley Using Remote Sensing Techniques Compared with Estimated Field Measurement Using Eddy-Correlation*, Ph.D. thesis University of Jordan, Amman, Jordan, 220p.

Appendix II Co-Author Publication – CASES-99

The CASES-99 dataset gathered and processed in the framework of this thesis has also been used by others. Where the focus of this thesis is on experimental techniques to adequately measure fluxes in the stable intermittent boundary layer, the work of the Van De Wiel et al. (2002a, 2002b and 2003) focuses on a conceptual model of intermittent turbulence. The model is described in Van De Wiel et al. (2002a and 2002b). In Van De Wiel et al. (2003), the model is tested against CASES-99 data.

In this Appendix the publication of Van De Wiel et al. (2003), of which the candidate is co-author, is given in its original format:

Van De Wiel, B.J.H., Moene, A.F., **Hartogensis, O.K.**, De Bruin, H.A.R. and Holtslag, A.A.M.: 2003, 'Intermittent turbulence and oscillations in the stable boundary layer over land Part III: a classification for observations during CASES99', *J. Atmos. Sci.* **60**, 2509-2522.

Intermittent Turbulence in the Stable Boundary Layer over Land. Part III: A Classification for Observations during CASES-99

B. J. H. VAN DE WIEL, A. F. MOENE, O. K. HARTOGENSIS, H. A. R. DE BRUIN, AND A. A. M. HOLTSLAG

Department of Meteorology and Air Quality, Wageningen University, Wageningen, Netherlands

(Manuscript received 22 July 2002, in final form 21 November 2002)

ABSTRACT

In this paper a classification of stable boundary layer regimes is presented based on observations of near-surface turbulence during the Cooperative Atmosphere–Surface Exchange Study-1999 (CASES-99). It is found that the different nights can be divided into three subclasses: a turbulent regime, an intermittent regime, and a radiative regime, which confirms the findings of two companion papers that use a simplified theoretical model (it is noted that its simplified structure limits the model generality to near-surface flows). The papers predict the occurrence of stable boundary layer regimes in terms of external forcing parameters such as the (effective) pressure gradient and radiative forcing. The classification in the present work supports these predictions and shows that the predictions are robust in a qualitative sense. As such, it is, for example, shown that intermittent turbulence is most likely to occur in clear-sky conditions with a moderately weak effective pressure gradient. The quantitative features of the theoretical classification are, however, rather sensitive to (often uncertain) local parameter estimations, such as the bulk heat conductance of the vegetation layer. This sensitivity limits the current applicability of the theoretical classification in a strict quantitative sense, apart from its conceptual value.

1. Introduction

On clear nights with weak winds, a frequently observed phenomenon is the weak and intermittent character of turbulence in the atmospheric boundary layer. Intermittent turbulence is characterized by brief episodes of turbulence with intervening periods of relatively weak or unmeasurably small fluctuations (Mahrt 1999). Despite its common nature, relatively little is known about the physical mechanisms behind the intermittent turbulence in the stable boundary layer (SBL). Intermittency can be generated by several physical mechanisms (see Van de Wiel et al. 2002a): by local shear effects (Ha and Mahrt 2001), by instability on the scale of the entire surface inversion layer, or by turbulence generated aloft diffusing to the surface [see the review on SBL issues by Mahrt (1999)]. Also, locally produced waves formed by Kelvin–Helmholtz instabilities could play a role in triggering turbulence bursts [e.g., Coulter 1990; Nappo 1991; also recently observed during the Cooperative Atmosphere–Surface Exchange Study-1999 (CASE-99; Poulos et al. 2002)].

In the present work and in the companion papers of Van de Wiel et al. [2002a,b, hereafter VdW(a,b)], we focus on an intermittency mechanism, which results

from a direct interaction between the lower atmosphere and the surface, in presence of a pressure gradient. According to this mechanism, described in detail in VdW(a,b), intermittency is generated by an alternating sequence of SBL collapse (cessation of turbulence) as a consequence of strong surface cooling, followed by a recovery of the SBL (generation of turbulence). The recovery is induced by acceleration of the air by the pressure gradient during the collapse period (period of reduced friction). This increases the shear until $Ri < R_c$, eventually providing the condition for turbulent mixing (Businger 1973; Turner 1973). It is noted that in VdW(a,b), interaction with higher shear levels (as in Ha and Mahrt 2001) was not considered, which may limit the generality of the present results.

In VdW(a) the physical essentials of the mechanism described above were extracted, resulting in a model system of three coupled nonlinear differential equations. As such it was shown that this truncated model was able to mimic the observed intermittent turbulence. Also, the model simulated *both* an intermittent and two nonintermittent regimes for different parameter ranges, resulting in three different regimes for clear-sky conditions. Furthermore, the simplified model essentially showed the same behavior as more complex models (e.g., Blackadar 1979; Lin 1990; Revelle 1993; McNider et al. 1995).

In a second paper, VdW(b), the model equations were studied analytically following a system dynamics ap-

Corresponding author address: Dr. B. J. H. Van de Wiel, Dept. Of Meteorology and Air Quality, Duiwendaal 2, Wageningen University, Wageningen 6701 AP, Netherlands.
E-mail: Bas.vandeWiel@wur.nl

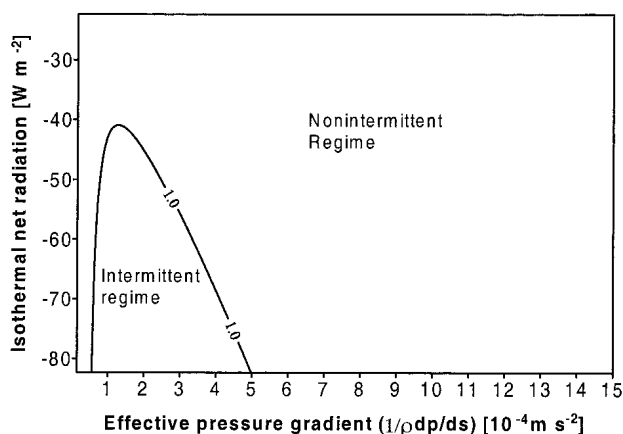


FIG. 1. Classification of SBL regimes in terms of external parameters. The figure represents a contour plot of Π values. Only one contour line is drawn, namely that of the critical level $\Pi = 1$. Within this line ($\Pi < 1$) intermittent cases are predicted, and nonintermittent cases are predicted outside this line ($\Pi > 1$).

proach. This resulted in a dimensionless parameter (denoted as Π), which was shown to be a predictor of the equilibrium behavior (e.g., intermittent or nonintermittent) of the simplified system. This critical parameter Π is merely a function of *external "forcings/parameters,"* such as the pressure gradient and the radiative forcing and of local properties, such as surface roughness, surface heat conductance, and surface heat capacity. As such, this parameter was proposed as a classification tool to predict intermittent and nonintermittent SBL regimes. It was shown that $\Pi < 1$ corresponds to intermittent situations and $\Pi \geq 1$ corresponds to nonintermittent cases.

For a specific location with fixed local properties the dependence of Π on external forcings can be drawn in a *classification diagram*, valid for that location. An example is given in Fig. 1 showing the critical level $\Pi = 1$ as a contour line for different values of the effective pressure gradient and of the isothermal net radiation Q_i . The isothermal net radiation is a measure for the radiative forcing (section 2), such that the upper part of Fig. 1 indicates cloudy conditions and the lower part corresponds to clear skies. According to the Π concept, all cases within the contour line $\Pi < 1$ correspond to nocturnal boundary layers with intermittent turbulence, and all cases outside the contour line $\Pi > 1$ correspond to nonintermittent cases. It is observed that under clear-sky conditions, three regimes are predicted, occurring at different values of the effective pressure gradient. This confirms the earlier findings from model simulations by VdW(a). For cloudy cases, only a single nonintermittent (i.e., continuous turbulent) regime is predicted.

With the theoretical work of VdW(a,b) as a point of departure, the present work investigates recent observations of SBL regimes during CASES-99. As such, the main goal of the present paper is to

- 1) classify the different nights of the CASES-99 field experiment into subregimes (section 3) based on flux time series (with a focus on near-surface measurements), wherein a key question is, Can we distinguish three different regimes as predicted?;
- 2) determine the value of Π for each night by using observations (section 4) wherein a key question is, Where would the CASES-99 nights be located in terms of Fig. 1?;
- 3) compare the classification based on this Π concept (using "external" parameters) with the independent classification based on observed flux time series (i.e., using internal variables; section 5).

The extensive cooperative field experiment CASES-99 was carried out by various groups from the United States and Europe in Kansas, in October 1999 (see this issue and Poulos et al. 2002). The experiment lasted for an entire month, under *various meteorological conditions*, which makes it extremely suitable to study different SBL regimes in relation to the external forcings.

The paper is organized as follows. In section 2, a short data description is given. Sections 3, 4, and 5 address objectives 1, 2, and 3 (above), respectively. Discussion and conclusions follow in sections 6 and 7.

2. Data description

The CASES-99 stable boundary layer experiment took place during October 1999, 50 km east of Wichita, Kansas. The experimental area, covered with dry, open prairie grass (0–0.25 m high), was relatively flat with some minor slopes in the order of 0.5 degrees. A vast array of instruments was deployed. For a general description of the experiment we refer to Poulos et al. (2002) and to the official CASES-99 Internet site at <http://www.colorado-research.com/cases/CASES-99.html> (data freely available).

The Meteorology Group of Wageningen University provided observations at one point (37°38.611'N, 96°44.233'W) in a nested network of flux stations around the central 55-m flux tower of the National Center for Atmospheric Research (NCAR). An eddy covariance system was set up at a height of 2.65 m and operated at 20 Hz. It consisted of a Campbell Scientific model CSAT3 sonic anemometer and model KH20 Krypton hygrometer. Raw data were stored on a laptop and processed as described in Hartogensis et al. (2002). In order to get detailed information about the temporal variation of the fluxes (section 3) a rather short averaging period of 5 min was chosen. Comparison with 30-min-averaged fluxes (not shown) gave little systematic difference, favoring the use of a short averaging period. At the same time it is recognized that, especially in very stable conditions, accurate flux estimations from sonic anemometers is not trivial, due to the fact that pathlength may not be small compared to (typical) eddy

size. This problem is, however, not discussed here (see, e.g., Moore 1986).

Shortwave radiation components were measured with a CM14 albedometer and longwave radiative components by a CG2 pyrgeometer (both manufactured by Kipp and Zonen), mounted on a tripod at 1.5 m. From these radiation components the net radiation was calculated. Two soil heat flux plates were employed (at -0.054 m; one manufactured by TNO; the other a REBS model HFT3) together with two Pt-100 soil thermometers (at -0.028 and -0.080 m; provided by Wageningen University). Both radiation and soil measurements were sampled at 5 s and averaged and stored every 10 min (on a Campbell Scientific 21X micrologger). For a more detailed description of all the measurements by the Wageningen Group, we refer to the Web site above.

The height of the turbulent boundary layer was inferred from sodar observations [returned signal strength (in decibels)] at Beaumont, Whitewater, and Oxford as part of the Argonne National Laboratory Boundary Layer Experiment (ABLE) program infrastructure (see Poulos et al. 2002).

3. Observed flow regimes during CASES-99

a. Method

In this section a classification based on observations of flux time series is made. This time series classification will be compared with the theoretical predictions using the classification diagram in section 5. The different nights are divided into classes according to the typical characteristics of their turbulent heat flux time series. The turbulent heat flux near the surface is chosen as indicator because the turbulent heat flux is directly influenced by two external key parameters: the synoptic pressure gradient and the isothermal net radiation (section 4). We note that our current flux analysis focuses on near-surface measurements, which may limit the generality of the results (see discussion).

From numerical simulations by VdW(a) and the analytical work by VdW(b), it became clear that three typical time traces of the turbulent heat flux are to be expected: 1) a regime with high turbulent transport and nonintermittent fluxes, 2) a regime with intermittent fluxes, 3) a regime with very low turbulent transport and nonintermittent fluxes. These theoretically predicted traces are used as a guideline for the time series classification introduced below. It will be shown that the time series could easily be evaluated by eye because the different regimes show very different behavior. In order to avoid subjectivity, only clear examples were classified (a priori) as such (see below).

b. Results: A classification of SBL regimes using observation of flux time series

From the time series of the surface fluxes (H and u_*) during the observational period, it is found that the

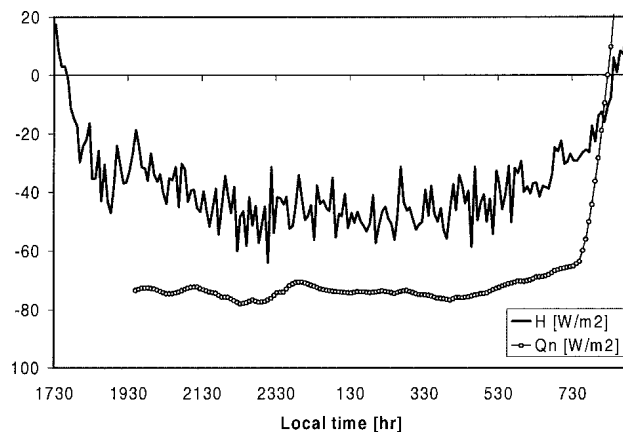


FIG. 2. A typical example of a time series of the sensible heat flux and net radiation during a continuous turbulent night (14–15 Oct).

CASES-99 nights (indeed) can be subdivided into the following regimes:

- 1) continuous turbulent regime,
- 2) intermittent regime,
- 3) radiative regime.

To illustrate the main features of each class, typical examples are given below.

1) CONTINUOUS TURBULENT NIGHTS

In Fig. 2 the turbulent heat flux is shown during a clear night with continuous turbulence (14–15 October). The sensible heat flux reaches a large value of about -45 W m^{-2} , due to strong radiative surface cooling ($Q_{\text{net}} \approx -75 \text{ W m}^{-2}$) in combination with strong turbulent mixing ($u_* \approx 0.5 \text{ m s}^{-1}$).

2) INTERMITTENT NIGHTS

In Figs. 3a,b two typical examples of intermittent nights are given. These examples give an impression about the typical timescales and amplitudes of the turbulent events and the quiet periods. It is observed that they are rather irregular. Some turbulent periods have very small amplitudes of 5 W m^{-2} and timescales of less than 10 min; others have amplitudes of 25 W m^{-2} and a duration of 4 h. The quiet periods may, but need not, result in a total decay of the flux, and the timescales also range from tens of minutes to a few hours.

An interesting result is given by the net radiation graphs of Figs. 3a,b, showing small deviations superimposed on a smooth decreasing trend (absolute value). The smooth trend results from a strong surface cooling during the night. The small deviations are caused by the turbulent bursts, leading to alterations of the surface temperature which immediately affects the net radiation [cf. model simulations by VdW(a)].

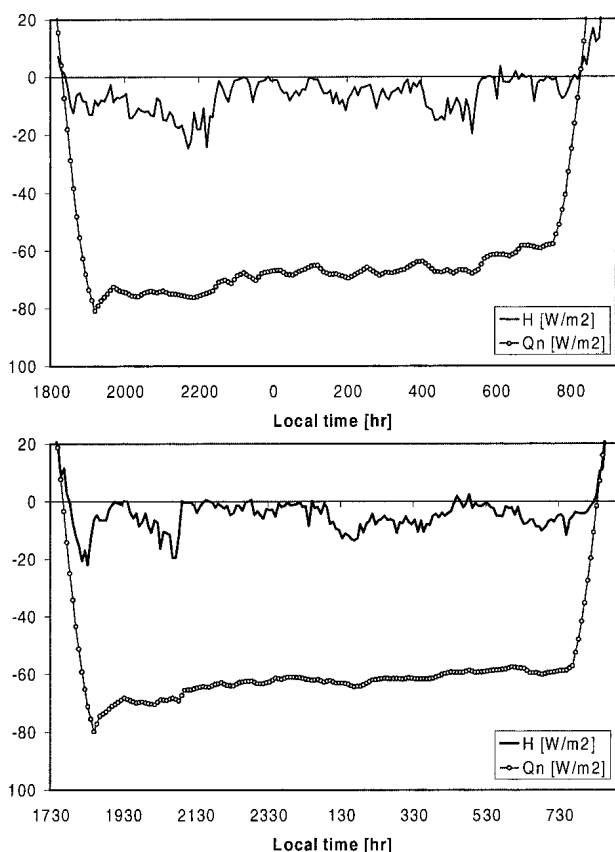


FIG. 3. Typical examples of the sensible heat flux and net radiation for two nights with intermittent turbulence: (top) 4–5 Oct and (bottom) 23–24 Oct.

3) RADIATIVE NIGHTS

In contrast to the well-mixed case of Fig. 2, a night with hardly any turbulent heat flux is shown in Fig. 4. Because the transport of energy through the atmosphere by turbulence is so small, we indicate these nights simply as “radiative nights.”

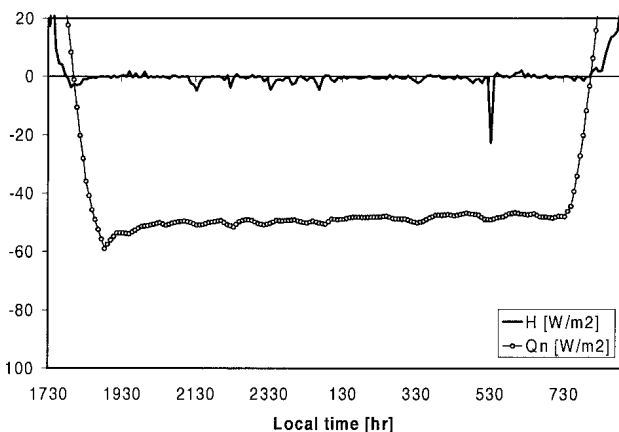


FIG. 4. A typical example of a time series of the sensible heat flux and net radiation during a radiative night (9–10 Oct).

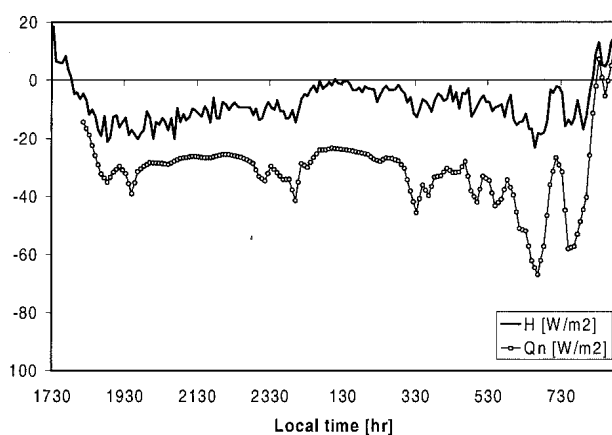


FIG. 5. Sensible heat flux and net radiation in a night with varying cloud cover (16–17 Oct).

4) A CLOUDY CASE

Contrary to the previous clear-sky examples, in Fig. 5 (16–17 October), a night with variable cloud cover is shown. In this case the turbulent heat flux demonstrates alternating higher and lower values. From this heat flux graph only, it looks as if this could be a night with intermittent turbulence. On the contrary, however, *it is a night with continuous turbulence*, as will be shown below. In the following, Fig. 5 is compared with Fig. 3a (4–5 October). Comparing the net radiation graphs of both figures, it is observed that the magnitude of the net radiation during 16–17 October is much smaller and more variable than during 4–5 October, indicating the presence of clouds in the first place. The contrast between the two nights becomes more evident in the friction velocity graphs (Fig. 6). In the intermittent situation (4–5 October) the values of u_* are very low and correlated with H . In the continuous turbulent case (16–17 October), the values of u_* are high and not correlated with H . These examples show that in the cloudy night the radiative factors are limiting for the turbulent heat

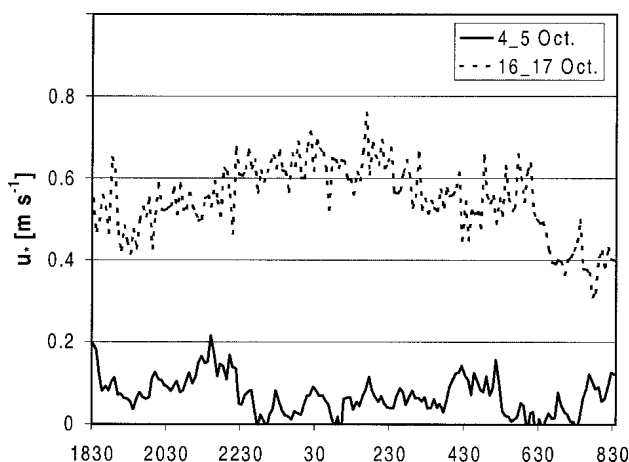


FIG. 6. Comparison of friction velocity time series during an intermittent and during a nonintermittent night.

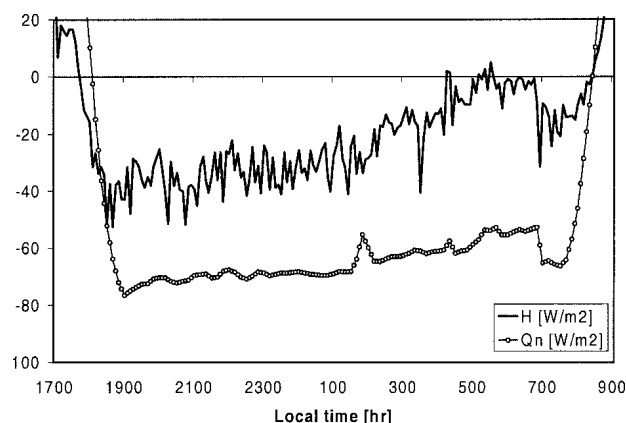


FIG. 7. Sensible heat flux and net radiation during a night with transient behavior (12–13 Oct).

flux, whereas in the clear night the mixing efficiency is the limiting factor for the turbulent heat flux. In terms of K theory, in the cloudy case the temperature gradient is the limiting factor (negative feedback mechanism), whereas in the clear-sky, intermittent case the turbulent diffusivity is limiting [positive feedback mechanism; De Bruin 1994; Derbyshire 1999; VdW(b)].

5) A TRANSIENT CASE

In the previous examples the behavior of near-surface turbulence was classified into three different regimes. It is realized that any SBL classification is only a simplification of real SBL complexity (Mahrt et al. 1998). This fact is illustrated by an example of a transient night given in Fig. 7. In the beginning of the night, the figure seems a perfect example of a night with continuous turbulence. After 0200 LST, however, it is observed that the heat flux H rapidly decreases from about -40 W m^{-2} to almost zero. This collapse of turbulence was also clearly visible in u_* (not shown) decreasing from about 0.35 m s^{-1} around 0 h to 0.05 m s^{-1} around 0600 LST. Apart from some influence of high-level clouds, the net radiation remains rather large. Around 0700 LST (40 min before sunrise) a sudden recovery of H and u_* (increasing from 0.02 – 0.22 m s^{-1} within 5 min) occurs. It seems that rapidly changing synoptic conditions strongly influenced the mechanical budget of the SBL. Several of these kinds and other transitional cases, were observed during CASES-99. In this study these cases are not classified explicitly but are indicated as *transient* or “*nonclassified*” cases.

c. Classification applied to the whole CASES-99 dataset

The classification of the previous section was applied to the whole CASES-99 data period. The results of this time series classification are summarized in Table 1. Also in Table 1, the mean values of some basic micro-

meteorological variables are given to indicate typical values occurring at different conditions/regimes. The averages were calculated over 0000–0600 LST. This period is chosen because it is often the most stationary period of the night (contrary to the period after sunset), although a purely stationary period [as assumed in VdW(b)] in its strict sense that the variables do not change in time, is not reached.

From Table 1, it occurs that 20 out of 28 nights were classified. Of these 20 classified nights, 8 nights (40%) showed continuous turbulence during the 6-h period, 8 nights (40%) showed intermittent turbulence, and 4 nights (20%) behaved as a radiative nights. From these frequency statistics, the number of intermittent and radiative nights may seem rather high compared to the number of turbulent nights. This can be explained by the large number of clear nights during the CASES-99 field campaign (Poulos et al. 2002). It is well known that clear-sky conditions favor moderately to strongly stable SBLs that may lead to radiative or intermittent nights. In more cloudy conditions the number of intermittent/radiative nights will be less.

Although a detailed discussion about the micrometeorological characteristics of each night is beyond the scope of this paper, some general characteristics are outlined.

- As expected, turbulent nights mostly occur in situations with strong winds and weak inversions. In the same way, intermittent and radiative nights tend to occur in low wind conditions with stronger temperature inversions.
- Most of the nights show large net radiation indicating clear nights.
- From the mechanical point of view, a large range in u_* values (0.02 – 0.59 m s^{-1}) is observed, leading to a broad range of stability conditions.
- Mostly, the latent heat flux is small.
- Generally speaking, the magnitude of the soil heat flux (SHF) is large compared to the other terms in the energy balance, showing the importance of this process. Therefore, a detailed description of the SHF measurements and its analysis are given in the appendix, together with some innovative results. Because the complete set of SHF instruments by Wageningen University was only available at the end of the experiment, only this part of the measurements is given.

4. Application of Π : Input parameters

a. Introduction

In this section the dimensionless Π number [VdW(b)] is evaluated for each night to predict the particular SBL regime for that night. Thus, for each night, the input parameters have to be estimated from the data, which is not a trivial task, in view of the simplified character of the theoretical model. Therefore, we discuss the pa-

TABLE 1. Classification of CASES-99 nights based on turbulent heat flux observations. Also, an overview of some basic micrometeorological variables is given (6-h averages). “**Trans.**” is for transient; “**Turb.**” is for turbulent, “**Int.**” is for intermittent, and “**Rad.**” is for radiative. (Source, Meteorology Group of Wageningen University.)

DOY (-)	Date (-)	Time [LST (h)]	Class (-)	u^* (m s ⁻¹)	Q_{net} (W m ⁻²)	H (W m ⁻²)	LvE (W m ⁻²)	G (W m ⁻²)	U_{10} (m s ⁻¹)	T_{10} (K)	T_s (K)
274	1 Oct	0000–0600	Trans.	0.150	-65.8	-23.4	4.5	—	3.42	285.27	282.57
275	2 Oct	0000–0600	Trans.	0.267	-35.2	-15.9	16.4	—	4.68	286.65	285.70
276	3 Oct	0000–0600	Turb.	0.295	-6.2	7.0	18.8	—	4.46	281.30	282.44
277	4 Oct	0000–0600	Trans.	0.213	-49.3	-2.9	2.3	—	3.76	276.99	277.36
278	5 Oct	0000–0600	Int.	0.061	-66.8	-5.9	-0.5	—	3.29	279.97	277.08
279	6 Oct	0000–0600	Int.	0.075	-61.7	-6.9	-2.2	—	2.82	285.16	281.41
280	7 Oct	0000–0600	Turb.	0.438	-71.2	-48.4	14.8	—	6.40	288.80	286.57
281	8 Oct	0000–0600	Int.	0.139	-48.3	-10.1	-5.6	—	3.15	287.49	285.82
282	9 Oct	0000–0600	Int.	—	—	—	—	—	—	—	—
283	10 Oct	0000–0600	Rad.	0.022	-48.6	-1.2	-0.6	—	2.03	288.62	284.45
284	11 Oct	0000–0600	Turb.	0.360	-65.8	-32.7	10.0	—	5.59	288.94	287.20
285	12 Oct	0000–0600	Turb.	0.217	-64.3	-20.4	-2.1	—	4.05	290.38	287.91
286	13 Oct	0000–0600	Trans.	0.199	-62.5	-17.5	-1.8	—	3.67	290.38	288.10
287	14 Oct	0000–0600	Rad.	0.031	-62.8	-1.4	-0.3	—	2.26	281.50	278.71
288	15 Oct	0000–0600	Turb.	0.494	-73.9	-45.6	5.7	—	7.21	292.79	290.41
289	16 Oct	0000–0600	Turb.	0.451	-58.9	-13.8	9.2	—	7.45	285.44	285.24
290	17 Oct	0000–0600	Turb.	0.594	-31.2	-5.7	12.5	-24.0	9.30	282.63	283.04
291	18 Oct	0000–0600	Int.	0.094	-55.6	-4.1	2.9	-39.7	2.97	277.02	275.01
292	19 Oct	0000–0600	Rad.	0.033	-57.6	-1.1	0.4	-45.1	2.14	279.87	276.65
293	20 Oct	0000–0600	Int.	0.070	-61.9	-5.7	0.1	-38.9	3.06	278.11	275.17
294	21 Oct	0000–0600	Trans.	0.115	-63.2	-14.3	-0.2	-32.1	3.94	283.37	279.19
295	22 Oct	0000–0600	Trans.	0.119	-60.7	-17.7	3.2	-30.9	4.50	286.16	280.68
296	23 Oct	0000–0600	Trans.	0.172	-70.1	-19.3	3.1	-42.6	4.35	278.86	276.71
297	24 Oct	0000–0600	Int.	0.067	-61.2	-4.8	0.5	-48.3	2.92	275.02	273.12
298	25 Oct	0000–0600	Turb.	0.296	-69.6	-34.5	3.9	-29.5	6.28	282.11	279.45
299	26 Oct	0000–0600	Rad.	0.018	-53.4	-1.7	-0.3	-39.6	2.02	285.29	277.64
300	27 Oct	0000–0600	Int.	0.158	-65.4	-27.8	0.0	-28.9	3.81	288.12	283.35
301	28 Oct	0000–0600	Trans.	0.230	-59.6	-28.9	0.3	—	4.19	287.97	285.28

rameters in relation to the available data, which will result in an overview table of input parameters and Π numbers. Due to its extremely complex form, the explicit form of the Π parameter is not discussed here. For the exact analytical form of Π and its derivation we refer to [VdW(b)].

b. Estimation of external forcing parameters

1) THE EFFECTIVE PRESSURE GRADIENT

VdW(a) showed that in the theoretical model, an *effective* value of the pressure gradient is used rather than the “real” pressure gradient, due to the negligence of Coriolis effects. Here, the effective pressure gradient is defined as the pressure gradient in the direction of the mean wind speed in the lower atmosphere. In practice it is not straightforward to estimate this effective value accurately.

- The mean wind direction close to the surface may vary in time, especially in conditions of intermittent turbulence, where changes in surface friction cause changes in the (cross isobaric) flow direction up to tens of degrees. This affects the effective component of the pressure gradient.
- In the SBL the “mean” wind may vary considerably with height (e.g., Nieuwstadt and Tennekes 1981), which makes it difficult to choose a single “representative” mean wind direction for the lower atmosphere.

• Often, from weather maps only limited time intervals with pressure data are available (e.g., each 6 h), whereas the pressure gradient may vary during these intervals.

Therefore, a different approach is followed in order to obtain a measure for the effective pressure gradient. The point of departure is the momentum budget of the mean wind speed following the model of VdW(a,b):

$$\frac{\partial U}{\partial t} = -\left(\frac{1}{\rho} \frac{\partial P}{\partial s}\right)_{\text{effective}} - \frac{u_*^2}{h}. \quad (1)$$

In this equation the influence of advection was neglected. Furthermore, a “classical” boundary layer structure was assumed (as, e.g., in Nieuwstadt 1984) where the stress decreases gradually with height until it vanishes at the boundary layer top. If the assumption of stationarity is adopted as well (as in the original derivation of Π), then the effective pressure gradient can be replaced by

$$-\left(\frac{1}{\rho} \frac{\partial P}{\partial s}\right)_{\text{effective}} = \frac{u_*^2}{h}. \quad (2)$$

This substitution is applied to Fig. 1 (Fig. 8). Note that the shape of Fig. 8 is unchanged compared to Fig. 1.

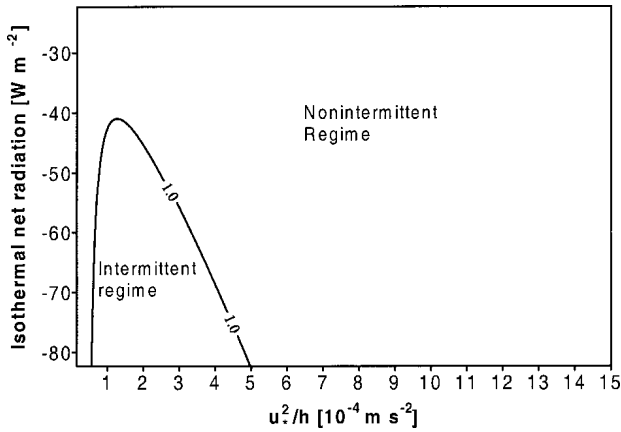


FIG. 8. As in Fig. 1, but with the horizontal axis in terms of u_*^2/h (6-h averages) instead of (effective) pressure gradient.

From now on, an axis as in Fig. 8 will be used. Adopting the assumptions above, the effective pressure gradient is estimated from the data by using 6-h-averaged values of the surface stress and of the boundary layer height (see section 4e).

It is, however, realized that many real SBLs do not show classical behavior. For example, Mahrt and Vickers (2002) show a number of CASES-99 nights where fluxes temporarily increase with height (upside-down boundary layers) before they decrease higher up. Also, SBL are often nonstationary by many causes, as with inertial oscillations. This means that Eq. (2) can, at best, only provide a crude approximation of the effective pressure gradient, limiting the generality of Fig. 8 (see discussion).

2) THE ISOTHERMAL NET RADIATION

A second key parameter determining the radiative forcing on the SBL system as defined in VdW(a,b) is the so-called isothermal net radiation (Monteith 1981; Holtslag and De Bruin 1988). The isothermal net radiation is defined as the net radiation that would occur if the near-surface layer were isothermal. This definition becomes clear by noting the linearized longwave radiation budget for the surface in the model (a small correction term is neglected):

$$Q_{\text{net}} \approx [-\sigma(\varepsilon_s - \varepsilon_a)T_{\text{ref}}^4 + N60] + 4\sigma T_{\text{ref}}^3(T_a - T_s). \quad (3)$$

This equation is derived by linearization of the original budget equation near a reference temperature T_{ref} [see VdW(a)]:

$$Q_{\text{net}} = \varepsilon_a \sigma T_a^4 + N60 - \varepsilon_s \sigma T_s^4. \quad (4)$$

By writing the net radiation equation as Eq. (3), it is clear that it can be divided in two parts: a part containing independent external parameters ε_a , ε_s , and cloud cover N (octa); and a part containing system variables T_a (air temperature) and T_s (surface temperature). The first part

of (3) is defined as the isothermal net radiation Q_i , because it equals the net radiation Q_{net} if $T_a = T_s$. For our dataset, Q_i is estimated from $Q_i = Q_{\text{net}} - 4\sigma T_{\text{ref}}^3(T_a - T_s)$, with T_a measured at 10 m, as in Table 1.

c. Local system parameters

An important parameter determining the vegetation–soil interaction is the so-called bulk conductance of the mulch/stagnant air layer within the vegetation [VdW(a)]. This bulk conductance is denoted with λ_m/δ_m $\text{W m}^{-2} \text{K}^{-1}$, where λ_m is the conductance (in $\text{W m}^{-1} \text{K}^{-1}$), and δ_m is the thickness of the mulch/stagnant air layer (in meters). It determines the heat flux through the vegetation layer, given a temperature difference between the vegetation top (radiation temperature T_s) and the soil surface (T_M):

$$G = (\lambda_m/\delta_m)(T_M - T_s). \quad (5)$$

For dense vegetation the bulk conductance can be easily determined by measuring G in combination with the radiation temperature of the vegetation T_s and the topsoil temperature T_M . In CASES-99, the surface was covered with dry, open prairie grass, so that bare soil was visible between the grass. Thus, the infrared camera (at 1.5 m), measures a composite of the vegetation top temperature T_s and the topsoil temperature T_M . If, for simplicity, we assume $\varepsilon_s = 1$ for both vegetation and bare soil, this can be approximated as

$$\sigma T_{\text{IRT}}^4 = A\sigma T_s^4 + (1 - A)\sigma T_M^4, \quad (6)$$

with $A[-]$, the fraction of vegetation cover. Regarding the approximation above, it is noted that the use of a slightly different power law (i.e., powers of 4.5 instead of 4) is probably more appropriate in the window region, although the results are very similar (within 1.5% error in $T_M - T_s$), that is, small compared to the uncertainties in the estimation of the vegetation fraction.

For a given vegetation fraction, the actual temperature of the vegetation top T_s can be calculated from the measured values T_{IRT} and T_M . Next, the value of G can be plotted as a function of $T_M - T_s$ in order to estimate the bulk conductance. In Fig. 9, this is applied to the CASES-99 data assuming two different values for the vegetation cover. The plots show surprisingly little scatter, given the strong empirical character of Eq. (5) not accounting for the complicated structure of real vegetation (leaf distribution/orientation). From Fig. 9, the following estimates for the bulk conductance are made (in $\text{W m}^{-2} \text{K}^{-1}$): $\lambda_m/\delta_m \approx 5$ for $A = 1.0$; $\lambda_m/\delta_m \approx 2$ for $A = 0.5$ [the intermediate case (not shown) gives $\lambda_m/\delta_m \approx 3.5$ using $A = 0.75$]. These “extremes” give a range for the bulk conductance at CASES-99. For comparison we note that Duynkerke (1999) found $\lambda_m/\delta_m \approx 3 \text{ W m}^{-2} \text{K}^{-1}$ for short, dense grass at Cabauw, comparable to the values given above.

Another vegetation parameter is the heat capacity C_v

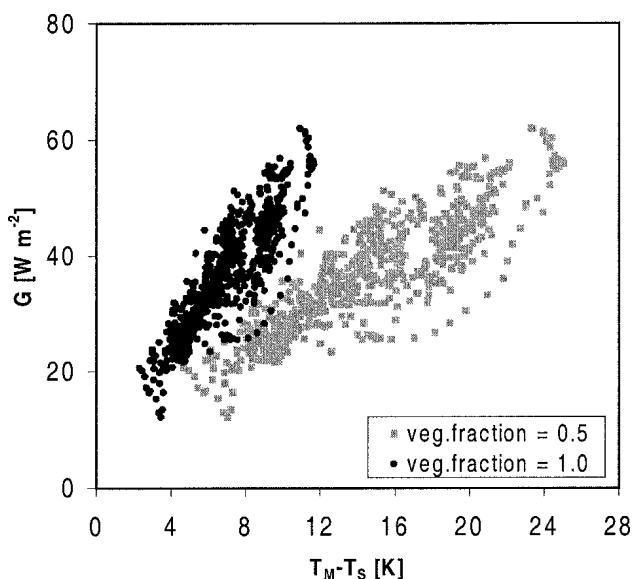


FIG. 9. Estimation of vegetation bulk conductance for two different fractions of vegetation cover.

of the vegetation top (per unit area). This parameter, which is difficult to estimate, was given an effective value of $2 \text{ kJ m}^{-2} \text{ K}^{-1}$ [as in VdW(a)], based on typical biomass estimations for grasslands (Atzema 1992), accounting for the dry and sparse character of the CASES-99 grass.

The momentum roughness length z_{0m} was taken to be 0.03 m, based on local measurements of momentum flux and wind profiles. In order to be consistent with the theoretical work, it was assumed that $z_{0m} = z_{0h}$. In future work this assumption could be refined.

d. Boundary conditions

1) BOTTOM BOUNDARY CONDITION FOR TEMPERATURE

In the simplified model the topsoil temperature T_M (the bottom system boundary) is assumed to be a known external variable, needed to calculate Π : T_M (at $z = 0.00 \text{ m}$) is inferred from Fourier analysis of soil temperature measurements as explained in the appendix.

2) TOP BOUNDARY CONDITION FOR TEMPERATURE

In order to estimate the radiative forcing on the SBL system, strictly speaking, a temperature T_{TOP} at the boundary layer height is needed. As a practical approach, the temperature at the top of the central mast (55 m) was taken as T_{TOP} . Because, the strongest temperature gradient is usually below 55 m, Π is not very sensitive to the exact height at which this top temperature is evaluated as long as it is not close to the surface.

e. Other input parameters

BOUNDARY LAYER HEIGHT

From sodar observations at Beaumont, Oxford, and Whitewater [strength of the returned signal (in decibels)], a composite estimate of the boundary layer height (h) was made, given in Table 2. For a few cases, h was small enough ($< 55 \text{ m}$) to compare it with flux data from the central NCAR tower. Although the sodar estimates showed somewhat larger values than estimates from mast data, the comparison seemed reasonable for most cases. Generally, it is stressed, however, that the 6-h-averaged values of the h are rather crude estimates. In

TABLE 2. Overview of input parameters used for evaluation of Π . The calculated Π values are given for two values of λ_m/δ_m . (For explanation of class, see Table 1.)

DOY (-)	Date (-)	Time [LST (h)]	Class (-)	u^2/h (m s^{-2})	Q_i (W m^{-2})	h (m)	T_{TOP} (K)	T_M (K)	$\Pi \lambda_m/\delta_m$ = 5 (-)	$\Pi \lambda_m/\delta_m$ = 2 (-)
279	6 Oct	0000–0600	Int.	7.5E-05	-77.2	75	290.01	284.31	23.8	2.1
280	7 Oct	0000–0600	Turb.	1.3E-03	-80.8	145	290.59	286.98	268.3	258.6
281	8 Oct	0000–0600	Int.	1.7E-04	-56.0	115	290.78	287.48	19.2	-20.2
283	10 Oct	0000–0600	Rad.	6.8E-06	-67.3	70	294.15	287.53	86.0	56.0
284	11 Oct	0000–0600	Turb.	7.4E-04	-73.5	175	291.39	288.86	202.3	142.9
286	13 Oct	0000–0600	Trans.	7.5E-04	-78.2	150	295.03	291.28	152.1	102.9
287	14 Oct	0000–0600	Rad.	1.0E-05	-73.9	90	284.76	285.10	80.5	46.5
288	15 Oct	0000–0600	Turb.	1.2E-03	-84.5	200	294.82	290.05	366.5	358.5
290	17 Oct	0000–0600	Turb.	5.0E-03	-29.3	70	283.39	285.72	254.7	301.7
291	18 Oct	0000–0600	Int.	1.8E-04	-63.4	50	281.81	282.05	19.3	0.2
292	19 Oct	0000–0600	Rad.	1.6E-05	-70.2	70	282.98	283.28	56.9	31.4
293	20 Oct	0000–0600	Int.	8.1E-05	-73.0	61	284.50	281.63	22.5	3.4
294	21 Oct	0000–0600	Trans.	1.1E-04	-79.8	120	285.99	283.72	21.7	-18.5
295	22 Oct	0000–0600	Trans.	2.0E-04	-83.0	70	291.49	284.54	13.8	-8.0
296	23 Oct	0000–0600	Trans.	2.9E-04	-78.1	100	281.79	282.63	44.9	-5.2
297	24 Oct	0000–0600	Int.	1.0E-04	-70.1	52	280.89	281.01	20.9	2.7
298	25 Oct	0000–0600	Turb.	8.6E-04	-80.0	102	284.15	282.71	127.8	90.7
299	26 Oct	0000–0600	Rad.	1.1E-05	-83.8	30	291.05	283.04	40.5	27.1
300	27 Oct	0000–0600	Int.	2.5E-04	-85.3	100	291.89	285.83	16.9	-17.3
301	28 Oct	0000–0600	Trans.	4.1E-04	-71.4	130	290.83	287.28	55.0	0.9

some cases (e.g., 24 October), h showed considerable variation during the averaging period, responding to changing intensity of SBL turbulence. It is noted that the final results are not very sensitive to the exact value for h .

f. Summary

The total set of input parameters derived from the CASES-99 data is given in Table 2. Only days with a complete set of input parameters, derived from various instruments, could be analyzed. This limited the number of days. Additionally, the following constants were used $\varepsilon_s = 1.0$ (—), $\varepsilon_a = 0.8$ (—), $z_{oh} = z_{om} = 0.03$ m, $T_{ref} = (T_{TOP} + T_M)/2$ K, and $C_v = 2$ kJ m⁻² K⁻¹. Unless stated otherwise, physical constants like Boltzmann's are given the same values as in VdW(a). Based on this input data, Π has been computed for two cases: $\lambda_m/\delta_m = 5$ (case 1), and 2 (case 2) (in W m⁻² K⁻¹). Before discussing the table results in the next section, we summarize explicitly the steps that are necessary to calculate Π . This in order to facilitate future application.

- 1) A list of input parameters [see also, overview Table 1 in VdW(a)] follows:
 - the effective pressure gradient (or, alternatively, u_*^2/h);
 - the isothermal net radiation Q_i [to be determined from Q_{net} and $(T_a - T_s)$, see section 4b];
 - the boundary layer height h , and the temperature at the boundary layer height T_{TOP} ;
 - the topsoil temperature T_M (see appendix);
 - estimations for the heat capacity C_v and the bulk conductivity λ_m/δ_m of the vegetation;
 - estimations for z_0 , ε_s , ε_a , and for a reference temperature T_{ref} ;
 - physical constants (standard notation), like σ , κ , and R_c .
- 2) Accounting for some scaling conversions and symbol definitions described explicitly in section 2 of VdW(b), the input parameters are substituted straightforwardly in the expressions for the equilibrium solutions of the system [VdW(b), appendix C].
- 3) Last, Π is found from substitution of this equilibrium solutions in the Π expression given in appendix D of VdW(b).

5. Comparison of theory and observations

a. Using full theory (Π)

In Fig. 10, the critical contour line $\Pi = 1$ from Fig. 8 is replotted. As before, this contour line is valid for a single location with a certain set of local parameters. Figure 10 (also the example in Fig. 8) is calculated for the CASES-99 site using local parameter estimations (e.g., z_{om}) as given in the previous section. Because some of the parameters are not true physical constants

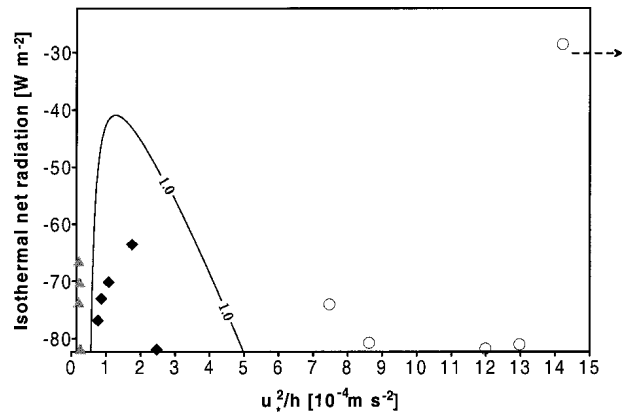


FIG. 10. Critical contour line $\Pi = 1$ for the CASES-99 site predicted by theory. Observed nights are located in this graph according to their values of Q_i and u_*^2/h . The nights are marked with different symbols according to their a priori time series classification described in section 3: gray triangles denote radiative nights; black diamonds, intermittent nights; and open circles, continuous turbulent nights (as in Fig. 11).

like T_M , T_{TOP} , and h they had to be given fixed values in order to plot this theoretical contourline. In Fig. 10 we assumed $T_M = T_{TOP} = 285$ K and $h = 80$ m.

For comparison, the CASES-99 nights are plotted in Fig. 10, according to their values of u_*^2/h and Q_i . The nights are marked with different symbols according to their a priori time series classification described in section 3. If we take the theoretical figure to be representative for the CASES-99 location (although, strictly speaking each night should have a slightly different contour line, due to the fact that each night has its own value of T_M , T_{TOP} , and h), then the observed nights with intermittent turbulence should be located within the contour line, and the nonintermittent nights should lie outside this contour line. Figure 10 shows that this is indeed the case, favoring the theoretical predictions (although the number of data points is limited). On the other hand, it is not clear how robust this result is in view of the assumptions and uncertainties in the parameter estimations. Therefore, a *sensitivity example* of the results in Fig. 10 is discussed below. First, however, some quantitative characteristics will be investigated.

Figure 10 represents a single contour line of a bowl-shaped figure (intermittent cases at the bottom of the bowl) showing Π as a function of u_*^2/h and Q_i . It would be interesting to know the exact Π values in Fig. 10; that is, what are the height of the observation points compared to the critical level ($\Pi = 1$)? First, we may simplify the representation of Fig. 10, by recognizing the fact that during CASES-99 clear-sky conditions prevailed over cloudy conditions. Thus, the isothermal net radiation was very similar for most of the nights, indicating that the dynamical differences between the nights are mainly caused by differences in u_*^2/h .

Therefore, we limit the parameter space by looking at Π as a function of u_*^2/h (Fig. 11a). Effectively, a

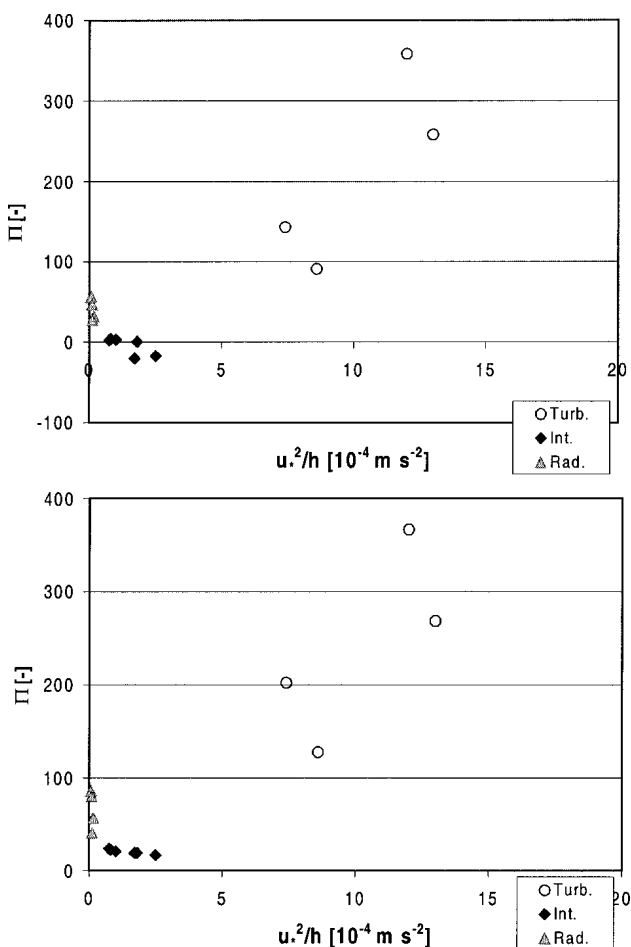


FIG. 11. Calculated Π values as a function of u_*^2/h for various CASES-99 nights [(top) with $\lambda_m/\delta_m = 2$]. Different symbols are used according to the a priori classification [as in Fig. 10; (bottom) with $\lambda_m/\delta_m = 5$].

horizontal slice is made in Fig. 10. The intersection of this slice with the contour line of Fig. 10 predicts the two pressure gradient values for which $\Pi = 1$ in Fig. 11a. Again, different symbols are used according to the a priori classification of section 3. In Fig. 11a it is shown that the nonintermittent nights show Π values larger than its critical value 1, and Π values below or just around the critical level coincide with observed intermittent nights, confirming the theoretical predictions of VdW(a,b). The data points do not exactly collapse on one single curve, due to small differences in Q_i , and differences in T_M , T_{TOP} , and h . But, roughly speaking, Figs. 11a and 10 indicate comparable results, confirming the predictive character of Π .

In Fig. 11b, the calculations of Π are identical to those in Fig. 11a, except for the fact that a bulk conductance λ_m/δ_m of $5 \text{ W m}^{-2} \text{ K}^{-1}$ is used, corresponding to a vegetation fraction of 1.0, instead of $\lambda_m/\delta_m = 2$ (vegetation fraction of 0.5). Although the qualitative shape of Fig. 11b is similar to that of Fig. 11a, its quantitative features are rather different. Figure 11b shows that, al-

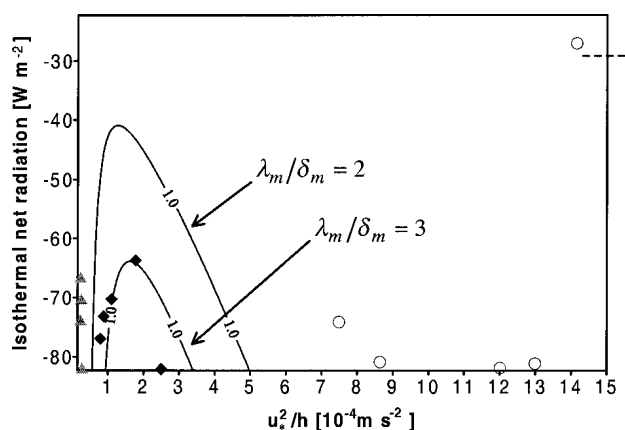


FIG. 12. As in Fig. 10, but for two values of λ_m/δ_m , namely, $\lambda_m/\delta_m = 2$ and $\lambda_m/\delta_m = 3 \text{ W m}^{-2} \text{ K}^{-1}$.

though the predicted Π values are low for the intermittent cases, they are not below the theoretical critical level of $\Pi = 1$, below which intermittency is predicted. Thus, although the observed intermittent cases are predicted to be most unstable (mathematically) of all, they are predicted just not unstable enough to be intermittent. The implications of this result for the general classifications Fig. 10 becomes clear in Fig. 12, showing two theoretical classifications for the CASES-99 site, using two different values of the bulk conductance. It is observed that the case with the highest bulk conductance ($\lambda_m/\delta_m = 3$) results in the smallest area with intermittent turbulence. The large value of λ_m/δ_m of $5 \text{ W m}^{-2} \text{ K}^{-1}$ (not shown) would not give a single Π value below the critical level 1 for any value of u_*^2/h and Q_i . As such, it could not be plotted as a contour line $\Pi = 1$. On the other hand, it is noted that even in this case of $\lambda_m/\delta_m = 5$, the most unstable cases are located in the same area as in the case of $\lambda_m/\delta_m = 2$ (as with Figs. 11a and 11b), indicating that the qualitative bowl-shaped dependence of Π remains unchanged. It is noted that the importance of the bulk conductance on the system stability was recognized/discussed in the previous studies of VdW(a,b).

In summary, although the regime predictions using this Π are robust and discriminative in a qualitative sense, the exact quantitative features have to be interpreted with caution, because of uncertainties in the parameter estimations.

b. A simplified approach

1) THEORETICAL BACKGROUND

A disadvantage of the Π parameter of VdW(b) is its complexity, which limits its applicability. Furthermore, due to this complexity this parameter does not provide insight in the physical cause of instability that generates intermittency. Therefore, in VdW(b), a less exact but simpler stability/classification criterion was given, which allows a physical interpretation. In this section,

this simplified criterion is applied to the CASES-99 dataset.

The approximate stability criterion (denoted as A-Cr.) is derived by application of a fixed shear criterion for instability (FSCI; Derbyshire 1999) to the surface energy balance equation. Here, only the result is given. The system is found to be mathematically/physically unstable (causing intermittency) when

$$\left(\frac{R_b}{R_c}\right)_{\text{eq}} > \frac{K + 1}{3}. \quad (7)$$

This criterion depends on two dimensionless groups

- the normalized equilibrium bulk Richardson number $(R_b/R_c)_{\text{eq}}$, and
- the partitioning parameter K .

Both groups are calculated from external variables. As expected, the equilibrium value of the bulk Richardson number is primarily determined by Q_i and by the effective pressure gradient. The second group, the so-called *partitioning parameter*, is physically interpreted as the ratio of the summed radiative and soil/vegetation conductance/exchange coefficient compared to the exchange coefficient for turbulent heat transport [VdW(b)]. If turbulent heat exchange were the only process involved, the criterion $(R_b/R_c)_{\text{eq}} > 1/3$ would imply a sufficient condition for system instability (assuming fixed shear). The discussion in the previous section, however, explained that a large soil heat flux (and additionally, the radiative flux) tends to stabilize the system, counteracting intermittency. This effect is accounted for in the partitioning parameter, making $(R_b/R_c)_{\text{eq}} > 1/3$ a necessary but not a sufficient condition.

For the application of the A-Cr., external parameters were estimated as with Π except for the following.

- T_{TOP} and T_M are not needed as input parameters.
- Instead, at the bottom boundary, G is needed as input. Because G was only available for a limited number of days (Table 2), G is estimated from the residual of the other energy balance terms, accounting for the gap in the energy balance closure (13 W m^{-2}).

2) RESULTS

For the available CASES-99 nights, both terms in the stability criterion of Eq. (7) were calculated (Fig. 13). Moreover, the *difference* between those two terms, $(R_b/R_c)_{\text{eq}} - (K + 1)/3$, is plotted, marked differently according to the a priori classification based on the flux time series, as in Figs. 11a,b. A positive difference means $(R_b/R_c)_{\text{eq}} > (K + 1)/3$, predicting instability (causing intermittency). Likewise, a negative difference predicts a nonintermittent situation.

To some extent the system stability is predicted correctly: negative differences coincide with radiative and turbulent nights, and the intermittent nights show pos-

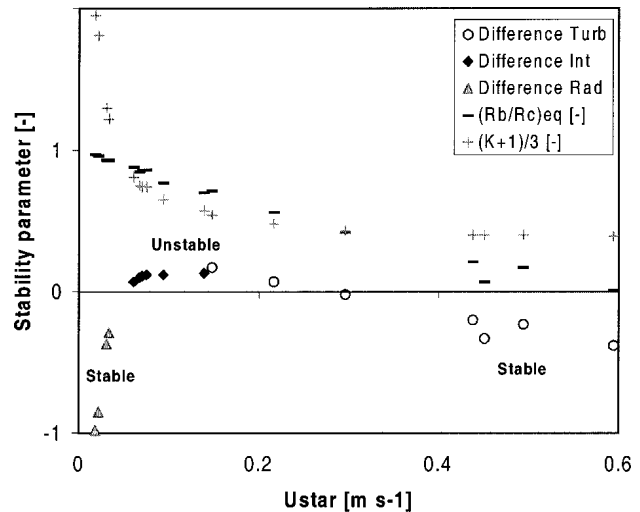


FIG. 13. The simplified stability parameter, indicated as the difference $(R_b/R_c)_{\text{eq}} - (K + 1)/3$, as a function of u_{*} . Different symbols are used (as in Fig. 10) according to the a priori classification (section 3). Separate terms of the stability parameter are given by dashes and crosses.

itive values. However, the “in between” cases show that some turbulent nights are incorrectly predicted as being unstable. Moreover, the slope between the intermittent and turbulent cases is rather flat, indicating that the figure is not very discriminative for these cases (contrary to the strong slopes in Figs. 11a,b). It is noted that the use of a larger bulk conductance, λ_m/δ_m of 5 instead of $2 \text{ W m}^{-2} \text{ K}^{-1}$, gave very similar results as with Π , that is, leading to system stabilization.

In summary, although the approximate criterion provides useful physical insight and predicts the extreme cases correctly, its predictions are incorrect or not very discriminative for the more subtle cases. For these cases the basic fixed shear assumption is probably not correct (Derbyshire 1999). Therefore, for these cases, the momentum equation needs to be accounted for in a coupled momentum–energy balance system as in the derivation of Π .

6. Discussion

a. Quantitative/qualitative features

The previous sections showed that the predictions with Π are robust in a qualitative sense: intermittency is most likely to occur under clear-sky conditions in presence of a moderately/weak pressure gradient, in agreement with what is generally observed (section 3). This robustness can be understood from the basic mechanism [see introduction; VdW(a,b)], which needs two basic ingredients: 1) a positive feedback of stratification on turbulent mixing, enabling decoupling; and 2) a pressure gradient that accelerates the flow after decoupling, enabling recoupling. In conditions of strong winds and/or large cloud cover the Richardson numbers are too

low to generate decoupling (no positive feedback, see Fig. 5) so that no intermittency will occur. In the other extreme, in the absence of a significant pressure gradient, the flow acceleration is either absent or not strong enough to generate intermittency.

Despite this qualitative robustness, our results [especially VdW(a)] indicate a large sensitivity of the Π value on (uncertain) parameter estimations. This means that a single Π value on itself cannot be interpreted as a reliable predictor of intermittent/nonintermittent SBL regimes. Rather, the *relative* value of Π compared to the Π values of other nights at the same location (under various conditions) tells more about the probability of finding a particular regime during this night. This result indicates that the qualitative/conceptual value of the present study is more important than its direct quantitative significance. This is certainly true in the light of the rather strict model assumptions.

b. Other classifications

The present paper tries to express/predict different SBL regimes in terms of *external forcing parameters* such as pressure gradient and cloud cover. First, it is believed that, eventually, these external parameters determine SBL behavior [apart from the discussion on predictability by McNider et al. (1995)]. Second, especially in the intermittent regime, external parameters tend to vary less than internal system parameters, like wind speed, temperature, u_* , L , etc. Section 4, however, shows that in practice, still internal input parameters such as u_*^2/h , h itself, T_M , and T_{TOP} , are needed (albeit using 6-h averages) to calculate Π . By inclusion of more model complexity in future studies, some of these internal variables could be related to external parameters. For example, the inclusion of Coriolis effects (separate U and V equations) translates the *effective* pressure gradient into a real pressure gradient as input parameter.

In literature SBL classifications have been proposed using *internal system parameters* such as z/L , z/Λ , h/L , and z/h , based on similarity arguments (Holtslag and Nieuwstadt 1986). Using z/L as an indicator, Mahrt et al. (1998) classified the stable surface layer into (a) weakly stable, (b) moderately stable, and (c) very stable. Although this classification proved to be very useful as a guideline to look at surface layer observations, it is not meant as an *exact* predictor of different SBL regimes (here, especially the intermittent regime). Generally speaking, the studies mentioned above indicate that intermittent turbulence is most likely at large stability conditions, that is, large values of Ri , z/Λ , z/L , or h/L . This fact is confirmed by the present study and others (e.g., Kondo et al. 1978; Howell and Sun 1999). Additionally, the present study stresses the importance of other heat exchange processes (besides turbulence) such as soil/radiative heat flux, that stabilize SBL intermittency.

c. Future research

It would be interesting to extend the present work, in a sense of analyzing SBL regimes in relation to external forcing parameters, to larger datasets (including cloudy cases), and for different types of land cover (with different physical properties). With this respect the authors suggest that a closer collaboration between NWP modelers and experimentalists will benefit these type of classification studies (particularly in relation to an accurate diagnosis of pressure gradients; see section 4b).

Apart from the present system analysis approach using a simplified model, there is need for more detailed studies on intermittency dynamics. Although the intermittency mechanism arising from a positive feedback between stratification and mixing efficiency in shear flow is an important candidate explaining the observed intermittency in SBLs, it is not clear whether this intermittency is caused by a direct surface–atmosphere interaction (present work), is formed in shear layers higher up (e.g., Coulter 1990; Ha and Mahrt 2001), or is a combination of both. It is challenging to extend the present work (both the theoretical and observational part) to the more general case, allowing both atmosphere–surface interaction and interaction with higher shear layers.

7. Conclusions

In this paper a classification of intermittent and nonintermittent turbulence is presented based on observations of near-surface turbulence during CASES-99. It is found that the different nights can be subdivided in three subclasses: 1) a turbulent regime, 2) an intermittent regime, or 3) a radiative regime. These classes reflect different SBL dynamics. Moreover, the existence of three regimes confirms the findings of VdW(a) who simulated three different SBL regimes with a simplified model.

This bulk model of VdW(a) showed both intermittent and nonintermittent SBL behavior for different parameter ranges. In VdW(b), analysis of the model equations resulted in a dimensionless number (Π), which is a function of external forcing parameters such as the (effective) pressure gradient and the radiative forcing. With this number, the model behavior (i.e., intermittent or nonintermittent) could be predicted.

The present study uses this parameter to classify/predict intermittent and nonintermittent nights at CASES-99. To this end, Π was evaluated from detailed analysis of the available data. Comparison of the predictions/classification using Π , with the actual observed regimes shows generally good agreement.

- Those nights predicted to be most (mathematically) unstable to disturbances, turned out to be intermittent.
- The most stable (mathematically) nights turned out to be nonintermittent, that is, continuously turbulent or radiative.

The qualitative features mentioned above are very robust and discriminative. Thus, under the assumptions made, the Π concept could be useful as a classification tool.

The exact quantitative value of Π shows to be rather sensitive to local parameters such as the bulk conductance of the vegetation layer, which is difficult to estimate exactly a priori. In practice, this makes Π unsuitable as an *absolute* predictor of stability/SBL regimes. However, useful information about the stability/regime of a particular night is obtained by comparing its Π value *relative* to other nights under different conditions.

In VdW(b) an approximation for the rather complex Π was derived. This approximation based on a fixed shear criterion for instability provided new insight in the relative importance of the different boundary layer processes (turbulence, radiation, soil conduction) in the instability mechanism [VdW(b)]. As in the Π case, the regime predictions are compared with the observed regimes. The approximate parameter correctly predicts extreme cases. However, in the more subtle cases the approximation shows to be less decisive or even incorrect, probably due to the fact that the fixed shear assumption is not a good approximation for these cases.

In light of the present work, it seems useful to investigate the occurrence of stable boundary layer regimes in relation to their external forcing parameters. As such, classification diagrams like Figs. 1 and 10 may provide a new conceptual perspective for future (observational and modeling) work on SBL regimes.

APPENDIX

Fourier Analysis of Soil Temperatures

To solve the surface energy balance one would like to measure the soil heat flux (SHF) directly at the soil surface. In practice this is often not possible without disturbing the surface properties, due to the presence of vegetation/roots. Therefore, the SHF is often measured a few centimeters below the soil surface. Thus, the mea-

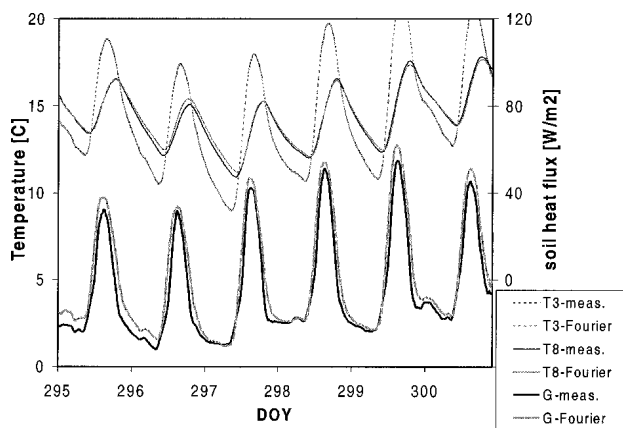


FIG. A1. Measured and modeled soil temperatures/fluxes.

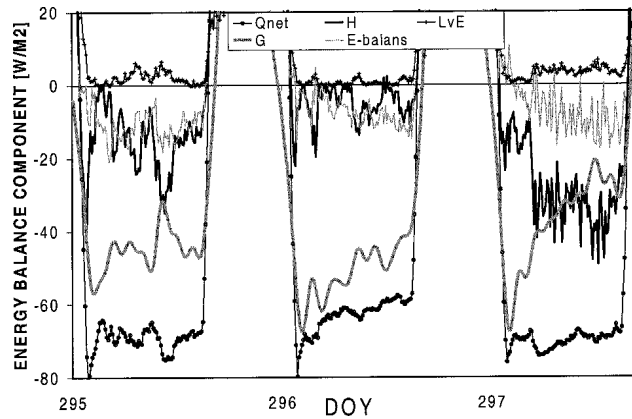


FIG. A2. Energy balance components in three typical nights.

sured values need to be extrapolated to the surface in a consistent way. A method is given below. For a detailed background of the theory we refer to van Wijk and de Vries (1963).

In the analysis, data from thermometers at -3 and -8 cm and an SHF plate at -5.4 cm are used, available during DOYs 289–301. The time series of the 3-cm temperature is decomposed in 150 Fourier components, which results in a nearly perfect fit (Fig. A1). Using standard theory of heat conduction (assuming homogeneity) the temperature signal at 8-cm depth is reconstructed (Fig. A1) using a “best fit” thermal diffusivity value κ_{th} . For our set this gave $\kappa_{th} = 0.155 \times 10^{-6} \text{ m}^2 \text{ s}^{-1}$, comparable to values for dry sand ($0.24 \times 10^{-6} \text{ m}^2 \text{ s}^{-1}$) and clay ($0.18 \times 10^{-6} \text{ m}^2 \text{ s}^{-1}$; Oke 1978). Knowing this κ_{th} value, $T(z, t)$ is known for every z, t assuming homogeneity of soil properties in space/time. In this way $T_M(t)$ was found substituting $z = 0$ (section 4).

Next, the SHF at 5.4-cm depth is reconstructed (Fig. A1) by differentiating $T(z, t)$ with respect to z , assuming a best fit value for the soil conductivity λ_s of $0.6 \text{ W m}^{-1} \text{ K}^{-1}$. With this λ_s value, $G(z, t)$ is known and the SHF at the surface $G(0, t)$ is found by substituting $z = 0$. The result is shown in Fig. A2, which gives an overview of the energy balance for three typical nights. Comparing Figs. A2 and A1 shows that both the magnitude and the shape of $G(0, t)$ has changed a lot compared to the original measured $G(-0.054, t)$, indicating the importance of the extrapolation.

An innovative element of this study are large temporal changes in $G(0, t)$, which are realistic features: the soil heat flux not only reacts on the peak value of the net radiation at the beginning of the night, but also reflects the intermittent behavior of the turbulent heat flux at DOY 296, and the “jump” in the heat flux at DOY 297. As such, strong fluctuations cancel out in the final energy balance budget. Apparently, the intermittent character in the turbulent flux is transferred into the soil and is still noticeable in the temperature measurements, despite its apparently smooth time series (A1).

REFERENCES

- Atzema, A. J., 1992: A model for the drying of grass with realtime weather data. *J. Agric. Eng. Res.*, **53**, 231–247.
- Blackadar, A. K., 1979: High-resolution models of planetary boundary layer. *Advances in Environmental Science and Engineering*, J. R. Pfafflin and E. N. Ziegler, Eds., Gordon and Breach, 50–85.
- Businger, J. A., 1973: Turbulent transfer in the atmospheric surface layer. *Workshop on Micrometeorology*, D. A. Haugen, Ed., Amer. Meteor. Soc., 67–100.
- Coulter, R. L., 1990: A case study of turbulence in the stable nocturnal boundary layer. *Bound.-Layer Meteor.*, **52**, 75–91.
- De Bruin, H. A. R., 1994: Analytic solutions of the equations governing the temperature fluctuation method. *Bound.-Layer Meteor.*, **68**, 427–432.
- Derbyshire, S. H., 1999: Boundary-layer decoupling over cold surfaces as a physical boundary instability. *Bound.-Layer Meteor.*, **90**, 297–325.
- Duynkerke, P. G., 1999: Turbulence, radiation and fog in Dutch stable boundary layers. *Bound.-Layer Meteor.*, **90**, 447–477.
- Ha, K.-J., and L. Mahrt, 2001: Simple inclusion of z -less turbulence within and above the modeled nocturnal boundary layer. *Mon. Wea. Rev.*, **129**, 2136–2143.
- Hartogensis, O. K., H. A. R. De Bruin, and B. J. H. van de Wiel, 2002: Displaced-beam small aperture scintillometer test. Part II: CASES-99 stable boundary layer experiment. *Bound.-Layer Meteor.*, **105**, 149–176.
- Holtstag, A. A. M., and F. T. M. Nieuwstadt, 1986: Scaling the atmospheric boundary layer. *Bound.-Layer Meteor.*, **36**, 201–209.
- , and H. A. R. De Bruin, 1988: Applied modelling of the nighttime surface energy balance over land. *Bound.-Layer Meteor.*, **27**, 689–704.
- Howell, J. F., and J. Sun, 1999: Surface-layer fluxes in stable conditions. *Bound.-Layer Meteor.*, **90**, 495–520.
- Kondo, J., O. Kanechika, and N. Yasuda, 1978: Heat and momentum transfers under strong stability in the atmospheric surface layer. *J. Atmos. Sci.*, **35**, 1012–1021.
- Lin, J. T., 1990: The effect of inertial and turbulence oscillations in the stable boundary layer and their role in horizontal dispersion. M.S. thesis, Dept. of Mathematics, University of Alabama in Huntsville, 82 pp.
- Mahrt, L., 1999: Stratified atmospheric boundary layers. *Bound.-Layer Meteor.*, **90**, 375–396.
- , and D. Vickers, 2002: Contrasting vertical structures of nocturnal boundary layers. *Bound.-Layer Meteor.*, **105**, 351–363.
- , J. Sun, W. Blumen, T. Delany, and S. Oncley, 1998: Nocturnal boundary layer regimes. *Bound.-Layer Meteor.*, **88**, 255–278.
- McNider, R. T., D. E. England, M. J. Friedman, and X. Shi, 1995: Predictability of the stable atmospheric boundary layer. *J. Atmos. Sci.*, **52**, 1602–1614.
- Monteith, J. L., 1981: Evaporation and surface temperature. *Quart. J. Roy. Meteor. Soc.*, **107**, 1–27.
- Moore, C., 1986: Frequency response corrections for eddy correlation systems. *Bound.-Layer Meteor.*, **37**, 17–35.
- Nappo, C., 1991: Sporadic breakdown of stability in the PBL over simple and complex terrain. *Bound.-Layer Meteor.*, **54**, 69–87.
- Nieuwstadt, F. T. M., 1984: The turbulent structure of the stable, nocturnal boundary layer. *J. Atmos. Sci.*, **41**, 2202–2216.
- , and H. Tennekes, 1981: A rate equation for the nocturnal boundary-layer height. *J. Atmos. Sci.*, **38**, 1418–1428.
- Oke, T. R., 1978: *Boundary Layer Climates*. Methuen and Co., 372 pp.
- Poulos, G. S., and Coauthors, 2002: CASES-99: A comprehensive investigation of the stable nocturnal boundary layer. *Bull. Amer. Meteor. Soc.*, **83**, 555–581.
- Revelle, D. O., 1993: Chaos and “bursting” in the planetary boundary layer. *J. Appl. Meteor.*, **32**, 1169–1180.
- Turner, J. S., 1973: *Bouyancy Effects in Fluids*. Cambridge University Press, 368 pp.
- Van de Wiel, B. J. H., R. J. Ronda, A. F. Moene, H. A. R. De Bruin, and A. A. M. Holtstag, 2002a: Intermittent turbulence and oscillations in the stable boundary layer over land. Part I: A bulk model. *J. Atmos. Sci.*, **59**, 942–958.
- , A. F. Moene, R. J. Ronda, H. A. R. De Bruin, and A. A. M. Holtstag, 2002b: Intermittent turbulence and oscillations in the stable boundary layer over land. Part II: A system dynamics approach. *J. Atmos. Sci.*, **59**, 2567–2581.
- van Wijk, W. R., and D. A. de Vries, 1963: Periodic temperature variations. *Physics of Plant Environment*, W. R. van Wijk, Ed., Interscience, 133–138.

Appendix III Co-Author Publication - RAPID

It was not feasible to publish as a first author on all the datasets gathered in the framework of this thesis. This is the case for the RAPID experiment that deals with stable boundary layers during daytime caused by advection of warm air over evaporating crops. The data was prepared, quality checked and processed as part of this thesis. A more detailed description of the data, and the backgrounds of the experiment are outlined in Section 2.2. Analysis of the data has been done in collaboration with others (e.g. Moene, 2003, De Bruin et al., 2005 and Van Dijk et al., 2006).

In this Appendix the RAPID publication the candidate was most involved in is given in its original format:

De Bruin, H.A.R., **Hartogensis, O.K.**, Allen, R.G., and Kramer, J.W.J.L., 2005: 'Note on the Regional Advection Perturbations in an Irrigated Desert (RAPID) Experiment', *Theor. Appl. Climatol.* **80**, 143-152.

¹ Wageningen University, Meteorology and Air Quality Group, Wageningen, The Netherlands² University of Idaho at Kimberly Research and Extension Center, Kimberly, Idaho, USA

Regional Advection Perturbations in an Irrigated Desert (RAPID) experiment

H. A. R. De Bruin¹, O. K. Hartogensis¹, R. G. Allen², and J. W. J. L. Kramer¹

With 12 Figures

Received October 17, 2003; accepted July 10, 2004

Published online November 17, 2004 © Springer-Verlag 2004

Summary

The RAPID field experiment took place in August–September 1999 at a site 25 km south of Twin Falls, Idaho, USA. The experiment concerned micrometeorological observations over extensive, well-irrigated fields covered with the fast-growing crop alfalfa. During daytime, on a number of days the sensible heat flux was negative and the latent heat flux exceeded net radiation. The energy required for the latent heat flux to be larger than net radiation has to be advected from elsewhere. As the fields were large, we refer to this process as “regional advection”. “Local advection”, on the other hand, refers to advection effects, where the wet to dry transition is on a field scale. Evidence is presented that the RAPID data are subject to regional advection conditions.

A simple model, based on Penman-Monteith, is derived that describes the regional-advection case rather well. The influence of wind speed under those conditions is illustrated using data and the model. The correlation coefficients between temperature and horizontal wind component appear to be good indicators for advection.

1. Introduction

Evapotranspiration, ET , or expressed in energy units, λET , where λ is the latent heat of vaporization, is generally some fraction of net radiation, R_n , for climates that have sufficient rainfall to support ET . In areas where the air mass is strongly modified by dry, desert conditions, however, the

ratio of λET to R_n can exceed 2. Figure 1 illustrates this for Kimberly, Idaho, where lysimeter measurements of 24-hour λET of full cover alfalfa divided by the corresponding R_n are presented. The measured λET exceeds the available energy (that is close to R_n for daily values, because the daily soil heat flux density, G , is usually small) by 50% for most of August and September. During this period, dry air is advected from the large desert areas upwind of Kimberly.

Considering the surface energy balance,

$$R_n - G = \lambda ET + H \quad (1)$$

one can see that under the conditions mentioned above, i.e. $\lambda ET > R_n$ and G is negligible, the sensible heat flux density, H , must be negative. The required additional energy, needed to maintain the high evaporation rate, must be supplied by extracting sensible heat from the lower atmosphere.

If we consider large horizontally homogeneous fields where the atmospheric flow is in equilibrium with the underlying surface, the air temperature and humidity in the atmospheric surface layer are well adapted to the irrigated field and no longer have the properties of the dry upwind terrain. Crucial for our considerations is that a negative H implies that the atmosphere just above the surface is stably stratified and the

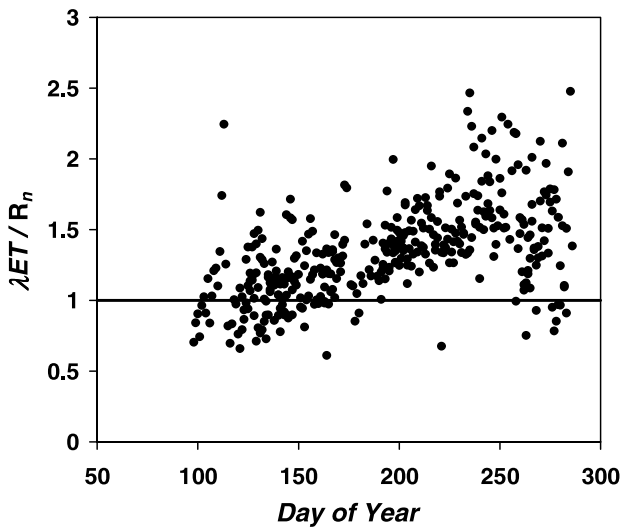


Fig. 1. Daily fraction of evapotranspiration, λET , to net radiation, R_n , versus Day of Year. Daily λET is based on lysimeter data, taken at Kimberly, Idaho between 1969 and 1971

negative buoyancy effects suppress turbulent motions. The turbulence needed for vertical transfer of water vapour, therefore, can only be generated in a mechanical way. This means that λET can exceed R_n only if there is enough wind to offset the damping effects of stability. Under calm conditions it is to be expected that daily λET cannot exceed R_n .

For small fields with finite size, on the other hand, things become more complicated. We define a small field as a field where under certain conditions the wind fetch is too small to adapt the advected, dry air mass to the irrigated surface. In that case, at any distance from the edge separating the irrigated field and the dry upwind desert, the influence of the upwind dry terrain will increase with increasing wind speed. For that reason λET is expected to increase with increasing wind speed due to the fact that dry desert air is forced to flow over the wet irrigated surface.

From this common sense reasoning, we deduce that λET of irrigated fields in dry deserts is enhanced by wind in two ways:

1. For large fields, i.e. large in the sense that the flow has adapted to the irrigated surface, wind enhances the mechanically generated turbulence needed to maintain vertical transfer under stable conditions. This is denoted as regional advection;
2. For small fields, i.e. small in the sense that the flow has not been fully adapted to the irri-

gated field, wind forces dry, 'non-adapted' desert air over the irrigated field, which enhances evaporation. This case is often called local advection.

Considering vertical exchange of eddies or air parcels under conditions that $H < 0$ and $\lambda ET > 0$, it is expected that upward moving eddies contain relatively cool and wet air, whereas downward moving parcels will be warm and dry. Consequently, the correlation coefficient of turbulent temperature and humidity measurements, R_{Tq} , is expected to be negative. Conversely, under 'normal' conditions, i.e. both H and λET are > 0 , R_{Tq} is expected to be positive. So, R_{Tq} seems an appropriate indicator for advection conditions. Also correlation coefficients between horizontal wind speed and temperature and humidity might be good indicators.

In the past a lot of work has been done on the behaviour of turbulent flow just after a sudden dry-to-wet step-change at the surface, i.e. local advection. In that case, the flow is not in equilibrium with the underlying surface and, e.g. Monin-Obukhov similarity theory breaks down (see for instance Kroon and DeBruin, 1995; Bink, 1995 and more recent studies by e.g. McNaughton and Laubach, 2000).

It is the purpose of the RAPID field experiment to gather micrometeorological data over a large irrigated field surrounded by very dry terrain. In this paper we will present some first results of the effect of wind speed on λET under advection conditions. In addition, we will discuss the relation between some statistical quantities, such as R_{Tq} , and advection.

2. Experimental

The RAPID experiment was carried out between 25 August and 19 September 1999 in an agricultural area of 70×25 km, located in Idaho, USA, 20 km south-east of Twin Falls. Staff members of the University of Idaho, Wageningen University, Campbell Scientific, Inc., Utah State University and USDA-ARS, Kimberly, Idaho, participated in RAPID. Four eddy-correlation systems were deployed, all consisting of CSAT3 sonic anemometer and a KH20 Krypton hygrometer, both from Campbell Scientific Inc., Logan, USA. Measurements were recorded by a Campbell

Scientific CR23X datalogger. Raw data were stored on a laptop and processed afterwards. In addition, two Bowen ratio systems and sensors to measure the components of the net radiation (CM14 pyranometer and CG2 pyrgeometer of Kipp and Zonen, Delft, the Netherlands), surface temperature (Everest 4000 infra-red thermometers, Tucson, USA) and soil heat flux (REBS HFT3 soil heat flux plates) were installed. During RAPID also a net radiometer manufactured by Swissteco has been operated. We adopted the results of a study in the Netherlands (Kohsiek, personal communication) that revealed that the 4-component Kipp and Zonen system provides the ‘correct’ net radiation values. Moreover, this has been confirmed by a detailed study by Kramer (2000), who compared data for all available RAPID radiation data. We estimate that the errors made in net radiation are less than 5%. Missing Kipp and Zonen data were replaced with observations made with the Swissteco radiometer accounting for the systematic difference of 8% found for this sensor compared with the Kipp and Zonen system. Kramer (2000) also analysed all available data concerning soil temperature and soil heat flux and determined the ‘best’ soil heat flux accounting for e.g. the heat storage in the layer between the surface and the soil heat flux plates. In this paper we will use mainly data of the eddy-correlation system operated at 3 m by Wageningen University. The micrometeorological equipment was installed between two centre-pivot irrigated alfalfa fields of approximately 1 mile by 1 mile. Towards the west, the dominant wind direction, beyond the field adjacent to the equipment, two more irrigated fields, of respectively alfalfa and wheat were grown. We can thus assume that the experimental area is large in terms of the definitions given in Section 1. The alfalfa crop height varied for the field west of our equipment between 10 cm at the start of the experiment to about 35 cm at the end, and between 15 and 35 cm at the east field. For more details on the RAPID experiment, see Kramer (2000).

The eddy-correlation data were processed to get 30 minute averaged fluxes using the latest version of the EC-pack software package, developed by the Wageningen University. The source code and documentation of the software can be found at www.met.wau.nl.

The eddy-correlation data at 3 m appear not to fulfil energy balance closure, i.e. $R_n - G > \lambda ET + H$. We corrected for this effect by multiplying both the measured H and λET with a constant factor of 1.5. In this way our data artificially close the energy balance. We realize that our approach is very arbitrarily and that other correction procedures can be applied also. Recently, the significance of the energy balance closure problem has been recognized internationally. It is outside the scope of this study to deal with this issue here. We confine ourselves to refer to a recent review paper by Culf et al. (2004).

3. Model

The aim of this paper is to illustrate the effect of wind speed on λET under advection conditions. For small fields there is still no simple theoretical approach, and will not be discussed here in detail. For large fields we will derive a simple model based on the Penman-Monteith method. We start with the governing equations on which Penman-Monteith is based. Besides Eq. (1) these are:

$$R_n = (1 - \alpha)K^\downarrow + \varepsilon_s(L^\downarrow - \sigma T_s^4) \quad (2)$$

$$H = \rho c_p \frac{T_s - T}{r_a} \quad (3)$$

$$\lambda ET = \frac{\rho c_p e_s(T_s) - e}{\gamma r_a + r_s} \quad (4)$$

where α is the albedo, K^\downarrow and L^\downarrow the incoming short- and long-wave radiation, σ the Stefan-Boltzmann constant, ε_s emissivity of the surface, T_s the surface temperature, ρ and c_p the density and specific heat at constant pressure of air, T and e the temperature and water vapour pressure of the air at standard level, γ the so-called psychrometer constant and r_a and r_s the aerodynamic and surface resistance. It is important to note that we account for stability effects on r_a by using an iterative calculation scheme based on the Monin-Obukhov similarity theory (MOST), including the buoyancy effect of water vapour. In this procedure the roughness length for momentum and heat, z_{0m} and z_{0h} play a role. We used the standard MOST functions of Businger-Dyer for unstable and those of Beljaars and Holtslag for stable cases (see Dyer, 1974; Beljaars and Holtslag, 1991 and Holtslag and DeBruin, 1988). The set of Eqs. (1) to (4) is solved for

H , λET and T_s at given K^\downarrow and L^\downarrow , G , T , e , α , ε_s , r_s , z_{0m} and z_{0h} using a numerical iterative scheme. For this purpose we used the standard MOST expressions for r_a that, in its turn, is dependent on the friction velocity, the Obukhov-length, the observation height and the roughness parameters z_{0m} and z_{0h} (see e.g. Stewart et al., 1994). Note that through Eq. (2) we account also for the influence of surface temperature on net radiation. We used the measured soil heat flux density.

We will apply this simple model for some selected ‘advection’ days during RAPID using the measured K^\downarrow and L^\downarrow , G , T , e and wind speed, in order to see whether the model is able to describe the advection conditions properly. Next we will apply the model as a prognostic tool to

investigate the effects of wind speed on λET . We repeat that the model applies to large fields only.

4. Results

4.1 Energy balance

In Fig. 2 the various components of the energy balance and the wind speed at 3 m are depicted for a day with low wind speed. Note that H and λET have been corrected according to the procedure described in Section 2. It is seen that H is positive and $\lambda ET < R_n$.

In Fig. 3 the same quantities are plotted but now for two successive days with daytime wind speed at 3 m greater than 3 m s^{-1} . H is negative both during day- and night-time and λET is

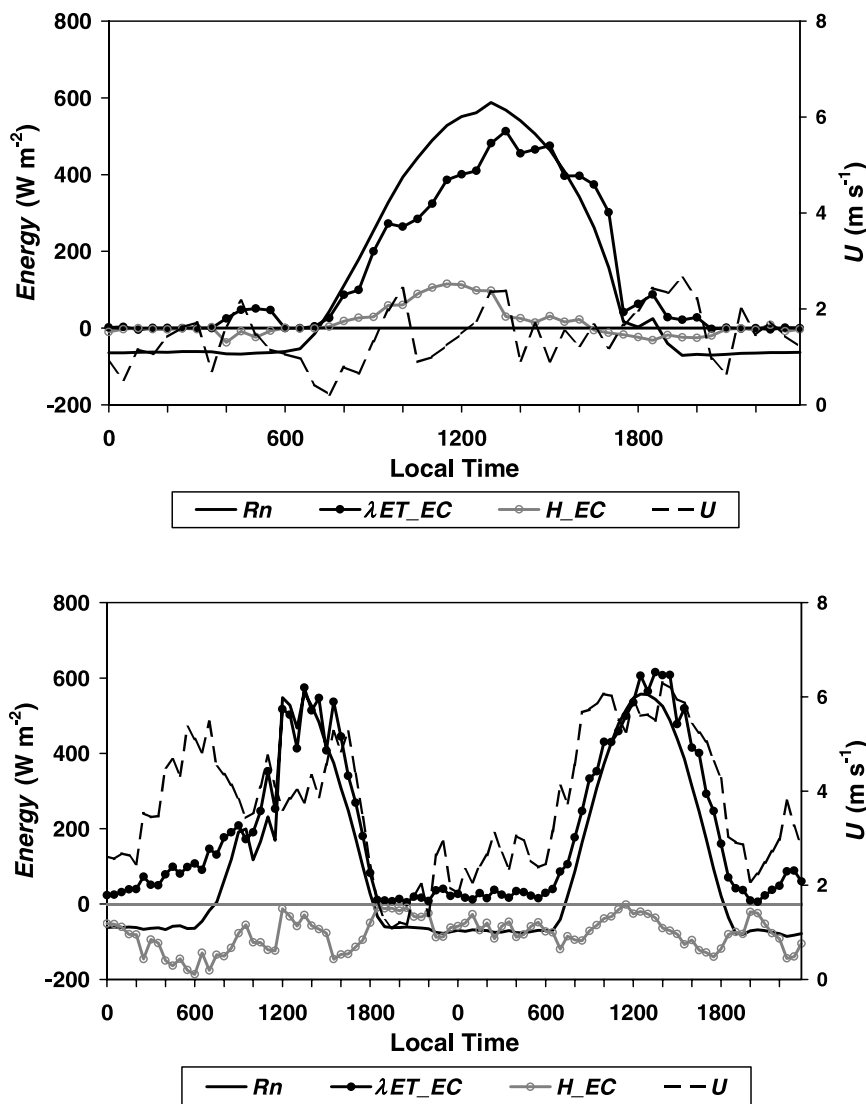


Fig. 2. Diurnal cycle of net radiation, R_n , sensible heat flux, H and evapotranspiration, λET on a calm day (DOY 247) during RAPID. The eddy-correlation determined H and λET are corrected for energy balance closure as described in Section 2

Fig. 3. As Fig. 2, for two consecutive days with high wind speed (DOY 253 and 254)

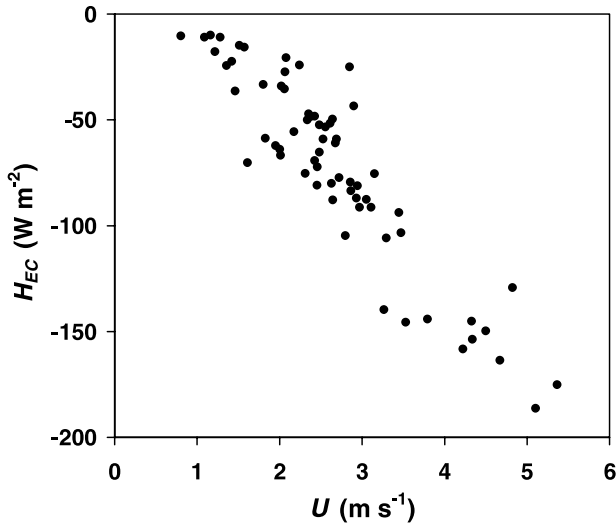


Fig. 4. Night-time (between 19:00 and 7:00) measured sensible heat flux at 3 m, H , against wind speed, u , for DOY 252 19:00 to 255 7:00. The eddy-correlation determined H , has been corrected for energy balance closure as described in Section 2

greater R_n , and at night greater than 0. Under night-time conditions H and G are the only available energy sources to feed λET as R_n is negative. This means that H must be negative, i.e. directed towards the surface, and, consequently, the stratification is stable. H is then expected to be related directly to wind speed, as wind is the only turbulence generator. In Fig. 4 this feature is illustrated by plotting for the same data set the night-time values of H against u . It is seen that H is related almost linearly to u .

In Fig. 5 the modelled and measured H and λET are compared for the same period depicted

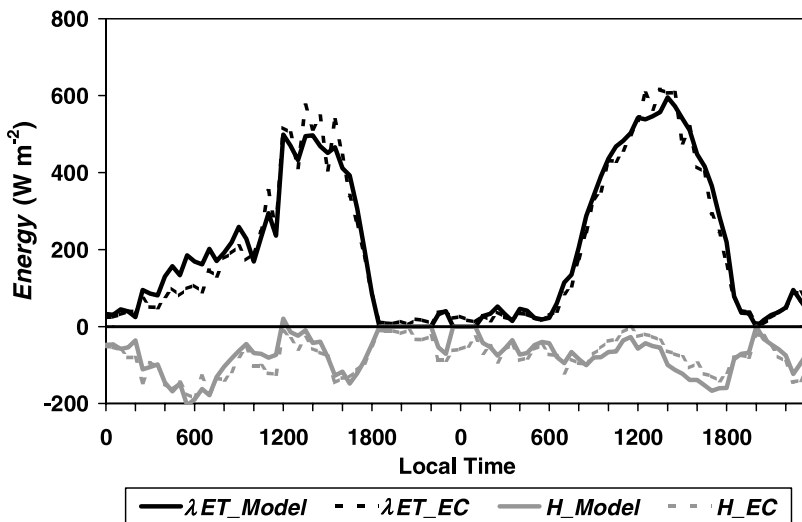


Fig. 5. Modelled and measured sensible heat flux, H and evapotranspiration, λET , versus Day of Year (DOY) for DOY 253 and 254. The eddy-correlation determined H and λET , have been corrected for energy balance closure as described in Section 2

in Fig. 3. We ‘tuned’ the model, i.e. we have chosen by trial-and-error, r_s , z_{0m} and z_{0h} , in such a way that the model agrees best with the measurements. We found $r_s = 20 \text{ s m}^{-1}$ for $R_n - G > 0$ (daytime) and $r_s = 120 \text{ s m}^{-1}$ otherwise (night-time), $z_{0m} = 0.005 \text{ m}$ and $z_{0h} = z_{0m}/10$ and used $\varepsilon_s = 0.98$. These values correspond fairly well with those found for alfalfa by Walter et al. (2002).

In Figs. 6 and 7 we compared the modelled and measured values of H and λET respectively. The calculated and observed surface temperatures are compared in Fig. 8. Although with some scatter, especially for H , the overall picture is that the tuned model describes the selected high-wind situation well. This is supported by Fig. 9, where the modelled H is plotted against u for the night-time conditions similarly to Fig. 4 for measured H . It is seen that the results compare well with the observations depicted in Fig. 3.

4.2 Some statistical quantities

We analysed also the correlation coefficients between temperature, T , and specific humidity, q , as well as the correlation coefficients between the horizontal wind vector, u , and T and q . In Fig. 10, the correlation coefficients R_{Tq} , R_{uT} and R_{uq} are plotted for the same days as Figs. 3 and 5. It is seen that R_{Tq} is negative and approaches at times -1 , R_{uT} averages about $+0.6$ and R_{uq} about -0.6 . Note that this figure refers to an advection case, so H is negative, i.e. $R_{wT} < 0$ and λET is positive, i.e. $R_{wq} > 0$.

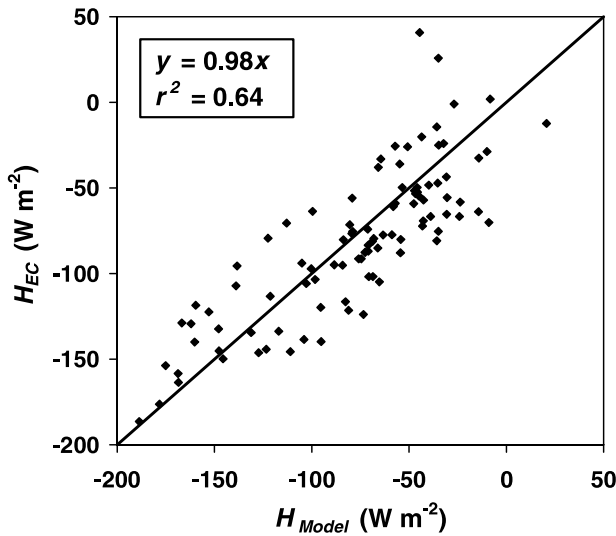


Fig. 6. Modelled versus measured sensible heat flux, H for DOY 252 19:00 to 255 7:00. The eddy-correlation determined H , has been corrected for energy balance closure as described in Section 2

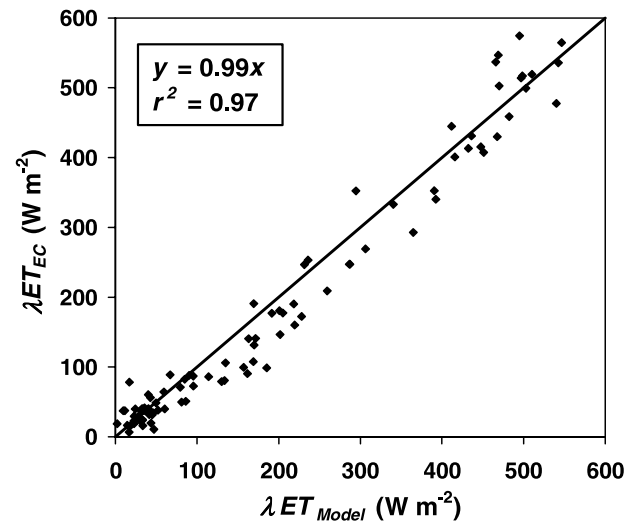


Fig. 7. As Fig. 6, for evapotranspiration, λET instead of H

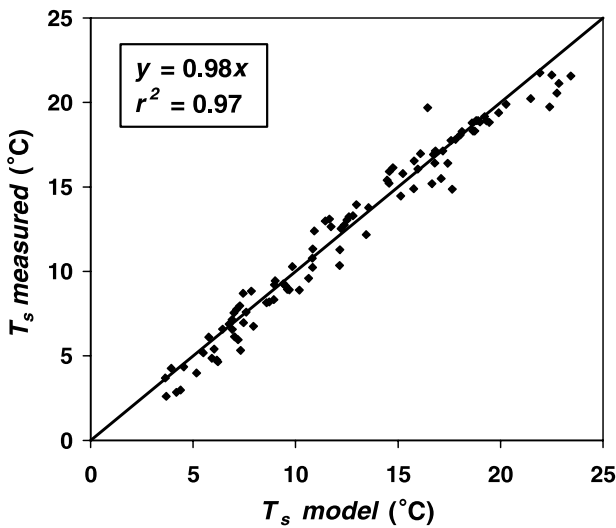


Fig. 8. Modelled versus measured surface temperature for DOY 252 19:00 to 255 7:00

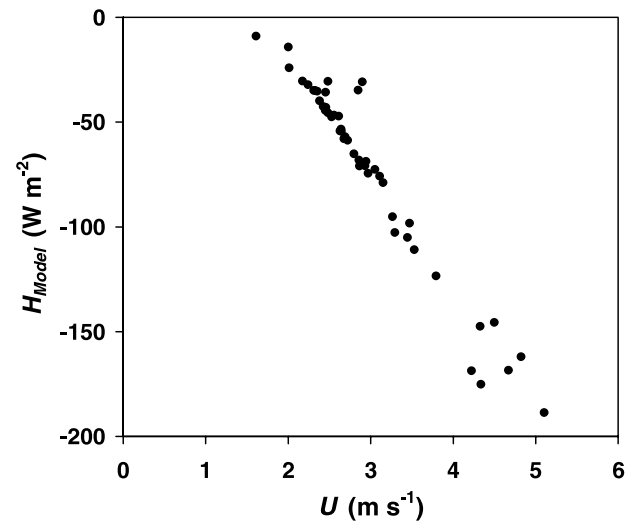


Fig. 9. As Fig. 4, for modelled instead of measured sensible heat flux, H

In Fig. 11 R_{Tq} is plotted against R_{uT} for the whole experiment with horizontal wind speed at 3 m greater than 4 m s^{-1} . It is seen that under these high wind speed conditions R_{Tq} and R_{uT} are strongly correlated.

It should be noted that our findings that R_{uq} and R_{uT} are connected through R_{uw} and R_{Tq} is of course not new. The point we want to make here is that apparently R_{uT} is an ‘advection’ indicator that might be measurable operationally as discussed in the next section.

5. Discussion

We recall that we corrected the measured eddy-correlation fluxes, both H and λET , with a factor 1.5 (see Section 2). As we consider cases where $H < 0$, this correction gives a higher λET than if we had assumed the measured H to be correct and λET determined as a residual of the energy balance, i.e. $\lambda ET = R_n - G - H$.

This study is devoted to regional advection, i.e. we selected an extensive irrigated agricultural fields surrounded by a desert. It was found that

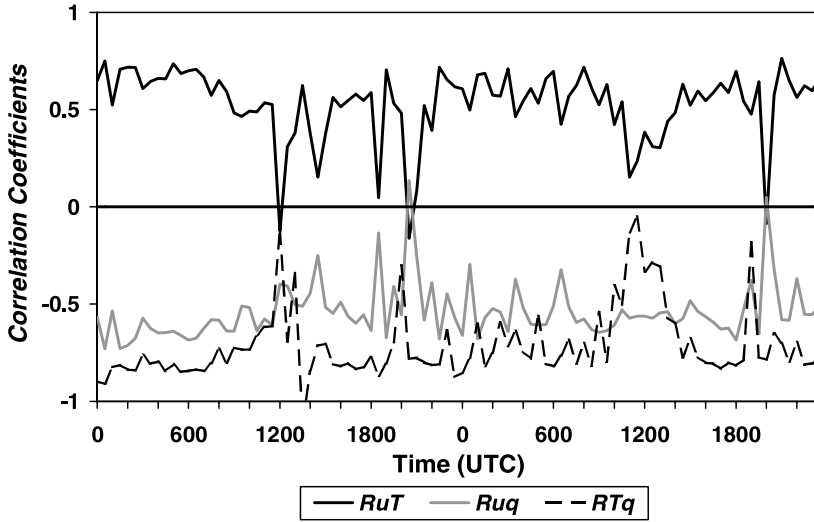


Fig. 10. Correlation coefficients between temperature and humidity, R_{Tq} , wind speed and temperature, R_{uT} and wind speed and humidity, R_{uq} for days with high wind speed (DOY 253 and 254)

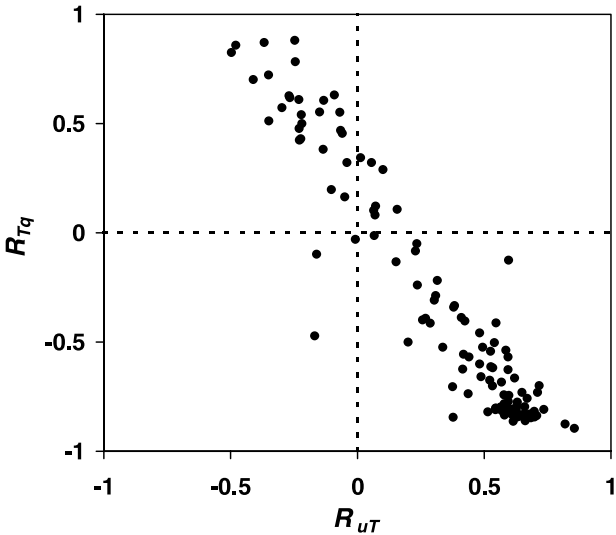


Fig. 11. Correlation coefficients between temperature and humidity, R_{Tq} , wind speed and temperature, R_{uT} for all RAPID data with wind speed at 3 m larger than 4 m s^{-1}

actual λET can exceed the available energy significantly under these conditions provided that there is sufficient wind. The reason is that $\lambda ET > R_n$ is possible only if the sensible heat is negative, and, consequently, the air close to the ground is stably stratified. Under those conditions buoyancy suppresses turbulent motions and wind is the only mechanism that can generate the turbulence required for the transport of heat and moisture.

This picture is confirmed by our data of the RAPID experiment. It is found that during night-time, turbulence is absent indeed when wind speed is less than a ‘critical’ value of about

2 m s^{-1} (see Figs. 2 and 3). This value will depend on various environmental conditions, for which we will derive an expression. A measure for the ‘critical wind speed’ can be inferred from the bulk-Richardson number, $R_{ib} \equiv \frac{g}{T_r} z \frac{\Delta T}{u^2}$, where $\Delta T = T_s - T$, g the acceleration of gravity, T_r the absolute temperature of the air layer between the surface and z and u the wind speed at z . Turbulence will vanish if R_{ib} exceeds its critical value R_{ibc} . Here we adopt $R_{ibc} = 0.25$. Considering the hypothetical case where conditions are just turbulent, then, if u decreases to its critical value u_c , turbulence will vanish, and H and λET will be zero (see e.g. Holtslag and DeBruin, 1988). For night-time conditions, the energy budget equation reads $\varepsilon_s(L^\downarrow - \sigma T_{sc}^4) - G = 0$, in which T_{sc} is the ‘critical’ surface temperature. This quantity can be determined from the measured incoming long-wave radiation and soil heat flux adopting a value for ε_s (here 0.98). In this way we obtain an expression for the night-time ‘critical’ wind speed, u_c given by

$$u_c = \sqrt{\frac{g}{T_r} z \frac{T - T_{sc}}{R_{ibc}}}, \quad (5)$$

with $R_{ibc} = 0.25$.

For the limited data set we analysed we found u_c between 1.5 and 3 m s^{-1} , which corresponds well with our observations (see Fig. 4). Note that in this simple approach the surface roughness does not play a role. Equation 5 can be used to determine u_c for night-time conditions independent of the surface type. It should be stressed that at low wind speed the stable flow can become intermittent, and

the derived model breaks down. It is outside the scope of this study to dwell on this complicated issue. For recent developments see e.g. Van de Wiel et al. (2001) or Hartogensis et al. (2002).

Our measurements show that during night-time λET can reach values up to 150 W m^{-2} when wind speed at 3 m is about 6 m s^{-1} . This means that if such high wind speed conditions persist for, say, 10 hours, λET can be as large as 2 mm per night. This refers to a case in which the surface resistance is very small (we fitted our model to the data with $r_s = 120 \text{ s m}^{-1}$ for night-time). λET of 2 mm per night then refers most likely to direct evaporation of irrigation water, so to periods just after irrigation. Substantial night-time λET rates have been observed also with the precision lysimeter at Kimberly (Jim Wright, personnel communication).

During daytime solar heating tends to make the conditions less stable and H never drops significantly below 0 when the sun is high, i.e. at midday. Moreover, during daytime the wind is not the only turbulence generator and the effect of wind speed on λET is less apparent. During overcast conditions the wind effect is expected to be important during daytime also.

The simple model we used reproduces the wind dependence shown in Figs. 4 and 5 as well as the features related to R_{ib} (not shown) with parameters such as z_{0m} , z_{0h} , ε_s and, above all, r_s tuned to the measurements. By tuning, we determined that for the advection period $r_s = 20 \text{ s m}^{-1}$ for $R_n - G > 0$ (daytime) and $r_s = 120 \text{ s m}^{-1}$ otherwise (night-time). In literature a minimum value for r_s of about 30 s m^{-1} is given for transpiration of most crops during daytime and a higher value for night-time (see e.g. Walter et al., 2002; Allen et al., 1996).

Our data set does not allow distinguishing between evaporation of liquid irrigation water and transpiration since the eddy-correlation method gives only the total λET . It might be possible that a part of the measured λET was due to direct evaporation of irrigation water. The centre pivot irrigation system was operating nearly continuously in the field upwind of our measuring systems. In any case, direct evaporation of irrigation water is loss of water resources for agriculture and may not correspond to increase in biomass. Our results might suggest that this loss can be significant at high wind speed. Consequently, it might be wise to recommend that farm-

ers do not irrigate if high wind speed is expected by local weather services, unless it is necessary to sustain soil water above critical values of course.

Since the tuned model gives results that compare well with the observed (corrected) data, and appears to represent a maximum limit of λET under wet conditions with advection it might be an alternative to the 'standard' FAO-method based the FAO Irrigation and Drainage Paper No. 56 (Allen et al., 1998) for this type of usage. An important difference is that hourly meteorological data are required, because the diurnal variation of wind speed and stability appear to play important roles.

We showed that the correlation coefficient between (fast) fluctuations of temperature and specific humidity, R_{Tq} , is a good indicator for advection conditions. Under these conditions, H is negative and λET positive and R_{Tq} approaches -1 . Note that under 'normal', non-advection conditions during daytime when both H and λET are positive R_{Tq} appears to be close to one, if the conditions are not too dry (for a detailed discussion see DeBruin et al., 1999). This study revealed that also another statistical quantity might serve as an advection-indicator, namely the correlation coefficient between the horizontal wind speed and temperature, R_{uT} . At a wind speed greater than 4 m s^{-1} , R_{Tq} appears to be highly related to R_{uT} (see Fig. 10). This quantity can be determined with a 2D sonic anemometer, which measures the horizontal wind vector and the so-called sonic-temperature and is a suitable alternative for the standard cup anemometer with wind vane currently used at standard weather stations.

Our results might be the basis for a simple method to determine actual λET under night-time advection conditions. First, with the 2D sonic R_{uT} is determined and next R_{Tq} . Next, advection situations can be selected for which, in the next step, H can be estimated using the tuned model. Finally, λET can be evaluated as residual from the energy balance equation, using measured R_n and G .

So far, we did not discuss the effect of wind in cases of local advection, i.e. when the irrigated fields are too small for full adjustment of the flow to the local irrigated surface. Then the air above the surface still contains properties of the upwind desert. Investigation of this feature requires flux measurements at different heights and at different distances from transition of the dry to the wet fields. During RAPID we did not have such an experimental set-up, so we cannot prove that local

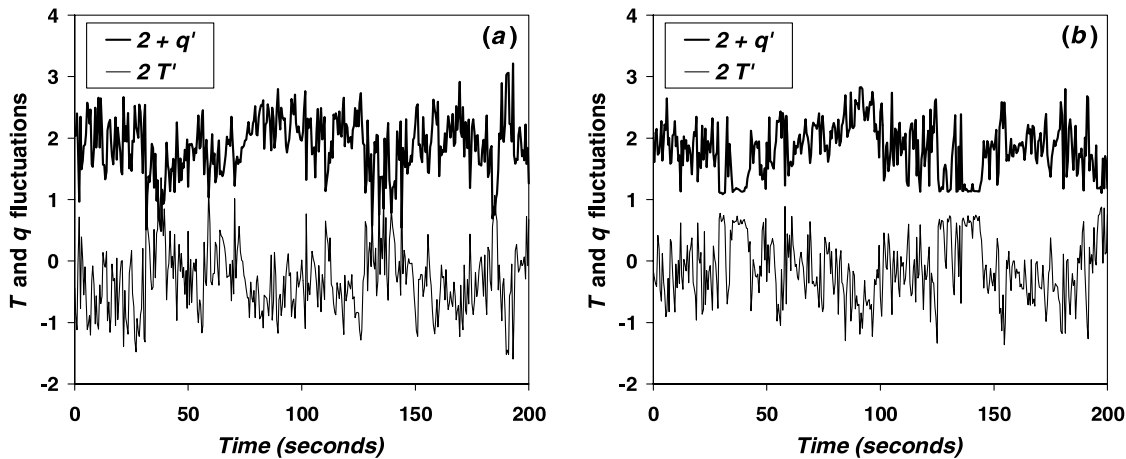


Fig. 12. Raw 20 Hz eddy-correlation data taken at 3 m (Fig. 12a) and 10 m (Fig. 12b), sub-sampled at 2 Hz, of temperature, T' , and humidity, q' , fluctuations versus time. A record of 200 s is selected between 16:00 and 17:00 on DOY 254. To avoid overlap a constant factor of 2 is added to q' and T' is multiplied by 2

advection effects were not present. We collected, however, raw eddy-correlation data at 3 m and at 10 m. In Fig. 12a and b we plotted for a period of 20 seconds the raw temperature and humidity data at 3 and 10 m. Figure 12b shows that the specific humidity at 10 m levels off at some minimum value, whereas at 3 m this effect is not present (see Fig. 12a). For temperature the same can be seen, but now there is a maximum level-off value for the 10 m measurements (Fig. 12b), which is not present in the 3 m measurements. This indicates that the turbulence in the first 3 m was adapted to the irrigated conditions, whereas at 10 m still some upwind ‘desert’ influences were present. Whether this is due to local advection at 10 m is not clear. Inevitably, the dry desert air will be present at greater heights also when the surface layer is fully adapted to the irrigated fields. Due to the nature of atmospheric turbulence individual eddies are expected to penetrated incidentally into the ‘adapted’ surface layer. This will lead to the ‘levelled-off’ q -signal shown in the raw data for 10 m. In a forthcoming paper we will analyse further our RAPID data set in order to investigate the penetration of ‘dry-warm’ events into the adapted surface layer.

6. Conclusions

Evapotranspiration, λET , of extensive irrigated fields in a desert environment can exceed net radiation under high wind conditions. We base this conclusion on eddy-correlation data taken during the RAPID experiment, which we corrected ac-

cording to the procedure described in Section 2. At night we observed that λET can be as large as 150 W m^{-2} when the 3 m wind speed exceeds 6 m s^{-1} . If such conditions prevail during a whole night, ET can be as large as 2 mm per night.

We applied a simple model that represents the advection conditions quite well. It is based on a set of governing equations similar to that from which the Penman-Monteith formula has been derived. The model accounts for stability effects in the aerodynamic resistance as well as for the influence of the (calculated) surface temperature on the outgoing long-wave radiation. We tuned the model parameters z_{0m} , z_{0h} , ϵ_s and r_s in order to get a fair resemblance between modelled and observed H and λET . This tuned model is able to describe the observed relation between H and wind speed u during night-time, which plays a key-role in the advection issue. One might consider applying our adapted Penman-Monteith approach to predict maximum rates of λET instead of the Penman-Monteith version now often used for that purpose, which is based on FAO Irrigation and Drainage Paper No. 56 (Allen et al., 1998). However, our model requires hourly standard meteorological data, whereas FAO Penman-Monteith equations require daily averaged data.

We hypothesized that the found high λET rates during windy conditions at night-time are due to evaporation of irrigation water. We cannot substantiate this idea with our data, as the observation methods used determine total λET and do not distinguish between evaporation of irrigation water and transpiration. At any rate, our results suggest

to recommend farmers not to irrigate if high winds speeds are forecasted, but it is realised that in some windy regions this is impossible.

We found that the correlation coefficient R_{uT} is a proper indicator for advection conditions. Together with the good correlation found between H and u , this feature might be suitable to determine λET under night-time advection circumstances. It is suggested to use a 2D sonic anemometer for this purpose, with which R_{uT} can be determined. More applied research is needed on this issue.

The above results apply to large irrigated fields, where the advected air mass is adapted fully to the surface, and the properties of the upwind desert do not play a role (regional advection). Our data set did not allow studying the flow above small, irrigated fields, where the fetch is small, and the air above the field still contains upwind desert properties (local advection). From the raw data shown in Fig. 12 it can be seen that for that example, the data taken at 3 m height were in a fully adapted layer, whereas at 10 m traces of the upwind desert are present in the data. Local advection might explain the fact that the Kimberly lysimeter data presented in Fig. 1 show daily- $\lambda ET > R_n$ even on calm days.

In this paper we presented some thoughts on the advection issue, which we substantiated with experimental evidence. We used selected cases, however, and a model that was tuned to the measurements. We stress that our results are a first initiative to deal with this issue rather than a final proof and we intend to carry out a more profound study on the RAPID data.

Acknowledgements

We thank Drs. Larry Hipps, Robert Hill, Christopher Neale, (Utah State University), Dr. James Wright (USDA-ARS, Kimberly) and Dr. Bert Tanner (Campbell Scientific, Inc.) for their valuable contribution to the RAPID field experiment. We highly appreciate the comments Larry Hipps made on the draft of this paper. Dr. James Wright provided the Kimberly lysimeter data presented in Fig. 1. The valuable remarks made by the reviewers are acknowledged also.

References

Allen RG, Pereira LS, Raes D, Smith M (1998) Crop evapotranspiration (guidelines for computing crop water requirements). FAO Irrigation and Drainage Paper No. 56, 290 pp
 Allen RG, Pruitt WO, Businger JA, Fritschen LJ, Jensen ME, Quinn FH (1996) Evaporation and transpiration. Chapter 4

- in ASCE Hydrology Handbook. New York, NY, pp 125–252
 Beljaars ACM, Holtslag AAM (1991) On flux parameterization over land surfaces for atmospheric models. *J Appl Meteor* 30: 327–341
 Bink NJ (1996) The structure of the atmospheric surface layer subject to local advection. Wageningen: PhD Thesis, Wageningen Agricultural University, 206 pp
 Culf AD, Foken T, Gash JHC (2004) The energy balance closure problem. In: Kabat et al. (eds) *Vegetation, water, humans and the climate. A new perspective on an interactive system*. Berlin, Heidelberg: Springer, pp 159–166
 De Bruin HAR, Van Den Hurk BJM, Kroon LJM (1999) On the temperature-humidity correlation and similarity. *Bound-Layer Meteorol* 93: 453–468
 Dyer AJ (1974) A review of flux-profile relationships. *Bound-Layer Meteorol* 7: 453–468
 Hartogensis OK, DeBruin HAR, Van de Wiel BJH (2002) Displaced-beam small aperture scintillometer test Part II: CASES-99 stable boundary layer experiment. *Bound-Layer Meteorol* 105: 148–176
 Hoedjes JCB, Zuurbier RM, Watts CJ (2002) Large aperture scintillometer used over a homogeneous irrigated area, partly affected by regional advection. *Bound-Layer Meteorol* 105: 99–117
 Holtslag AAM, De Bruin HAR (1988) Applied modeling of the night-time surface energy balance over land. *J Appl Meteor* 27: 689–704
 Kramer JWJL (2000) Surface fluxes in a large irrigated area affected by regional advection. Wageningen: MSc thesis Wageningen University, Meteorology and Air Quality Group, 65 pp
 Kroon LJM, De Bruin HAR (1995) The Crau field experiment: turbulent exchange in the surface layer under conditions of strong local advection. *J Hydrol* 166: 327–351
 McNaughton KG, Laubach J (2000) Power spectra and co-spectra for wind and scalars in a disturbed surface layer at the base of an advection inversion. *Bound-Layer Meteorol* 96: 143–185
 Stewart JB, Kustas WP, Humes KS, Nichols WD, Moran MS, De Bruin HAR (1994) Sensible heat flux-radiative temperature relationship for 8 semi-arid areas. *J Appl Meteorol* 33: 1110–1117
 Van de Wiel BJH, Ronda RJ, Moene AF, DeBruin HAR, Holtslag AAM (2001) Intermittent turbulence and oscillations in the stable boundary layer over land Part I: A bulk model. *J Atmos Sci* 59: 942–958
 Walter IA, Allen RG, Elliott R, Itenfisu D, Brown P, Jensen ME, Mecham B, Howell TA, Snyder R, Eching S, Spofford T, Hattendorf M, Martin D, Cuenca RH, Wright JL (2002) *The ASCE Standardized Reference Evapotranspiration Equation*. Washington DC: American Society of Civil Engineers, 171 pp

Authors' addresses: H. A. R. De Bruin (e-mail: henk.debruin@wur.nl), O. K. Hartogensis, J. W. J. L. Kramer, Wageningen University, Meteorology and Air Quality Group, Duivendal 2, 6701 AP, Wageningen, The Netherlands; R. G. Allen, University of Idaho at Kimberly Research and Extension Center, Kimberly, Idaho, USA.

References

- Andreas, E.L.: 1989, 'Two-wavelength method of measuring path-averaged turbulent surface heat fluxes', *J. Atmos. and Ocean Tech.* **6**, 280-292.
- Andreas, E.L.: 1990, *Selected Papers on Turbulence in a Refractive Medium*, SPIE Milestone Series 25, SPIE – The International Society for Optical Engineering, Bellingham, 693 pp.
- Andreas, E.L., 1991: 'Using scintillation at two wavelengths to measure path-averaged heat fluxes in free convection' *Boundary-Layer Meteorol.* **54**, 167-182.
- Andreas, E.L.: 1992, 'Uncertainty in a path-averaged measurement of the friction velocity u_* ', *J. Appl. Meteorol.* **31**, 1312-1321.
- Andreas, E.L.: 2002, 'Parameterizing scalar transfer over snow and ice: A review', *J. HydroMeteorol.* **3**, 417-432.
- Andreas, E.L. and Hicks, B.B.: 2002, 'Comments on "Critical Test of the Validity of Monin-Obukhov Similarity during Convective Conditions"', *J. Atmos. Sci.* **59**, 2605-2607.
- Beljaars, A.C.M., and Holtslag, A.A.M.: 1991, 'Flux parameterization over land surfaces for atmospheric models', *J. Appl. Meteorol.* **30**, 327-341.
- Beljaars, A.C.M. and Viterbo, P.: 1998, 'Role of the Boundary Layer in a Numerical Weather Prediction Model', in '*Clear and Cloudy Boundary Layers*', Holtslag, A.A.M., Duynkerke, P.G. and Jonker, P.J. Eds, Royal Netherlands Academy of Arts and Sciences, Amsterdam, pp. 287-304.
- Beyrich, F., De Bruin, H.A.R., Meijninger, W.M.L., and Schipper, J.W.: 2002, 'Experiences from one-year continuous operation of a large aperture scintillometer over a heterogeneous land surface', *Boundary-Layer Meteorol.* **105**, 85-97.
- Broersen, P.M.T.: 2002: 'Automatic Spectral Analysis with Time Series Models', *IEEE Transactions on Instrumentation and Measurement* **51**, 211-216.
- Businger, J.A., Wyngaard, J.C., Izumi, Y., and Bradley, E.F.: 1971, 'Flux-Profile Relationships in the atmospheric surface layer', *J. Atmos. Sci.* **28**, 181-189.
- Champagne, F.H., Friehe, C.A., LaRue, J.C., and Wyngaard, J.C.: 1977, 'Flux measurements, flux estimation techniques, and fine-scale turbulence measurements in the unstable surface layer over land', *J. Atmos. Sci.* **34**, 515-530.
- Chebouni, A., Kerr, Y.H., Watts, C., Hartogensis, O., Goodrich, D., Scott, R., Schieldge, J., Lee, K., Shuttleworth, W.J., Dedieu, G., and De Bruin, H.A.R.: 1999, 'Estimation of area-average sensible heat flux using a large-aperture scintillometer during the Semi-Arid Land-Surface-Atmosphere (SALSA) experiment', *Water Resour. Res.* **35**, 2505-2511.
- Cheng, Y., Parlange, M.B., and Brutsaert, W.B.: 2005, 'Pathology of Monin-Obukhov similarity in the stable boundary layer', *J. Geophys. Res.* **110**, D06101, 10p.

- Churnside, J.H.: 1990, 'A spectrum of refractive turbulence in the turbulent atmosphere', *J. Mod. Opt.* **37**, 13-16.
- Clifford S.F., Ochs G.R., and Lawrence R.S.: 1974, 'Saturation of Optical Scintillation by Strong Turbulence', *J. Opt. Soc. Amer.* **64**, 148-154.
- Corrsin, S.: 1951, 'On the spectrum of isotropic temperature fluctuations in isotropic turbulence', *J. Appl. Phys.* **22**, 469-473.
- Cuxart J., Morales G., Terradellas E., and Yague C.: 2002, 'Study of coherent structures and estimation of the pressure transport terms for the nocturnal stable boundary layer', *Boundary-Layer Meteorol.* **105**, 305-328.
- De Bruin, H.A.R., Kohsiek, W. and Van den Hurk, B.J.J.M.: 1993, 'A Verification of Some Methods to Determine the Fluxes of Momentum, Sensible Heat and Water Vapour using Standard Deviation and Structure Parameter of Scalar Meteorological Quantities', *Boundary-Layer Meteorol.* **63**, 231-257.
- De Bruin, H.A.R., Van den Hurk, B.J.J.M., and Kohsiek, W.: 1995, 'The scintillation method tested over a dry vineyard area', *Boundary-Layer Meteorol.* **76**, 25-40.
- De Bruin, H.A.R.: 2002, 'Introduction, renaissance of scintillometry', *Boundary-Layer Meteorol.* **105**, 1-4.
- De Bruin, H.A.R., Meijninger, W.M.L., Smedman, A.S. and Magnusson, M.: 2002, 'Displaced-Beam Small Aperture Scintillometer test Part I: the WINTeX data set', *Boundary-Layer Meteorol.* **105**, 129-148.
- De Bruin, H.A.R., and Hartogensis, O.K.: 2005, 'Variance method to determine fluxes of momentum and sensible heat in the stable atmospheric surface layer', *Boundary-Layer Meteorol.* **116**, 385-392.
- De Bruin, H.A.R., Hartogensis, O.K., Allen, R.G., and Kramer, J.W.J.L., 2004: 'Note on the Regional Advection Perturbations in an Irrigated Desert (RAPID) Experiment', *Theor. Appl. Climatol.* **80**, 143-152.
- De Bruin, H.A.R., 2005: *Atmosphere-Land Interactions*. Lecture notes, Wageningen University, Wageningen, Netherlands, 119pp
- De Waele, S., Van Dijk, A., Broersen, P., and Duynkerke, P.G.: 2002, 'Estimation of the integral time scale with time series models', In: *Proceedings 15th Symposium on Boundary Layers and Turbulence Diffusion*, Wageningen, Netherlands. American Meteorological Society.
- Duynkerke P.G.: 1999, 'Turbulence, radiation and fog in Dutch stable boundary layers' *Boundary-Layer Meteorol.* **90**, 447-477.
- Dyer, A.J.: 1974, 'A review of flux-profile relationships', *Boundary-Layer Meteorol.* **7**, 363-372.
- Fleagle, R.G. and Businger, J.A., 1980: *An Introduction to Atmospheric Physics*, Academic Press, New York, second edition, 432 pp.
- Frederickson, P. A., K. L. Davidson, C. R. Zeisse, and C. S. Bendall, 2000: Estimating the refractive index structure parameter (C_n^2) over the ocean using bulk methods. *J. Appl. Meteorol.* **39**, 1770-1783.

- Frehlich, Rod: 1992, 'Laser scintillation measurements of the temperature spectrum in the atmospheric surface layer', *J. Atmos. Sci.* **49**, 1494-1509.
- Frenzen, P. and Vogel, C.A.: 1992, 'The turbulent kinetic energy budget in the atmospheric surface layer: A review and experimental re-examination in the field', *Boundary-Layer Meteorol.* **60**, 49-76.
- Frenzen, P. and Vogel, C.A.: 2001, 'Further studies of atmospheric turbulence in layers near the surface: Scaling the TKE budget above the roughness sublayer', *Boundary-Layer Meteorol.* **99**, 173-206.
- Green, A.E., and Hayashi, Y.: 1998, 'Use of the scintillometer technique over a rice paddy', *Japanese J. Agric. Meteorol.* **54**, 225-234.
- Green, A.E., Astill, M.S., McAneney, K.J., and Nieveen, J.P.: 2001, 'Path-averaged surface fluxes determined from infrared and microwave scintillometers', *Agric. For. Meteorol.* **109**, 233-247.
- Hartogensis, O.K., De Bruin, H.A.R., Van De Wiel, B.J.H.: 2002, 'Displaced-Beam Small Aperture Scintillometer Test. Part II: Cases-99 Stable Boundary-Layer Experiment', *Boundary-Layer Meteorol.* **105**, 149-176.
- Hartogensis, O.K. and De Bruin, H.A.R., 2005: 'Monin-Obukhov similarity functions of the structure parameter of temperature and TKE dissipation rate in the Stable Boundary Layer', *Boundary-Layer Meteorol.* **116**, 253-276.
- Hicks, B.B.: 1981, 'An examination of turbulence statistics in the surface boundary layer', *Boundary-Layer Meteorol.* **21**, 389-402.
- Hill, R.J.: 1978, 'Models of the scalar spectrum for turbulent advection. *J. Fluid Mech.* **88**, 541-562.
- Hill, R.J. and Clifford, S.F.: 1978, 'Modified spectrum of the atmospheric temperature fluctuations and its application to optical propagation', *J. Opt. Soc. Amer.* **68**, 892-899.
- Hill, R.J. and Ochs, G.R.: 1978, 'Fine Calibration of Large-Aperture Optical Scintillometers and an Optical Estimate of the Inner Scale of Turbulence', *Appl. Optics* **17**, 3608-3612.
- Hill, R.J.: 1982, 'Theory of measuring the path-averaged inner scale of turbulence by spatial filtering of optical scintillation', *Applied Optics* **21**, 1201-1211.
- Hill, R.J. and Lataitis, R.J.: 1989, 'Effect of refractive dispersion on the bichromatic correlation of irradiances for atmospheric scintillation', *Applied Optics* **28**, 4121-4125.
- Hill, R.J.: 1991, 'Comparison of experiment with a new theory of the turbulence temperature structure function', *Phys. Fluids A* **3**, 1572-1576.
- Hill, R.J. and Frehlich, R.G.: 1996, 'Onset of strong scintillation with application to remote sensing of turbulence inner scale', *Appl. Optics* **35**, 986-997.
- Hill, R.J.: 1997, 'Algorithms for obtaining atmospheric surface-layer fluxes from scintillation measurements', *J. Atmos. and Ocean Tech.* **14**, 456-467.
- Hoedjes, J.C.B., Zuurbier, R.M., and Watts, C.J.: 2002, 'Large aperture scintillometer used over a homogeneous irrigated area partly affected by regional advection', *Boundary-Layer Meteorol.* **105**, 99-117.

- Högström, U.: 1990, 'Analysis of turbulence in the surface layer with a modified similarity formulation for near neutral conditions', *J. Atmos. Sci.* **47**, 1949-1972.
- Högström, U.: 1996, 'Review of some characteristics of the atmospheric surface layer', *Boundary-Layer Meteorol.* **78**, 215-246.
- Holtslag, A.A.M. and Nieuwstadt, F.T.M.: 1986, 'Scaling the atmospheric boundary-layer', *Boundary-Layer Meteorol.* **36**, 201-209.
- Holtslag, A.A.M. and De Bruin, H.A.R.: 1988, 'Applied modelling of the night time surface energy balance over land', *J. Appl. Meteorol.* **27**, 689-703.
- Johansson, C., Smedman, A-S., Högström, U., and Brasseur, J.G.: 2002, 'Reply to Comments on "Critical Test of the Validity of Monin-Obukhov Similarity during Convective Conditions"', *J. Atmos. Sci.* **59**, 2608-2614.
- Kahlsa, S.J.S.: 1980, 'Surface layer intermittency investigated with conditional sampling', *Boundary-Layer Meteorol.* **19**, 135-153.
- Kaimal, J. C. and Finnigan, J. J.: 1994, *Atmospheric Boundary Layer Flows - Their Structure and Measurement*. Oxford University Press, New York, USA, 289 pp
- Kohsiek, W., Meijninger, W.M.L., Moene, A.F., Heusinkveld, B.G., Hartogensis, O.K., Hillen, W.C.A.M. and De Bruin, H.A.R.: 2002, 'An extra large aperture scintillometer (XLAS) with a 9.8 km path length', *Boundary-Layer Meteorol.* **105**, 119-127.
- Kohsiek, W., Meijninger, W.M.L., De Bruin, H.A.R., and Beyrich, F.: 2006, 'Saturation of the Large Aperture Scintillometer', *Boundary-Layer Meteorol.* (in press).
- Kolmogorov, A.N.: 1941, 'The local structure of turbulence in an incompressible viscous fluid for very large Reynolds numbers', *Dokl. Akad. Nauk.* **30**, 299-303.
- Kramer, J.W.J.L., 2000: *Surface fluxes in a large irrigated area affected by regional advection*. MSc thesis, Wageningen University, Wageningen, 65 pp
- Lagouarde J.P., Bonnefond J.M., Kerr Y.H., McAneney K.J., and Irvine M.: 2002, 'Integrated sensible heat flux measurements of a two-surface composite landscape using scintillometry' *Boundary-Layer Meteorol.* **105**, 5-35.
- Mahrt, L., Sun, J., Blumen, W., Delany, T., and Oncley, S.: 1998, 'Nocturnal boundary layer regimes', *Boundary-Layer Meteorol.* **88**, 255-278.
- Mahrt, L.: 1999, 'Stratified atmospheric boundary layers', *Boundary-Layer Meteorol.* **90**, 375-396.
- McAneney, K.J., Green, A.E., and Astill, M.S.: 1995, 'Large-aperture scintillometry: the homogeneous case', *Agric. For. Meteorol.* **76**, 149-162.
- Meijninger, W.M.L., and De Bruin, H.A.R.: 2000, 'The sensible heat fluxes over irrigated areas in western Turkey determined with a large aperture scintillometer', *J. Hydrology* **229**, 42-49.
- Meijninger, W.M.L., Hartogensis, O.K., Kohsiek, W., Hoedjes, J.C.B., Zurbier, R.M., and De Bruin, H.A.R.: 2002a, 'Determination of area averaged sensible heat fluxes with a large aperture scintillometer over a heterogeneous surface – Flevoland field experiment', *Boundary-Layer Meteorol.* **105**, 37-62.

- Meijninger, W.M.L., Green, A.E., Hartogensis, O.K., Kohsiek, W., Hoedjes, J.C.B., Zuurbier, R.M., and De Bruin, H.A.R.: 2002b, 'Determination of area-averaged water vapour fluxes with large aperture and radiowave scintillometers over a heterogeneous surface – flevoland field experiment', *Boundary-Layer Meteorol.* **105**, 63-83.
- Meijninger, W.M.L., 2003: *Surface Fluxes over Natural Landscapes Using Scintillometry*. Ph.D. thesis, Wageningen University, Wageningen, Netherlands, 164pp
- Moene, A.F.: 2003, 'Effects of water vapour on the structure parameter of the refractive index', *Boundary-Layer Meteorol.* **107**, 635 – 653.
- Moene, A.F., Meijninger, W.M.L., Hartogensis, O.K., Kohsiek, W., and De Bruin, H.A.R., 2004: *A review of relationships describing the signal of a Large Aperture Scintillometer*, Internal Report 2004/2, Meteorology and Air Quality Group, Wageningen University, Wageningen, the Netherlands, 39 pp.
- Monin, A.S. and Obukhov, A.M.: 1954, 'Basic Laws of Turbulent Mixing in the Ground Layer of the Atmosphere', *Trans. Geophys. Inst. Akad. Nauk.* **151**, 163–187.
- Monin, A.S., and Yaglom, A.M., 1971: *Statistical Fluid mechanics of Turbulence Vol. 1*. MIT Press, Cambridge, MA, USA, 769 pp
- Monin, A.S., and Yaglom, A.M., 1975: *Statistical Fluid mechanics of Turbulence Vol. 2*. MIT Press, Cambridge, MA, USA, 874 pp
- Moore, C.: 1986, 'Frequency response corrections for eddy correlation systems', *Boundary-Layer Meteorol.* **37**, 17-35.
- Nappo, C.J. and Johansson, P-E.: 1999, 'Summary of the Lövånger International Workshop on Turbulence and Diffusion in the Stably Stratified Planetary Boundary Layer', *Boundary-Layer Meteorol.* **90**, 345-374.
- Nieuwstadt, F.T.M.: 1984, 'The Turbulent Structure of the Stable, Nocturnal Boundary-Layer', *J. Atmos. Sci.* **41**, 2202-2216.
- Nieveen, J. P., Green, A. E. and Kohsiek, W.: 1998, 'Using a large-aperture scintillometer to measure absorption and refractive index fluctuations', *Boundary-Layer Meteorol.* **87**, 101-116.
- Obukhov, A.M.: 1946 (English translation in Obukhov, A.M.: 1971, 'Turbulence in an Atmosphere with a Non-Uniform Temperature', *Boundary-Layer Meteorol.* **2**, 7–29.
- Obukhov, A.M.: 1949, 'Structure of the temperature field in turbulent flow', *Izv. Akad. Nauk.* **13**, 58-69.
- Ochs, G. R., and R. J. Hill, 1982: *A Study of Factors Influencing the Calibration of Optical C_n^2 Meters*, NOAA Tech. Memo. ERL WPL-106, NOAA Environmental Research Laboratory, Boulder, Colorado, 24 pp.
- Ochs, G. R., and J. J. Wilson, 1993: *A Second-Generation Large-Aperture Scintillometer*, NOAA Tech. Memo. ERL WPL-232, NOAA Environmental Research Laboratory, Boulder, Colorado, 24 pp.
- Oncley, S.P., Friehe, C.A., Larue, J.C., Businger, J.A., Itsweire, E.C., and Chang, S.S.: 1996, 'Surface –layer fluxes, profiles, and turbulence measurements over uniform terrain under near-neutral conditions', *J. Atmos. Sci.* **53**, 1029-1044.

- Pahlow M., Parlange, M.B., and Porte-Agel, F.: 2001, 'On Monin-Obukhov similarity in the stable atmospheric boundary layer', *Boundary-Layer Meteorol.* **99**, 225-248.
- Panofsky, H. A., and J. A. Dutton, 1984: *Atmospheric Turbulence: Models and Methods for Engineering Applications*. John Wiley&Sons, New York. 397 pp.
- Poggio, P., Furger, M., Prévôt, A.S.H., Graber, W.K. and Andreas, E.L.: 2000, 'Scintillometer wind measurements over complex terrain', *J. Atmos. and Ocean Techn.* **17**, 17-26.
- Poulos, G.S., Fritts, D.C., Blumen, W., and Bach, W.D.: 2000, CASES-99 field experiment: an overview. *Proc. 14th Symp. on Boundary Layer and Turbulence*, Aspen, CO, 7-11 August 2000, , American Meteorological Society., 45 Beacon St, Boston, MA, pp. 618-621.
- Poulos, G.S., Blumen, W., Fritts, D.C., Lundquist, J.K., Sun, J., Burns, S.P., Nappo, C., Banta, R., Newsom, R., Cuxart, J., Terradellas, E., Balsley B., and Jensen, M.: 2002, 'CASES-99: A Comprehensive Investigation of the Stable Nocturnal Boundary Layer', *Bull. Amer. Meteorol. Soc.* **83**, 555-581.
- Salmond J.A., and McKendry, I.G.: 2005, 'Review of turbulence in the very stable nocturnal boundary layer and its implications for air quality', *Progress Phys. Geo.* **29**, 171-188.
- Schotanus, P., Nieuwstadt, F., and De Bruin, H.: 1983, 'Temperature measurement with a sonic anemometer and its application to heat and moisture fluxes', *Boundary-Layer Meteorol.* **26**, 81-93.
- Shuttleworth, W.J., Gash, J.H.C., Lloyd, C.R., McNeal, D.D., Moore, C.J., and Wallace, J.S.: 1988, 'An Integrated Micrometeorological System for Evaporation Measurement', *Agric. For. Meteorol.* **43**, 295-317.
- Steenefeld, G.J, Holtslag, A.A.M, and DeBruin, H.A.R.: 2006a, 'Fluxes and Gradients in the Convective Surface Layer and the possible role of Boundary-Layer depth and Entrainment flux', *Boundary-Layer Meteorol.* **116**, 237-252.
- Steenefeld, G.J., Van De Wiel, B.J.H. and Holtslag, A.A.M.: 2006b, 'Modeling the evolution of the atmospheric boundary layer for three contrasting nights in CASES-99', *J. Atmos. Sci.* (in press).
- Stull, R.B., 1988: *An introduction to boundary layer meteorology*. Kluwer academic publishers, Dordrecht, 666 pp.
- Tatarskii, V.I.: 1961, *Wave propagation in a turbulent medium*. McGraw-Hill Book Company Inc., New York, 285 pp.
- Thiermann, V. and Grassl, H.: 1992, 'The measurement of turbulent surface-layer fluxes by use of bi-chromatic scintillation', *Boundary-Layer Meteorol.* **58**, 367-389.
- Thiermann, V.: 1992, 'A displaced-beam scintillometer for line-averaged measurements of surface layer turbulence', *10th symposium on turbulence and diffusion*, 29 September – 2 October 1992, Portland, OR.
- Thiermann, V.: 1996, *Surface Layer Scintillometer SLS20/SLS40, user's manual*, Scintec Atmosphärentchnik GmbH, Tübingen, Germany, 74 pp.
- Thierman, V. and Rummel, A.G.: 1998. *Correction for transmitter vibrations in laser scintillation measurements*. In: Proceedings European Symposium on Remote Sensing IV – Barcelona, Spain.

- Van De Wiel, B.J.H., Ronda, R.J., Moene, A.F., De Bruin, H.A.R., and Holtslag, A.A.M.: 2003a, 'Intermittent turbulence and oscillations in the stable boundary layer over land Part I: A bulk model.', *J. Atmos. Sci.* **59**, 942-958.
- Van De Wiel, B.J.H., Moene, A.F., Ronda, R.J., De Bruin, H.A.R., and Holtslag, A.A.M.: 2003b, 'Intermittent turbulence and oscillations in the stable boundary layer over land Part II: A system dynamics approach', *J. Atmos. Sci.* **59**, 2567-2581.
- Van De Wiel, B.J.H., Moene, A.F., Hartogensis, O.K., De Bruin, H.A.R. and Holtslag, A.A.M.: 2003c, 'Intermittent turbulence and oscillations in the stable boundary layer over land Part III: A classification for observations during CASES99', *J. Atmos. Sci.* **60**, 2509-2522.
- Van Dijk, A., Kohsiek, W., and De Bruin, H.A.R.: 2003, 'Oxygen sensitivity of krypton and Lyman-alpha hygrometers', *J. Atmos. Oceanic Tech.* **20**, 143-151.
- Van Dijk, A., Moene, A.F., and De Bruin, H.A.R., 2004: *The principles of surface flux physics: theory, practice and description of the ECPACK library*, Internal Report 2004/1, Meteorology and Air Quality Group, Wageningen University, Wageningen, the Netherlands, 99 pp.
- Van Dijk, A., De Bruin, H.A.R., Hartogensis, O., and Kohsiek, W.: 2006, 'Humidity effects on the Kolmogorov length and the structure parameter of the index of refraction estimated with a displaced-beam small aperture scintillometer', (in preparation)
- Vickers, D. and Mahrt, L.: 2003, 'The cospectral gap and turbulent flux calculations', *J. Atmos. Ocean Tech.* **20**, 660-672.
- Wang, T.I., Ochs, G.R. and Clifford, S.F.: 1978, 'A saturation resistant optical scintillometer to measure C_n^2 ', *J. Opt. Soc. Amer.* **69**, 334-338.
- Watts, C.J., Chehbouni, A., Rodríguez, J.C., Kerr, Y.H., Hartogensis, O., and De Bruin, H.A.R.: 2000, 'Comparison of sensible heat-flux estimates using AVHRR with scintillometer measurements over semi-arid grassland in northwest Mexico', *Agric. For. Meteorol.* **105**, 81-89.
- Wesely, M.L.: 1976, 'The combined effect of temperature and humidity on the refractive index', *J. Appl. Meteorol.* **15**, 43-49.
- Wilczak, J.M., Oncley, S.P. and Stage S.A.: 2001, 'Sonic anemometer tilt correction algorithms', *Boundary-Layer Meteorol.* **99**, 127-150.
- Wright, J.L.: 1982, 'New evapotranspiration crop coefficients', *J. Irrig. Drain. Div., Am. Soc. Civ. Eng.* **108**, 57-74.
- Wyngaard, J.C., and Coté, O.R.: 1971, 'The budgets of turbulent kinematic energy and temperature variance in the atmospheric surface layer', *J. Atmos. Sci.* **28**, 190-201.
- Wyngaard, J.C., Izumi, Y., and Collins Jr., S.A.: 1971, 'Behaviour of the refractive index structure parameter near the ground', *J. Opt. Soc. Am.* **15**, 1177-1188.
- Wyngaard, J.C.: 1973, 'On surface layer turbulence', in D.A. Haugen (ed.), *Workshop on Micrometeorology*, American Meteorological Society, Boston, MA, pp. 101-149.

Samenvatting

Dit proefschrift heeft tot doel meetmethodes te onderzoeken voor het meten van warmte en impulsuitwisseling, alsmede kentallen die turbulentie karakteriseren in de atmosferische oppervlaktelaag (SSL). De SSL is gedefinieerd als het onderste gedeelte van de stabiele grenslaag (SBL) waar de oppervlakte-fluxen nagenoeg constant zijn met de hoogte. De SBL beperkt zich vaak tot een dunne laag boven het oppervlak en is geregeld intermitterend van aard, dwz rustige periodes met vrijwel laminaire stroming worden afgewisseld met periodes van turbulente uitwisseling. Deze omstandigheden compliceren flux-metingen aanzienlijk, omdat zij bij voorkeur bepaald dienen te worden pal boven het aardoppervlak en over korte periodes, ter voorkoming van middeling over non-stationaire periodes. Een standaard methode om fluxen te meten, de eddy-covariantie (EC) methode, is conceptueel gezien eenvoudig. In de praktijk, echter, zitten er vele haken en ogen aan in de vorm van additionele correcties. Verder heeft de EC-methode twee specifieke nadelen in de non-stationaire en vaak zeer ondiepe SBL. Ten eerste, het vereist stationaire condities voor een periode van ten minste 10 minuten om een statistisch stabiele flux te bepalen. Ten tweede, in zeer stabiele omstandigheden zal een significant deel van de turbulente wervels niet worden gemeten door de EC-sensor, omdat ze kleiner zijn dan het pad waarover het instrument meet en worden daarom niet meegenomen in de flux-bepaling. Deze aspecten hebben ertoe geleid de toepasbaarheid van scintillometers in the SSL nader te bestuderen. Dit is het hoofddoel van dit proefschrift.

De scintillometers die zijn gebruikt in het kader van dit proefschrift zijn optische instrumenten die bestaan uit een zender en een ontvanger. Twee types scintillometers worden beschouwd, te weten de kleine openingshoek scintillometer met verschoven bundels (“displaced beam small aperture scintillometer”, afgekort als “DBSAS”) en de grote openingshoek scintillometer (“large aperture scintillometer”, afgekort als “LAS”). De DBSAS gebruikt een laser die wordt gesplitst in twee evenwijdige bundels die 2.7 mm ten opzichte van elkaar verschoven zijn en kan worden gebruikt over een afstand van ~ 100 tot 250 m. De LAS gebruikt een enkele bundel van, in dit geval, 10 cm doorsnee en kan worden gebruikt over een afstand van $\sim 100 - 2000$ m. Beide scintillometers meten intensiteitsfluctuaties van de lichtbundel die door de zender wordt uitgezonden en geregistreerd door de ontvanger. Deze fluctuaties worden veroorzaakt door refractie of breking van de bundel op zijn tocht door de turbulente oppervlaktelaag en zijn een maat voor de structuurparameter van temperatuur, C_T^2 . De DBSAS verkrijgt ook de dissipatiesnelheid van de turbulente kinetische energie (TKE), ε , uit de correlatie, r_{12} , tussen de fluctuaties van de twee verschoven bundels. Op zichzelf zijn beiden grootheden belangrijke kentallen van atmosferische turbulentie. Bovendien, als de oppervlaktelaag turbulent is zijn ze op grond van de Monin-Obukhov similariteits theorie (MOST) verbonden met de turbulente fluxen van warmte, H , en impuls, τ , doorgaans uitgedrukt als de snelheidsschaal u^* .

Voor de LAS waarmee alleen C_T^2 kan worden bepaald, is het gebruikelijk om gemeten windsnelheid op één hoogte en een schatting van de ruwheidslengte toe te voegen om H en u^* op te lossen. Tevens hebben we ook gekeken naar combinaties van DBSAS en LAS om samen ε en C_T^2 op te lossen.

De DBSAS is de meest geschikte scintillometer om gebruikt te worden in de SBL, omdat het een maat geeft voor de mechanisch gegeneerde turbulentie, dwz turbulentie gegeneerd door windschering, hetgeen in stabiele omstandigheden de drijvende kracht is van turbulentie.

In alle scintillometertoepassingen dient er een aanname te worden gedaan over de wettelijke uitdrukking van het n -spectrum (n is de brekingsindex), welke voor optische scintillometrie gelijk kan worden verondersteld aan het temperatuurspectrum. De DBSAS ziet vooral de kleinste wervels van het turbulente spectrum die onderdeel zijn van de dissipatie-range. Een modelbeschrijving van dit gedeelte van het spectrum is gegeven door Hill (1978) en is gebaseerd op slechts enkele waarnemingen. Het laat zien dat op de overgang van de inertial naar de dissipatie-range het spectrum een klein hobbeltje heeft, de zogenaamde Hill-bump. Een lengteschaal die deze overgang markeert is de inner-scale, l_0 , welke wordt gebruikt om het dissipatie spectrum te beschrijven. De DBSAS methode lost l_0 op waaruit ε direct te bepalen is. De LAS ziet voornamelijk wervels van een grootte die in de inertial-range van het spectrum valt, en hiervoor is alleen de alom geaccepteerde beschrijving van dit deel van het spectrum nodig om C_T^2 op te lossen.

Scintillometers hebben het grote voordeel dat zij zowel tijd- als ruimtemiddeling van turbulentie combineren, in tegenstelling tot de EC-methode, die alleen in tijd middelt. Hierdoor is het mogelijk met de scintillometer veel kortere flux middelingsintervallen toe te passen tot minder dan 1 minuut. Verder zijn scintillometers gevoelig voor één enkele wervel (eddy)-grootte en vullen de rest van de turbulente schalen in dmv een theoretisch spectrum, itt de EC-methode die de flux integreert over alle gemeten wervel-schalen. Dit betekent dat de scintillometer methode niet gevoelig is voor pad-middelingseffecten en pal boven het oppervlak kan worden opgesteld (< 1 m).

We hebben bijgedragen aan twee veldexperimenten die de basis vormen van dit proefschrift, te weten het CASES-99 experiment (Kansas, USA, 1999, zie hoofdstukken 3 en 4), dat gaat over de nachtelijke SBL, en het BBC experiment (Cabauw, Nederland, 2001, zie hoofdstuk 5), waar we verschillende veldschaal scintillometer configuraties hebben getest. Een derde experiment, RAPID (Idaho, USA, 1999), gaat over SBLs overdag is niet geanalyseerd als onderdeel van dit proefschrift. Er is wel een co-auteur publicatie uitgekomen die opgenomen is in de appendix. We hebben tevens een oude scintillometer data-set geanalyseerd van het La-Poza experiment (Sonora, Mexico, 1996, zie hoofdstuk 6), waar we het effect van een variërende scintillometer bundelhoogte hebben bestudeerd. De conclusies van deze studies zijn gerangschikt per hoofdstuk.

Hoofdstuk 3: Toepassing van de DBSAS in stabiele omstandigheden tijdens het CASES-99 experiment.

De toepassing van de DBSAS in de SBL was onderzocht met data verzameld tijdens CASES-99. De DBSAS was opgesteld over een padlengte van 112 m. We hebben laten zien dat de DBSAS superieur is over de EC-methode in het bepalen van H en u^* dichtbij het oppervlak en over korte (< 1 minuut) middelingsintervallen.

Om een onafhankelijke maat te hebben voor ε en C_T^2 is er een script ontwikkeld dat automatisch deze waarden schat uit EC-data, dwz uit metingen van een sonische windsnelheidsmeter. De methodes die hiervoor worden gebruikt zijn gebaseerd op de definitie van structuurparameters en theoretische inertial-range spectra.

We hebben systematische fouten gevonden voor de DBSAS ε en C_T^2 in vergelijking met de uit EC-data bepaalde waarden, hetgeen ook resulteerde in systematische fouten in de DBSAS H en u^* . De gevonden spreiding, echter, was zeer laag. De systematische fouten in H komen vooral voort uit fouten in u^* , welke door de DBSAS wordt overschat voor lage u^* en onderschat voor hoge u^* . We waren in staat hiervoor te corrigeren door de bundelafstand, d , aan te passen van 2.7 mm naar 2.6 mm in de berekeningen; een aanpassing die valt binnen de nauwkeurigheid waarmee de fabrikant d specificeert. Deze aanpassing is gepresenteerd als een werkhypothese, niet als een algemene oplossing.

We hebben ook de gevoeligheid van de DBSAS methode laten zien voor de exacte vorm van het dissipatie-range spectrum (we gebruiken de vorm gegeven door Frehlich, 1992). Voor grote l_0 , dwz kleine u^* , wordt slechts een klein deel van het spectrum meegewogen. Dit geeft aan dat de theoretische basis voor de DBSAS zeer klein wordt voor grote l_0 ; het hangt zeer sterk af van de exacte vorm van het spectrum in dit gebied en dat van de spectrale wegingfunctie.

In de appendix die in dit proefschrift aan deze studie is toegevoegd worden, naast de d -aanpassing, nog drie heuristische benaderingen besproken die de systematische fouten aanpakken. Ten eerste hebben we het dissipatie-range spectrum dusdanig aangepast dat de theoretische r_{12} versus l_0 relatie convergeerde met de DBSAS gemeten r_{12} versus EC-data bepaalde l_0 . Met deze benadering verdwijnen de systematische fouten in ε , maar de fouten in C_T^2 , en daarmee ook in H , worden juist verergerd. Ten tweede hebben we direct een mathematische relatie gefit tussen de DBSAS gemeten r_{12} en EC-data bepaalde l_0 . Deze aanpak werkte bevredigend voor zowel ε als C_T^2 . Als derde hebben we alle stappen die zitten tussen ruwe metingen en fluxen gepasseerd door deze direct aan elkaar te relateren. Deze aanpak doet het verassend genoeg erg goed. Alle ad-hoc relaties die we zo hebben afgeleid kunnen alleen worden toegepast op een specifieke opstelling en stabiliteitsrange waarvoor ze zijn bepaald.

Hoofdstuk 4: Bepaling van MOST schalingsfuncties voor ε en C_T^2 in de SSL.

Om oppervlaktefluxen te bepalen met scintillometers zijn de MOST functies f_ε en f_T van de dimensieloze ε en C_T^2 groepen nodig. Volgens MOST zijn deze een universele functie van de dimensieloze hoogte, $\zeta = z/L$, waar z staat voor hoogte en L is de Monin-Obukhov lengte.

Voor stabiele condities waren f_ε en f_T nog niet goed bepaald. Gebruik makend van de CASES-99 dataset, die een uiterst grote stabiliteitsrange kent (ζ tot ~ 10 , voor $z = 2.5$ m), hebben we deze relaties bepaald gebaseerd op ε , C_T^2 en flux-schattingen uit EC-data gemeten op 2.65 m. De beste fit werd gegeven door $f_\varepsilon = 0.8 + 2.5\zeta$ en $f_T = 4.7[1 + 1.6(\zeta)^{2/3}]$, die iets verschillen van eerder gepubliceerde functies.

De neutrale limiet $f_\varepsilon = 0.8$ houdt in dat er in het vereenvoudigde TKE budget een imbalans is tussen TKE productie en dissipatie. Evenzo vonden we een productie-dissipatie imbalans voor het temperatuur variantie budget. Met een correctie voor deze imbalansen, hebben we uit f_ε en f_T de ‘standaard’ MOST functies voor de dimensieloze windsnelheid en temperatuur gradiënten (ϕ_m en ϕ_h) bepaald en vergeleken met de ϕ_m en ϕ_h en flux- en gradiënt Richardson-getal uitdrukkingen in de literatuur. Onze resultaten laten zien dat het bepalen van ϕ_m en ϕ_h , gebruik makend van ε and C_T^2 bepaald uit sonische anemometer metingen op een enkele hoogte, een goed alternatief vormt in zeer stabiele omstandigheden, daar in die stabiliteitsrange de fouten in gradiëntmetingen erg groot zijn.

Hoofdstuk 5: Test van veldschaal scintillometers tijdens het BBC experiment.

We hebben drie veldschaal scintillometer configuraties vergeleken tijdens het BBC experiment: de DBSAS, de LAS en gecombineerde DBSAS-LAS configuraties. Met veldschaal bedoelen we korte padlengtes van ~ 100 tot 200 m. Het doel van deze studie was de drie scintillometer configuraties met elkaar te vergelijken en te zien of de LAS en de gecombineerde scintillometer configuraties dezelfde systematische fouten in ε , C_T^2 en de fluxen zouden laten zien als de DBSAS voor stabiele omstandigheden tijdens CASES-99 (hoofdstuk 3). Verder, diende het ook als een onafhankelijke test voor de nieuw gepubliceerde stabiele MOST functies die zijn gebaseerd op CASES-99 data (hoofdstuk 4).

We hebben een 10 cm openingshoek LAS gebruikt die iets l_0 gevoelig is, dwz gevoelig voor de Hill-bump. Het concept van een gecombineerde LAS-DBSAS is volledig nieuw. Hoewel we ook onstabiele omstandigheden hebben geanalyseerd, gaan we hier alleen in op de resultaten voor stabiele omstandigheden. Het onderlinge vergelijk tussen de verschillende scintillometer configuraties is gedaan ten opzichte van EC-data bepaalde ε , C_T^2 en fluxen. De padlengte van alle scintillometers was ~ 120 m.

Voor de DBSAS vonden we dezelfde systematische afwijkingen en heel weinig spreiding voor ε , C_T^2 en de resulterende u^* en H , in lijn met wat we ook vonden in hoofdstuk 3 voor CASES-99.

De LAS C_T^2 -schatting is beter dan de DBSAS C_T^2 -schatting. Echter, de u^* en H van de LAS zijn beduidend slechter dan de DBSAS waarden. In stabiele omstandigheden wordt de turbulentie gevoed door mechanische turbulentie (u^*), welke in de LAS methode slechts indirect wordt geschat uit windsnelheidsmeting en een schatting voor de ruweidslengte.

De DBSAS-LAS configuratie waarin l_0 en C_T^2 tezamen worden opgelost uit de gemeten fluctuaties van één LAS en één DBSAS bundel geeft hetzelfde resultaat voor C_T^2 als met de LAS, maar een tegenvallende resultaat voor l_0 (zeer veel spreiding). Dit vindt zijn weerslag in

de flux-schattingen; u^* geeft zeer veel spreiding dat weer op zijn beurt veel spreiding geeft in H .

De DBSAS-LAS configuratie waarin l_0 en C_T^2 worden opgelost uit beide DBSAS bundels en de enkele LAS bundel geeft betere resultaten. In deze configuratie geeft de LAS C_T^2 en de DBSAS ε . Deze set-up combineert de sterke kanten van beide instrumenten. C_T^2 wordt bepaald met de LAS op inertial-range wervel schalen, and ε wordt bepaald met de DBSAS over hetzelfde pad als C_T^2 . Echter, itt de DBSAS heeft u^* van de LAS en de twee DBSAS-LAS configuraties een beperkte range vergeleken met de EC- u^* . Als gevolg hiervan geeft H van deze configuraties meer spreiding dan de DBSAS in stabiele omstandigheden.

We hebben een praktische aanpak geïntroduceerd om te corrigeren voor de LAS inner-scale afhankelijkheid, die afhangt van de openingshoek van de LAS en l_0 . De LAS die we hier hebben gebruikt hebben, had een openingshoek van 10 cm. Bij lage windsnelheid, als l_0 groot is, kan deze correctie dan oplopen tot 30 % op C_T^2 .

We hebben een nieuwe analytische uitdrukking geïntroduceerd voor Hill's model van het temperatuurspectrum in de dissipatie-range (Hill, 1978). Deze analytische fit voldoet aan de condities gedefinieerd door Frehlich, (1992) en vergemakkelijkt de berekening van l_0 uit de ruwe DBSAS-data.

Hoofdstuk 6: De afleiding van een effectieve scintillometer hoogte.

In de praktijk varieert de LAS bundel hoogte vaak over het pad om uiteenlopende redenen. In deze studie leggen we uit welke effectieve hoogte in dit soort situaties te gebruiken, als het doel is om H te berekenen. Verscheidene aspecten worden behandeld: een schuin pad over een vlak terrein, golvend terrein en variërende bundelhoogte door de kromming van de aarde. Om de afgeleide effectieve hoogte formuleringen te testen gebruiken wij LAS-data die we hebben verzameld in september en oktober 1996 in een natuurlijk weidelandschap in Sonora, Mexico. In experiment I was de LAS opgesteld met een schuin pad, variërend van ~ 10 tot 45 m boven het oppervlak en over een padlengte van 3200 m. In experiment II, was de LAS opgesteld met een horizontaal pad op ~ 30 m hoogte en een padlengte van 1100 m. De resulterende H is vergeleken met EC-data die bevredigende resultaten gaf voor zowel de volledige effectieve hoogte formulering, die een functie is van stabiliteit, als voor de benaderingsuitdrukkingen, die geen functie zijn van stabiliteit, voor zowel onstabiele als stabiel omstandigheden.

Met inachtneming van de instrumentele en theoretische aannames kan worden geconcludeerd dat de DBSAS zich bewezen heeft als een goed onderzoeksinstrument voor de bestudering van de SBL. De voornaamste voordelen van de DBSAS zijn zijn superioriteit over de traditionele EC-methode in het verkrijgen van fluxen zeer dicht aan het oppervlak en over zeer korte middelingsintervallen met uiterst weinig spreiding. Echter de systematische fouten van de DBSAS verkregen ε , C_T^2 en de resulterende fluxen is nog steeds een onopgeloste kwestie. Toepassing van de LAS en combinaties van DBSAS en LAS leverden geen verbetering op. De systematische fouten werden wel aangepakt middels verscheidene ad-hoc

oplossingen die niet universeel toepasbaar zijn. We zijn ons ervan bewust dat details van onze aanpak in deze oplossingen twijfelachtig mogen zijn, maar ze zijn wel bruikbaar om waardevolle informatie te verkrijgen over de variabelen die stabiele, turbulente stromingen drijven.

Zaken die nog onderzocht kunnen worden waarvan wij denken dat ze bijdragen aan een beter begrip van de systematische afwijkingen van de DBSAS en alternatieve scintillometer methodes die succesvol toegepast kunnen worden in de SBL:

- Het verrichten van metingen van atmosferische dissipatie-range temperatuurspectra onder verschillende stabiliteitscondities. We hebben reeds gepoogd deze metingen uit te voeren, maar zijn daarin niet geslaagd. Puntmetingen van turbulentie op de allerkleinste schalen zijn technische zeer veeleisend wat betreft de gebruikte materialen, ruisvrije elektronica van de brugmeting, datalogstelsel etc. Een alternatieve methode leidt het spectrum af uit scintillometer metingen naar Frehlich (1992), die een enkele zender gebruikte met een rij ontvangers. Dit idee kan uitgebreid worden gebruik makend van fotogevoelige chips, waarmee, in principe, een oneindige rij ontvangers van verscheidene afmetingen en in alle richtingen kan worden gesimuleerd (Hill, persoonlijke communicatie).
- Onderzoek de mogelijkheid van een gecombineerde laser – large-aperture scintillometer geïntegreerd in één sensor. In hoofdstuk 5 hebben we met dit idee geëxperimenteerd gebruik makend van aparte sensors, hetgeen uiteindelijk niet succesvol bleek. Met integratie van de sensors verzekert men zich ervan dat precies hetzelfde pad wordt bemeaten en dat de timing van de metingen en het datalogstelsel exact synchronisatie loopt.
- Onderzoek de mogelijkheid van een gecombineerde enkele LAS zender die l_0 gevoelig is (openingshoek van minder dan 10 cm) en twee of meer LAS ontvangers (bv met een openingshoek van 1 en 5 cm) om daaruit tezamen l_0 en C_T^2 op te lossen.

Curriculum Vitae

Ik, Oscar Karel Hartogensis, werd geboren op 28 februari 1972 te Baarn. Na het doorlopen van het VWO op het Griffland College in Soest wat ik heb afgerond op het Goois Dag- en Avond College te Hilversum ben ik in 1991 naar Wageningen gekomen om Bodem-Water-Atmosfeer te studeren met als specialisatierichting Meteorologie. Begin 1995 heb ik 3 maanden vakken gevolgd bij de department of Meteorology van de University of Reading, Engeland in het kader van het Europese ERASMUS uitwisselingsprogramma. Later dat jaar ging ik op reis naar Mexico voor een stage bij het instituut CIDESON (Centro de Investigación y Desarrollo de Sonora) in Hermosillo, Sonora. Daar heb ik een unieke mogelijkheid gehad om dat wat ik leuk vind aan het vakgebied meteorologie verder te ontdekken en te ontplooiën; te weten micro-meteorologisch onderzoek en dan in het bijzonder het uitvoeren van veldexperimenten. Na deze stage, was ik enkele maanden later weer terug op CIDESON voor een veldonderzoek in het kader van mijn afstudeervak. We hebben toen bij dezelfde opstelling die we eerder dat jaar hadden geïnstalleerd een scintillometer opgesteld. Dit werk heeft uiteindelijk geleid tot een publicatie dat ook onderdeel is van dit proefschrift. In 1997 heb ik 4 maanden voor het Franse CESBIO - destijds ORSTOM genaamd – gewerkt, wederom in Sonora, Mexico in het kader van het Amerikaans-Mexicaanse project SALSA. Na mijn afstuderen in 1998 heb ik vele aanstellingen mogen genieten bij de vakgroep Meteorologie en Luchtkwaliteit (MAQ) van de Wageningen Universiteit die mij tot op de dag van vandaag aan deze groep verbinden. Ik ben begonnen als toegevoegd onderzoeker in het kader waarvan ik betrokken ben geweest bij verschillende nationale en internationale veldexperimenten, waaronder het CASES-99 experiment in 1999 in Kansas, USA. Een overzicht met een beknopte beschrijving en wetenschappelijke output van al deze experimenten is gegeven in Appendix I. Vanaf 2001 ben ik aangesteld als onderzoeker in opleiding (OIO) op het door NWO gefinancierde project “Intermittent turbulence in the atmospheric surface layer; a Dutch contribution to the International Project CASES”. Het resultaat hiervan ligt thans voor u. Uiteindelijk heeft dit onderzoek zich gefocusseerd op de toepassing van scintillometrie in de stabiele grenslaag over land. Naast de OIO baan had ik in het tweede traject van de promotie nog twee andere aanstellingen, namelijk het Europees gefinancierde IRRIMED project en als toegevoegd onderzoeker bij MAQ. In het kader van de laatstgenoemde aanstelling ben ik ook betrokken geweest bij het onderwijs van MAQ, te weten bij het vak Atmosfeer Land Interacties (werkcolleges vanaf 2003) en het micro-meteorologisch veldpracticum (reeds vanaf 1999).

This study was carried out at the Meteorology and Air Quality Group, Wageningen University, Netherlands within the framework of the Buys Ballot Research School and financed by the research council of the Netherlands Organization of Scientific Research (NWO) under project number 810.033.005.

Thesis printing: Grafisch Service Centrum Van Gils BV, Wageningen

Back cover: Photos from the experiments covered in this thesis. From top to bottom:

- CASES-99 (Kansas, USA, 1999)
- RAPID (Idaho, USA, 1999)
- BBC (Cabauw, the Netherlands, 2001)
- La Poza (Sonora, Mexico, 1996)